Microstructuring inkjet-printed deposits from silver nanoparticules coalescence to the fabrication of interconnections for electronic devices.

Romain Cauchois

Ecole Nationale Supérieure des Mines
SAINT-ETIENNE

NNT : *2012 EMSE 0643*

THÈSE

présentée par

Romain CAUCHOIS

pour obtenir le grade de
Docteur de l'École Nationale Supérieure des Mines de Saint-Étienne

Spécialité : Microélectronique

MICROSTRUCTURATION DES DEPOTS IMPRIMES PAR JET D'ENCRE : DE LA COALESCENCE DES NANOPARTICULES D'ARGENT VERS LA REALISATION D'INTERCONNEXIONS DE COMPOSANTS ELECTRONIQUES

Soutenue au Centre Microélectronique de Provence à Gardanne, le 07 février 2012

Membres du jury

Président :	Frédéric BERNARD	Professeur, Université de Bourgogne, Dijon
Rapporteurs :	Fred ROOZEBOOM	Professeur, TU Eindhoven, Pays-Bas
	Didier BOUVARD	Professeur, Grenoble INP, Grenoble
Examinateurs :	András BORBÉLY	Maître de Recherche, ENSM-SE, Saint-Etienne
	Heikki SEPPÄ	Professeur, VTT, Espoo, Finlande
Directeur de thèse :	Karim INAL	Professeur, ENSM-SE, Gardanne
Co-encadrante :	Béatrice DUBOIS-BONVALOT	Ingénieur R&D, Gemalto, Gémenos
Co-encadrant :	Mohamed SAADAOUI	Chargé de recherche, ENSM-SE, Gardanne
Invités :	Christophe SERBUTOVIEZ	Chercheur, CEA LITEN, Grenoble
	Olivier VENDIER	Ingénieur R&D, Thales Alenia Space, Toulouse

Spécialités doctorales :
SCIENCES ET GENIE DES MATERIAUX
MECANIQUE ET INGENIERIE
GENIE DES PROCEDES
SCIENCES DE LA TERRE
SCIENCES ET GENIE DE L'ENVIRONNEMENT
MATHEMATIQUES APPLIQUEES
INFORMATIQUE
IMAGE, VISION, SIGNAL
GENIE INDUSTRIEL
MICROELECTRONIQUE

Responsables :
J. DRIVER Directeur de recherche – Centre SMS
A. VAUTRIN Professeur – Centre SMS
F. GRUY Professeur – Centre SPIN
B. GUY Maître de recherche – Centre SPIN
J. BOURGOIS Professeur – Fayol
E. TOUBOUL Ingénieur – Fayol
O. BOISSIER Professeur – Fayol
JC. PINOLI Professeur – Centre CIS
P. BURLAT Professeur – Fayol
Ph. COLLOT Professeur – Centre CMP

Enseignants-chercheurs et chercheurs autorisés à diriger des thèses de doctorat (titulaires d'un doctorat d'État ou d'une HDR)

AVRIL	Stéphane	MA	Mécanique & Ingénierie	CIS
BATTON-HUBERT	Mireille	MA	Sciences & Génie de l'Environnement	Fayol
BENABEN	Patrick	PR 1	Sciences & Génie des Matériaux	CMP
BERNACHE-ASSOLLANT	Didier	PR 0	Génie des Procédés	CIS
BIGOT	Jean-Pierre	MR	Génie des Procédés	SPIN
BILAL	Essaïd	DR	Sciences de la Terre	SPIN
BOISSIER	Olivier	PR 1	Informatique	Fayol
BORBELY	Andras	MR	Sciences et Génie des Matériaux	SMS
BOUCHER	Xavier	MA	Génie Industriel	Fayol
BOUDAREL	Marie-Reine	PR 2	Génie Industriel	DF
BOURGOIS	Jacques	PR 0	Sciences & Génie de l'Environnement	Fayol
BRODHAG	Christian	DR	Sciences & Génie de l'Environnement	Fayol
BURLAT	Patrick	PR 2	Génie industriel	Fayol
COLLOT	Philippe	PR 1	Microélectronique	CMP
COURNIL	Michel	PR 0	Génie des Procédés	SPIN
DAUZERE-PERES	Stéphane	PR 1	Génie industriel	CMP
DARRIEULAT	Michel	IGM	Sciences & Génie des Matériaux	SMS
DECHOMETS	Roland	PR 1	Sciences & Génie de l'Environnement	Fayol
DESRAYAUD	Christophe	MA	Mécanique & Ingénierie	SMS
DELAFOSSE	David	PR 1	Sciences & Génie des Matériaux	SMS
DOLGUI	Alexandre	PR 1	Génie Industriel	Fayol
DRAPIER	Sylvain	PR 2	Mécanique & Ingénierie	SMS
DRIVER	Julian	DR 0	Sciences & Génie des Matériaux	SMS
FEILLET	Dominique	PR 2	Génie Industriel	CMP
FOREST	Bernard	PR 1	Sciences & Génie des Matériaux	CIS
FORMISYN	Pascal	PR 1	Sciences & Génie de l'Environnement	Fayol
FRACZKIEWICZ	Anna	DR	Sciences & Génie des Matériaux	SMS
GARCIA	Daniel	MR	Génie des Procédés	SPIN
GIRARDOT	Jean-Jacques	MR	Informatique	Fayol
GOEURIOT	Dominique	MR	Sciences & Génie des Matériaux	SMS
GRAILLOT	Didier	DR	Sciences & Génie de l'Environnement	Fayol
GROSSEAU	Philippe	MR	Génie des Procédés	SPIN
GRUY	Frédéric	MR	Génie des Procédés	SPIN
GUY	Bernard	MR	Sciences de la Terre	SPIN
GUYONNET	René	DR	Génie des Procédés	SPIN
HERRI	Jean-Michel	PR 2	Génie des Procédés	SPIN
INAL	Karim	PR 2	Microélectronique	CMP
KLÖCKER	Helmut	DR	Sciences & Génie des Matériaux	SMS
LAFOREST	Valérie	CR	Sciences & Génie de l'Environnement	Fayol
LERICHE	Rodolphe	CR CNRS	Mécanique et Ingénierie	SMS
LI	Jean-Michel	EC (CCI MP)	Microélectronique	CMP
MALLIARAS	George Grégory	PR 1	Microélectronique	CMP
MOLIMARD	Jérôme	MA	Mécanique et Ingénierie	SMS
MONTHEILLET	Frank	DR 1 CNRS	Sciences & Génie des Matériaux	SMS
PERIER-CAMBY	Laurent	PR 2	Génie des Procédés	SPIN
PIJOLAT	Christophe	PR 1	Génie des Procédés	SPIN
PIJOLAT	Michèle	PR 1	Génie des Procédés	SPIN
PINOLI	Jean-Charles	PR 0	Image, Vision, Signal	CIS
STOLARZ	Jacques	CR	Sciences & Génie des Matériaux	SMS
SZAFNICKI	Konrad	MR	Sciences & Génie de l'Environnement	Fayol
THOMAS	Gérard	PR 0	Génie des Procédés	SPIN
TRIA	Assia		Microélectronique	CMP
VALDIVIESO	François	MA	Sciences & Génie des Matériaux	SMS
VIRICELLE	Jean-Paul	MR	Génie des procédés	SPIN
WOLSKI	Krzysztof	DR	Sciences & Génie des Matériaux	SMS
XIE	Xiaolan	PR 1	Génie industriel	CIS

Glossaire :

PR 0	Professeur classe exceptionnelle
PR 1	Professeur 1ère classe
PR 2	Professeur 2ème classe
MA(MDC)	Maître assistant
DR	Directeur de recherche
Ing.	Ingénieur
MR(DR2)	Maître de recherche
CR	Chargé de recherche
EC	Enseignant-chercheur
IGM	Ingénieur général des mines

Centres :

SMS	Sciences des Matériaux et des Structures
SPIN	Sciences des Processus Industriels et Naturels
Fayol	Institut Henri Fayol
CMP	Centre de Microélectronique de Provence
CIS	Centre Ingénierie et Santé

Dernière mise à jour le : 23 août 2011

- Voici mon secret. Il est très simple: on ne voit bien qu'avec le cœur. L'essentiel est invisible pour les yeux.

- L'essentiel est invisible pour les yeux, répéta le petit prince, afin de se souvenir.

- C'est le temps que tu as perdu pour ta rose qui fait ta rose si importante.

- C'est le temps que j'ai perdu pour ma rose... fit le petit prince, afin de se souvenir.

- Les hommes ont oublié cette vérité, dit le renard. Mais tu ne dois pas l'oublier. Tu deviens responsable pour toujours de ce que tu as apprivoisé. Tu es responsable de ta rose...

- Je suis responsable de ma rose... répéta le petit prince, afin de se souvenir.

Antoine de Saint-Exupéry.
Le Petit Prince (1943).

Avant-propos et remerciements

Une thèse est toujours une grande aventure dans laquelle on se lance sans toujours bien savoir où elle va nous conduire, ni surtout par quels chemins. Et, parfois, quand on ne sait pas trop où on va, on peut finalement se retrouver ailleurs… C'est ce qui fait la beauté de la science et qui mène parfois à de grandes découvertes, si tant est qu'on soit pourvu d'un rouleau de scotch (*dixit* G. Charpak) ! Si certains comparent la thèse à un marathon ou, dans le pire des cas, à une course d'obstacles, mes racines bretonnes me poussent davantage vers une métaphore maritime. En effet, bien des fois, j'ai eu le sentiment que cette thèse s'apparentait à la traversée d'un océan, accompagnée de ses vents contraires, de ses mers d'huile, de sa houle, voire même de tempêtes où tout l'équipage doit s'activer sur le pont. Heureusement, les vents sont parfois plus cléments et, passé l'excitation du départ en mer, la fatigue laisse finalement place au soulagement quand on aperçoit un bout de terre et que le navire rejoint enfin son port d'amarrage, signant la fin du périple.

Jusqu'à ce jour, personne ne m'a encore questionné sur les raisons qui m'ont poussé à opter pour ce sujet de thèse plutôt qu'un autre. Aujourd'hui, l'occasion m'est donnée d'éclaircir un peu les raisons de ce choix qui m'a engagé pour 3 années de dur labeur. Si, bien évidemment, le facteur humain a joué un rôle important dans cette décision (avoir passé toute une année avec des gens formidables est en effet rarement négligeable, mais j'y reviendrai par la suite…), le sujet et le contenu de cette thèse sont loin d'avoir été anodins. Alors, certes, avoir précédemment travaillé dans le domaine de la métallurgie des poudres m'a permis d'être déjà familier avec le phénomène de frittage au cours duquel des agglomérats de poudre sont solidifiés. Avec cette thèse, l'occasion s'est présentée de travailler sur des objets à l'échelle nanométrique et d'analyser avec finesse ce qui pouvait donner lieu à ce phénomène si particulier qu'est la coalescence. Car, au fond, qu'est ce que la coalescence sinon une opération magique qui permet à des particules isolées de former une structure interconnectée ? Et j'avoue que la simple idée qu'une entité aussi petite et insignifiante parvienne à créer ces ponts avec d'autant plus de facilités, me fascine pour le moins. L'être humain étant tout aussi petit et insignifiant à l'échelle de l'univers, je ne vois pas en quoi nous serions moins aptes à mettre en œuvre la même magie. Aussi, toi lecteur, si tu fais partie des *happy few* dont la curiosité est piquée par cette magie, je t'invite à t'amuser des parallèles qui peuvent être dressés à partir des résultats obtenus dans cette thèse. Tu verras alors que ces travaux auront un écho tout particulier qui, je l'espère, te feront prendre conscience que, si elle prend parfois des chemins détournés, la Nature est quand même grandiose.

Pour revenir à nos moutons, même si cela est plutôt inhabituel comme propos, je voulais ici profiter de cette tribune qui m'est offerte pour dire à quel point j'ai pu apprécier de faire cette thèse. En plus d'un bilan particulièrement riche sur les plans scientifique et technique (comme peuvent le prouver j'espère les quelque 220 pages qui vont suivre), cette aventure a été tout autant, voire plus, trépidante sur le plan humain. J'ai passé au sein de ce laboratoire de belles années où j'ai pu rencontrer des gens formidables qui, chacun à leur manière, m'ont enrichi. Et indépendamment des expériences ratées, des machines en panne, des hypothèses et espoirs invalidés, de tout ce qui fait en somme le quotidien d'un jeune chercheur en formation, je peux vous l'avouer aujourd'hui, j'ai pris plaisir à venir travailler chaque jour à vos côtés. D'une certaine façon, vous avez également contribué à la bonne tenue de ces travaux, et je voudrais en profiter pour vous exprimer toute ma gratitude via ces quelques lignes.

Je tiens en premier lieu à remercier les initiateurs de ce projet de recherche, pour tout le temps qu'ils y ont consacré depuis les fonts baptismaux jusqu'à un certain 7 février 2012. Parmi ces armateurs de talents, au sein de Gemalto, je remercie notamment Jean-Christophe Fidalgo, responsable du groupe Innovation d'IMT, pour avoir défendu, parfois contre vents et marées, l'introduction de cette technologie d'impression au niveau industriel. Je tiens aussi à exprimer toute ma reconnaissance à Béatrice Dubois-Bonvalot, responsable de l'équipe de packaging avancé, pour m'avoir laissé une très grande liberté d'action dans la conduite de mes travaux de recherche. Son professionnalisme, ses connaissances et son apport ont été inestimables. Sa disponibilité, sa bonne humeur permanente et sa très grande capacité à l'autodérision ont toujours été au cours des trois années de véritables bouffées d'oxygène.

Du côté des porteurs académiques de ce projet, je remercie tout d'abord mon directeur de thèse, Karim Inal, sans qui cette thèse n'aurait pas vu le jour. Je lui suis particulièrement reconnaissant pour la confiance qu'il m'a accordée et pour avoir fait preuve d'une très grande compréhension à mon égard face à un pragmatisme assumé. Merci pour ta patience et ta proximité. Je tiens également à remercier chaleureusement Mohamed Saadaoui pour tout son investissement et sa disponibilité tout au long de ces trois années. Merci pour toutes ces soirées et ces week-ends passés à travailler, à discuter de tout et de rien, à refaire le monde autour d'une de ces fameuses glaces du cours Mirabeau. Les mots me manquent pour exprimer tout ce que je lui dois pour son excellent encadrement scientifique, sa rigueur et ses conseils. Son implication et ses encouragements dépassent à mon sens largement ce qu'un doctorant peut attendre de son encadrant, et je m'estime chanceux d'avoir pu bénéficier de son expérience. Sois assuré de ma profonde reconnaissance et de mon amitié sincère. Saha ya sahbi.

Pour l'honneur qu'ils m'ont fait de participer à mon jury de thèse et pour leur analyse critique de ce mémoire de thèse, j'exprime également mes remerciements à Fred Roozeboom et Didier Bouvard qui ont rapporté ce travail de thèse, ainsi qu'à Frédéric Bernard, András

Borbély et Heikki Seppä qui l'ont examiné. Je remercie également Christophe Serbutoviez et Olivier Vendier pour l'intérêt qu'ils ont manifesté à ces travaux. Ce fut un réel plaisir pour moi d'avoir pu discuter, débattre et échanger des points de vue avec autant d'experts reconnus.

Ces travaux de thèse se sont déroulés au sein du Centre Microélectronique de Provence, sur le site Georges Charpak de l'École Nationale Supérieure des Mines de Saint-Etienne. Je remercie Philippe Collot, le directeur du Centre, ainsi que Patrick Benaben, responsable de l'équipe de Packaging et Supports Souples (PS2) pour leur accueil. J'adresse également toute ma reconnaissance et ma sympathie aux petites mains qui restent dans l'ombre, mais sans qui la maison ne tournerait pas si bien. Je veux bien sûr parler de toutes les fonctions supports, depuis le service info, jusqu'au service infra, en passant par l'administration et l'accueil. En particulier, un grand merci à la dream team : Véronique (qui chouchoute les doctorants comme personne malgré le lot de misères administratives qu'on peut parfois lui causer), Barbara (la gardannaise, la vraie, mais "un peu" fan de l'OM quand même !), Sabine (dis, dis, j'ai battu le record alors ? Et, promis, des photos tu auras !), Tess et Alexa (le premier sourire matinal) et bien sûr Manon, Michelle, Anne-Marie et Christelle. La gent masculine n'est pas non plus en reste : un grand merci à Gracien (une [res]source fiable jamais avare en prompts dépannages, en matériel et en traits d'humour, et toujours avec le sourire malgré 36h de travail quotidien), Axel (président exilé au pays des Caribous), Georges (notamment pour les voyages Gardanne-Sainté et une certaine visite des cuisines lors d'un épisode neigeux apocalyptique digne du « *Jour d'après* »), Serge (qui fait souffler le chaud et le froid au CMP) ainsi que Jonathan, Denis et Grégory.

Je remercie également tout le personnel scientifique du CMP pour tous les bons moments et les échanges autour d'un café, au détour d'un couloir ou de manière plus informelle sur un terrain, une terrasse ou une plage. Je pense surtout à Anne-Lise, Laurent (pour ses vêtements tactiles), Jean-Baptiste, Jean-Max et Serge du département Sécurité et Architectures Sécurisées, à Bernard, Agnès et Nabil du département des Sciences de la Fabrication et de la Logistique, ainsi que George Malliaras, Róisín et Leslie du département de Bioélectronique pour leur aide précieuse. Pour tous les bons moments passés ensemble, je remercie l'ensemble des membres de PS2 : Mathieu F., François (dont les grains en cuivre de 10 km font toujours référence dans le domaine des MEMS), Abdel (-watwo), Mathieu M, Sylvain B., Jacques, Jean-Michel, Man, Gaëlle (spécialiste des boîtes et des cafés froids en fin de pause), Cyril, Aurélie, Sylvain N., Oussama, Aline, Xavier (pour m'avoir, le premier, donné ma chance), Henda (tes éclats de rire résonnent jusqu'à la lune), Éloïse, Véronique O., Mathieu R., Thomas, Alex, Daniel, Malika, Jérôme, Hoang-Sinh, Diana, Romuald L., Simon, Arthur, Ali, Mylène, Maryam, Julie, Thibault et bien sûr Ruoteng (l'inimitable miss Verdon). Toutes mes pensées accompagnent également Pierre, disparu trop tôt, mais toujours présent dans ma mémoire avec une vive émotion.

J’adresse aussi mes vifs remerciement à toute l’équipe gemaltienne de gardanne : Fred et Thierry (les inséparables siamois, aka Tic&Tac, ♪*in the Gardanne* ♫), Marie-Edith, Michel, Pierre-Antoine, Raphaël, mais également de Gémenos : Jean-Marie, Alain, Laurence, Aurélie et François (Oum Oum).

Enfin, j’adresse toute ma sympathie à celles et ceux qui partagent (ou ont partagé) ma condition de doctorant, et dont j’ai défendu les intérêts du mieux possible. Je pense notamment à Selma, Amir, Sylvain, Minh Huu, Ali, Lobna, Scherrine, Manuelle, Pierre, Dion, Eleni, Diego et Gloria. Je n’oublie pas bien sûr mes partenaires lors des trépidantes aventures du bureau D-204, que ce soit avec les désormais jeunes docteurs : Mamadou, Pierre-Yves (aka PyD), Romuald, Renaud, Romain et Brice (10+2) ; mais aussi les futurs docteurs : Bassem, Etienne, Amina (pour son rôle clé), Clément et Olivier. Je leur souhaite bon courage pour tout ce qui les attend. Je remercie également mes collègues représentants des doctorants à Saint-Etienne, que ce soit au Comité de la Recherche ou au Conseil Scientifique, ou dans les autres instances, notamment Super Lauralala, Julie et Alexandre.

Enfin, puisque cette expérience n’aurait pas tout à fait été la même sans eux, je remercie tout particulièrement :

- Romain, mon très cher voisin de bureau, qui a su être présent pour moi, en toute circonstance, même dans les moments difficiles que ce soit pour éteindre les braises du doute ou raviver les flammèches de la motivation. Un énorme merci à toi, et, méfiance, même Shakira (waka waka he he) ne peut rien pour toi sur Sokratous…

- Thierry, pour son exubérance toute marseillaise et qui s'est attaché à me faire découvrir les trésors de la Provence et de la Méditerranée, et qui, a n'en point douter en incarne l'un des plus notables. D’ailleurs, finalement, qui de toi ou de Shakira avait raison sur la présence ou non d’ail dans cette fameuse tapenade ? De la terrasse de l’Exit sur le Vieux-Port jusqu’au semi marathon de Marseille-Cassis, ce qui me manquera le plus sera sans doute tes expressions si… euh… poétiques…

- Jessica, pierre angulaire de PS2 tant sur le plan technologique qu’humain. Les séances chansons et fous rires en salle imagerie resteront gravées dans ma mémoire, tout comme ta bonne humeur permanente, tes chorés à la Vaness et les récaps de Desperate et Koh Lanta… Deux petits conseils à garder en tête : fuis toute coupe de cheveux incluant des mèches colorées rose et jaune (toi-même tu sais), et surtout, surtout, quoi qu’il arrive, garde ton si joli sourire Colgate ! Et, oh, au fait, j’allais oublier : DOUZEEEE !

- Étienne, mon compagnon de voyage, que ce soit pour relier quotidiennement Aix aux terres d’énergie de Gardanne ou pour des contrées plus exotiques à travers le monde. Au final, d’Est en Ouest, de Jeju à San Francisco, on doit bien avoir un ou deux tours du Monde au compteur… Des paysages majestueux, des instants de grande complicité, des discussions franches, des sirotages de maté, voilà ce que je retiendrai. Ces petits moments privilégiés me manqueront, mais il y en a tellement d’autres à venir…

Bien que relativement longue, cette liste de remerciements n'a pas la prétention d'être exhaustive. Aussi, j'espère sincèrement que ceux n'y trouvant pas leur nom ne m'en tiendront pas rigueur. Cela ne remet absolument pas en cause leur contribution aux excellents souvenirs que je garderai de ces années écoulées.

À l'heure du bilan, et de la conclusion de ce volet *Remerciements*, il me revient en mémoire une anecdote qui s'est déroulée, il y a quelques mois maintenant. Alors que j'écrivais un courrier électronique à un fournisseur pour tester un équipement, j'ai été amené à me présenter, à expliquer sur quoi je travaillais et pourquoi je faisais appel à lui. À cette occasion, je me suis rendu compte qu'une faute de frappe m'avait amené à écrire que je faisais partie de l'École des Miens. Et, de cette petite inversion involontaire de lettres, j'ai pris conscience de l'importance que vous aviez tous pris dans ma vie et à quel point je me sentais, ici, parmi les miens. Pendant toutes ces années, j'ai finalement eu le sentiment de faire partie d'une famille. Je suis fier d'avoir fait partie de cette famille, d'avoir vécu tant de choses avec vous et d'avoir grandi à vos côtés. C'est grâce à vous, chaque matin, que je venais travailler avec plaisir car je savais que j'allais vous y retrouver… Cependant, il arrive tous les jours des choses que nous ne souhaitons pas voir se produire mais que nous devons accepter, des faits que nous préférerions ignorer mais dont nous devons tenir compte et des gens dont nous ne pouvons pas nous passer, que nous devons accepter de quitter. Mais, si je vous quitte aujourd'hui, sachez que j'emporte avec moi un petit peu de chacun d'entre vous.

Je terminerai enfin par dire un grand merci à David, Kevin, Lucie, Ronan et Elo pour leur précieuse amitié et à ma famille pour leur soutien, notamment ma mère Jocelyne, ma grand-mère Félicité, mon frère Renaud, ainsi que mon neveu et ma nièce adorés, Ethan et Marine.

Merci à tous.

Romain CAUCHOIS
Aix-en-Provence, le 7 juin 2012

Homo sum; humani nihil a me alienum puto
Terence, "Heautontimorumenos"

Table of contents

CHAPTER 2 - Microstructure of inkjet-printed thin films

CHAPTER 3 - Fabrication of inkjet-printed interconnects for electronic packaging

MICROSTRUCTURATION DES DEPOTS IMPRIMES PAR JET D'ENCRE : DE LA COALESCENCE DES NANOPARTICULES D'ARGENT VERS LA REALISATION D'INTERCONNEXIONS DE COMPOSANTS ELECTRONIQUES

General introduction

I. Background

Additive printing technologies have gained tremendous interest as a pathway to large area and flexible electronics. Among several printing methods, drop-on-demand inkjet printing is a non contact and digital technique that allows fast prototyping without any waste. This technology can thus be advantageously adapted for the realization of interconnects on silicon integrated circuits for low-cost electronic packaging [1]. These features should exhibit a low electrical resistivity and high mechanical properties in order to be compatible with subsequent electronics micro-packaging step.

In the past few years, the use of metallic nanoparticles has undergone major development in microelectronics thanks to sintering achievements [2, 3]. In addition to their use as fillers in conductive (ACA/ACF) and non-conductive films (NCF) dedicated to fine-pitch flip-chip applications [4], nanoparticles can be used to perform circuitry on rigid or flexible substrates after being dispersed in a solvent-based vehicle [4]. Prevalence of their high surface area to volume ratio and its benefit on sintering activation by reducing melting temperature has been reported in previous works [5, 6]. These colloidal suspensions exhibit a high processability which enables the use of high resolution, large area and low cost techniques, such as inkjet-printing.

Inkjet-printing technology allows the reduction of process steps by a factor of three compared with common photolithography (see Figure 1). Photolithography is basically divided into six steps, which include coating the base layer with several materials, masking to transfer the circuitry patterns from a dedicated mask to the substrate, and finally etching and stripping. In comparison, inkjet-printing is limited to the pattern direct-printing on the base layer and the subsequent curing of the deposited ink in order to remove solvents, to initiate the film cohesion and to improve electrical contact between nanoparticles. This curing step can be carried out using either a conventional oven or other selective techniques such as laser, microwave and Joule heating [7-9].

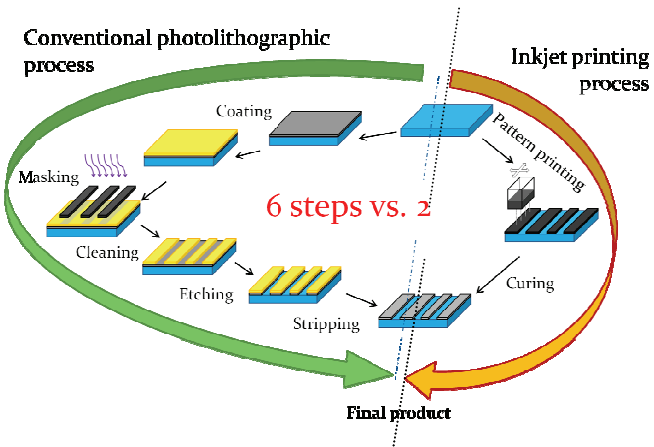

Figure 1: Comparative approaches to fabricate a microelectronic product using conventional photolithography or inkjet-printing. Adapted from Inktec.

The ability to design features without the requirement of additional process step enhances the yield. This additive approach is both time and cost-saving for the fabrication of 2D interconnects and passive electronics. Niche applications have also been identified and functional devices have been demonstrated. Amongst specific applications that has been developed with this technology, one could notably quote interconnects in microcircuits, electrodes for antennas and photovoltaics, active layers for organic transistors, light emitting diodes, batteries and photovoltaic cells.

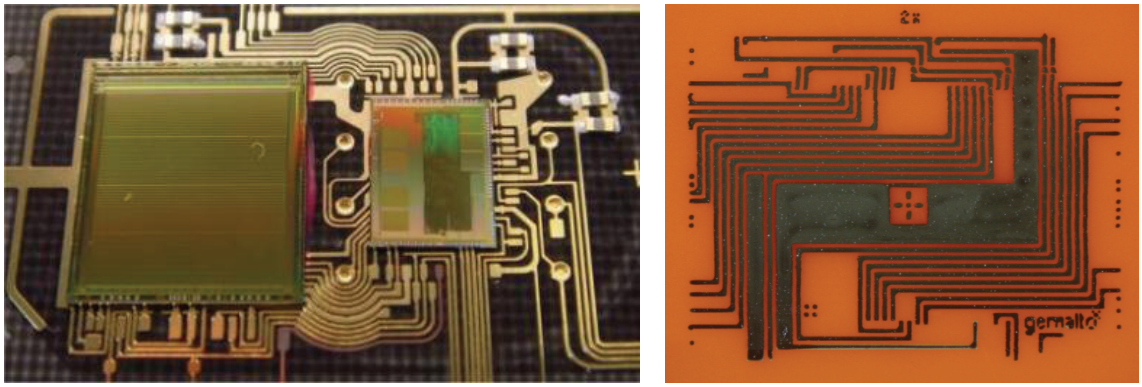

Figure 2: Typical features fabricated using conventional lithography (left) and a layout inkjet-printed on JetPac (right).

Unfortunately, films produced using inkjet-printing are usually nanoporous which simultaneously affects the electrical and the mechanical properties of resulting structures [11]. Tuning the physical properties is particularly challenging, requiring an optimization of microstructure through solid-state sintering. Sintering occurs when two particles in contact are cured. A neck is first formed and then grows, resulting in a proper conduit for the conduction of electrons. Hence, a proper post-process compatible with integrated circuit using a well-timed temperature profile has to be properly adjusted.

II. Thesis objectives

A. Technological objectives

As a provider of secured and mobile solutions, Gemalto is at the forefront of innovative processes and solutions. Recently, major evolutions have been driven by software innovations, while hardware breakthroughs have been supported by microelectronic foundries. In the near future, innovation will be led by the extension of hardware technologies to new form factors or by the integration of heterogeneous devices in what is called Systems-in-Package (SiP). Introduction of devices such as MEMS, flash memories or CPUs will drastically renovate the ISO form factor which has remained unchanged for 25 years with the smartcard patent developed by Moreno [10].

Gemalto's ambitions are to diversify its device providers in a more competitive approach through cost reduction. These new devices present multiple Input/Output, ground, power supply and clock pads which are variously located at the chip surface. This new approach thus requires a modification of device assemblies which are usually correlated to the development of complex and expensive leadframes. Using redistribution layers directly on the surface of device to fulfill interconnections between each component therefore appears as a viable solution. Applications integrating passive structures on the device surface are also being considered.

The interest of inkjet-printing technology is particularly important in the smartcard industry where new applications are dedicated to mobile solutions with an extension to flexible electronics. Studies on inkjet-printed electronic patterns are quite recent [11-13] and implementation of a stable, selective and reproducible process at low temperature is still a challenge. Combination of several techniques can only be investigated if a better understanding of underlying phenomena is achieved. In this framework, inkjet-printing technology is strongly dependent on the post-process curing which has to be optimized through time and temperature variation.

Viability of this technology at an industrial scale can only be achieved if low-cost substrates can suitably be processed. These conditions are usually limited to a low temperature curing below 300 °C – or even worse, below 150 °C for an ABS substrate – and to a fast post-processsing step. In the field of printed electronics, the curing step is clearly the bottleneck in the process flow. A better understanding and consecutive optimization of the sintering of nanoparticles is thus necessary for a technological paradigm.

The industrial goal is to achieve functional demonstrators which can be implemented on thin and flexible substrates with a characteristic thickness below 200 µm. If the inkjet-printing technique is very promising in terms of results and yields to fit the market demands, Gemalto has a competitive incentive to develop its knowledge in what will probably be the cornerstone of future development of sustainable microelectronics.

B. Scientific objectives

The goal of this thesis from an academic point of view is to contribute to the tailoring of materials/process interactions and to understand how they subsequently impact the properties of 2D interconnection structures based on printed silver nanoparticles.

The aim is thus to develop and adapt the processes in order to connect several chips with advanced interconnect structures made using the inkjet-printing technology. This technology has been demonstrated previously in the CMP laboratory of the Ecole Nationale Supérieure des Mines de Saint-Etienne in Gardanne for the fabrication of conducting metal electrodes and organic transistors with low actuation voltage [14, 15].

The first approach was thus to develop the process on the upgraded version of JetPac printing equipment, recently reacquired by the lab. The aim of this extensive work was to develop a reproducible and stable printing process through the optimization of the jetting parameters, as discussed in Chapter 1. In particular, the performance and robustness of the interconnect structures will be correlated to evolutions of microstructure, mechanical state and resistivity which occur at key stages of the manufacturing process.

A first part of the thesis has been consecrated to understand and master the relationship between materials and processes, and how they control the stability, reliability and electrical resistivity of printed patterns. In Chapter 2, significant importance was given to the tailoring of the microstructure, as a way to prepare the best conditions of robustness for subsequent electronics micro-packaging such as wire bonding.

The correlation between the microstructure of inkjet-printed silver thin films and electrical/mechanical properties is discussed in Chapter 3. Furthermore, this approach has been extended in Chapter 3 to the study of the combination of inkjet materials with electroless selective growth. Performance of the printed patterns has also been evaluated through electrical and mechanical tests, some of which have been linked to dedicated thermal cycles. Special attention was put on the wire-bondability of printed contacts in order to be compatible with industrial products.

References

[1] D. Kim and J. Moon, "Highly conductive ink jet printed films of nanosilver particles for printable electronics," *Electrochemical and Solid-State Letters*, vol. 8, pp. J30–J33, 2005.

[2] G.-Q. Lu, Calata, J.N., G. Lei, and X. Chen, "Low-temperature and pressureless sintering technology for high-performance and high-temperature interconnection of semiconductor devices," in *International conference on thermal, mechanical and multi-physics simulation experiments in microelectronics and micro-systems*, pp. 609–613, 2007.

[3] K.-S. Moon, H. Dong, R. Maric, S. Pothukuchi, A. Hunt, Y. Li, and C. Wong, "Thermal behavior of silver nanoparticles for low-temperature interconnect applications," *Journal of Electronic Materials*, vol. 34, pp. 168–175, 2005.

[4] D. Kim, S. Jeong, B. K. Park, and J. Moon, "Direct writing of silver conductive patterns: Improvement of film morphology and conductance by controlling solvent compositions," *Applied Physics Letters*, vol. 89, pp. 264101–3, 2006.

[5] P. Buffat and J.-P. Borel, "Size effect on the melting temperature of gold particles," *Physical Review B*, vol. 13, pp. 2287–2298, 1976.

[6] A. Safaei, M. A. Shandiz, S. Sanjabi, and Z. H. Barber, "Modelling the size effect on the melting temperature of nanoparticles, nanowires and nanofilms," *Journal of Physics: Condensed Matter*, vol. 19, no. 21, pp. 216216–, 2007.

[7] S. H. Ko, H. Pan, C. P. Grigoropoulos, C. K. Luscombe, J. M. J. Fréchet, and D. Poulikakos, "All-inkjet-printed flexible electronics fabrication on a polymer substrate by low-temperature high-resolution selective laser sintering of metal nanoparticles," *Nanotechnology*, vol. 18, no. 34, p. 345202, 2007.

[8] J. Perelaer, B.-J. de Gans, and U. Schubert, "Ink-jet printing and microwave sintering of conductive silver tracks," *Advanced Materials*, vol. 18, no. 16, pp. 2101–2104, 2006.

[9] M. L. Allen, M. Aronniemi, T. Mattila, A. Alastalo, K. Ojanperä, M. Suhonen, and H. Seppä, "Electrical sintering of nanoparticle structures," *Nanotechnology*, vol. 19, no. 17, pp. 175201–, 2008.

[10] R. Moreno, "Data-transfer system," Patent, 1974.

[11] S. Joo and D. F. Baldwin, "Performance of silver nano particles as an electronics packaging interconnects material," in *Electronic Components and Technology Conference*, pp. 219–226, 2007.

[12] S.-M. Yi, J.-K. Jung, S.-H. Choi, I. Kim, H. C. Jung, J. Joung, and Y.-C. Joo, "Effect of microstructure on electrical and mechanical properties: impurities of inkjet-printed Ag and

Cu interconnects," in *Electronic Components and Technology Conference*, pp. 1277–1281, 2008.

[13] B. K. Lok, Y. N. Liang, P. Gian, S. Xuechuan, and A. C. W. Lu, "Process integration of inkjet printing and electroless plating for LTCC substrates," in *Electronics Packaging Technology Conference*, pp. 202–205, 2007.

[14] S. Sanaur, A. Whalley, B. Alameddine, M. Carnes, and C. Nuckolls, "Jet-printed electrodes and semiconducting oligomers for elaboration of organic thin-film transistors," *Organic Electronics*, vol. 7, pp. 423–427, 2006.

[15] M. Barret, *Impression par jet de matière de transistors organiques sur support souple*. PhD thesis, Ecole Nationale Supérieure des Mines de Saint-Etienne, 2007.

1

Implementation of inkjet-printing for microelectronic interconnects

Introduction

In this first chapter, a general description of state-of-the-art techniques to fabricate microelectronics layouts and thin films using direct-writing technologies will be given. A particular interest has been drawn on the inkjet-printing process and especially to its drop-on-demand version for its propensity to be quite easily implemented in an industrial process flow. Direct-writing has appeared since the last two decades as a paradigm shift away from traditional approaches based on lithographic techniques. The process flow is thus reduced from six main steps in the photolithographic process to only two steps in the inkjet-printing process. In particular, its proficiency to create conductive patterns with around 100 µm line-widths on advanced substrates such as polymer that requires to be treated at low temperature has been proven.

Conductive inkjet-printed patterns are usually fabricated using metallic inks based on nanoparticles. A special interest has been developed towards noble metals as silver, gold or copper. These metallic nanoparticles have to be stabilized in a solvent vehicle in order to be jetted. This stabilization process is a key step that will be detailed in this chapter. Many synthesis routes have been developed involving mechanical attrition, chemical synthesis or vapor nucleation. Still, all these methods are very complex to carry out due to the nanoscale range. Fabrication of devices based on conductive polymers as PEDOT or PANI, or with organometallic inks has also emerged in the recent years.

This chapter is characterized by a meticulous concern on the optimization of inkjet-printing implementation for fabrication of microelectronics packages, as much from the root materials as from the process.

I. Direct-writing technologies

Direct-writing technologies encompass all approaches that can be exploited for the production of electronic devices or, in the most general case, of controlled architectures in the mesoscale or the nanoscale range. Such a technique is an efficient way to dispense or deposit any given material with extreme precision on various surfaces according to a preset pattern without any help of a mask or an etching step thus limiting the loss of active materials.

A. Tip-based direct-writing

Originating from the Eigler's landmark breakthrough in atom manipulation [1], nano-

patterning methods emerged at the end of the 90's with the first demonstration of Dip-Pen Nanolithography® (DPN) by Mirkin and co-workers [2]. This kind of direct-writing technique usually involves Atomic Force Microscopy (AFM) cantilever tips: either traditional AFM tips [3], hollow tips for nanofountain probe method [4] or thermal tips [5]. Basically, DPN is based on the common capillary effect observed during an AFM scan. This phenomenon can suitably be exploited for dispensing an ink in which the tip has been previously dipped (see Figure I--a). If the wettability of the ink on the considered substrate is sufficient, materials will be adequately transferred on this substrate and the spreading of the ink operates either by molecular transport, self-assembly or lateral diffusion [6].

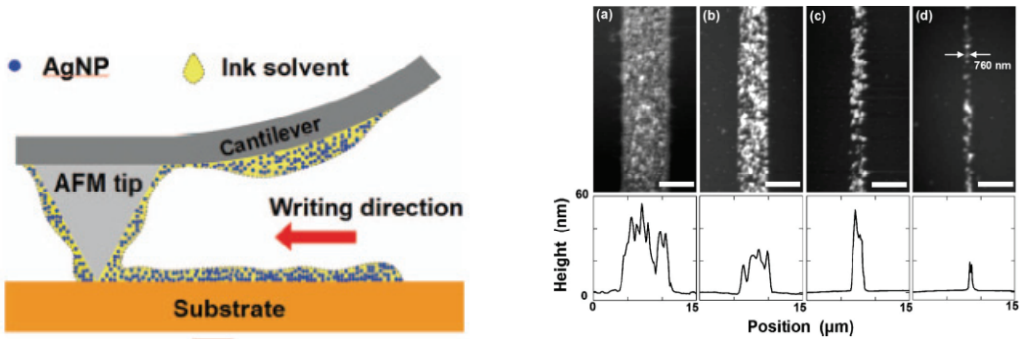

(a) (b)

Figure I-1: Schematic of the DPN principle with silver nanoparticles ink patterned on SiO_x substrate (left) and AFM topography images of silver nanoparticles traces fabricated with a tip speed of 10 µm/s (right) [3]. Scale bars are 5 µm each.

Although tip-based direct-writing has been mainly used for the deposition of biological inks such as DNA, active enzymes, proteins or polymers, several authors have reported the deposition of conductive traces. In this case, the most straightforward approach is to dip the tip either in a metal nanoparticle-based ink [3, 7, 8] or in an ionic solution containing metallic salt complexes [9]. An impressive line resolution of 12 nm has been achieved [10]. However, such geometrical scaling leads to very poor materials continuity (see Figure I--b), thus increasing the electrical resistivity above expectations. Indeed, Hung *et al.* were the firsts in 2010 to report submicron conductive silver lines with an average resistivity of 28.8 µOhm·cm after being annealed at 150 °C for 10 min [11].

Another considered approach is to heat a thermally-compatible AFM tip previously coated with metal in a solid form. By heating the tip above the melting temperature, the material is deposited on the substrate by heat transfer. Thermal Dip-Pen Nanolithography (tDPN) has successfully been implemented by Nelson *et al.* to fabricate indium nanostructures of a width inferior to 80 nm on glass and silicon substrates [5]. The main drawback of this technique is obviously the availability of tips capable of undergoing high thermal energies, especially for the deposition of noble metals, whose melting temperature is much higher than indium

(usually about 1000 °C). In addition, only heat resistant substrates can be used.

The writing speed of tip-based direct-writing is nonetheless a major hindrance to the deployment of this technique in rapid prototyping applications for large-area printed electronics. In addition, while being well suited for fine line resolutions, fabrication of multi-scale patterns cannot be addressed.

B. Laser-based techniques

Laser technology has been widely considered for the realization of conductors in printed electronics by the ablation of fully metalized structures. Matrix Assisted Pulsed Laser Evaporation (MAPLE) [12], Laser Chemical Vapor Deposition (LCVD) or laser-assisted electroplating [13] are indeed some of laser-based direct-write techniques that have been developed in recent years. Basically, two approaches have received major support from the community: Laser-Induced Forward Transfer (LIFT) and Laser-Guided Direct-Write (LGDW) techniques.

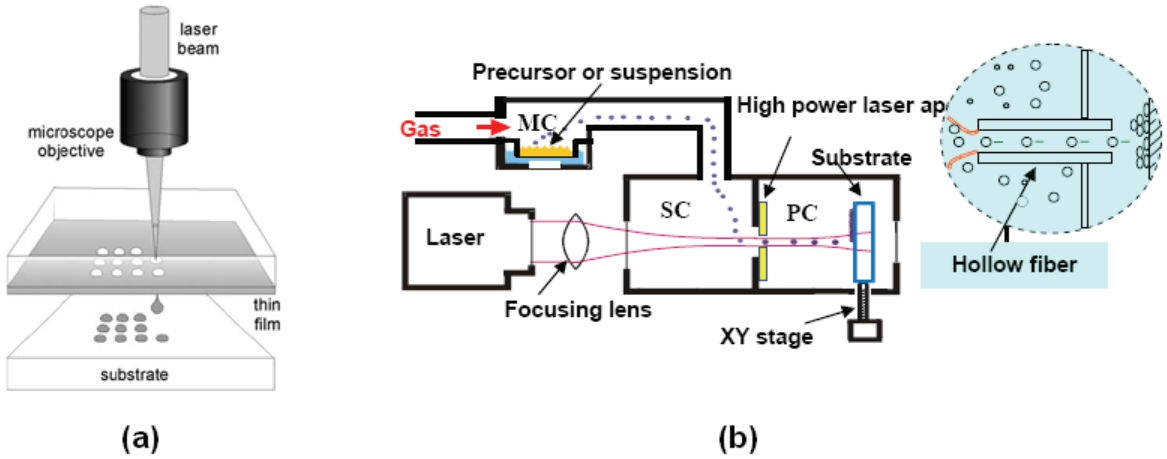

Figure I-2: Schematic of the LIFT (a) and LGDW (b) process principles, where MC is the mist chamber, SC is the supply chamber and PC is the process chamber [14, 15].

In the LIFT method, a pulsed laser beam is used to release materials from thin donor films to a receiving substrate (see Figure I-2-a). The donor material is deposited in liquid or solid form on a laser-transparent support, before being brought in parallel to the acceptor substrate within a distance of 25-100 µm [16]. Under the action of a focused laser pulse directed through the donor film backside, a small quantity of material is locally vaporized at the interface between the donor and its support. Volumetric expansion induced by the vaporization propels the material forward until reaching the substrate where solidification occurs. First experiments were performed by Bohandy *et al.* on copper and silver transfer

using excimer KrF or Nd:YAG lasers [17, 18]. Deposition of high resolution lines or patterns from thin solid films of silver or gold proved to be very difficult [19]. A quick fragmentation of the transferred donor material is indeed observed after the ablation, indicating that the best option for silver transfer with LIFT has to be made from the liquid form.

In the LGDW technique, a laser is used as a guiding flow for aerosols containing liquid precursors or colloid suspensions (see Figure I-2-b). The mist is prepared thanks to ultrasonic or pneumatic atomization. The underlying mechanism involves a photophoresis phenomenon where a momentum transfer occurs from the laser beam to the aerosol droplets. It has been shown that this migration is due to a non-uniform distribution of temperature in the nanoparticle thus generating an internal electric field [20, 21]. Indeed, the radiation pressure of photons induces a migration of particles which present a higher refractive index than surrounding solvent molecules [22]. In the free-molecular regime approximation, the amount of pressure P_r exerted by the absorption/scattering of photons on colloid is given by:

$$P_r = \frac{1}{2} P \left(\frac{T_p}{T_g} \right)^{1/2} \qquad \text{(I-1)}$$

where P is the local pressure within the beam, T_p is the particle's temperature and T_g is the gas temperature. The deposition rate of this technique ranges from 1 to 10000 particles per second with an accuracy of position of ± 2 µm [10, 23].

The major advantage of using laser direct-writing technologies is the ability to transfer and deposit a large variety of materials (metals, ceramics, semi-conductors, biomaterials, etc.). Meanwhile, a potential limitation could be the preparation of the donor substrate, which may be incompatible with large-area processing. Adhesion of transferred materials to the substrate is another suspected problem that can be alleviated using adequate surface treatment or by transferring liquid materials that include an adhesion promoter.

C. Aerosol jet print

The aerosol jet printing technique uses basically the same principle as LGDW transfer to atomize the functional material. Here, the aerosol is guided toward the print head using an inert gas such as nitrogen. The created aerosol is then aerodynamically focused and collimated inside the nozzle using a secondary gas flow. The generated coaxial stream is subsequently sprayed onto the substrate (see Figure I-3). This technique is patented and has been commercialized recently by Optomec, Inc. US under the name M3D (Maskless Mesoscale Material Deposition).

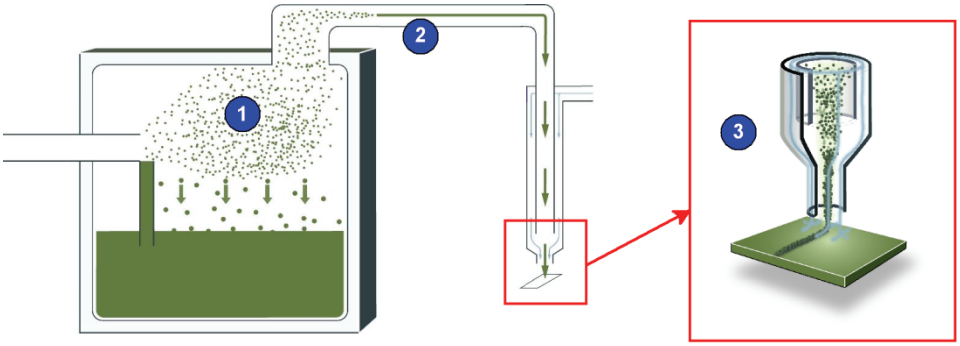

Figure I-3: Principle of the M3D system: atomization of the ink via ultrasonic or pneumatic system (1), transport of the produced aerosol (2) and deposition driven by sheath gas on XYZ moving substrate (3). Courtesy of Optomec.

In focused aerosol beam, the local shear flow of viscous fluid induces a steady lift force known as the Saffman force F_s (see Figure I-4). This force has been identified to have an additional major impact on fluid dynamics [24, 25] together with the Stoke's forces. This effect is quite opposite to the expected behavior predicted by the classical aerodynamic theory in which only gravity and Stokes forces are considered.

When high velocity particles are flowing through a micro-capillary system, they experience a shear lift force F_s given by:

$$F_S = 6.45\, a^2 \left(u_f - u_P\right) \sqrt{\rho_l\, \mu \left|\frac{\partial u_f}{\partial y}\right|}\; Sign\left(\frac{\partial u_f}{\partial x}\right) \qquad \text{(I-2)}$$

where a is the radius of the spherical particle, u_f is the fluid velocity at the location of mass center of particle, u_p is the particle velocity, $\frac{\partial u}{\partial x}$ is the shear rate and ρ_l and μ are respectively the fluid density and viscosity.

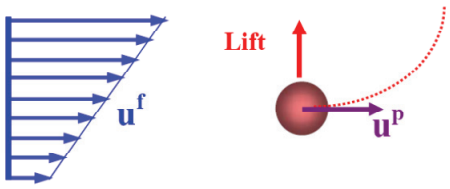

Figure I-4: Schematics of a particle in a shear flow.

Aerosol jet printing is compatible with a large variety of materials with viscosities ranging from 0.7 to 2500 mPa·s and with nanoparticle diameters as small as 20 nm. The flow-guided

aerosol nozzle generates droplets with a diameter of 1 to 5 µm allowing feature sizes from 5 µm to 5 mm. Thin films printed with this technique exhibit a thickness comprised between 10 nm, up to 10 µm. Large surface areas can be printed by integrating up to 40 nozzles within the same system.

Key applications of the aerosol jet technique include the deposition of 2D and 3D interconnects for micro-packaging, passive devices, and photovoltaics. Yet, aerosol printing is limited by the low throughput and the ability to fabricate patterns with rounded corners and straight lines.

D. Inkjet-printing technique

The inkjet-printing technique is based on the same principle as office or home printers. It became widely used in the 1980s in the field of electronic manufacturing thanks to the huge development of functional inks. This concept was recently pursued in printed electronics, primarily for the realization of organic transistors on flexible substrates, OLEDs, smart RFID antennas and interconnects [26, 27].

The basic principle of inkjet-printing is the breaking-up of liquid into droplets at the nozzle boundary under imposed surface tensions, also known as the Rayleigh-Tomotika instability [28, 29]. The ejection of droplets from the nozzle is realized either continuously or intermittently. The later technique, usually described as a Drop on Demand (DoD) inkjet-printing approach, is very often used in printed electronics. In DoD, detachment of controlled droplets onto the substrate can be achieved using either a thermal or a piezoelectric (PZT) printhead.

In a thermal system, an electrical pulse is applied to a resistive heater which creates a bubble by local vaporization of the ink within the nozzle reservoir (see Figure I-5-a). The resistive heater is contained in a submicron metallic thin film placed in each channel to separately control each nozzle ejection. The electrical current flowing through the resistor during about 1 µs explosively boils the first 10 nm of ink that is in contact with the heater. The volume expansion during the vaporization creates a pressure pulse in the fluid. Droplets are consecutively ejected from the nozzle by the relative overpressure with the atmosphere. When the gaseous bubble vanishes during cool-down, the relative under-pressure leads to the cavity refilling. At this point, the cycle is complete and the system comes back to a steady state.

This technique is usually used for the home printer and it is not widely considered for printed electronics. Thermal heating indeed requires the use of volatile solvents in the ink and is usually not suitable for ejecting inks based on metallic nanoparticles. Nonetheless, in the case of metal inks, the working temperature represents a major drawback for the development of this process.

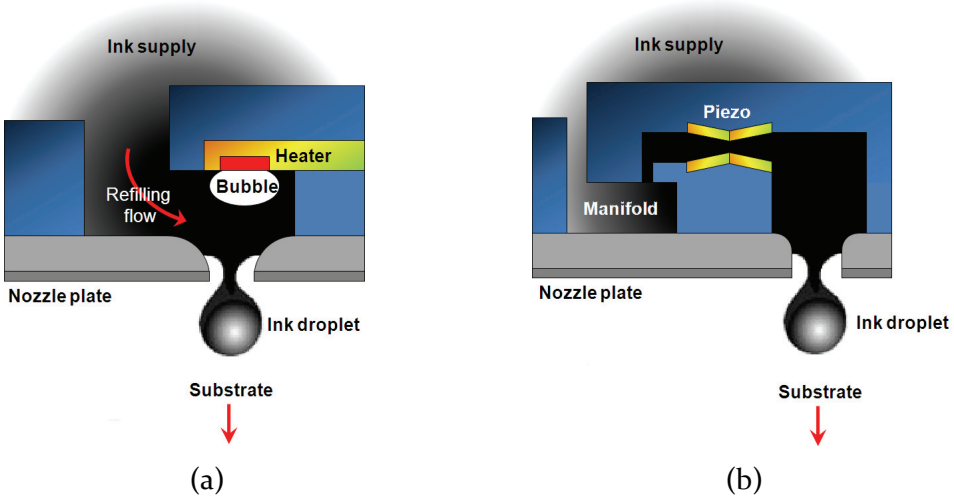

Figure I-5: Schematics of DoD inkjet-printing system: the thermal inkjet (a) and piezo inkjet systems (b).

In a piezoelectric system, the droplet is generated by increasing the pressure within the nozzle cavity with the use of a PZT crystal (see Figure I-5-b). Similarly to the thermal inkjet system, actuation is operated by a bipolar voltage pulse applied to the piezo-element whose mechanical deformation is sufficient to generate a pressure wave through the channel and to propel an ink droplet from the nozzle. Usually, the compression of the fluid in the channel is performed either by bimorphs or elongating rods. The printhead is designed so that when the channel is squeezed by applying a negative voltage, the ink flows downstream toward the ejection orifice and not backwards towards the ink supply. The reservoir is then refilled when a positive voltage is applied.

The major benefit from inkjet technology is its ability to precisely print on a large surface area with high writing speed. This is associated with the manufacturing maturity of inkjet printheads where thousands of nozzles can be integrated within the same system. However, challenges associated with inkjet-printing remain the control and the stability of the jetting. Due to the ink and process instability, undesired artifacts such as deviated jets or unwanted additional droplet generation – also known as satellite droplets – can occur. These defects can originate from nozzle plate defects or nozzle clogging and usually result in open or short circuits on printed features. Moreover, inkjet-printing is limited by the provision of functional ink with consistent rheology and performances (viscosity, surface tension, etc.) which are hard to achieve for printed electronics applications. More interestingly, functional inks are developed by some research laboratories which are not usually commercialized or available.

To summarize, direct-writing is identified as a new emerging and attractive technology area that can handle a large variety of materials. Table I-1 gives a summary of the main characteristic of the previously mentioned direct-writing technologies.

Table I-1: Summary of direct-writing process characteristics (μ is the dynamic viscosity) [10, 16]. Values for inkjet and aerosol techniques are only indicated for a single nozzle system.

Technique	Line resolution	Deposition rate	Materials
DPN	10-1000 nm	0.2-5 $\mu m \cdot s^{-1}$	Liquid (molecule, NP)
LIFT	10-200 μm	3-50 $mm \cdot s^{-1}$	Solid or liquid
LGDW	2 μm	10^{-4} $mm^3 \cdot s^{-1}$	Liquid ($\mu < 2.5$ Pa·s)
Aerosol jet	5 μm- 5 mm	0.25 $mm^3 \cdot s^{-1}$	Liquid ($\mu < 2.5$ Pa·s)
DoD inkjet	15-200 μm	0.3 $mm^3 \cdot s^{-1}$	Liquid ($1 < \mu < 20$ mPa·s)

Currently, direct-writing using inkjet-printing followed by laser processes are the most mature technology for metal deposition. Aerosol printing has shown some very interesting progress. In the ideal case, the combination of these technologies will be key in addressing multi-scale and large-area printed electronics issues. Remaining challenges of direct-writing technologies include process modeling, stability, and metrology. Moreover, the preparation and deposition of a large variety of nanofluids and inks are still a bottleneck to be addressed.

II. Nanofluids

Colloidal suspensions of nanoparticles can be regrouped under the general term of nanofluids. Theses fluids exhibit very specific properties ranging from heat-transfer to plasmonic resonance or antibacterial activity. In order to fabricate interconnects for microelectronic packages, inkjet-printing requires functional inks which fulfill specific conditions of surface tension and viscosity. As will be developed in this part, these inks are made of noble metallic nanoparticles in suspension in a solvent vehicle, which usually involves a mixture of several solvents that interact with nanoparticles to comply with the jettability requirements. The fabrication of metallic nanoparticles and the formulation of adequate solvent mixtures are ultimately tuned by ink suppliers to enhance their properties.

A. Preparation of metallic nanoparticles powder

Nanoparticles have been used in more and more applications, ranging from catalytic agents to antibacterial treatments [30], and have thus been put under considerable interest during the last decade. Because of the volume downscaling to the nanoscale, optical, electrical, and thermo-mechanical properties are enhanced. According to the constraints related to their application, several preparation routes have been developed, either by a bottom-up or a top-down approach.

i. Vapor phase synthesis

Historically, the first methods for massive production of nanoparticles were carried out in a vapor phase by atom condensation. Actually, this bottom-up technique was developed well before institutional research took an interest in nanoparticle assets in a wide range of scientific fields. Initial developments were based on the Inert Gas Condenstion (IGC) process where a metal is evaporated inside an ultra-high vacuum chamber (see Figure I-6-a) [31, 32]. The chamber is then backfilled with a low partial pressure (from 1 to 10 torr) of inert gas such as argon or helium. Since the collision mean free path is very small, evaporated metal clusters are rapidly quenched by colliding with gas atoms. The supersaturated metal vapor then promotes homogeneous nucleation leading to cluster growth. Evaporation of metal from a refractory crucible is usually performed by Joule heating even though thermal plasma [33, 34], laser ablation [35] and spark ablation [36] have also been reported.

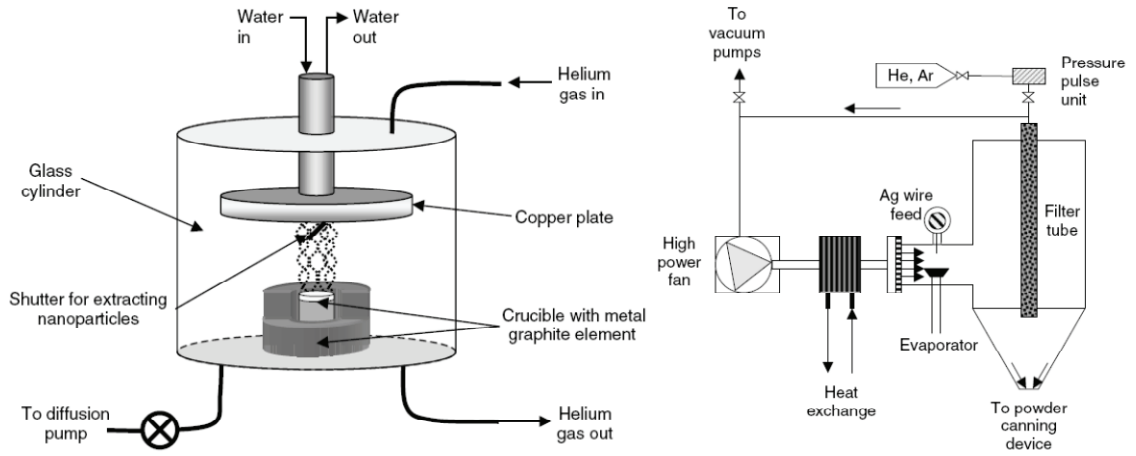

Figure I-6: Schematic of the IGC setup as used by Granqvist (left) and the modified system developed by the Fraunhofer Institute (right) [37].

The main drawbacks of IGC process are the nanoparticle collection method and the production rate. With IGC, nanoparticles are indeed scraped off directly on a plate or on a so-called cold finger where they condensate. This manipulation is susceptible to nanoparticle agglomeration, which would require an additional process step of cluster separation, *e.g.* by ultrasonication or polar dilution. Another concern is the production yield of IGC, as the first setup produced only 1 g per run. Huge developments have been pursued by researchers to increase the evaporation rate by modifying the initial setup up to 50 g/h by use of a thermal plasma. In particular, the Fraunhofer Institute has recently developed a closed-loop system (see Figure I-6-b) which is continuously fed by a metal wire and a cross-flow of carrier gas [37].

Another vapor phase production option is a flame-based synthesis which has been widely used for production of oxidized silicon and carbon black nanoparticles, especially by Cabot Corp [38]. During this process, a metallic precursor is pyrolyzed in a hydrocarbon-oxygen flame (see Figure I-7). Over the last two decades, efforts have been made to control the size and uniformity of formed nanoparticles without agglomeration. This process was at first restricted to the production of oxide ceramic because of the combustion in an oxygen atmosphere. Nonetheless, working with atomized noble metal in an oxy-hydrogen flame allows generation of high-purity metal nanoparticles. Micron-sized aerosol droplets can be produced close to the flame either by thermal spray, ultrasonic atomizer or centrifugal atomizer [39, 40]. Once again, the shape and the size of nanoparticles are affected by the partial pressure, the temperature of the flame, the gas velocities and the Gibbs free energy of raw materials. This technique enables high production yield of spherical nanoparticles with diameter in the range of 100 to 1000 nm [37].

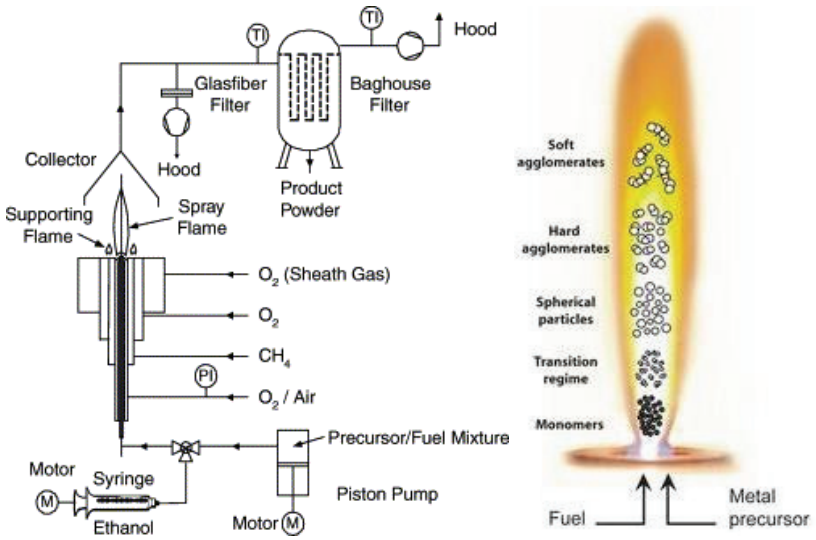

Figure I-7: Schematic of the flame based synthesis of nanoparticles [37, 41].

The main limitation of this technique lies in the ability to monitor the exact size of the produced nanoparticles and to easily extract them when the target size is achieved. This is a challenging aspect since the production of 100 nm particles is almost instantaneous.

ii. Chemical route

In this bottom-up method, molecular or ionic precursors are used to control the aggregation of metal atoms, thus guarantying small sizes and uniformity of prepared nanoparticles. This technique usually produces nanoparticles in the range of 10-12 nm. Faraday was the first to report a stable synthesis of aqueous dispersions of gold nanoparticles

[42]. Since then, the most widely used method to produce metal nanoparticles has been performed by chemical reduction of the corresponding salt in a stabilized solution. For example, gold nanoparticles can thus be achieved by the reduction of Au^{III} ions (typically originating from chloroauric acid) to Au^{0} atoms by citrate ions. Copper nanoparticles were obtained by reduction of copper sulfate by potassium borohydride under alkaline conditions. Silver nanoparticles can be produced by reduction of silver nitrate with either sodium borohydride NaBH4 [43] or sodium citrate $Na_3C_6H_5O_7$ [44]:

$$AgNO_3 + NaBH_4 \rightarrow Ag + \frac{1}{2}H_2 + \frac{1}{2}B_2H_6 + NaNO_3 \qquad \text{(I-3)}$$

To prevent nanoparticles from aggregation and oxidation, a protective agent is used, either organic or inorganic. The conventional approach is to cover them with a polarized capping to enhance the electrostatic repulsion force. When inorganic agents as borohydride anions (BH^-) are in solution, direct adsorption of these anions on the nanoparticles surface during the chemical synthesis can acts as a protective shield. However the borohydride fraction must be finely controlled since an over-concentrated BH^- solution would increase the overall ionic strength and would entail a precipitation of nanoparticles [45].

The most common approach is to add an organic molecule, such as Poly(vinyl pyrrolidone) (PVP), during the synthesis as a protective agent. The adsorption process of PVP on silver nanoparticles has been described by Wang *et al.* (see Figure I-8) [46]. They have shown that for nanoparticles with a diameter below 50 nm, only the nitrogen atom of PVP was in coordination with silver. As a result, the PVP layer not only serves as a dispersant agent avoiding agglomeration of nanoparticles, but also hinders their subsequent growth in the solution, thus acting as a diffusion barrier. The latter property will prove to be a sintering retardant as will be seen afterwards.

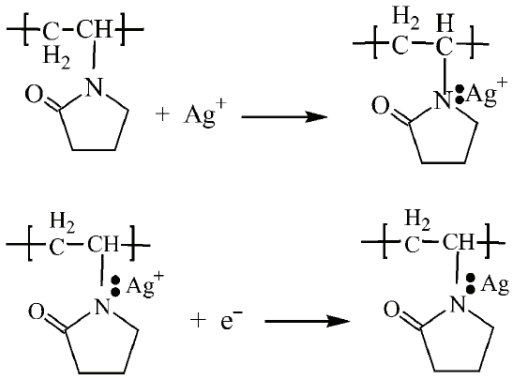

Figure I-8: Chemical reaction describing the formation of the complex between PVP and silver [46].

To be efficient, this method requires the formation of stable silver nuclei following the Equation (I-4). Once the initial nucleus is formed, the consecutive growth is driven by the minimization of the Gibbs free energy, μ_v. However, the formation of the nucleus is counter balanced by the surface energy, μ_s, created by the solid phase cluster which will tends to dissolve the nucleus to reduce the overall free energy [47, 48]. The total change of the chemical potential induced by the nucleation is given by:

$$\Delta G = \Delta\mu_v + \Delta\mu_s = \frac{4}{3}\pi r^3 \Delta G_v + 4\pi r^2 \gamma \qquad \text{(I-4)}$$

with

$$\Delta G_v = -\frac{kT}{\Omega}\ln\left(\frac{C}{C_0}\right) \qquad \text{(I-5)}$$

where r is the radius of the spherical nucleus, ΔG_v is the variation of Gibbs free energy per unit volume of the solid phase, γ is the surface energy per unit area, k is the Boltzmann constant, T is the absolute temperature, Ω is the atomic volume, C is the concentration of the solute and C_o is the equilibrium concentration or solubility.

Thus, a critical radius r_c is defined as the radius above which the nucleus will be stable enough to initiate the growth (see Figure I-9). According Equations (I-4) and (I-5), this critical value is defined by:

$$r_c = -\frac{2\gamma}{\Delta G_v} \qquad \text{(I-6)}$$

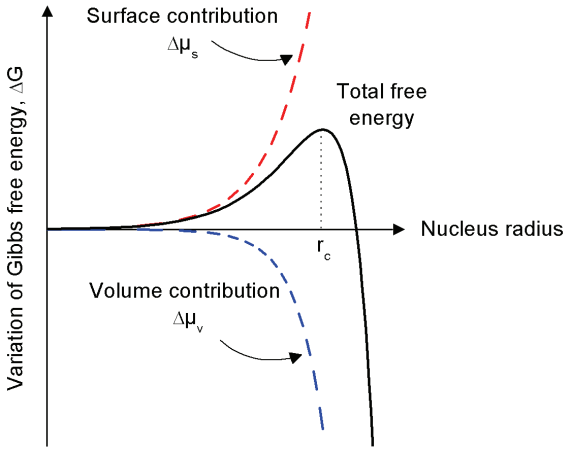

Figure I-9: Variation of the total Gibbs free energy, together with surface and volume contributions, as functions of nucleus radius.

As mentioned above, this fabrication method leads to monodispersed nanoparticles when a capping agent is subsequently used to control the growth. This sharp distribution in a colloidal suspension will tend to inhibit the initial grain growth when larger nanoparticles are growing at the expense of smaller ones. This phenomenon tends to limit the densification of thin film which is usually targeted to enhance electrical conduction.

iii. Mechanical attrition

Mechanical attrition, also known as ball milling, of powders is a top-down method to fabricate fine particles from bulk solids. The refinement of powder is achieved by the action of grinding balls in a chamber which is rotated around its own axis. When the milling chamber is rotated in a planetary movement (see Figure I-10), powder trapped between two balls clanking each other is grinded by severe plastic deformation. During this process, a very high degree of strain is imparted to particles leading to a high density of crystalline defects (less than 10^{16} m^{-2}) [49, 50]. Comminution of particles is limited by the material properties and the process variables [51]. The ultimate particle size achievable by mechanical attrition, d_{min}, depends on the balance between crack propagations initiated by plastic deformation during milling and thermal recovery induced by friction [52].

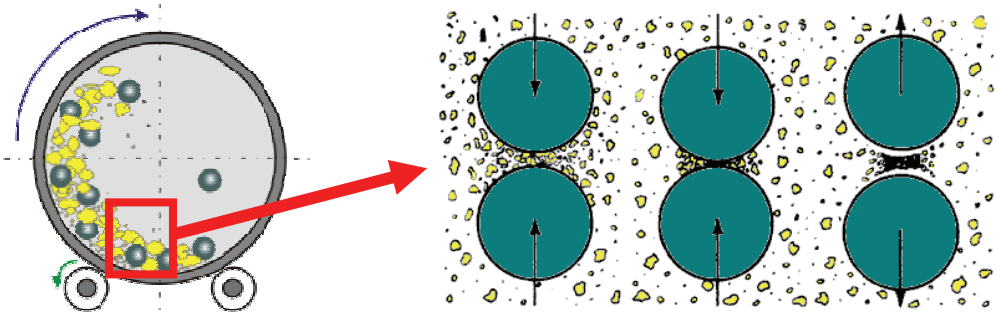

Figure I-10: Schematic principle of planetary motion of a mechanical attrition chamber [49].

Fabrication of nanoparticles by mechanical attrition was first reported with body-centered cubic and hexagonal close-packed crystals by Fecht *et al.* in 1990 [53]. The team of Eckert has later shown that the lowest minimum particle size obtainable for Face-Centered Cubic (FCC) metals were reached for high melting temperature materials [52]. Thus, for metals with moderate melting point such as silver (T_{melt} = 961 °C), d_{min} was found to inversely depend on their melting temperature (see Figure I-11). Indeed, particle size is reduced until reaching a critical size when the thermal energy is sufficiently high to overcome the comminution and provoke the melting of nanoparticles. This threshold temperature is reduced because the nanoparticle size is small, as will be explained later. Considering the milling of silver, the minimum particle size achievable is thus estimated to be approximately 20 nm [54]. It should

be noted that proceeding with the milling step at low temperature, *e.g.* at -85 °C, tends to further reduce the achievable particle size of crystals [55].

The problem of mechanical attrition is usually the high contamination observed within the produced powder. Indeed, possible sources of contamination in this process are degradation of the milling balls or chamber and the oxidation activated by the thermal energy induced by friction. Contamination is more pronounced with high energy ball milling [56]. In addition, according to the grain size, impacts of the milling balls and consecutive clusters agglomeration/destruction steps could entail an amorphization of the polycrystals.

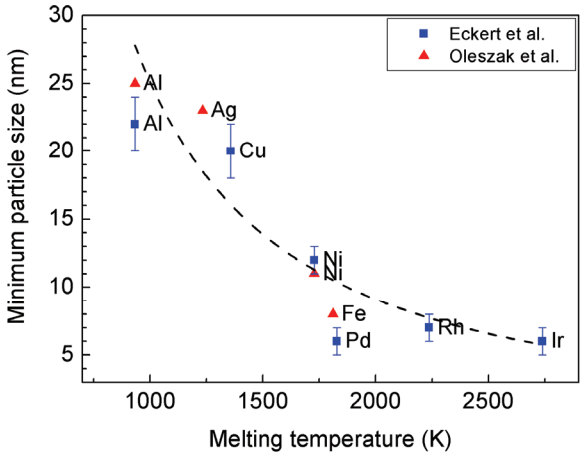

Figure I-11: Minimum average partilcle size achievable by mechanical attrition for face-centered cubic metals according to the bulk melting temperature. Data gathered from references [54, 57].

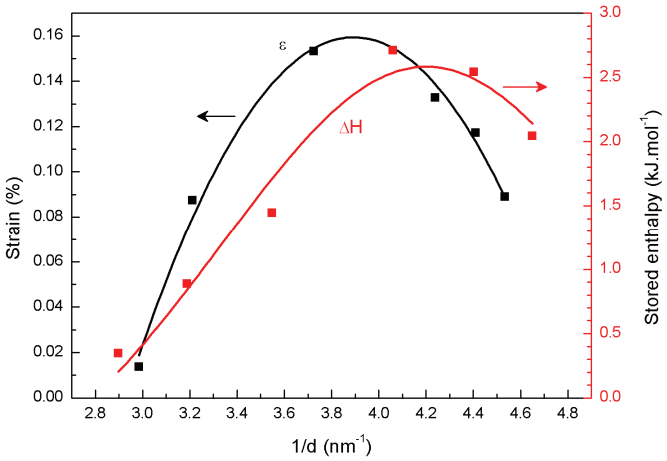

Figure I-12: Lattice strain ε and stored enthalpy (ΔH) according to the reciprocal silver grain size [54].

Nanocrystalline structures undergo mechanical deformation during milling under both dislocation and grain boundary deformation mechanisms. Presence of these crystalline defects gives rise to a lattice microstrain which exhibits a broad maximum with the reciprocal particle size (see Figure I-12) [52, 54]. Regarding the stored enthalpy, the same

tendency is observed. However, the maximum value of enthalpy is usually observed when particle sizes are smaller than the maximum of lattice microstrain (See Figure I-12). This enthalpy thus originates not only from the strain associated with grain boundaries but also from the generation of new boundaries [52, 54]. As will be considered later in this work, this stored energy could affect subsequent steps of the curing process.

It has also been observed that microstrains of nano-objects were highly size-dependent. Experiments conducted by Aifantis *et al.* on silver and gold nanocrystalline thin films have indeed shown that small nanoparticles in the range of 10 nm cannot contain dislocations. In this case, microstrain mainly derives from grain boundary rotation and sliding [58-60]. In addition, nanocrystals with grains in the range of 100 nm show evidence of more expected deformation mechanisms such as extensive dislocation activity, ligament formation and ductile fracture within the grain.

B. Colloidal dispersions of metallic nanoparticles for inkjet-printing

To be used in an inkjet-printing system, nanoparticles have to be dispersed in a solution to form a functional ink. This ink has to fulfill given conditions. Firstly, the viscosity of the ink has to be adjusted in order to pass through the printhead channel. Typically, viscosities are in the range of 1 to 20 mPa·s. Then, the distribution of nanoparticle diameters has to be linked to the printhead nozzle diameter in order to avoid clogging. In addition, according to the target application, the nanoparticle size and the nature of solvents have to be adequately considered. Moreover, for temperature sensitive substrates like plastic, nanoparticles with diameters smaller than 3-5 nm are desired in order to lower the curing temperature of the ink. The concentration of nanoparticles has to be well adjusted in order to achieve homogeneous thin films. Eventually, a long shelf life and stability is also required to prevent any agglomeration and sedimentation that could happen in the printhead channel and in the ink reservoir.

i. Noble metal selection for nanoparticles-based inks

Usually, the choice of a conductive ink for the fabrication of low resistive interconnects via inkjet-printing relies on two criteria: first, the compatibility of the colloidal suspension with the inkjet-printing system and second, the electrical resistivity of the printed pattern once cured. Other criteria are also taken into consideration such as the adhesion and the hardness of the deposit on the substrate, the potential threat of solvents or the crystalline structure of initial nanoparticles. To date, the most widely studied materials are metals with the lowest bulk electrical resistivity: silver, gold and copper. Some essential properties of those metals are presented in Table I-2.

Table I-2: Bulk properties of some usual metals used in microelectronics at 300 K [61, 62].

	Ag	**Cu**	**Au**	**Al**
Electrical resistivity (μΩ.cm)	1.617	1.712	2.255	2.709
Young's modulus (GPa)	82.4	128.7	79.4	70.4
Poisson's ratio	0.364	0.345	0.424	0.345
Vickers hardness (GPa)	0,251	0,369	0,216	0,167
CTE (10^{-6} K^{-1})	18.9	16.5	14.2	23.1
Thermal conductivity ($W{\cdot}cm^{-1}{\cdot}K^{-1}$)	4.29	4.01	3.17	2.37
Melting temperature (°C)	961.8	1084.6	1064.2	660.3

Experimental studies are usually focused on silver because of its low electrical resistivity compared to other metals. Polycrystalline bulk silver indeed exhibits a resistivity of 1.617 μΩ·cm [61]. According to the curing process and to the nanoparticle size, electrical resistivity of deposited silver ink can range from 3 to 10 times the bulk value. Previous work from Greer *et al.* [63] proved that thin films made from spin-coated silver inks could be as conductive as the bulk ones under optimal curing conditions. Spin coating of silver nanoparticles with a mean diameter of 40 nm and dispersed in a mixture of ethanol, ethylene glycol and glycerol were performed on a {100} silicon substrate. Electrical resistivity of such deposits were measured at 5 μΩ·cm (200 °C, 10 min) for a final thickness of about 115 nm. Fuller *et al.* [64] have also shown that silver nanoparticles with a diameter of 5-7 nm in an alpha terpineol suspension presented a resistivity of 3 μΩ·cm (300 °C, 10 min). During their experiments, Lee *et al.* [65] repurposed the piezoelectric printhead of a commercial desktop printer. This printhead was used to deliver 3 pl droplets of conductive ink onto a glass substrate with an encouraging resistivity of 16 μΩ·cm (260 °C, 3 min) with nanoparticle diameter of 50 nm.

Nonetheless, while silver doesn't react with molecular oxygen under normal circumstances (without plasma or O_3 treatment), silver is highly reactive to sulfur compounds such as hydrogen sulfide or sulfur dioxide in air. This sulfuration of silver leads to the formation of Ag_2S [66]. Both reactions are equilibrated as follow:

$$4\,Ag_{(s)} + O_{2\,(g)} \rightarrow 2\,Ag_2O_{\,(s)} \tag{I-7}$$

$$4\,Ag_{(s)} + O_{2\,(g)} + H_2S_{(g)} \rightarrow 2\,Ag_2S_{\,(s)} + 2H_2O \tag{I-8}$$

The standard Gibb's free energy ΔG^0 of the oxidation reaction is defined by:

$$\Delta G^0 = \Delta H^0 - T \cdot \Delta S^0 \tag{I-9}$$

where the standard molar enthalpy ΔH^0 is defined from the standard molar enthalpy of

formation enthalpy of each compound (see Table I-3) by:

$$\Delta H^0 = 2 \cdot \Delta_f H^0{}_{Ag_2O} - 4 \cdot \Delta_f H^0{}_{Ag} - \Delta_f H^0{}_{O_2} = -62.2 \text{ kJ.mol}^{-1} \quad \text{(I-10)}$$

and the standard molar entropy ΔS^o:

$$\Delta S^0 = 2 \cdot S^0{}_{Ag_2O} - 4 \cdot S^0{}_{Ag} - S^0{}_{O_2} = -133.6 \text{ J.mol}^{-1}.\text{K}^{-1} \quad \text{(I-11)}$$

Since the standard Gibb's free energy is negative (ΔG^o=-22.4 kJ·mol^{-1}) at 298 K, the oxidation occurs spontaneously at room temperature. As for the sulfuration of silver, the standard Gibb's energy is -570.5 kJ·mol^{-1}. Thus, even though the formation of silver oxide and silver sulfide are both thermodynamically favorable, silver sulfide is more stable and accordingly called the thermodynamic product.

Table I-3: Standard thermodynamic properties of involved substances used for calculations [61].

	$\Delta_f H^o$ (kJ.mol^{-1})	**S^o (J.mol^{-1}.K^{-1})**
Ag *(s)*	0	42.6
Ag_2O *(s)*	-31.1	121.3
Ag_2S *(s)*	-32.6	144.0
O_2 *(g)*	0	205.2
H_2O *(l)*	-285.8	70
H_2S *(g)*	-20.6	205.8

In parallel, experiments on gold nanoparticles were conducted despite a slightly higher resistivity than silver or copper. Gold is indeed already used in microelectronics notably for the wire bonding process because of its high stability in air. In 2004, Bieri *et al.* [67] worked with 2-5 nm gold nanoparticles in suspension in toluene and achieving a resistivity of 14 μΩ·cm after a laser sintering step. The same year, Szczech *et al.* [68] printed layouts with 100 μm-wide lines using gold nanoparticles of 5-20 nm. They achieved resistivities below 10 μΩ·cm (300 °C, 15 min), *i.e.* about 4.5 times the bulk gold resistivity. Nonetheless, the use of gold nanoparticles is very expensive because of the high cost of the bulk metal, nearly 50 times the cost of bulk silver (1680 €/oz vs 32 €/oz for gold and silver respectively, as for the 10th Oct. 2011, 1 oz=28.3 g).

Driven by cost saving considerations, copper nanoparticles are starting to attract more interest. Since copper quickly oxidizes in air (having a redox potential of 0.34 V), copper nanoparticles must be handled in an inert atmosphere during the printing and the post-treatment steps. Another solution implemented by Park and coworkers [69] is to work in

vacuum. In this case, sintering was carried out at 325 °C in a vacuum oven during 1h to reach a resistivity of 17.2 μΩ·cm. While encouraging, this solution is nonetheless poorly compatible with industrial production. Another solution would be to develop copper nanoparticles which are stable in air as did Luechinger *et al.* [70]. They indeed stabilized the nanocolloids using a graphene capping in order to print lines with a resistivity of only $6.4 \cdot 10^5$ μOhm·cm. Until recently, this copper capping method was the only available solution.

Other syntheses have been developed using either the same capping agent (PVP) as silver [71-73] or with a native copper oxide shell [74, 75]. These approaches lead to electrical resistivities of respectively 4 μOhm·cm (200 °C, 20 min) and 75 μOhm·cm after a photonic curing of 30 μs with an energy density of 0.77 $J \cdot cm^{-2}$. Photonic curing is nonetheless a very expensive technology since high energy is required to reduce the copper oxide. Another approach consists in depositing a thin layer (2-4 nm) of silver by transmetalation reaction around copper nanoparticles to prevent oxidation. During this operation, silver ions Ag^+ are reduced directly by the surface copper atoms [76] to finally produce a Cu/Ag core-shell structure (see Figure I-13).

Even though copper is very promising for the realization of low-cost interconnects, the throughput of copper nanoparticle synthesis is very low thus limiting the mass production of conductive ink for electronics applications. This problem was radically alleviated by the chemically controlled fabrication of copper nanoink introduced by Lee *et al.* with the reduction of copper sulfate with sodium hypophosphite [77]. It is therefore a new perspective of progress for printed electronics.

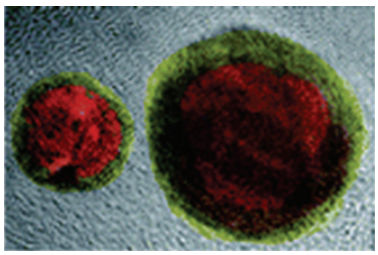

Figure I-13: Artificially colored TEM micrograph of copper/silver core-shell nanoparticles. Reproduced from [78].

Amongst the several noble metals, it should be noted the very recent emergence of aluminum nanoparticle-based ink. While being commercially available, very limited data and publications have been reported to date. With an electrical resistivity of about 30 μOhm·cm reported by the supplier after being fired at 550 °C, this ink has only been developed in the frame of solar cells fabrications. Further optimization has to be performed to further lower the sintering temperature to be compatible with printed electronic applications.

ii. Effect of nanoparticles size and concentration for functional inks

When dispersed in solvents, the nanoparticle sizes influences the ability of the ink to be correctly jetted without clogging of the nozzles. In addition, as shown by Kim and Moon [1], decreasing the nanoparticles diameter by a factor 2.2 generates a decrease of the electrical resistivity by a factor 3 when sintered at 200 °C. Shimada *et al.* [80] demonstrated that the morphology of printed metal structures depends on the original size of nanoparticles. Indeed, as will be shown in the next chapter, the high surface area to volume ratio of nanoparticles meliorates the agglomeration and lowers their melting temperature. This result has been demonstrated as soon as 1976 by Buffat and Borel [5] on gold nanoparticles and will be further developed in Chapter 2.

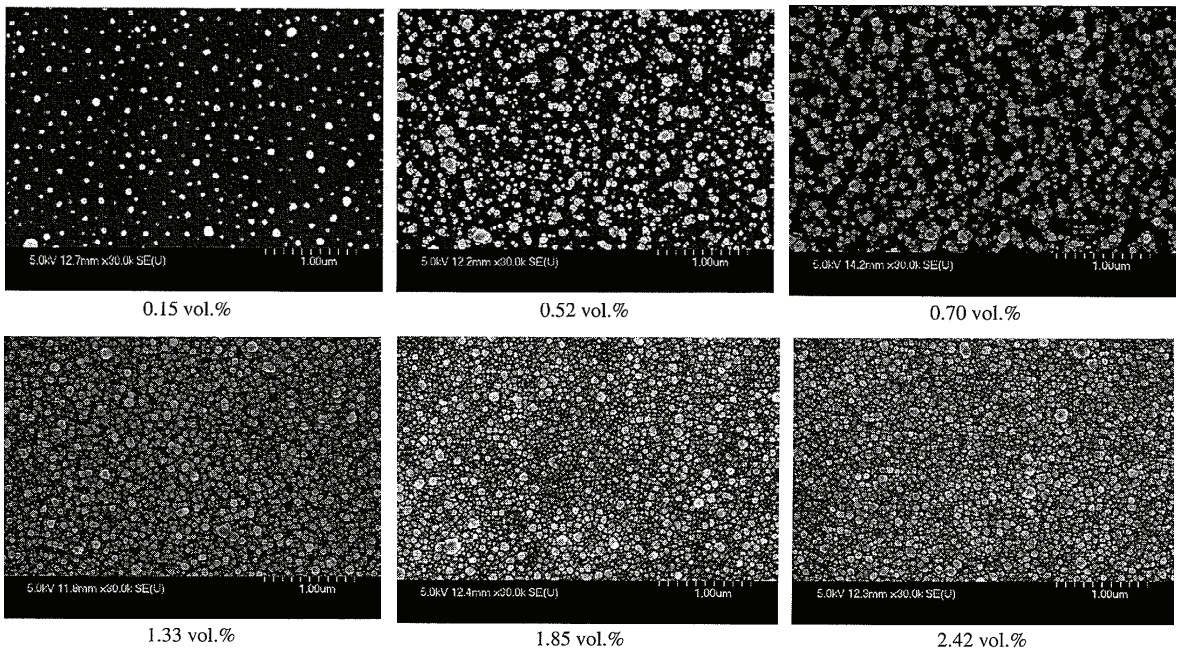

Figure I-14 : SEM micrographs of nanoparticulate deposits with various concentrations after a spin-coating step at 6000 rpm during 30 seconds [82].

In addition, concentration of colloids in the ink plays a role of utmost importance during the printing process. High concentration of nanoparticles in the ink gives rise to an increase of both the viscosity and the surface tension of the ink [65]. Both of them impact the inkjet-printing process since they determine if an ink can be used with a given printhead according to the manufacturer specifications. As depicted in Figure I-14, there is a critical concentration value under which the printed film becomes irregular. Usually, commercially available silver inks are filled with a metal content comprised between 10 and 50 % of the total weight of the ink. Highly concentrated inks print thicker films which are expected to lower the sheet resistance if an optimal curing is performed.

iii. Dispersion of the nanoparticles powder for metal ink formulation

For uniform dispersion of nanoparticles in ink, agglomeration of nanoparticles should be avoided, since the attraction potential could be very high compared to the repulsion potential (see Figure I-15). Interactions between nanoparticles in a solution are indeed ruled by two major forces: the repulsive electrical double-layer force and the attractive van der Waals force. The electrical double-layer is a model describing the variation of electrical potential near a surface due to a local accumulation of charges during nanoparticles motion in the fluid [83]. The mean-field theory developed by Dejarguin, Landau, Verwey and Overbeek (DLVO) describes the interaction between two colloids as a linear combination of these both forces [84, 85]. Derived from the equation of dispersion interaction energy between atoms and molecules [86], Hamaker expressed the van der Waals potential between two spheres of G_1 and G_2 diameters [87] by:

$$V_A = -\frac{A}{12}\left[\frac{y}{x(x+y+1)} + \frac{y}{(x+y)(x+1)} + 2\ln\frac{x(x+y+1)}{(x+y)(x+1)}\right] \quad \text{(I-12)}$$

with $x=d/G_1$ and $y=G_2/G_1$, where d is the distance between the surfaces of two particles and A is the Hamaker constant which describes the attraction strength of the two particles in a medium (A = 30-40.10^{-20} J, [88]). Expression of the double-layer repulsion potential between two identical particles of diameter G if a constant charge is assumed can be defined by [89]:

$$V_R = -\pi\varepsilon G\psi_\delta^2 \ln[1-\exp(-\kappa d)] \quad \text{(I-13)}$$

with

$$\kappa = \sqrt{\frac{e^2\sum_i n_i z_i^2}{\varepsilon k_B T}} \quad \text{(I-14)}$$

where ε is the dielectric constant of the suspending medium, ψ_δ is the Stern potential of the nanoparticle, κ is the reciprocal of the Debye-Hückel length, e is the elementary charge, n_i is the number of ions i per unit volume and z_i is the ion valence. Thus, the higher the electrical potential of the particle, the more stable the colloidal suspension will be.

In the electrical double layer model, the immediate surroundings of nanoparticles are divided into three regions. In the first one, according to the electric charge of the nanoparticle surface, ions with the opposite charge will be strongly bound to the surface due to electrostatic attraction. This ionic capping, known as the Stern layer, will artificially screen the electric surface charge with a characteristic Stern potential. At short range distance, this Stern potential will affect charged molecules of the solvent, thus limiting the tangential stress. A slipping plane is thus theoretically defined beyond which the fluid mobility is

complete. This surface of hydrodynamic shear is defined by its potential, named as zeta potential (ζ). The magnitude of the zeta potential thus indicates the potential stability of the system. A large zeta potential will indeed tend to repel nanoparticles and prevent flocculation. A critical value of ±30 mV is usually admitted as the threshold value for suspensions stability.

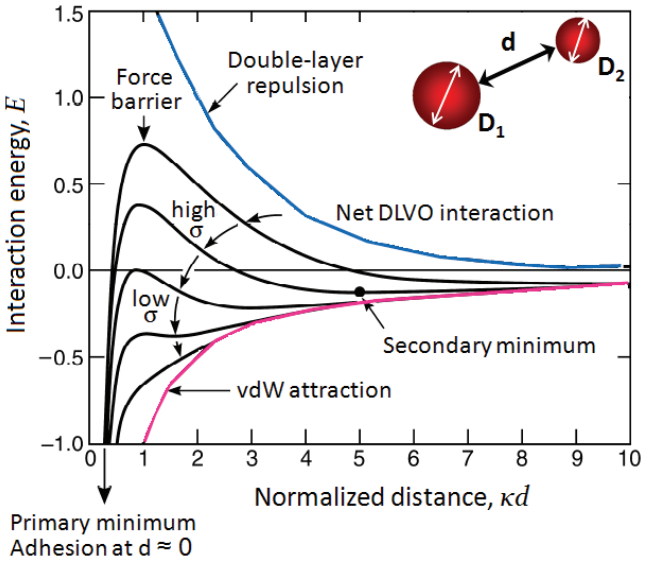

Figure I-15: DLVO curves with the contribution from the attractive van der Waals potential and the repulsive electrostatic potential, in the case of equal size spherical particles (D_1=D_2). Adapted from [90].

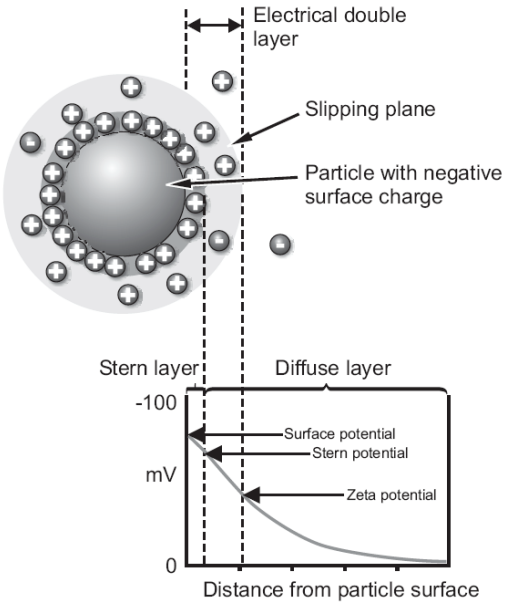

Figure I-16: Schematic of the double layer structure around a negatively charged particle together with the evolution of the apparent electrical potential with respect to the distance from the particle surface [91].

Since silver nanoparticles are poorly charged, the Stern potential can be assimilated to the zeta potential whose measurement has been reported at -20 mV in the unmodified state [92]. In such a case, the repulsion forces cannot overcome the van der Waals forces and the colloids are very likely to initiate coagulation. The PVP, used during the production of silver nanoparticles in liquid phase, modifies the surface electrical potential. Functional groups of the PVP molecule are indeed inducing a steric repulsion effect sufficient to repel nanoparticles in the solvent vehicle (see Equation (I-15) for the steric interaction potential V_s in the case of equal size nanoparticles). This consideration justifies the use of a dispersant agent in the ink, as explained in part II-ii. In fact, the presence of a ligand shell, such as PVP, not only prevents agglomeration but also promotes the suspension of colloids.

$$V_S = 2\pi G k_B T \left(\frac{1}{2} - \chi\right) \Gamma^2 \exp\left(1 - \frac{d}{2\delta}\right) \qquad \text{(I-15)}$$

where G is the diameter of the equal size nanoparticles, k_B is the Boltzmann constant, T is the temperature, χ is the adsorption energy (Flory parameter), Γ is the gamma function, d is the distance between the two nanoparticles and δ is the polymer layer thickness around the nanoparticle. A thickness of 2-3 nm is then sufficient for a good steric repulsion.

Other major concerns when formulating an ink is to avoid nozzle clogging during idle periods (machine inactivity, delivery time from ink supplier, etc.). In these periods, solvents tend to inopportunely evaporate leading to nanoparticles attraction and agglomeration. This is why solvents with moderate to high boiling point (at least above 50 °C) have to be used. A single solvent vehicle is usually not sufficient to meet the requirements of viscosity and surface tension. Since high boiling point solvents are more viscous, a mixture of several solvents with high and low boiling points is used. In general, a tradeoff between fluidity to flow through the printhead and spreading properties on the substrate is sought.

Today, silver ink is very popular and very often used for printed electronics even though other metal inks are emerging. Silver ink is quite easy to manufacture and its shelf life is sufficient to make it very stable (up to six months). This stability allows silver ink manufacture to be compatible with mass production in opposite to other metal inks like aluminum and copper. In fact, silver ink is cost saving by now. Data of several commercially available conductive silver inks for inkjet-printing is reported in Table I-4.

In this study, nanosilver ink supplied by Sun Chemical has been used for historical reasons in our inkjet-printing equipments. Their ink is base on silver nanoparticles with a mean diameter of 25 nm provided by Cabot Corp. Cabot was the first company to develop silver nanoparticle-based inks, fabricated through a chemical synthesis [38], for printed microelectronics.

Table I-4: Comparative data of commercially available silver ink for inkjet-printing.

Supplier	Mean diam. (nm)	Silver content (wt%)	Viscosity (mPa·s)	Surface tension (mN/m)	Curing Temp. (°C)	Electrical resistivity (µOhm·cm)	Product reference
Cabot	60-80	20	11-15	30-33	100-350	5-15	CCI 300
Sun Chemical	30-50	20	10-13	27-31	150-200	6-20	Suntronics U5603
ANP	10	40-45	2-16	28-37	100-150	11	DGP 40LT- 15C
Harima	5-12	52-57	8-15	-	120-150	6	NPS-JL
Bayer	60	22	3-4	28	120	1600	BayInk TP S LT
NanoMas	2-10	10-30	10-13	-	70-150	4	NTS05
Ulvac	3-7	55-60	5-15	-	150	10	L-Ag1TeH
Applied Nanotech	3-10	30	3-12	28-35	70-200	3-150	Ag-iJ10
UTDot	7-10	10-50	1-10	-	90-200	3-10	UTDAg

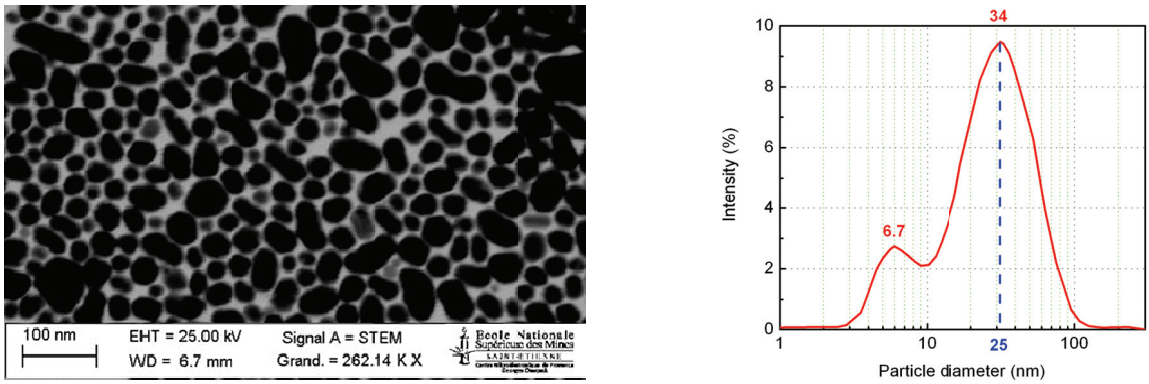

Figure I-17: STEM micrograph of the colloidal silver suspension used in this study (left) and size distribution of intensity obtained from a granulometer (Zetasizer nano series).

Although the average nanoparticle diameter is relatively small (26 nm), the distribution measured by granulometry indicates that particle as big as 100 nm can be found in the suspension (see Figure I-17). As will be shown afterwards, the electrical resistivity achieved with this ink is nonetheless very good when optimized curing conditions are used. Compared to its competitors, the 6 month shelf life of the Sun Tronic U5603 is also suitable for research experiments where small volumes are required. Storage/Conservation of the ink is thus primordial to avoid the waste of expensive inks.

III. Optimization of inkjet-printing parameters

The rheology of the jetted nanofluids and the fine scale geometry of the printheads could affect the intrinsic variability of inkjet-printing technology. As seen in the previous part, nanofluidics integrates a solvent mixture as well as metallic colloids at the nanoscale. A huge process development was performed in order to fabricate high quality patterns with an acceptable/adequate reproducibility. In this part, the inkjet-printing prototype used in this work is presented before introducing the optimization process. This process encompasses the tuning of the droplet ejection, wetting and spreading on the substrate which is presented both theoretically and experimentally in this chapter section.

A. JetPac: an in-line inkjet-printing prototype

As soon as 2003, the Ecole des Mines de Saint-Etienne and Gemalto worked hand in hand, in collaboration with the LP3 and IM2NP laboratories of CNRS, Impika and ST Microelectronics, to develop a consortium around printed electronics applications: the JetPac platform. Since then, this prototype is continually under development to integrate new in-line equipments and increase the stability and reproducibility of the inkjet-printing process.

JetPac prototype is designed to be a semi-industrial equipment which combines inkjet printheads modules together with pre- and post-treatment tools. The aim is to develop a sheet-to-sheet process capable of fabricating electronic devices. By settling several printheads within the same equipment, deposition of metal, insulator and semi-conductor features is possible. Each printhead is dedicated to a specific ink. Except mentioned otherwise in the text, all the inkjet-printed work of this thesis has been conducted on this equipment.

The present system is equipped with two Spectra Galaxy JA 256/30 printheads for metal and dielectric/semi-conductor printing (see Figure I-18). These printheads involve 256 nozzles delivering droplets with an average volume of 28 pL on 300 x 300 mm^2 conveyor stage. The printhead chambers and channels are automatically filled up with an ink which is jetted using DoD piezoelectric technology. Also, it is possible to heat the ink at the nozzle level thus allowing the ejection of inks with different viscosities. Finally, JetPac printing modules is also equipped with a CCD camera to perform die recognition and pattern alignment in accordance with initial layout and die position.

The printing procedure starts by designing the layout of the desired structure in a digital TIFF file using a graphics editing software as Adobe Photoshop. The layout file uses pixel units and not physical dimensions as would be used in vector graphics. In this file, only three colors are accessible for the image pixels: black for the conductive layout (which is aimed to be printed with the silver ink), blue for the insulator pattern (not presented in this work) and white for keeping the bare substrate without any printing (null value). The layout

file is ripped to the printing server of corresponding printhead, and the matrix data is translated to a waveform for DoD piezoelectric crystals.

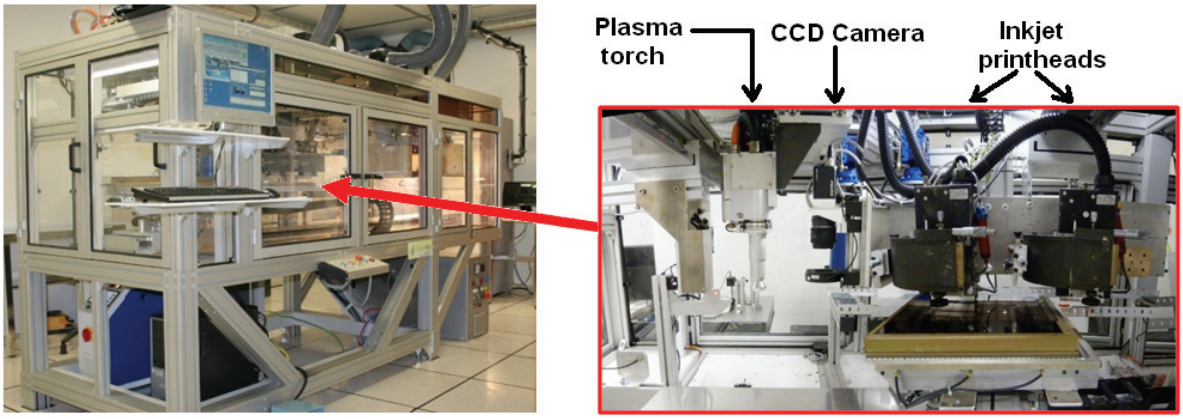

Figure I-18: Inside view of the JetPac prototype in the class 1000 cleanroom environment (left) with a detail view of the printhead modules (right).

Since the 256 nozzles are spaced with 254 µm, the printheads are slanted in order to increase the printing resolution is 608 dpi (dot per inch). This resolution corresponds to a theoretical pixel of 41 x 41 µm². This resolution is related to the frequency of ejection, *i.e.* a droplet is ejected according to a sampling matrix meshed with a pitch of 41 µm. Note that the effective pixels and droplet size will depend on the droplet spreading on the substrate. Typically, the effective diameters of the deposited droplet on polyimide and on silicon nitride substrates are 50 µm and 80 µm, respectively. As depicted in Figure I-19, the difference between the ejection resolution and effective diameter on substrates guaranty the overlapping of the printed droplet to ensure the continuity of the pattern.

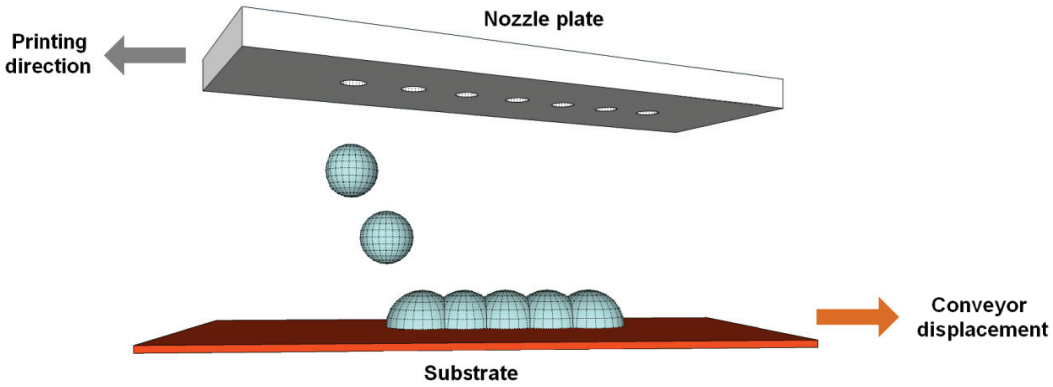

Figure I-19: Schematic showing the overlapping of the printed droplets on the substrate.

JetPac integrates a pre-processing tool which can perform a surface treatment with an atmospheric plasma torch in order to enhance the wettability of the substrate prior to the printing step. This plasma treatment requires to be coupled with an adequate UV treatment or a chemical primer to finely tune the surface energy [93].

The post-processing of inkjet-printed structures is performed using either an ultraviolet lamp (mercury lamp with a power of 80-200 $W{\cdot}cm^{-1}$) to reticulate polymer insulating inks or a microwave cavity for metallic inks (see Figure I-20). Eventually, microwave curing can also be used for the sintering of semiconductor inks [94]. As regard to microwave curing of metal ink, a special configuration has been developed jointly with Lambda Technologies Inc, US. Variable frequency microwaves are generated in a MicroCure 2100 standalone oven. The electromagnetic waves are then driven to the JetPac microwave cavity through a waveguide (see Figure I-20).

The combination of microwave and conductive heating in a Hybrid Variable Frequency Microwave (HVFM) configuration is performed using a thermally conductive susceptor, typically silicon. This silicon is integrated on the top surface of JetPac conveyor stage. Microwave leakage is prevented using a Faraday cage.

Figure I-20: View of the post-treatment equipments integrated in JetPac: UV lamp and microwave cavity in a HVFM configuration.

Thermal curing of printed metal nanoparticle ink is performed jointly through the fast absorption of microwaves by nanoparticles together with the convective heat coming from the silicon conveyor stage. Printed devices are then processed using a HVFM mode with a central frequency of 6.425 GHz with a bandwidth of 1.15 GHz and a sweep rate of 0.1 second. For setting and controlling the curing temperature process, a feedback loop is used through the adjustment of the RF forward power. A non-contact infrared pyrometer is used to measure the system temperature taking account a calibrated surface emissivity of the ink and substrate.

B. Ejection of droplets in a drop-on-demand inkjet system

As presented in the previous part, in a drop-on-demand piezoelectric inkjet system, a conductive ink is maintained in a channel of the printhead by counterbalancing interfacial energy of capillarity. When in idle state, the pressure inside the fluid is indeed controlled automatically in order to contain the meniscus within the nozzle thus avoiding unwanted droplets generation. Yang *et al.* [95] have shown that the gravitational force is not sufficient to overcome the surface tension of the ink at the nozzle level. Indeed, equating both forces (gravity and surface tension) would result in a critical radius for droplet ejection of:

$$r_{crit} = \left(\frac{3}{2}\frac{r_c \cdot \gamma_{lv}}{\rho_l \cdot g}\right)^{1/3} \quad \text{(I-16)}$$

where r_c is the radius of the capillary, ρ_l is the liquid density, g is the local gravitational field (taken as 9.81 m·s^{-2}) and γ_{lv} is the surface tension. When applied to the geometry of the Spectra Galaxy JA 256/30 printheads (r_c = 36 µm), a critical radius of 584 µm is obtained. This value is very large compared to the radius of generated droplets which is in the same order than r_c.

In fact, a droplet can be ejected if the fluid is given a sufficiently high kinetic energy to overcome the capillary forces. In our geometry, such a critical velocity is given by:

$$v_{crit} = 2\left(\frac{\gamma_{lv}}{\rho_l \cdot r_c}\right)^{1/2} = 2\ m \cdot s^{-1} \quad \text{(I-17)}$$

This kinetic energy is generated by the PZT-driven compression of the fluid inside the channel. This mechanical deformation of PZT is tunable by acting on the electrical signal characteristics (frequency, amplitude and profile). It is commonly admitted that the positive portion of the pulse induces a radial expansion of the PZT that increases the volume of the ink within the channel [68, 96]. Generally, a bipolar pulse waveform is used as an excitation signal for the PZT crystal (see Figure I-21) to avoid skewed trajectories and the formation of secondary droplets, also known as satellite droplets. Typical PZT bias voltage ranges from -100 V to +100 V.

This brutal expansion generates an acoustic wave (see Figure I-21) that propagates in both directions inside the channel (b) and which is reflected either at cross-section or compliance variations of the structure (c) [97]. The resultant positive pressure wave after the reflection at open ends is amplified by the fluid compression originating from the negative pulse applied to the PZT crystal (see Figure I-22).

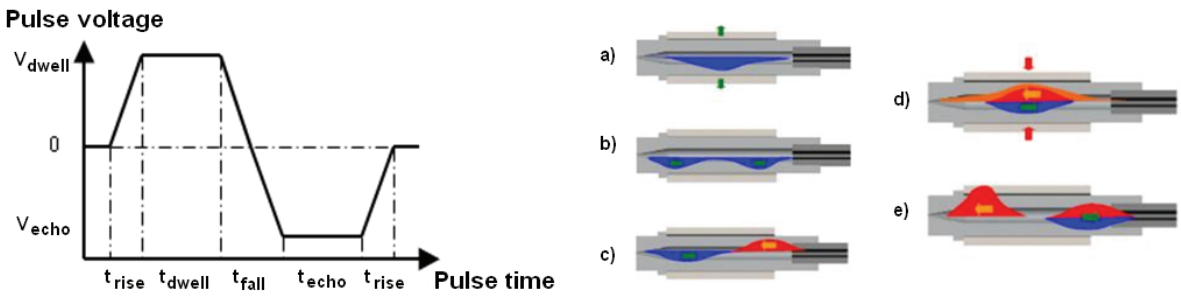

Figure I-21: Schematic diagram of a typical bipolar pulse sent to the piezoelectric actuator (left) and its impact on the acoustic wave interactions (right) [98].

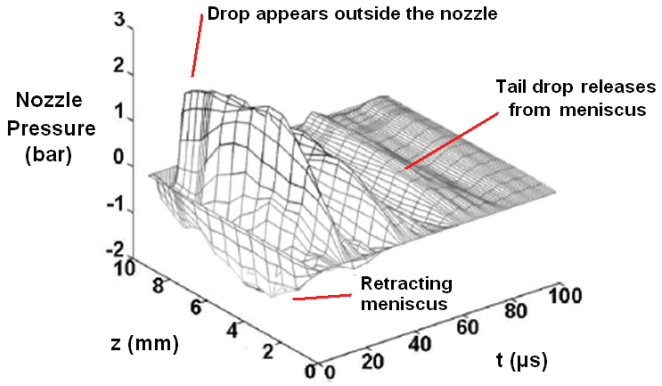

Figure I-22: Simulation results of the pressure field inside the ink channel as a function of time and position (adapted from [96]). Computation has been realized for a channel length of 8 mm and a nozzle diameter of 32 µm.

The characteristic of the ejection waveform is a very critical step for stable inkjet-printing process. This waveform has to be finely tuned in accordance with the printhead geometry and with the ink properties. The bias voltage and its duration (t_{dwell}) have to be optimized so that both acoustic waves are constructively interacting to drive the ink through the nozzle with the maximum velocity. Experiments conducted by Antohe and Wallace [99] pointed out that the optimal time for the up-signal is based on geometrical considerations:

$$t_{dwell} = \frac{2(l + 0{,}61r_c)\sqrt{1 + \rho_l \cdot c_0 \cdot \delta}}{c_0} \qquad \text{(I-18)}$$

where l is the distance between the centre of the PZT crystal and the nozzle extremity, r_c is the nozzle radius, ρ_l is the fluid density, c_o the sound velocity in the considered fluid and δ is the relative modification of the nozzle section.

Increasing the ejection frequency enables the overlap of droplets which increases the electrical conduction, the regularity and the thickness of printed lines. According to Reis and Derby [100], high frequency jetting tends to increase the probability of satellite droplets,

especially for low viscosity fluids (see Figure I-24). As for the pulse amplitude and duration, PZT frequency greatly determines the generated acoustic wave during the droplet ejection since both the ejection velocity and the droplet diameter are impacted. Eventually, the signal profile – corresponding to dissymmetric square signal – affects the stability of the propelled droplet.

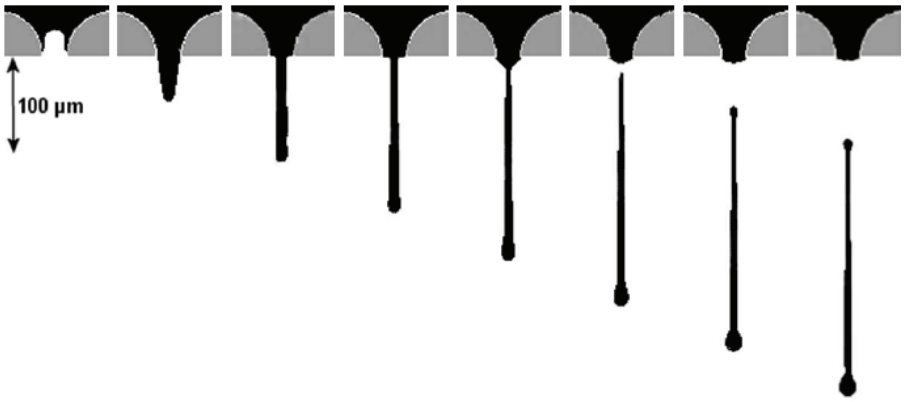

Figure I-23: Sequence of a droplet ejection with a 10 µs timeframe from left to right [96]. In idle state, a slight vacuum depression is applied to maintain the meniscus slightly ingested.

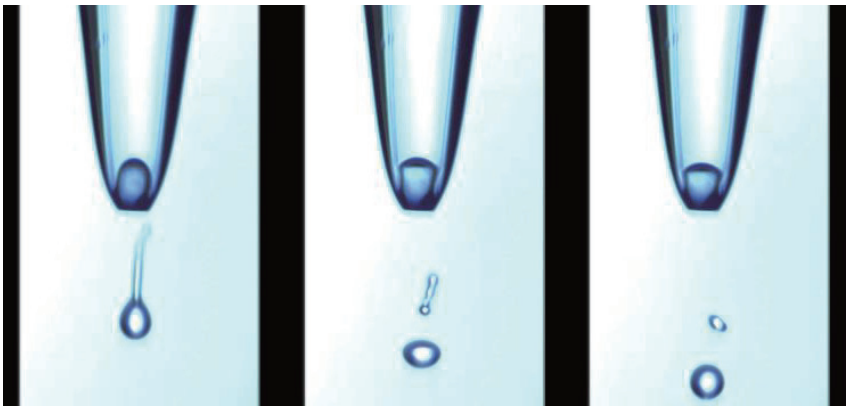

Figure I-24: Sequence showing the formation of a satellite droplet from the break-up of the main droplet tail [101].

In order to finely tune the waveform used for printing silver ink with JetPac, the inkjet process variability has been studied. This variability can originate both from the properties of the silver ink which can misfit with ejecting parameters and from the mechanical accuracy and synchronization between printhead modules and the conveyor stage. Furthermore, nozzle clogging and defective printheads that could happen during the inkjet-printing process is another issue. The process variability can thus be studied through the characterization of dimensions and positions of corresponding droplets on the substrate. It should be pointed out that higher kinetic energy will tend to increase the droplet spreading on the substrate.

For this purpose, a test pattern consisting of 9 rows of punctual dots, each of them corresponding to a specific nozzle, has been prepared on polyimide substrate (see Figure I-25). In order to avoid overlapping of printed droplets, pattern dots were spaced with a few pixels. However, all the nozzles were characterized by reproducing the same pattern several times with a shift, *i.e.* if the first pixel of the first pattern solicits the first nozzle, the following test pattern will begin with the second nozzle. The dot matrix was then reproduced with a shift of 1 pixel until each nozzle has been solicited.

After being cured in an oven (150 °C, 20 min), an image analysis is performed on the picture of the deposited silver droplets (see Figure I-26). Results of image analysis are summarized in Figure I-27 and Figure I-28.

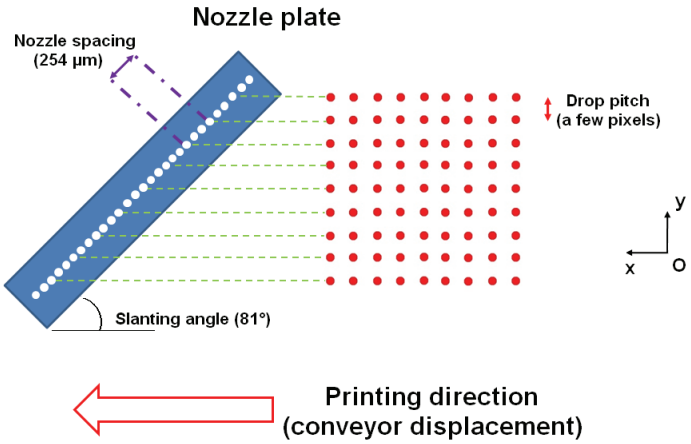

Figure I-25: Schematic of the procedure for inkjet-printing of dots using slanted nozzle plate.

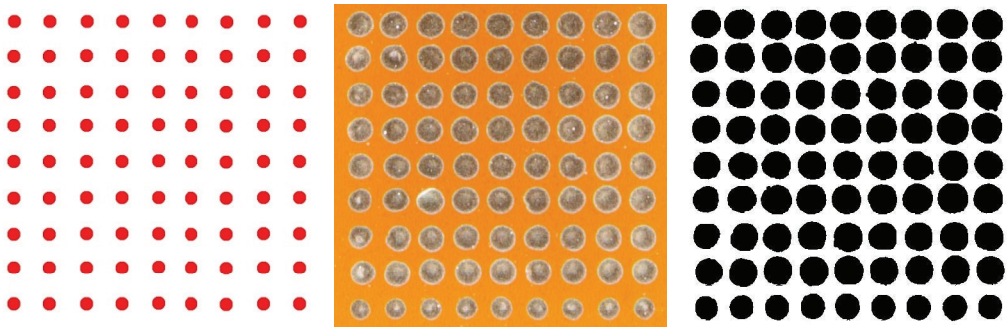

Figure I-26: Resultant test pattern printed on polyimide substrate (center) and corresponding detected objects after image analysis (right). The printing direction is directed towards the left.

The Root Mean Square (RMS) misplacement is characterized by measuring the offset of the drop placement both in the printing direction (Ox axis) and in the orthogonal direction to the printing direction (Oy axis) from the theoretical position on the grid. Distribution of the root mean square misplacement (defined as $(\Delta x^2+\Delta y^2)^{1/2}$) is represented in Figure I-27-a

and follows a log-normal distribution with a mean value of 10.3 µm and a standard deviation of 0.85 µm. Placement accuracy of printed droplets can be analyzed separately in the Ox and Oy directions. In this case, is has been observed that the contribution in the Oy direction is in average four times as much as the x component. This indicates that the main discrepancy is coming from the error in the orthogonal direction to the printing direction. If a precise pattern has to be printed, the Ox axis must thus be privileged. Several origins for this discrepancy can be suggested: a positioning error of the printhead module or the conveyor stage, a rolling vibration movement of the conveyor, a manufacturing error of the nozzle holes which lead to deviated jets.

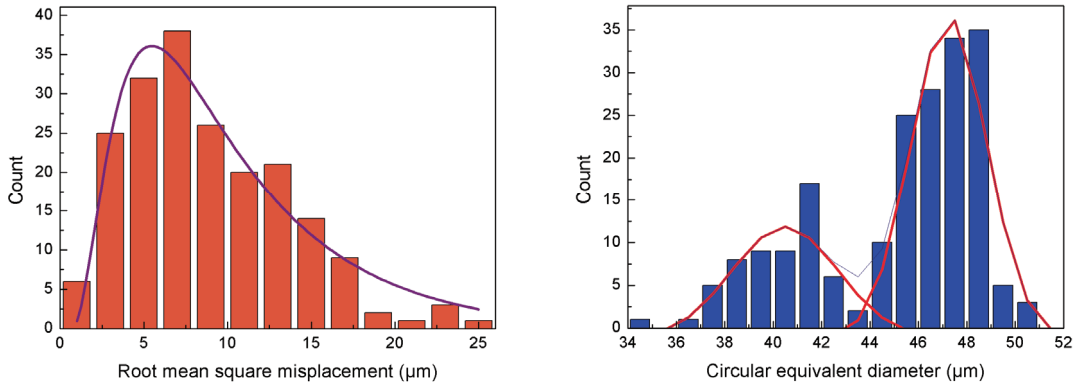

(a) (b)

Figure I-27: Distribution of the root mean square misplacement (left) and of the equivalent diameters of the 30 pL droplets printed on polyimide.

The equivalent diameter of the splats which characterizes how the droplet spreads on the substrate is closely related to both the ejection velocity and the droplet volume. The surface area of detected object is extracted using image analysis (see Figure I-26), and a circular equivalent diameter is computed. The resultant distribution is bimodal as depicted in Figure I-27-b. Equivalent diameters follow Gaussian distributions where the first one is centered at 41 µm with a standard deviation of 4 µm, and the second one being centered on 48 µm with a standard deviation of 3.4 µm.

In order to elucidate the origin of discrepancy observed on droplet diameter, the printed splats are then compared to their position on the substrate according to their corresponding nozzle. A correlation appears between them: smaller splats are only observed at the printed pattern periphery, *i.e.* when external nozzles are excited. It is believed that this discrepancy is due to the closed ends in the printhead manifold which causes a negative offset in the pressure field. Indeed, the incident and reflected waveform could destructively interact thus limiting the pressure value in the nozzle channel. Furthermore, the slight tilt of the printhead that is susceptible to occur during the inkjet-printing process can lead to issues is the provision of ink in the nozzle. Usually the first nozzle is thus higher than the 256th nozzle

which can lead to troubles when the trimming of each jetting channel is not performed dutifully.

Further investigation of the printing process variability can be achieved by considering the ellipticity of printed droplets. Indeed, a short-range flying distance of a few hundreds of microns should lead to a circular impact when the droplet impacts the substrate. Image analysis of the abovementioned droplet impacts led to a Gaussian distribution of the ellipticity centered at $4.8 \cdot 10^{-3}$ (see Figure I-28-a), indicating a slight elliptic shape. A further analysis of this deviation was conducted by measuring the orientation of the major elliptic axis according to the printhead displacement direction. This analysis led to a Gaussian distribution of the droplets orientation centered on 86.2° indicating a disorientation of nearly 4° to the printing direction (see Figure I-28-b).

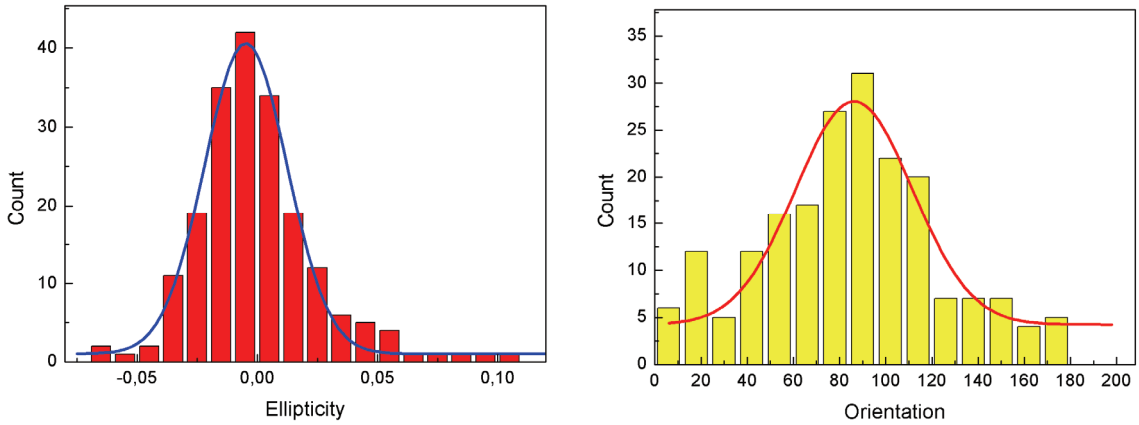

(a) **(b)**

Figure I-28: Distribution of ellipticity of droplets (left) and their respective orientation (right). An ellipticity of 0 indicates a circular droplet while an orientation of 90° corresponds to the printing direction.

Any fluctuation from the circular shape could derive from a deviation of the jet due to the presence of a defect at ejection orifice and/or from the velocity of the stage during the impact. The influence of the stage velocity on the spreading shape of a droplet was addressed by Toivakka in 2003 [102]. An example of the spreading simulation is shown in Figure I-29 for a stage velocity of 16.6 $m \cdot s^{-1}$. His work clearly demonstrated that for a high stage velocity, the droplet tends to elongate. A fine analysis of the splat ellipticity is thus strong indicator to tune the stage velocity without any deformation.

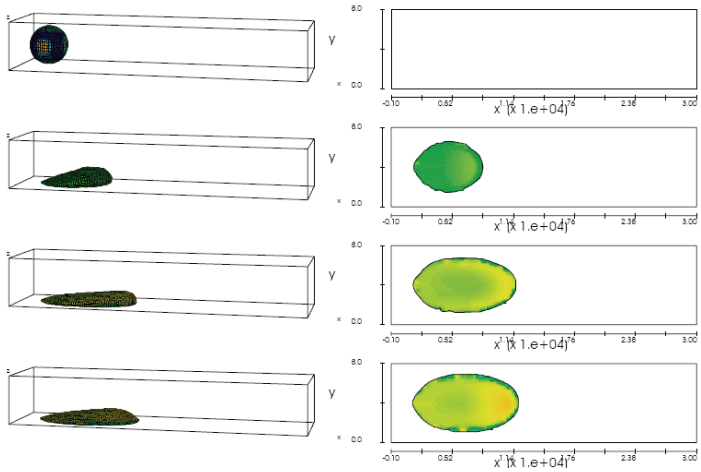

Figure I-29: Numerical simulations of a droplet spreading on a substrate moving to the left at 16.6 m·s^{-1}, with contact area indicated on the right hand side [102].

Due to the high resolution required to print electronic circuits, the erratic deviation associated with inkjet technology can lead to inconsistent line conformality (see Figure I-30). As can be seen on this picture, the initial design represents parallel lines with a two pixel width and pitch printed on polyimide. Once printed and cured, the nominal width of central lines and pitch is about 100 µm thus corresponding to the initial layout. However, deviation of jetted droplets leads to printed lines with different width of 128 µm (3 pixels) and 64 µm (1 pixel). In this example, the jetting deviation is about two pixels leading to a pitch of about three pixels instead of two. The resultant pattern is thus achieved with various line widths and pitch. This artifact is particularly detrimental when conformal and precise control of dimensions is required such as for fine pitch interconnects and radiofrequency applications.

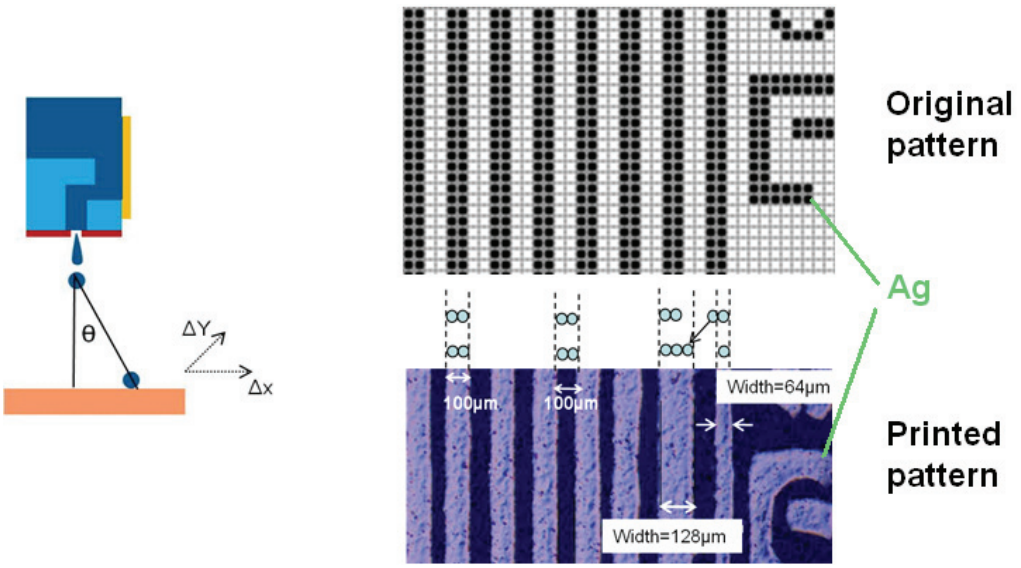

Figure I-30: Deviation of ink jets can lead to discrepancies in the printed structure. Image of a conductive pattern printed on polyimide by JetPac exhibiting lines of three and one pixels-wide instead of two. In the picture, silver appears as clear lines while the substrate appears in dark blue.

C. Wetting and spreading of an inkjet droplet on a solid surface

The comprehensive understanding of the physic-chemical interactions between the liquid and the substrate is a key point when considering an ink for the fabrication of conductive traces. Indeed, the spreading of the ink on the surface will directly impact the final printed line geometry. Control of the ink wettability has to be considered afterwards. This control is defined by the equilibrium between the liquid, the solid and the vapor phases determined by the Young relation [103]:

$$\gamma_{sv} = \gamma_{lv} \cos\theta + \gamma_{sl} \quad \text{(I-19)}$$

where γ_{sv}, γ_{lv} and γ_{sl} are the surface tensions between the three phases and θ is the apparent contact angle (see Figure I-30). For a given ink, the surface energy is an intrinsic property and the control of the ink spreading extent will only be possible by modifying the surface energy of the substrate. This step could only be performed by changing the type of substrate directly or by altering the surface energy using a chemical (*e.g.* using a primer) or physical (*e.g.* using a corona, UV-O_3, atmospheric plasma, etc.) processes. Surface energies of typical substrates used in this work were measured and have been synthesized in Table I-5.

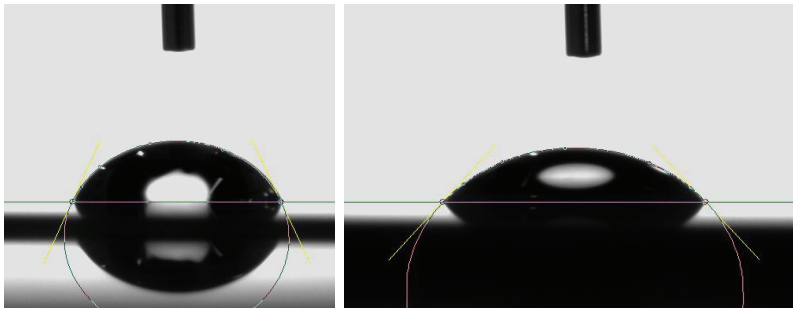

Figure I-31: Water droplet profile on silicon (left) and on silicon nitride (right), exhibiting a variation of the contact angle from 68° to 51° respectively.

Table I-5: Typical surface energy measured on substrates used in this work (determined by the OWRK method).

Substrate	**Surface energy, γ_{sl} (mN·m^{-1})**
Silicon	66.2
Silicon oxide	62.6
Silicon nitride	57.9
Glass	48.1
Polyimide Kapton	42.8
PET coveme	42.0

Even though wettability plays a key role in the inkjet-printing process, dynamic behavior also has to be taken into account. The description of dynamics underlying the impact and the initial spreading of inkjet-printed droplets on the substrate is adequately characterized by the triplet composed by the Reynolds number (*Re*), the Ohnesorge number (*Oh*) and the Weber number (*We*) defined as follow:

$$Re = \frac{\rho_l U_0 D_0}{\mu} \tag{I-20}$$

$$Oh = \frac{\mu}{\sqrt{\rho_l \cdot \gamma_{lv} \cdot D_0}} \tag{I-21}$$

$$We = \frac{\rho_l \cdot D_0 \cdot U_0^2}{\gamma_{lv}} = (Oh \cdot Re)^2 \tag{I-22}$$

where ρ_l is the fluid density, U_o and D_o are the velocity and the diameter respectively of the droplet before impact, μ is the dynamic viscosity of the fluid and γ_{lv} is the surface tension. The Reynolds number measures the ratio of inertial forces to viscous forces, thus indicating the flow regime of the fluid [104]. The ratio between the interfacial oscillation period and the viscous damping time is defined by the Ohnesorge number. Such a ratio is particularly valuable to quantify the damping of interfacial oscillations after the droplet impact. Eventually, the Weber number denotes the relative contribution of the inertial forces to the surface tension. This number is usually employed to describe the propensity of the fluid to spread on a surface and to form secondary droplets.

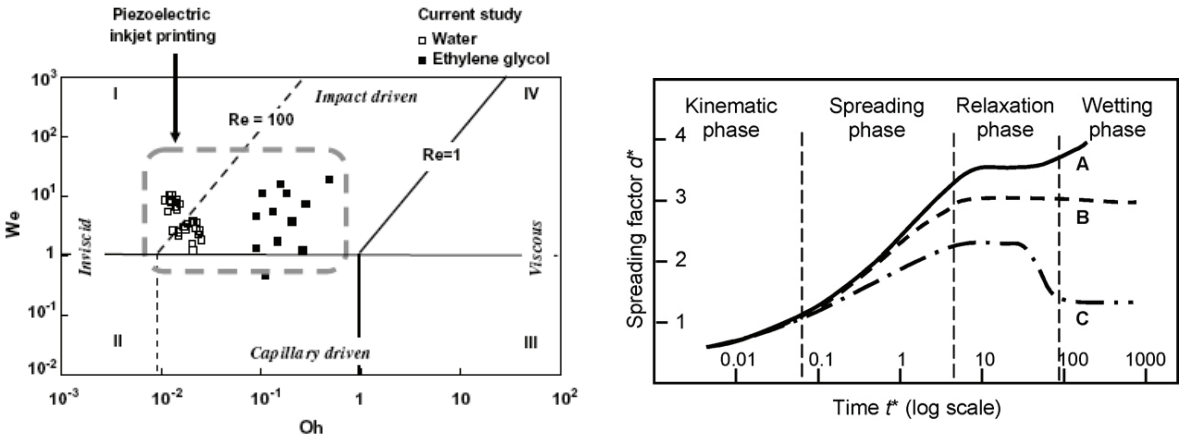

Figure I-32: Diagram of the characteristic impact regimes according to the Weber and Reynolds numbers (left) [105] and the spreading behaviors of liquid drop according with respect to time (right) [16].

Four regimes of droplet impact on substrate were described in previous studies by Schiaffino and Sonin according to these dimensionless numbers (see Figure I-32) [106]. However, the final shape of the droplet only depends on the surface tension and the surface energy because they rule the equilibrium state. Once impacted, four phases can be distinguished in the droplet initial spreading: a kinematic phase, a spreading phase, a relaxation phase and an equilibrium phase. The end of the spreading phase is marked by the maximal extent of the droplet diameter d_1 (see Figure I-33), whose expression is given by equation (I-22) as a function of the initial droplet diameter d_0 [107]. The droplet is then retracting until reaching the equilibrium diameter d. The whole damping process lasts a few hundred microseconds from impact in the case of picoliter droplets [105].

$$\frac{d_1}{d_0} = \left(\frac{We^2 + 12}{3(1 - \cos\theta) + 4\frac{We^2}{Re^{1/2}}} \right)^{1/2} \tag{I-23}$$

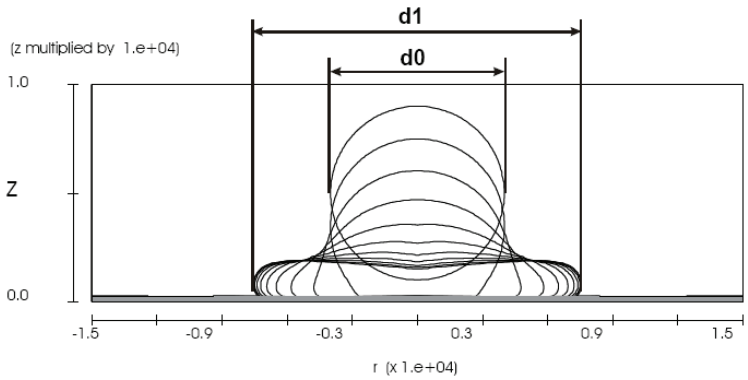

Figure I-33: Dynamics of the impact spreading of a droplet [102]. The initial droplet diameter d_0 is 80 µm, impact velocity 10 $m \cdot s^{-1}$, viscosity 50 mPa·s, surface tension 73 $mN \cdot m^{-1}$ and static angle of 90°.

During the equilibrium phase, the droplet reaches an equivalent diameter d. Since the wetting angle is inferior to 90° in the case of hydrophilic substrate, a sessile droplet has the shape of a spherical cap whose diameter can geometrically be derived [105]:

$$\frac{d}{d_0} = \left(\frac{4\sin\theta(1 + \cos\theta)}{(1 - \cos\theta)(2 + \cos\theta)} \right)^{1/3} \tag{I-24}$$

According to the wetting properties, fabrication of continuous conductive lines is performed either by printing adjacent droplets or with a given overlap. Figure I-34 shows several line morphologies printed using different drop overlaps. An optimal overlap can be achieved for which the conformality of printed lines is respected (see Figure I-34). In the

absence of contact line pinning, drops will merge due to a surface energy minimization phenomenon. The width w of such a printed line formed from individual drops that are separated by a distance p will thus be modified according to [108]:

$$w = \left(\frac{2\pi d_0^3}{3p\left((\theta / \sin^2 \theta) - (\cos \theta / \sin \theta) \right)} \right)^{1/2} \quad \text{(I-25)}$$

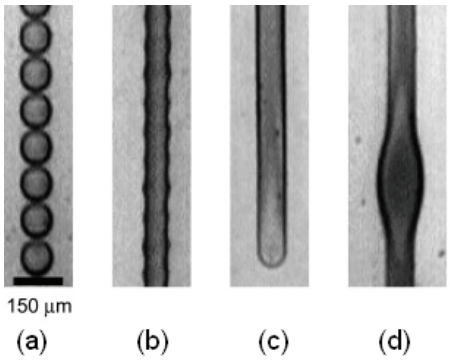

Figure I-34: Printed PEDOT lines exhibiting principal behaviors when drop spacing is reduced: individual drops (a), scalloped (b), uniform (c) and bulging (d) lines [109].

Surface wetting properties can be modified using either physical treatments such as plasma, or chemical treatments using promoting agents. Atmospheric pressure plasma treatment is used to increase the surface energy creating hydroxyl and/or carbonyl hydrophilic groups which enhance the substrate wettability. Other chemical compounds, such as hexamethyldisilazane (HMDS, $[(CH_3)_2Si]_2NH$) can also be coated on the substrate to enhance adhesion through the elimination of aqueous traces at the surface. HMDS is indeed very reactive to hydroxyl groups located at the surface with the formation of a new siloxane product, $Si\text{-}O\text{-}Si(CH_3)_3$. Being more hydrophobic, the spreading of the printed conductive ink is limited and a better pinning is achieved. A measure of the surface energy before and after the coating of HMDS on silicon nitride gives a variation from 60 $mN{\cdot}m^{-1}$ to 47.9 $mN{\cdot}m^{-1}$.

All the printing issues presented in this part have been addressed during the thesis and a huge process development has been performed in order to achieve a good adequacy between the conductive silver ink from Sun Chemical and the main substrates used (polyimide, silicon and silicon nitride). In addition, a specific attention was put on the development of maintenance procedures which notably requires a meticulous trimming of each nozzle individually and a scraping of the nozzle plate to remove residual ink. All these optimizations steps required a significant time to be developed during the thesis and led to a standardized inkjet-printing procedure on the JetPac equipment. Except mentioned otherwise, future printing operation will be performed using parameters listed in Table I-6.

Table I-6: Printing parameters used in this work.

Parameter	Value
Printhead	Nova JA 256/30 AAA
Metal ink	Suntronics U5603
Waveform voltage	100 V
Printhead temperature	39 °C
Stage temperature	RT (~23 °C)
Stage velocity	3 $m \cdot s^{-1}$
Printing distance	500 µm
Pulse width, t_{dwell}	5.8 µs
Rise time, t_{rise}	1.2 µs
Fall time, $t_{fall}/2$	1.2 µs

IV. Curing of printed metallic nanoparticle-based inks

Once the pattern or the thin film is inkjet-printed on the substrate, a curing step is required to generate the solid film and reach low electrical resistivity. Indeed, as mentioned previously silver nanoparticles from Sun Chemical are in suspension in a solvent vehicle composed by ethanol, ethylene glycol and glycerol. In addition to this solvent mixture, nanoparticles are coated with a polymer shell of polyvinylpyrrolidone (PVP) [38]. Thus, electrical contact between nanoparticles can only happen once solvents have evaporated and the PVP has begun to degrade enough. According to the thermal treatment, colloids will tend to accumulate either at the edge or at the center of pattern driven by evaporation fluxes. It is therefore essential to understand how solvents evaporate and especially at which temperature before focusing on the sintering step and how it modifies the microstructure.

A. Solvent evaporation process: hinder the coffee stain effect

The final shape of printed lines will be highly subordinated to the sintering process during which the solvents evaporate and particles operate rearrangement. Self-organization of those nanoparticles is indeed an accommodation response to the moving liquid front toward the substrate. Several regimes can be observed depending on the solvent properties and on the thermal treatment. While thoroughly studied, extensive understanding of the colloids behavior during evaporation is nonetheless undermined by the difficulty to monitor the displacement of nanosized colloids and to observe the liquid fluxes in droplets in the picolitre range.

During evaporation of solvents, many physical phenomena are occurring such as convection, Marangoni effect and hydrodynamic flows driven by temperature gradients inside the droplet. The first artifact that has been reported in drying drops is the "*coffee stain effect*" (see Figure I-35) which induces an accumulation of nanoparticles at the edge of the drop and forms a solid ring [110]. When the colloidal suspension is drying on a rough substrate, the contact line of the droplet tends to remains fully anchored during the evaporation process, preventing the drop from receding. As explained by Deegan *et al.* [110], since the surface to volume ratio of liquid is larger near the contact line, a liquid flux is generated within the droplet which carries colloids from the center toward the edge. Inversely, when the solvents are highly volatile, the nanoparticles tend to migrate toward the center of the droplet because of convection flows [111, 112].

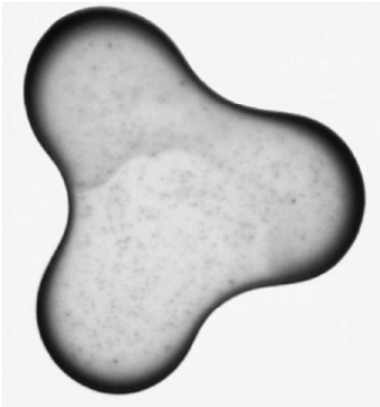

Figure I-35: Coffee rings observed after complete drying of a coffee droplet with 1 wt% of solid content [110].

This situation is only taking place when the evaporation process is prevailing on other solidification process such as phase change on impact, e.g. when using wax-based inks [113]. However, the coffee stain can be avoided by increasing the contribution from the Gibbs-Marangoni effect. This mass transfer rises from the surface tension gradient that exists within the droplets due to the differential evaporation rate between the edge and the center of the droplet. Indeed, since surface tension is assumed to decrease when temperature increases, the temperature gradient induced by the improved evaporation at the edge entails a maximal surface tension at the center of the drop (see Figure I-36). The Gibbs-Marangoni effect can also be amplified using a mixture of solvents with different vapor pressure and surface tension [114]. A surface tension gradient will thus be generated from the preferential evaporation of the higher vapor pressure solvent at the contact line. Impact of this solvent mixture is even greater than what would be achieved by a temperature gradient to suppress coffee rings. In particular, this effect justifies the use of glycerol solvent in the Sun Tronic silver ink as a hindrance to the coffee ring, while ethanol and ethylene glycol are only controlling the ink rheology.

Significance of the Gibbs-Marangoni flow in the liquid droplet during its evaporation can be described by the dimensionless Marangoni number *Ma* defined as [115]:

$$Ma = \frac{\Delta\gamma \cdot r}{\eta D} \tag{I-26}$$

where $\Delta\gamma$ is the surface tension difference, r is the characteristic length (e.g. the radius of the spread drop on the substrate), η is the fluid viscosity and D is the solute diffusion coefficient. To limit the accumulation of nanoparticles at the edges of the printed deposit, it is usually admitted that *Ma* should be over 100.

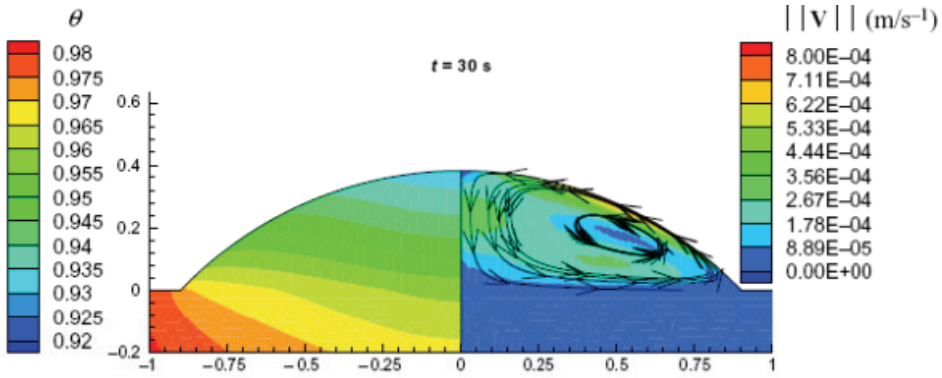

Figure I-36: Temperature distributions and speed distribution of Marangoni flow within a 500 nL toluene droplet on a Teflon substrate [116].

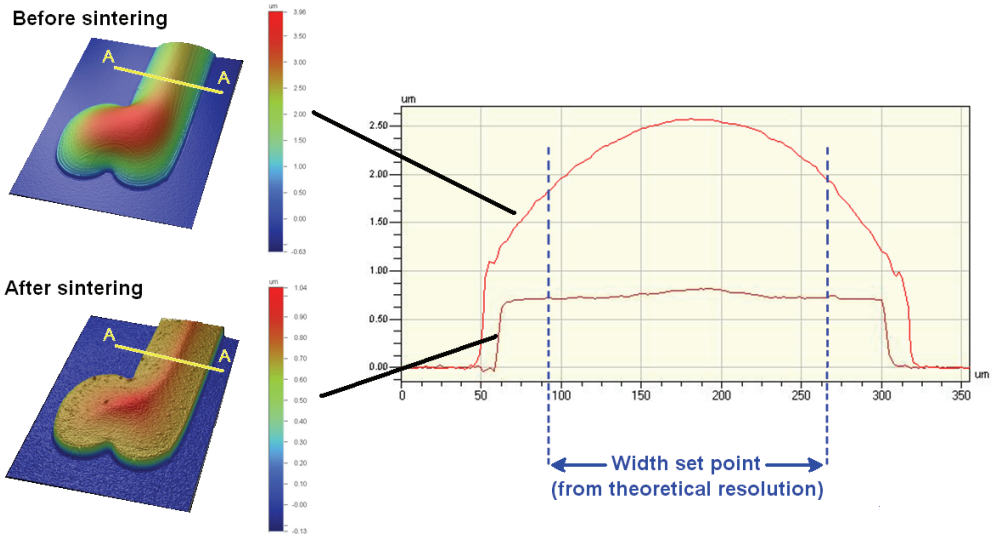

Figure I-37: Line profile (optical profilometry) of printed silver lines on silicon nitride before and after a sintering step of 250 °C during 15 min.

After a few microseconds, the contact angle of the droplet reaches an equilibrium state and a second evaporation regime is activated [105]. During this regime, the evaporation at a constant contact area is replaced by evaporation at a constant contact angle during which the diameter of the droplet usually decreases. This constant contact angle matches the equilibrium receding angle of the fluid. When a rough substrate is used for the printing, the evaporation phase at constant contact angle tends to be delayed because it enhances the pinning phenomenon.

Experiments were performed on the SunTronic silver ink printed on silicon nitride and show evidence of reverse Gibbs-Marangoni effect (see Figure I-37). Here, the coffee ring is prevented using ethylene glycol. After the curing step at 250 °C, the volume and dimensions of the printed lines are evolving. The line thickness is reduced by 1.8 µm which represents a thickness loss of 71 %. The width is also shrunk by 13 % thus indicating that the ink is somehow pinned to the substrate during solvent evaporation.

B. Impact of thermal conditions on the solvents evaporation

In order to analyze the ink behavior under a thermal source, Differential Scanning Calorimetry (DSC) can adequately be exploited to observe the impact of thermal conditions on inks (times, temperature, thermal ramp, and atmosphere). Figure I-38 shows the principle of DSC measurement.

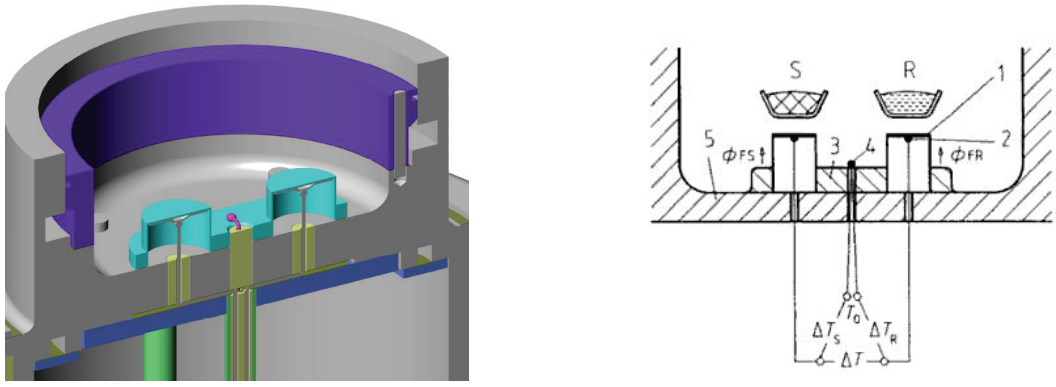

Figure I-38: Schematic view of a DSC chamber cross-section (left) with the principle of differential temperature measurement (right) between the sample pan (S), the reference pan (R) and the chamber thermocouple [117].

During the DSC experiment, the temperature of a sample deposited in a hermetic pan is monitored and compared to a reference sample which is inert in the working temperature range. An empty pan is used as reference to subtract the thermal inertia induced by the metallic pan from the sample heat flow signal. The thermal flow exchanged between the heating system and the sample during a thermal cycle is derived. When the sample under

analysis undergoes a phase transition, a chunk of enthalpy is exchanged. While thermal energy is required for endothermic events such as solvent evaporation, the heat flow resulting from the exothermic events such as coalescence should be positive since some energy is returned to the system. When thermocouples measure a different temperature between the sample and the reference, the calorimeter compensate the difference by providing more thermal energy for an endothermic event such as solvent evaporation. The resulting calorific power is thus monitored and plotted with time and temperature in the form of a thermogram.

When considering biphasic fluids such as colloidal suspensions, the problem is to differentiate the intense endothermic signal of the solvent's evaporation from the shallow exothermic signal originating from the sintering. Previous characterization of the electrical resistivity has shown that sintering occurs at low temperature. Based on the works from Greer [118] and Woo [119], the first coalescence mechanisms were indeed observed around 100 °C for nanoparticles with a diameter comprised between 20 and 40 nm. DSC analysis was thus performed on the Sun Chemical ink to determine the evaporation temperature range of solvents and to confirm the low sintering temperature. Essential properties of solvents present in the studied ink are summarized in Table I-7.

Table I-7: Main properties of the constitutive solvents of the Sun Chemical silver ink.

	Ethanol	**Ethylene glycol**	**Glycerol**
Molecular formula	C_2H_6O	$C_2H_6O_2$	$C_3H_8O_3$
Skeletal formula	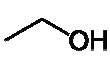	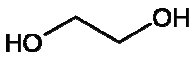	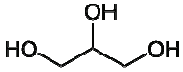
Boiling point	79°C	197°C	290°C
Thermal conductivity	0.18 W/m.K	0.26 W/m.K	0.30 W/m.K
Surface tension	0.022 N/m	0.048 N/m	0.059 N/m
Dipolar moment [120, 121]	1.69 D	2.28 D	2.67 D
Volume content [122]	25-40 vol%	25-40 vol%	10-25 vol%

In order to be as close as possible to the thermal behavior of deposited ink under thermal curing, inkjet-printed square structures with controlled volume are printed both on 5 mm² silicon and silicon nitride substrate instead of standard aluminum pans. The objective is to carry on the DSC analysis on picolitre volumes as in the inkjet process instead of microliter volumes deposited in the pan. DSC analysis on printed structures requires a specific calibration procedure. In parallel, about 5 mg of ink is drop casted on conventional hermetic pan made of aluminum. Figure I-39 shows the normalized DSC peaks for the three studied cases.

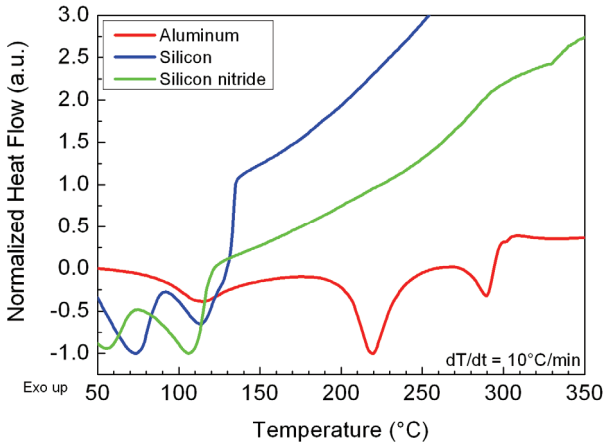

Figure I-39: DSC thermograms of silver nanoparticles ink dropcasted in an aluminum pan or inkjet-printed on silicon-based substrates (Si and SiNx). Signals are normalized on the peak intensiy of ethylene glycol.

In the case of conventional hermetic pan, DSC analysis shows three endothermic peaks that are observable below 300 °C. Those three peaks are attributed to the evaporation of the main solvents in the conductive ink: ethanol, ethylene glycol and glycerol (see Table I-7). Because of the low silver metal content within the ink (20 wt%), the exothermic peak corresponding to the sintering is not detectable.

When printed ink is analyzed, only two endothermic peaks are distinguished at 45 °C and 90 °C. Those peaks are attributed to the evaporation of ethylene glycol and glycerol, respectively. The very low amount of ethanol present in printed structures is supposed to evaporate around room temperature. However, one can still see that there is a slight difference between DSC profile obtained both on silicon and silicon nitride even when the calibration procedure is supposed to subtract the thermal inertia of substrate. This is due to the fact that the considered volume of substrate during DSC calibration is little bit different since cleaving of 5 mm^2 square silicon samples is not very reproducible.

Pressure-mediated evaporation of solvent is a well understood phenomenon. According to the Clausius-Clapeyron relation, increasing the pressure will tend to increase the temperature of the phase transition [123, 124]. Boiling points are thus occurring at higher temperature when hermetic pan are used since the pressure is increasing as solvents evaporate. DSC characterization indicates that when very low volume is considered – as for inkjet-printed silver ink -, solvents tend to be evaporated at low temperature thus enabling a fast initiation of the silver nanoparticles sintering. This ensures that the printed layouts will start to be conductive after the curing even at low temperature (120°C to 150°C) which is particularly convenient for flexible electronics on plastic substrates.

C. Thermal curing of inkjet-printed metal nanoparticles features

During the sintering step, atomic diffusion mechanisms are activated to support the formation of a material continuum driven by energy minimization. This atomic mass transport results in both structural and electrical changes. As shown in Figure I-40, sintering is highly temperature-dependent. Indeed, the higher the curing temperature is, the more advanced the sintering will be. As a consequence, the solid-state diffusion of atoms between contacted nanoparticles is accelerated and the electron transport is enhanced.

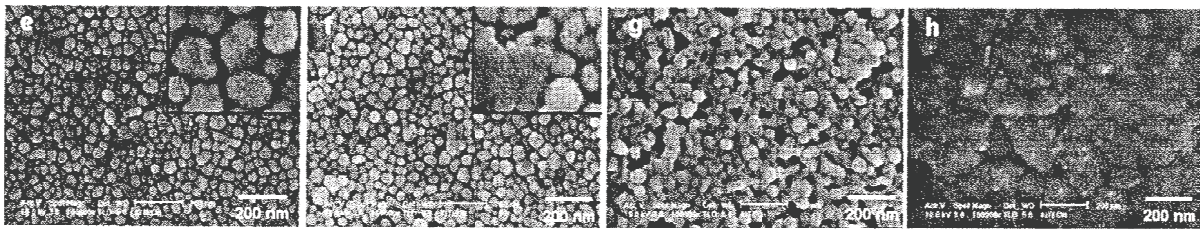

Figure I-40 : Microstructural evolution of a nanoparticulate film with an initial size of 47 nm, after a sintering step at 100 °C (e), 160 °C (f), 200 °C (g) et 300 °C (h) [1].

As a result of silver nanoparticles sintering, electrical resistivity is quickly decreasing with the curing temperature until nearly reaching the asymptotic value of bulk (*i.e.* 1.62 µΩ·cm [61]). This opens real prospects for achieving an acceptable electrical conductivity at low temperature which is compatible with industrial process. The higher the curing temperature is, the shorter the time required for obtaining close-to-bulk resistivity will be. Thus, as obtained by Greer *et al.* [63], a resistivity of 5 µΩ·cm requires a 10 min treatment at 200 °C or 30 min at 150 °C.

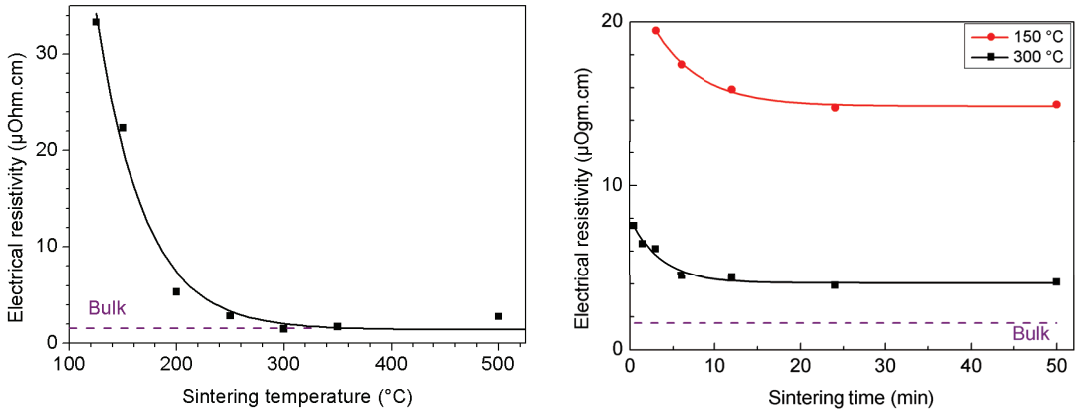

Figure I-41 : Evolution of electrical resistivity of our inkjet-printed silver films on a silicon substrate respectively to the sintering temperature (sintering time of 15 min) and time, with a thermal ramp of 10 °C/s.

Curing of printed silver nanoparticulate films can be achieved in a conventional convective oven. However, the convection limits the use of temperature sensitive substrate like plastic (PET, ABS, PC, etc.) which are of great interest in printed electronics. Indeed, since both substrate and ink are heated, the curing temperature is limited around the glass transition temperature. High temperature and long time thus cannot be operated on plastics to achieve near-bulk electrical resistivity. Consequently, the standard oven has been rejected especially for product industrialization purpose. Several alternative sintering technologies have been reported and tested: intense light absorption (laser IR and photonics) [7-127], plasma [128], chemical agents [129], 2.45 GHz microwave [8] and electrical sintering [39] were used for selective and fast sintering of metal ink especially by reducing the heat affected zone.

For the development of an in-line process using JetPac platform, the hybrid variable frequency microwave curing has been used. This variable frequency mode improves the distribution of the electromagnetic field within the cavity and impedes arcing phenomena that could happen on metal surface. In parallel, Rapid Thermal Annealing (RTA) oven (JetFirst 100 from Jipelec) is used for the development of fast heating approach and especially to study the impact of fast heating ramp on microstructure evolution. Such fast heating ramps are indeed similar in RTA and microwave ovens and will be compared afterwards. Accelerated heating ramp is one of the key points for all developed fast sintering approaches reported in the literature.

While heat transfer by conduction and radiation is mainly affecting the film interfaces in a RTA oven, microwaves provide rapid volumetric heating. Thus, microwave heating usually achieve more uniform sintering since the energy is dissipated within the layer due to internal friction between atoms with a thermal flux moving outward from the layer core [131]. Since bulk metals are usually assumed to reflect microwave radiations, a coupling can be achieved with metallic powder [132]. The absorbed power per unit volume, P is given by:

$$P = \frac{E^2}{\rho} = \omega \cdot \varepsilon'' \cdot E^2 \qquad \text{(I-27)}$$

where ρ is the electrical resistivity, ω=2πf is the angular frequency of the microwave radiation, ε" is the dielectric loss factor and E is the amplitude of the electromagnetic field.

Given the high electrical conduction of metals, microwave radiations only interact with the extreme surface of metals, known as the skin depth defined by:

$$\delta_p = \frac{c \cdot \varepsilon_0}{2\pi f \cdot \varepsilon''} = \left(\frac{2\rho}{\omega \cdot \mu}\right)^{1/2} \qquad \text{(I-28)}$$

where μ is the absolute magnetic permeability of the material and ε_0 is the permittivity of the free space. So that, for a frequency of 6.425 GHz, the electromagnetic wave is confined within 80 nm of silver. Since nanoparticles size is well below this value, the electromagnetic field across the nanoparticle is uniform and causes volumetric heating without arcing [133]. In both sintering systems, a feedback controller regulated the temperature ramp by adjusting the forward power level. Figure I-42 compares the forward power needed to reach 300°C for both sintering systems.

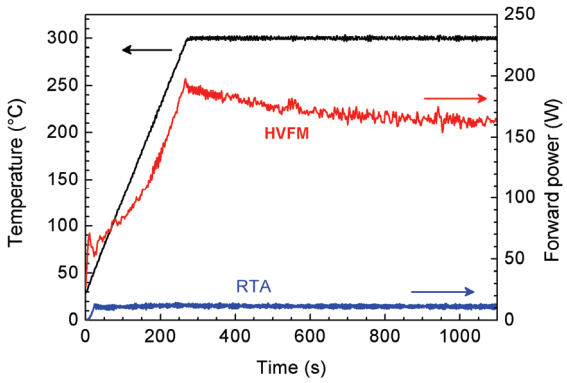

Figure I-42: Temperature and forward power profiles with respect to time for both RTA and HVFM configurations for a sintering temperature of 300 °C and a ramp of 1 °C/s

As explained earlier, a pyrometer (λ = 8-14 μm, far infrared) is used to measure the temperature of printed structures. Since inkjet-printed layers vary from liquid to solid state, emissivity is expected to change accordingly during the heating step. A calibration is thus performed on the temperature range using thermocouple. The profile of emissivity has been compared to DSC thermogram as reported in Figure I-43. By comparing both graphs, it is shown that the shrink of emissivity happens between 120°C and 130°C. It fits well with an endothermic peak that corresponds to the evaporation of solvents ending in the same range of temperature. The consecutive increase of the heat flow can directly be related to the initiation of the sintering process. Indeed, as soon as the last solvent is removed, contact between nanoparticles is enabled and atomic diffusion processes initiated. The accurate control of emissivity change and thus, the temperature control in both sintering systems, is a major key point to achieve the desired electrical resistivity in a fast way and without substrate damage.

SEM micrographs exhibit a very high dependency of printed silver microstructure to the thermal system and cycle, and especially to the dwell temperature (see Figure I-44 and Figure I-45). During the heat treatment, both coarsening and densification are occurring. While RTA curing seems to induce a partial sintering of the film with a high number of small porosities, a bimodal distribution of grains is observable at 300 °C with HVFM curing (see Figure I-45).

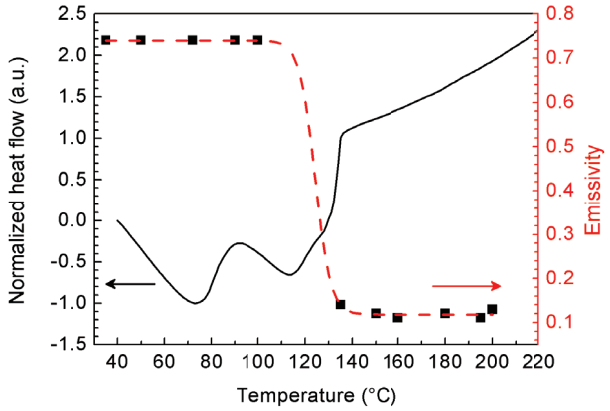

Figure I-43: Exothermic thermogram of the nanoparticle-based ink deposited on a silicon substrate obtained by DSC (plain line) and variation in infrared emissivity calibrated with a pyrometer and a thermocouple on inkjet-printed ink (dotted line).

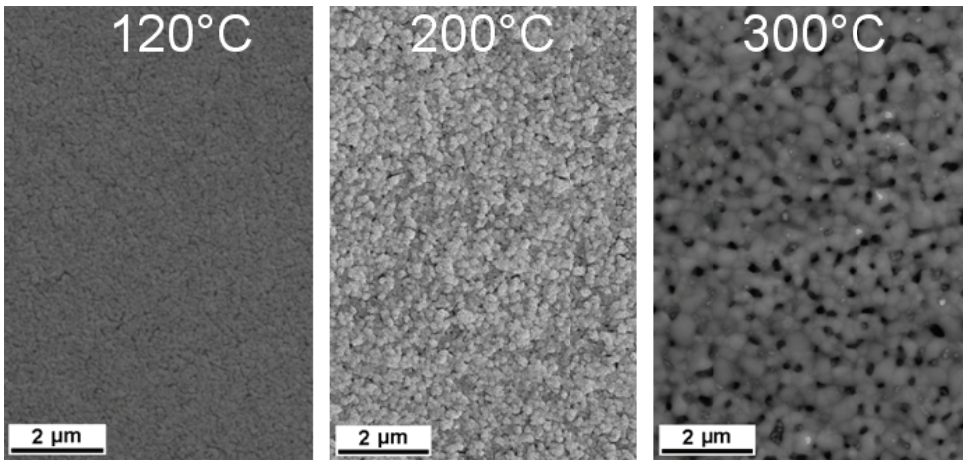

Figure I-44: Microstructural evolution of silver thin films surface after being sintered in a RTA oven during 15 min with a thermal ramp of 10 °C/s.

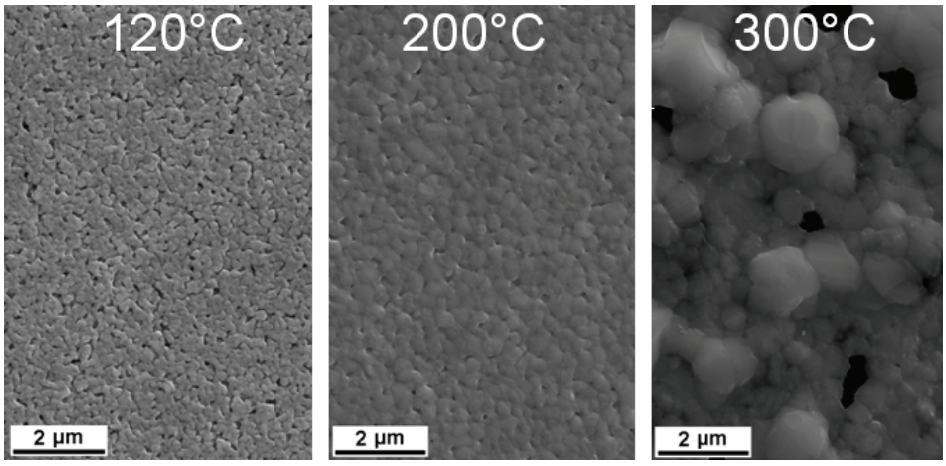

Figure I-45: Microstructural evolution of silver thin films surface after being sintered in a HMMW oven during 15 min with a thermal ramp of 10 °C/s.

According to the sintering condition such as the curing system, the temperature and the thermal ramp, the microstructure could significantly evolve. As will be seen in the next chapter, these process parameters will condition the initiation of sintering mechanisms that could lead to densification and grain growth. Impact of this microstructural evolution on the electrical and mechanical behavior will be further investigated in Chapter 3. The fine tuning of inkjet-printing parameters as well as the curing conditions lead to the fabrication of some functional demonstrators for feasibility purposes. A realization is presented in the following figure.

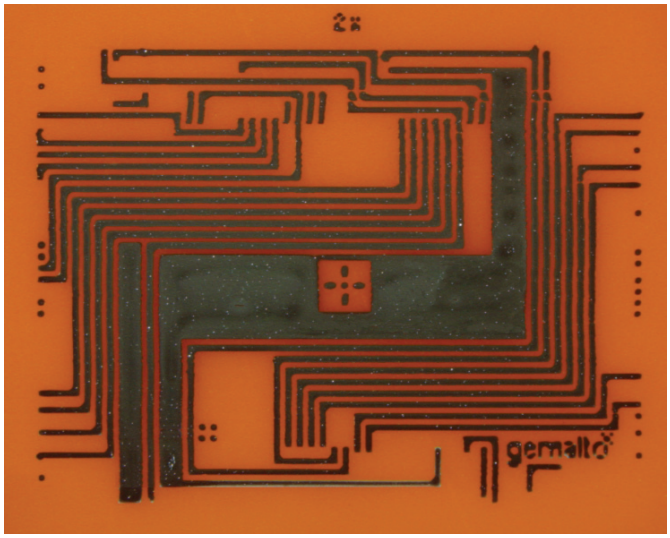

Figure I-46: Redistribution lines layout printed on polyimide treated by HMDS. Unit line is 100 µm wide.

Chapter conclusions

In this chapter, the several techniques to produce nanoparticle-based jettable inks from the preparation of metallic nanoparticles to its dispersion in a solvent vehicle have been described. Emphasis was put on the importance of the microstrains and related stored energy generated within nanoparticles during attrition milling or chemical synthesis for the subsequent sintering step. The coalescence phenomenon is indeed driven by the minimization of the system energy originating from either the high curvature stress or the crystalline microstrain when a high concentration of dislocations or point defects is observed.

A state of the art in direct-writing technologies that can be used for packaging application has also been presented in this part. In particular, the assets and drawbacks of the inkjet-printing technology have been presented. Drop-on-demand printing has proved to be successful in the fabrication of printed devices either on rigid or flexible substrates. In particular, the semi-industrial printing prototype developed in the laboratory (JetPac) has been presented together with an extensive optimization of its process for microelectronics applications.

Finally, the utmost importance of the solvents evaporation control and optimization has been addressed in order to guarantee conformality of the sintered deposits. In particular, the rheology of the jettable ink turned out to be the key parameter to enhance the Gibbs-Marangoni flow which hinders the coffee ring effect. A better understanding of the solvent evaporation process through differential scanning calorimetry enabled the optimization of the sintering process to reveal the conductive properties of silver films.

In the next chapter, the impact of the sintering conditions will be further analyzed through the observation of microstructural evolution. Particular attention will be paid to coalescence physics which drives the morphological conversion. The contribution of printed thin films morphology will then be addressed from a mechanical point of view as much from stress as from a stiffness perspective.

References

[1] D. M. Eigler and E. K. Schweizer, "Positioning single atoms with a scanning tunnelling microscope," *Nature*, vol. 344, pp. 524–526, 1990.

[2] R. D. Piner, J. Zhu, F. Xu, S. Hong, and C. A. Mirkin, ""dip-pen" nanolithography," *Science*, vol. 283, pp. 661–663, 1999.

[3] W. M. Wang, R. M. Stoltenberg, S. Liu, and Z. Bao, "Direct patterning of gold nanoparticles using dip-pen nanolithography," *ACS Nano*, vol. 2, no. 10, pp. 2135–2142, 2008.

[4] K.-H. Kim, N. Moldovan, and H. D. Espinosa, "A nanofountain probe with sub-100 nm molecular writing resolution," *Small*, vol. 1, no. 6, pp. 632–635, 2005.

[5] B. A. Nelson, W. P. King, A. R. Laracuente, P. E. Sheehan, and L. J. Whitman, "Direct deposition of continuous metal nanostructures by thermal dip-pen nanolithography," *Applied Physics Letters*, vol. 88, no. 3, p. 033104, 2006.

[6] J. Jang, S. Hong, G. C. Schatz, and M. A. Ratner, "Self-assembly of ink molecules in dip-pen nanolithography: A diffusion model," *The Journal of Chemical Physics*, vol. 115, no. 6, pp. 2721–2729, 2001.

[7] H. Wang, L. Huang, Z. Xu, C. Xu, R. Composto, and Z. Yang, "Sintering metal nanoparticle films," in *Flexible Electronics and Displays Conference and Exhibition* pp. 1–3, 2008.

[8] B. Basnar and I. Willner, "Dip-pen-nanolithographic patterning of metallic, semiconductor, and metal oxide nanostructures on surfaces," *Small*, vol. 5, no. 1, pp. 28–44, 2009.

[9] B. W. Maynor, Y. Li, and J. Liu, "Au ink for afm dip-pen nanolithography," *Langmuir*, vol. 17, no. 9, pp. 2575–2578, 2001.

[10] Y. Zhang, C. Liu, and D. Whalley, "Direct-write techniques for maskless production of microelectronics: A review of current state-of-the-art technologies," in *International Conference on Electronic Packaging Technology & High Density Packaging. DOI - 10.1109/ICEPT.2009.5270702*, pp. 497–503, 2009.

[11] S.-C. Hung, O. A. Nafday, J. R. Haaheim, F. Ren, G. C. Chi, and S. J. Pearton, "Dip pen nanolithography of conductive silver traces," *The Journal of Physical Chemistry C*, vol. 114, pp. 9672–9677, 2010.

[12] A. Piqué, D. Chrisey, R. Auyeung, J. Fitz-Gerald, H. Wu, R. McGill, S. Lakeou, P. Wu, V. Nguyen, and M. Duignan, "A novel laser transfer process for direct writing of electronic and sensor materials," *Applied Physics A: Materials Science & Processing*, vol. 69, pp. S279–S284, 1999.

[13] R. J. von Gutfeld, E. E. Tynan, R. L. Melcher, and S. E. Blum, "Laser enhanced electroplating and maskless pattern generation," *Applied Physics Letters*, vol. 35, no. 9, pp. 651–653, 1979.

[14] E. M. Nadgorny, C. Zhou, J. Drelich, and R. Zahn, "MTU laser-based direct-write techniques: recent development and nanoparticles patterning results," in *Materials Research Society Fall Meeting*, vol. 758, 2003.

[15] M. Colina, P. Serra, J. Fernandez-Pradas, L. Sevilla, and J. Morenza, "DNA deposition through laser induced forward transfer," *Biosensors and Bioelectronics*, vol. 20, pp. 1638–1642, 2005.

[16] K. Hon, L. Li, and I. Hutchings, "Direct writing technology–advances and developments," *CIRP Annals - Manufacturing Technology*, vol. 57, no. 2, pp. 601–620, 2008.

[17] F. J. Adrian, J. Bohandy, B. F. Kim, A. N. Jette, and P. Thompson, "A study of the mechanism of metal deposition by the laser-induced forward transfer process," *Journal of Vacuum Science and Technology B*, vol. 5, no. 5, pp. 1490–1494, 1987.

[18] J. Bohandy, B. F. Kim, F. J. Adrian, and A. N. Jette, "Metal deposition at 532 nm using a laser transfer technique," *Journal of Applied Physics*, vol. 63, no. 4, pp. 1158–1162, 1988.

[19] L. Rapp, *Impression par laser (LIFT) de transistors organiques en films minces*. PhD thesis, Université de la méditerranée (Aix-Marseille II), 2010.

[20] A. Lushnikov and A. Negin, "Aerosols in strong laser beams," *Journal of Aerosol Science*, vol. 24, pp. 707–735, 1993.

[21] S. Tehranian, F. Giovane, J. Blum, Y.-L. Xu, and B. . S. Gustafson, "Photophoresis of micrometer-sized particles in the free-molecular regime," *International Journal of Heat and Mass Transfer*, vol. 44, pp. 1649–1657, 2001.

[22] A. Ashkin, "History of optical trapping and manipulation of small-neutral particle, atoms, and molecules," *IEEE Journal of Selected Topics in Quantum Electronics, DOI - 10.1109/2944.902132*, vol. 6, no. 6, pp. 841–856, 2000.

[23] A. Piqué and D. B. Chrisey, *Direct-write technologies for rapid prototyping applications: sensors, electronics, and integrated power sources*. Academic Press, 2002.

[24] P. G. Saffman, "The lift on a small sphere in a slow shear flow," *Journal of Fluid Mechanics*, vol. 22, no. 2, pp. 385–400, 1965.

[25] P. G. Saffman, "The lift on a small sphere in a slow shear flow - corrigendum," *Journal of Fluid Mechanics*, vol. 31, no. 3, p. 624, 1968.

[26] M. Allen, A. Alastalo, M. Suhonen, T. Mattila, J. Leppäniemi, and H. Seppä, "Contactless electrical sintering of silver nanoparticles on flexible substrates," *IEEE Transactions On Microwave Theory And Techniques*, vol. 59, no. 5, pp. 1419–1429, 2011.

[27] T. Williams, K. McVicker, A. Shaikh, T. Koval, S. Shea, B. Kinsey, and D. Hetzer, "Hot melt ink technology for crystalline silicon solar cells," in *IEEE Photovoltaic Specialists Conference*, pp. 352–355, 2002.

[28] L. Rayleigh, "On the capillary phenomena of jets," *Proceedings of the Royal Society of London*, vol. 29, pp. 71–97, 1879.

[29] S. Tomotika, "On the instability of a cylindrical thread of a viscous liquid surrounded by another viscous fluid," *Proceedings of the Royal Society of London. Series A, Mathematical and Physical Sciences*, vol. 150, no. 870, pp. 322–337, 1935.

[30] A. Panáek, L. Kvítek, R. Prucek, M. Kolár, R. Veerová, N. Pizúrová, V. K. Sharma, T. Nevená, and R. Zboril, "Silver colloid nanoparticles: synthesis, characterization, and their antibacterial activity," *The Journal of Physical Chemistry B*, vol. 110, pp. 16248–16253, 2006.

[31] H. Gleiter, "Nanocrystalline materials," *Progress in Materials Science*, vol. 33, no. 4, pp. 223–315, 1989.

[32] C. G. Granqvist and R. A. Buhrman, "Ultrafine metal particles," *Journal of Applied Physics*, vol. 47, no. 5, pp. 2200–2219, 1976.

[33] S. L. Girshick, C.-P. Chiu, and P. H. McMurry, "Modelling particle formation and growth in a plasma synthesis reactor," *Plasma Chemistry and Plasma Processing*, vol. 8, no. 2, pp. 145–157, 1988.

[34] M. Shinde, A. Pawar, S. Karmakar, T. Seth, V. Raut, S. Rane, S. Bhoraskar, and D. Amalnerkar, "Uncapped silver nanoparticles synthesized by DC arc thermal plasma technique for conductor paste formulation," *Journal of Nanoparticle Research*, vol. 11, no. 8, pp. 2043–2047, 2009.

[35] M. F. Becker, J. R. Brock, H. Cai, D. E. Henneke, J. W. Keto, J. Lee, W. T. Nichols, and H. D. Glicksman, "Metal nanoparticles generated by laser ablation," *Nanostructured Materials*, vol. 10, pp. 853–863, 1998.

[36] S. Schwyn, E. Garwin, and A. Schmidt-Ott, "Aerosol generation by spark discharge," *Journal of Aerosol Science*, vol. 19, pp. 639–642, 1988.

[37] G. Skandan and A. Singhal, *Nanomaterials handbook*, ch. Perspectives on the science and technology of nanoparticle synthesis. Taylor & Francis, 2006.

[38] Cabot, "Printable electrical conductors," Patent US20060163744 A1, 2006.

[39] J. Tikkanen, K. Gross, C. Berndt, V. Pitkänen, J. Keskinen, S. Raghu, M. Rajala, and J. Karthikeyan, "Characteristics of the liquid flame spray process," *Surface and Coatings Technology*, vol. 90, pp. 210–216, 1997.

[40] M. Rajala, K. Janka, and P. Kykkänen, "An industrial method for nanoparticle synthesis with a wide range of compositions," *Reviews on Advanced Materials Science*, vol. 5, pp. 493–497, 2003.

[41] E. K. Athanassiou, R. N. Grass, and W. J. Stark, "Chemical aerosol engineering as a novel tool for material science: From oxides to salt and metal nanoparticles," *Aerosol Science and Technology*, vol. 44, pp. 161–172, 2009.

[42] M. Faraday, "The bakerian lecture: Experimental relations of gold (and other metals) to light," *Philosophical Transactions of the Royal Society of London*, vol. 147, pp. 145–181, 1857.

[43] A. M. Ahern and R. L. Garrell, "In situ photoreduced silver nitrate as a substrate for

surface-enhanced raman spectroscopy," *Analytical Chemistry*, vol. 59, pp. 2813–2816, 1987.

[44] P. C. Lee and D. Meisel, "Adsorption and surface-enhanced raman of dyes on silver and gold sols," *Journal of Physical Chemistry*, vol. 86, pp. 3391–3395, 1982.

[45] D. L. Van Hyning, W. G. Klemperer, and C. F. Zukoski, "Silver nanoparticle formation: Predictions and verification of the aggregative growth model," *Langmuir*, vol. 17, pp. 3128–3135, 2001.

[46] H. Wang, X. Qiao, J. Chen, X. Wang, and S. Ding, "Mechanisms of pvp in the preparation of silver nanoparticles," *Materials Chemistry and Physics*, vol. 94, pp. 449–453, 2005.

[47] G. Cao, *Nanostructures & nanomaterials: synthesis, properties & applications*. Imperial College Press, 2004.

[48] E. Matijevic, "Preparation and properties of uniform size colloids," *Chemistry of Materials*, vol. 5, pp. 412–426, 1993.

[49] C. L. de Castro and B. S. Mitchell, *Synthesis, functionalization and surface treatment of nanoparticles*, ch. Nanoparticles from mechanical attrition. American Scientific Publishers, 2002.

[50] H. J. Fecht, "Nanostructure formation by mechanical attrition," *Nanostructured Materials*, vol. 6, no. 1-4, pp. 33–42, 1995.

[51] C. Koch, "The synthesis and structure of nanocrystalline materials produced by mechanical attrition: A review," *Nanostructured Materials*, vol. 2, pp. 109–129, 1993.

[52] J. Eckert, J. Holzer, C. K. III, and W. Johnson, "Structural and thermodynamic properties of nanocrystalline FCC metals prepared by mechanical attrition," *Journal of Materials Research*, vol. 7, no. 7, pp. 1751–1761, 1992.

[53] H. Fecht, E. Hellstern, Z. Fu, and W. Johnson, "Nanocrystalline metals prepared by high-energy ball milling," *Metallurgical and Materials Transactions A*, vol. 21, no. 9, pp. 2333–2337, 1990.

[54] D. Oleszak and P. H. Shingu, "Nanocrystalline metals prepared by low energy ball milling," *Journal of Applied Physics*, vol. 79, no. 6, pp. 2975–2980, 1996.

[55] T. Shen and C. C. Koch, "The influence of dislocation structure on formation of nanocrystals by mechanical attrition," *Materials Science Forum*, vol. 179-181, pp. 17–24, 1995.

[56] C. Koch, "Synthesis of nanostructured materials by mechanical milling: problems and opportunities," *Nanostructured Materials*, vol. 9, no. 1-8, pp. 13–22, 1997.

[57] J. Eckert, "Relationships governing the grain size of nanocrystalline metals and alloys," *Nanostructured Materials*, vol. 6, pp. 413–416, 1995.

[58] W. Milligan, S. Hackney, M. Ke, and E. Aifantis, "In situ studies of deformation and fracture in nanophase materials," *Nanostructured Materials*, vol. 2, pp. 267–276, 1993.

[59] S. A. Hackney, M. Ke, W. W. Milligan, and E. C. Aifantis, *Processing and properties*

of nanocrystalline materials, ch. Grain size and strain rate effects on the mechanisms of deformation and fracture in nanostructured metals, pp. 421–426. Minerals, Metals & Materials Society, 1996.

[60] M. Ke, S. A. Hackney, W. W. Milligan, and E. C. Aifantis, "Observation and measurement of grain rotation and plastic strain in nanostructured metal thin films," *Nanostructured Materials*, vol. 5, pp. 689–697, 1995.

[61] D. Lide, *CRC handbook of chemistry and physics*. CRC Press, 81st ed., 2000.

[62] M. Levy, H. E. Bass, R. R. Stern, and V. Keppens, *Handbook of Elastic Properties of Solids, Liquids, and Gases: Elastic properties of solids: theory, elements and compounds, novel materials, technological materials, alloys, and building materials*. Academic Press, 2001.

[63] J. R. Greer and R. A. Street, "Thermal cure effects on electrical performance of nanoparticle silver inks," *Acta Materialia*, vol. 55, pp. 6345–6349, 2007.

[64] S. Fuller, E. Wilhelm, and J. Jacobson, "Ink-jet printed nanoparticle microelectromechanical systems," *Journal of Microelectromechanical Systems*, vol. 11, pp. 54–60, 2002.

[65] H.-H. Lee, K.-S. Chou, and K.-C. Huang, "Inkjet printing of nanosized silver colloids," *Nanotechnology*, vol. 16, no. 10, pp. 2436–2441, 2005.

[66] R. Chen, N. T. Nuhfer, L. Moussa, H. R. Morris, and P. M. Whitmore, "Silver sulfide nanoparticle assembly obtained by reacting an assembled silver nanoparticle template with hydrogen sulfide gas," *Nanotechnology*, vol. 19, no. 45, pp. 455604–, 2008.

[67] N. R. Bieri, J. Chung, D. Poulikakos, and C. P. Grigoropoulos, "Manufacturing of nanoscale thickness gold lines by laser curing of a discretely deposited nanoparticle suspension," *Superlattices and Microstructures*, vol. 35, pp. 437–444, 2004.

[68] J. B. Szczech, C. M. Megaridis, J. Zhang, and D. R. Gamota, "Ink jet processing of metallic nanoparticle suspensions for electronic circuitry fabrication," *Nanoscale and Microscale Thermophysical Engineering*, vol. 8, no. 4, pp. 327–339, 2004.

[69] B. K. Park, D. Kim, S. Jeong, J. Moon, and J. S. Kim, "Direct writing of copper conductive patterns by ink-jet printing," *Thin Solid Films*, vol. 515, pp. 7706–7711, 2007.

[70] N. A. Luechinger, E. K. Athanassiou, and W. J. Stark, "Graphene-stabilized copper nanoparticles as an air-stable substitute for silver and gold in low-cost ink-jet printable electronics," *Nanotechnology*, vol. 19, no. 44, pp. 445201–, 2008.

[71] H. Kang, H. S. Jung, J. Y. Kim, J. C. Park, M. Kim, H. Song, and K. H. Park, "Immobilized CuO hollow nanospheres catalyzed alkyne-azide cycloadditions," *Journal of Nanoscience and Nanotechnology*, vol. 10, no. 10, pp. 6504–6509, 2010.

[72] D. J. Lee and J. H. Oh, "Inkjet printing of conductive Ag lines and their electrical and mechanical characterization," *Thin Solid Films*, vol. 518, no. 22, pp. 6352–6356, 2010.

[73] L. Q. Pham, J. H. Sohn, C. W. Kim, J. H. Park, H. S. Kang, B. C. Lee, and Y. S. Kang, "Copper nanoparticles incorporated with conducting polymer: Effects of copper

concentration and surfactants on the stability and conductivity," *Journal of Colloid and Interface Science*, vol. 365, pp. 103–109, 2012.

[74] N. Marjanovic, J. Hammerschmidt, J. Perelaer, S. Farnsworth, I. Rawson, M. Kus, E. Yenel, S. Tilki, U. S. Schubertc, and R. R. Baumann, "Inkjet printing and low temperature sintering of CuO and CdS as functional electronic layers and schottky diodes," *Journal of Materials Chemistry*, vol. 21, pp. 13634–13639, 2011.

[75] K. A. Schroder, I. M. Rawson, D. S. Pope, and S. Farnsworth, "Photonic curing explanation and application to printing copper traces on low temperature substrates," in *44th International Symposium on Microelectronics IMAPS*, 2011.

[76] A. Kamyshny, J. Steinke, and S. Magdassi, "Metal-based inkjet inks for printed electronics," *The Open Applied Physics Journal*, vol. 4, pp. 19–36, 2011.

[77] Y. Lee, J. rak Choi, K. J. Lee, N. E. Stott, and D. Kim, "Large-scale synthesis of copper nanoparticles by chemically controlled reduction for applications of inkjet-printed electronics," *Nanotechnology*, vol. 19, no. 41, p. 415604, 2008.

[78] M. Grouchko, A. Kamyshny, and S. Magdassi, "Formation of air-stable copper-silver core-shell nanoparticles for inkjet printing," *Journal of Materials Chemistry*, vol. 19, no. 19, pp. 3057–3062, 2009.

[79] D. Kim and J. Moon, "Highly conductive ink jet printed films of nanosilver particles for printable electronics," *Electrochemical and Solid-State Letters*, vol. 8, pp. J30–J33, 2005.

[80] M. Shimada, T. Seto, and K. Okuyama, "Size change of very fine silver agglomerates by sintering in a heated flow," *Journal of Chemical Engineering of Japan*, vol. 27, no. 6, pp. 795–802, 1994.

[81] P. Buffat and J.-P. Borel, "Size effect on the melting temperature of gold particles," *Physical Review B*, vol. 13, pp. 2287–2298, 1976.

[82] K.-S. Chou, K.-C. Huang, and H.-H. Lee, "Fabrication and sintering effect on the morphologies and conductivity of nano-Ag particle films by the spin coating method," *Nanotechnology*, vol. 16, no. 6, pp. 779–784, 2005.

[83] M. Hosokawa, K. Nogi, M. Naito, and T. Yokoyama, *Nanoparticle technology handbook*. Elsevier, 2007.

[84] B. Derjaguin and L. Landau, "Theory of the stability of strongly charged lyophobic sols and of the adhesion of strongly charged particles in solution of electrolytes," *Acta Physicochimica URSS*, vol. 14, pp. 633–662, 1941.

[85] E. Verwey and J. Overbeek, *Theory of the Stability of Lyophobic Colloids*. Elsevier, 1948.

[86] F. London, "The general theory of molecular forces," *Transactions of the Faraday Society*, vol. 33, pp. 8b–26, 1937.

[87] H. Hamaker, "The London-van der Waals attraction between spherical particles," *Physica*, vol. 4, pp. 1058–1072, 1937.

[88] V. A. Parsegian and G. H. Weiss, "Spectroscopic parameters for computation of van der Waals forces," *Journal of Colloid and Interface Science*, vol. 81, pp. 285–289, 1981.

[89] G. R. Wiese and T. W. Healy, "Effect of particle size on colloid stability," *Transactions of the Faraday Society*, vol. 66, pp. 490–499, 1970.

[90] M. Ruths, "Interfacial forces and friction on the nanometer scale," in *STLE/ASME International Joint Tribology conference*, 2008.

[91] Malvern Instrument Ltd, *Zetasize Nano series User Manual*, 2004.

[92] J. Soukupová, L. Kvítek, A. Panácek, T. Nevecná, and R. Zboril, "Comprehensive study on surfactant role on silver nanoparticles (NPs) prepared via modified tollens process," *Materials Chemistry and Physics*, vol. 111, pp. 77–81, 2008.

[93] A. Yakoub, A. Le-Henry, C. Calmes, M. Saadaoui, and P. Benaben, "Multilayer printed 3d resistors fabricated by an in-line inkjet process for RFID," in *Large-area, Organic and Printed Electronics Convention*, 2011.

[94] E. Drahi, S. Blayac, and P. Benaben, "Silicon thin-films from nanoparticle dispersion: tailoring morphological, electrical and optical characteristics.," in *Materials Research Society Spring Meeting*, 2011.

[95] L. Yang, I. Akhatov, M. Mahinfalah, and B. Z. Jang, "Nano-fabrication: a review," *Journal of the Chinese Institute of Engineers*, vol. 30, pp. 441–446, 2007.

[96] H. Wijshoff, *Structure- and fluid-dynamics in piezo inkjet printheads*. PhD thesis, University of Twente, 2008.

[97] D. B. Bogy and F. E. Talke, "Experimental and theoretical study of wave propagation phenomena in drop-on-demand ink jet devices," *IBM Journal of Research and Development DOI - 10.1147/rd.283.0314*, vol. 28, no. 3, pp. 314–321, 1984.

[98] J. Perelaer, *Microstructures prepared via inkjet printing and embossing techniques*. PhD thesis, Technische Universiteit Eindhoven, 2009.

[99] B. V. Antohe and D. B. Wallace, "Acoustic phenomena in a demand mode piezoelectric ink jet printer," *Journal of Imaging Science and Technology*, vol. 46, pp. 409–414, 2002.

[100] N. Reis and B. Derby, "Ink jet deposition of ceramic suspensions: modelling and experiments of droplet formation," in *Proceeding of Materials Development for Direct Write Technology Symposium*, vol. 624, pp. 65–70, 2000.

[101] T. Yamada and K. Sakai, "Study of microdroplet generation by ultrasonic propagation," in *Symposium on Ultrasonic Electronics*, vol. 31, pp. 145–146, 2010.

[102] M. Toivakka, "Numerical investigation of droplet impact spreading in spray coating of paper," in *Advanced Coating Fundamentals Symposium*, TAPPI Press, 2003.

[103] P. G. de Gennes, "Wetting: statics and dynamics," *Reviews of Modern Physics*, vol. 57, pp. 827–863, 1985.

[104] G. G. Stokes, "On the effect of the internal friction of fluids on the motion of pendulums," *Transactions of the Cambridge Philosophical Society*, vol. 9, p. 8, 1851.

[105] T. Lim, S. Han, J. Chung, J. T. Chung, S. Ko, and C. P. Grigoropoulos, "Experimental study on spreading and evaporation of inkjet printed pico-liter droplet on a heated substrate," *International Journal of Heat and Mass Transfer*, vol. 52, pp. 431–441, 2009.

[106] S. Schiaffino and A. A. Sonin, "Molten droplet deposition and solidification at low weber numbers," *Physics of Fluids*, vol. 9, no. 11, pp. 3172–3187, 1997.

[107] K. A. M. Seerden, N. Reis, J. R. G. Evans, P. S. Grant, J. W. Halloran, and B. Derby, "Ink-jet printing of wax-based alumina suspensions," *Journal of the American Ceramic Society*, vol. 84, no. 11, pp. 2514–2520, 2001.

[108] P. Smith, D.-Y. Shin, J. Stringer, B. Derby, and N. Reis, "Direct ink-jet printing and low temperature conversion of conductive silver patterns," *Journal of Materials Science*, vol. 41, no. 13, pp. 4153–4158, 2006.

[109] D. Soltman and V. Subramanian, "Inkjet-printed line morphologies and temperature control of the coffee ring effect," *Langmuir*, vol. 24, no. 5, pp. 2224–2231, 2008.

[110] R. D. Deegan, O. Bakajin, T. F. Dupont, G. Huber, S. R. Nagel, and T. A. Witten, "Capillary flow as the cause of ring stains from dried liquid drops," *Nature*, vol. 389, pp. 827–829, 1997.

[111] H. Hu and R. G. Larson, "Marangoni effect reverses coffee-ring depositions," *The Journal of Physical Chemistry B*, vol. 110, no. 14, pp. 7090–7094, 2006.

[112] W. D. Ristenpart, P. G. Kim, C. Domingues, J. Wan, and H. A. Stone, "Influence of substrate conductivity on circulation reversal in evaporating drops," *Physical Review Letters*, vol. 99, p. 234502, 2007.

[113] P. Smith, B. Derby, N. Reis, A. Wallwork, and C. Ainsley, "Measured anisotropy of alumina components produced by direct ink-jet printing," *Key Engineering Materials*, vol. 264-268, pp. 693–696, 2004.

[114] B.-J. de Gans and U. S. Schubert, "Inkjet printing of well-defined polymer dots and arrays," *Langmuir*, vol. 20, pp. 7789–7793, 2004.

[115] B. Derby, "Inkjet printing ceramics: from drops to solid," *Journal of the European Ceramic Society*, vol. 31, pp. 2543–2550, 2011.

[116] R. Bhardwaj, X. Fang, and D. Attinger, "Pattern formation during the evaporation of a colloidal nanoliter drop: a numerical and experimental study," *New Journal of Physics*, vol. 11, p. 075020, 2009.

[117] TA Instruments, *Differential Scanning Calorimetry*, 2007.

[118] J. R. Greer and R. A. Street, "Mechanical characterization of solution-derived

nanoparticle silver ink thin films," *Journal of Applied Physics*, vol. 101, pp. 103529–5, May 2007.

[119] K. Woo, D. Kim, J. S. Kim, S. Lim, and J. Moon, "Ink-jet printing of Cu-Ag-based highly conductive tracks on a transparent substrate," *Langmuir*, vol. 25, pp. 429–433, 2009.

[120] A. Gerschel, *Liaisons intermoléculaires: les forces en jeu dans la matière condensée*. Série Chimie, Savoirs actuels., 1995.

[121] H. A. Rizk and M. Elanwar, "Dipole moments of glycerol, isopropyl alcohol, and isobutyl alcohol," *Canadian Journal of Chemistry*, vol. 46, no. 507, pp. 507–513, 1968.

[122] Sun Chemical, "Suntronic jettable silver u5603 datasheet," 2008.

[123] B. P. E. Clapeyron, "Puissance motrice de la chaleur," *Journal de l'École Royale Polytechnique*, vol. XIV, pp. 153–190, 1834.

[124] R. Clausius, "On the moving force of heat and the laws regarding the nature of heat itself which are deducible therefrom," *Philosophical Magazine*, vol. 2, no. 1-21, pp. 102–119, 1851.

[125] S. H. Ko, H. Pan, C. P. Grigoropoulos, C. K. Luscombe, J. M. J. Fréchet, and D. Poulikakos, "All-inkjet-printed flexible electronics fabrication on a polymer substrate by low-temperature high-resolution selective laser sintering of metal nanoparticles," *Nanotechnology*, vol. 18, no. 34, p. 345202, 2007.

[126] H.-S. Kim, S. Dhage, D.-E. Shim, and H. Hahn, "Intense pulsed light sintering of copper nanoink for printed electronics," *Applied Physics A: Materials Science & Processing*, vol. 97, pp. 791–798, 2009.

[127] W.-S. Han, J.-M. Hong, H.-S. Kim, and Y.-W. Song, "Multi-pulsed white light sintering of printed Cu nanoinks," *Nanotechnology*, vol. 22, no. 39, p. 395705, 2011.

[128] I. Reinhold, C. E. Hendriks, R. Eckardt, J. M. Kranenburg, J. Perelaer, R. R. Baumann, and U. S. Schubert, "Argon plasma sintering of inkjet printed silver tracks on polymer substrates," *Journal of Materials Chemistry*, vol. 19, no. 21, pp. 3384–3388, 2009.

[129] S. Magdassi, M. Grouchko, O. Berezin, and A. Kamyshny, "Triggering the sintering of silver nanoparticles at room temperature," *ACS Nano*, vol. 4, pp. 1943–1948, 2010.

[130] J. Perelaer, B.-J. de Gans, and U. Schubert, "Ink-jet printing and microwave sintering of conductive silver tracks," *Advanced Materials*, vol. 18, no. 16, pp. 2101–2104, 2006.

[131] M. Gupta, E. Leong, and W. Wong, *Microwaves and metals*. John Wiley & Sons, 2007.

[132] R. Roy, D. Agrawal, J. Cheng, and S. Gedevanishvili, "Full sintering of powdered-metal bodies in a microwave field," *Nature*, vol. 399, pp. 668–670, 1999.

[133] S. Takayama, G. Link, S. Miksch, M. Sato, J. Ichikawa, and M. Thumm, "Millimetre wave effects on sintering behaviour of metal powder compacts," *Powder Metallurgy*, vol. 49, no. 3, pp. 274–280, 2006.

2

Microstructure of inkjet-printed thin films

Introduction

In the previous chapter, some state-of-the-art direct-writing technologies have been presented and the DoD inkjet-printing technique was specifically developed. The properties of the inkjet-printing step were optimized according to the interactions between the silver nanoparticle-based ink and the substrates. The process was significantly improved as much from the development of a maintenance procedure as from the piezoelectric parameters. A few examples have been shown as interesting results of this optimization process with line resolution down to 100 µm.

In this chapter, the post-treatment operation will be treated with the different sintering mechanisms that lead to the formation of necks between nanoparticles and the grain growth when undergoing a thermal treatment. This demonstrates that microstructure is therefore dependent on the curing process. These mechanisms involve several diffusion routes which are thermally activated. Due to their thermodynamic size effect, this activation occurs at lower temperatures than those reported in literature for microparticles or even macroparticles.

I. Coalescence phenomenon in nano-objects

Coalescence is a complex physical phenomenon where bonds are created between particles when submitted to a thermal treatment. During this phenomenon, the particle surface tends to liquefy on a short range in the sense that surface atoms present a higher mobility and diffuse along several paths as depicted in Figure II-1. In this domain, nanoparticles are particularly interesting because of their low temperature reactivity. During thermal treatment, several atomic diffusion routes occur inside nanoparticles with activation energies lower than bulk materials. Usually, according to the thermal budget, sintering operates concomitantly with grain growth, so that it is usually difficult to discriminate one from the other. In this section, the principal sintering mechanisms will be addressed.

A. Thermodynamic size effect in nanoparticles

Nanomaterials can be distinguished from conventional materials by at least one characteristic dimension confined to the nanoscale range (below 100 nm). In this classification of nanomaterials against the number of confined dimensions, nanoparticles are specifically described as zero-dimensional nanomaterials. When several nanoparticles agglomerate, the term nanocluster is then preferred. In general, size does matter since the physical properties of such materials are dimension-dependent and greatly depend on the number of atoms in the particle. The finite size of metal nanoparticles induces a confinement

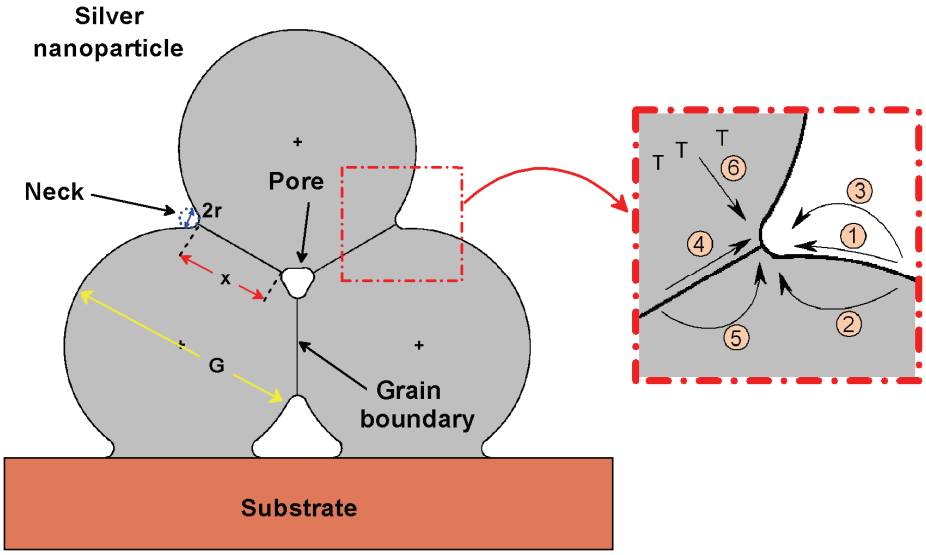

Figure II-1: Schematic depicting three nanoparticles in an advanced sintered state on a substrate with six alternative diffusion paths (numbered from 1 to 6) contributing to neck growth (inset).

of electron spatial distribution and a discretization of energy levels [1]. Indeed, when the nanoparticles are confined to a few nanometers, a Quantum-Size Effect (QSE) is observable which replaces the continuity of the conduction band by a set of discrete energy levels. In the case of 25 nm nanoparticles, the QSE is almost negligible and will not be considered.

Since the coordination number of the lattice is 12 for a Face-Centered Cubic structure (FCC), *i.e.* each atom has twelve neighbors, the silver nanocrystal cannot be perfectly spherical but instead produces a polyhedron. The equilibrium shape of these nanoparticles is defined by the minimization of surface energy, so that $\sum A_i \cdot \gamma_i$ (where A_i is the surface area and γ_i is the surface energy) is as low as possible. Solutions to this problem can be determined using the Wulff construction where the crystal growth is governed by the directional dependence of the surface tension. Due to the surface atomic density, the high-symmetry planes exhibit surface energies which grow when the packing decreases, so that $\gamma_{\{111\}} < \gamma_{\{100\}} < \gamma_{\{110\}}$. The smallest crystalline structure is the Wigner-Seitz cell which is composed of 13 atoms forming a truncated cubo-octahedron: one bulk atom at the center and 12 surface atoms. Six square {100} faces and height hexagonal {111} faces form this tetradecahedron (cf. Figure II-2).

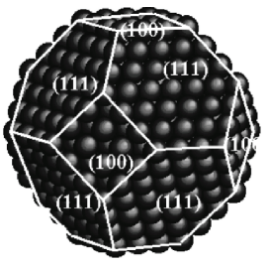

Figure II-2: Representation of a truncated cubo-octahedral FCC cluster containing about 1 000 atoms with (111) hexagonal faces and (100) square faces (reproduced from [2]).

Additional silver atoms originating from diffusion process will subsequently settle on the most favorable surface. If a whole layer is filled up, the particle shape will be conserved and a series of structural magic numbers can be derived (see Table II-1) [3]. In particular for n layers of atoms, the number of surface atoms is given by:

$$N_{surface} = 10\,n^2 - 20\,n + 12 \qquad \text{(II-1)}$$

The average radius of the resulting particle can be approximated by [4]:

$$\frac{N_{surface}}{N_{total}} = \frac{8 \cdot a_0}{G} \qquad \text{(II-2)}$$

where a_o is the atomic radius of the element (here, the metallic radius of silver is considered, a_o=144 pm) and G is the particle diameter.

Table II-1: Structural magic numbers of a cubo-octahedral FCC nanoparticle and its average radius.

Number of shells	Average radius (nm)	Surface atoms	Bulk atoms	Fraction of surface atoms (%)
2	0.6	12	1	92.3
3	0.8	42	13	76.4
4	0.9	92	55	62.6
5	1.1	162	147	52.4
10	2.0	812	2057	28.3
100	19.3	98 012	3 185 687	3
200	38.5	$4{\cdot}10^5$	$3{\cdot}10^7$	1.5
300	57.7	$9{\cdot}10^5$	$9{\cdot}10^7$	1

Since atoms located at a free surface are not in the same environment as those located in the bulk material, they exhibit very specific behavior. For each surface atom which is not bonded to another atom in the direction normal to the surface plane, an excess internal energy of ε/2 will be available compared to bulk atoms (ε being the energy of the bond shared between two atoms, see Figure II-3). Another contribution to high free energy of nanoparticles originates from the higher degree of freedom of surface atoms which confers more entropy to the surface. As a consequence, the more surface atoms the particle presents,

the more reactive it will be [5]. As seen in Table II-, the ratio of surface atoms compared to the bulk atoms is particularly important when nanoparticle size is constrained under 20 nm.

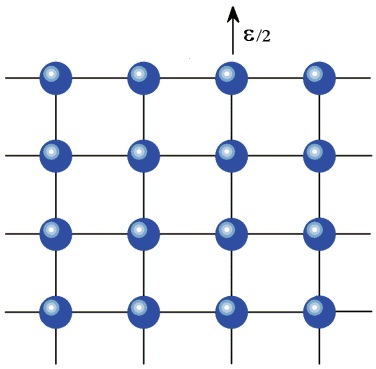

Figure II-3: The four atomic layers at the extreme surface of a crystal exhibiting dangling bonds giving an excess internal energy to nanoparticles.

Another contribution to the higher reactivity of small nanoparticles comes from their higher surface curvature. Indeed, the Gibbs free energy is highly impacted by any variation of pressure that can occur when the surface curvature evolves. Due to capillary effect, nanoparticles will tend to contact each other, which consecutively creates an area of localized high curvature, (see Figure II-1) where the associate stress is given by the Laplace equation [6]:

$$\sigma = \gamma \vec{\nabla} \cdot \vec{n} = \gamma \left(\frac{1}{R_1} + \frac{1}{R_2} \right) \qquad \text{(II-3)}$$

where γ is the surface energy of the material and R_i the principal radii of curvature. Principal curvatures are related to the surface curvature along two perpendicular axes. By convention, convex regions have a positive curvature. A concave surface will thus exhibit a compressive stress that the system will tend to reduce through atomic diffusion to reduce the curvature. This phenomenon is thus driven by the minimization of surface energy. This stress is usually termed the sintering driving force because of its impact on atomic diffusion. Being inversely proportional to the nanoparticle radius, the smaller the radius, the higher the driving force will be. As a result, the process will tend to progressively be inhibited as the contact surface grows. Experimentally, it has been observed that this surface stress activates sintering processes for homologous temperature comprised between 0.5 and 0.8 [6], the homologous temperature being the ratio between the initiation temperature of sintering and the bulk melting temperature.

The high curvature observable in nanoparticles also alters the equilibrium vacancy concentrations, C_{vac}. Indeed, since mass transport is mediated by vacancies, the higher

number of vacancies in high curvature areas will create an atomic flow to compensate the difference. The difference in vacancy concentration is thus given by [3, 7]:

$$\Delta C_{vac} = exp\left(\frac{-\Delta G_{vac}^{bulk}}{k_B T}\right) \cdot \left[exp\left(\frac{-\gamma\Omega}{R k_B T}\right) - 1\right] \qquad \text{(II-4)}$$

where k_B is the Boltzmann constant, Ω is the atomic volume, T is the absolute temperature and R is the radius of curvature. Effects are such dramatic that the sintering stress is two magnitudes higher for a 10 nm particle than for a 1 µm particle.

A more noticeable impact of the thermodynamic size effect of nanoparticles has been reported on their melting temperature. Indeed, experiments conducted by Buffat and Borel in the seventies on gold nanoparticles showed evidence of particle size-dependency on the melting point [5]. Several models were derived to describe experimental observations as a function of hypothetic melting processes according to the material (see Figure II-4).

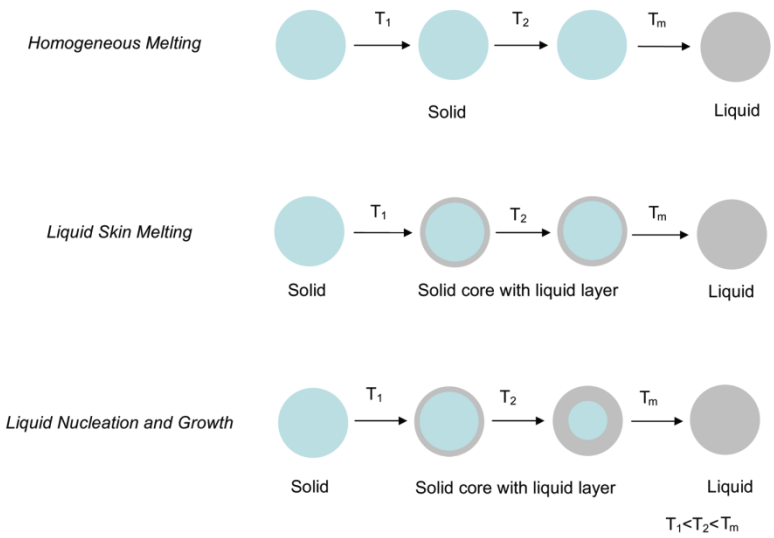

Figure II-4: Process of the three melting hypothesis for nanoparticles.

If a Homogeneous Melting (HM) hypothesis is assumed, the solid nanoparticle is in equilibrium with an entirely melted particle of the same mass at the melting temperature $T_m(r)$. Historically the first developed, the HM model results from thermodynamic considerations at the melting point where the equilibrium state guaranties the identity of the Gibbs free energy between the solid and liquid states [5, 9]:

$$G_s(r=\infty) + \frac{2\gamma_{sv}V_s}{r_s} = G_l(r=\infty) + \frac{2\gamma_{lv}V_l}{r_l} \qquad \text{(II-5)}$$

where G_s and G_l are the free energy of bulk in solid or liquid state respectively, γ_{sv} and γ_{lv} are respectively the surface energies of the solid-vapor and liquid-vapor interfaces of the material, V_s and V_l are the volumes of the solid and liquid particles, and r_s and r_l are their respective radii. The Pawlow equation thus formulates the size-dependent melting point of these particles as:

$$\frac{T_m(r)}{T_m(r=\infty)} = 1 - \frac{2}{\rho_s r_s L_m}\left[\gamma_{sv} - \gamma_{lv}\left(\frac{\rho_s}{\rho_l}\right)^{2/3}\right] \quad \text{(II-6)}$$

where $T_m(r=\infty)$ is the melting temperature of the bulk metal, ρ_s and ρ_l are the solid and liquid densities and L_m is the enthalpy of fusion.

The Liquid-Skin Melting (LSM) model considers that a slight liquefaction of the metal occurs at the surface of the solid core during the heating step. This layer is assumed to appear at low temperatures and to remain unchanged until the total fusion of the nanoparticle. The LSM hypothesis is thus based on the equilibrium between the solid particle and the liquid shell and results in the Hanszen-Wronski equation [10, 11]:

$$\frac{T_m(r)}{T_m(r=\infty)} = 1 - \frac{2}{\rho_s r_s L_m}\left[\frac{\gamma_{sl}}{1-\delta/r_s} - \gamma_{lv}\left(1-\frac{\rho_s}{\rho_l}\right)\right] \quad \text{(II-7)}$$

where δ is the thickness of the liquid overlayer. A different approximation following the same formalism has been developed by Sambles [12] with:

$$ln\left(\frac{T_m(r)}{T_m(r=\infty)}\right) = -\frac{2}{\rho_s r_s^* L_m}\left(\frac{\rho_s}{\rho_l}\right)^{1/3}\left[\gamma_{lv}\left(1-\frac{\rho_s}{\rho_l}\right) + \gamma_{sl}\left(1-\frac{\delta_l}{r_s^*}\left(\frac{\rho_s}{\rho_l}\right)^{1/3}\right)^{-1}\right] \quad \text{(II-8)}$$

where r_s^* is the hypothetical radius of the nanoparticle in the completely solid form.

If a liquid layer nucleates as an outlayer surrounding the particle and consecutively grows into the solid phase when the temperature increases, the phenomenon is described as the liquid nucleation and growth (LNG) model. In this process, the hypothesis is based on the equality of the chemical potentials of both the liquid layer and the solid core. If the atomic volumes of the solid and liquid phases are assumed as equal, the formation of the liquid shell induces a change of the free energy given by:

$$\begin{aligned}\Delta G(T) = {} & \frac{L_m \cdot [T_m(r=\infty) - T]}{T_m(r=\infty)} \cdot \frac{4}{3}\pi[r^3 - (r-\delta)^3] \\ & + \gamma_{sl} \cdot 4\pi(r-\delta)^2 + (\gamma_{lv} - \gamma_{sv}) \cdot 4\pi r^2\end{aligned} \quad \text{(II-9)}$$

In this model, the surface-induced nature of melting depends on the wetting properties of the metal solid by its own liquid. In most cases, the solid-liquid transition is privileged by the surface term and is retarded by the volume term. The melting temperature is given by the Couchman equation [13]:

$$\frac{T_m(r)}{T_m(r=\infty)} = 1 - \frac{3}{\rho_s r_s L_m}\left[\gamma_{sv} - \gamma_{lv}\left(\frac{\rho_s}{\rho_l}\right)^{1/2}\right] \qquad \text{(II-10)}$$

When considering experimental data from previous studies on silver nanoparticles [14, 15], it is found that the best fitting model for silver is based on the liquid-skin melting hypothesis (see Figure II-5).

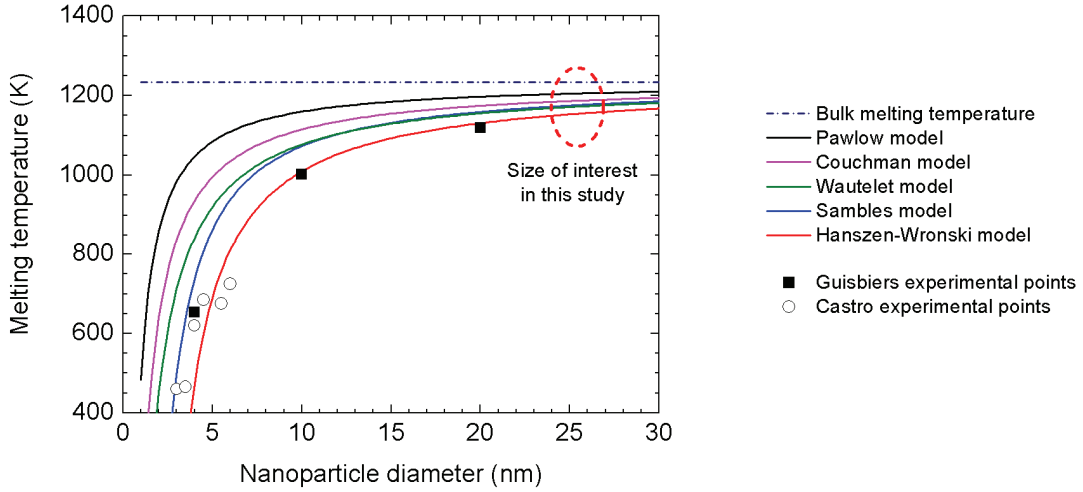

Figure II-5: Impact of the silver nanoparticle diameter on their melting point according to five recognized models [13, 16, 17] with experimental points from Guisbiers [14] and Castro [15].

Table II-2: Thermodynamic parameters used for the melting point curves of metal nanoparticle in Figure II-5 [18].

	$T_m(r=\infty)$ [K]	ρ_s [g.cm^{-3}]	ρ_l [g.cm^{-3}]	γ_{sv} [J.m^{-2}]	γ_{lv} [J.m^{-2}]	γ_{sl} [J.m^{-2}]	L_m [J.g^{-1}]	δ_l [Å]
Au	1337	18.4	17.4	1.38	1.14	0.30	63.7	4
Ag	1234	9.82	9.32	1.14	0.95	0.35	104.5	8

It should be noted nonetheless, that despite what is currently asserted in literature, the thermodynamic size effect seems to have little effect in the low temperature sintering of nanoparticles. Indeed, as shown in Figure II-5, the melting temperature of silver nanoparticles falls below 300 °C only for radii below 2 nm. Since we previously demonstrated that nanoparticulate printed films are highly conductive when cured at 200 °C, the low

temperature sintering would be credited instead to the higher stress density in nanoparticles or to a cold sintering mechanism operating as soon as the capping agent is degraded.

B. Mass transport mechanisms during sintering

During the curing operation, the calorific system induces an increase of thermal agitation in the sample by thermal transfer. The coupling can be performed by various means, either by conductive transfer in a thermal oven, by convective transfer with an infrared illumination or by radiative transfer as in a microwave oven. Combination of these methods can also be advantageously be performed using a silicon susceptor as in a Rapid Thermal Annealing (RTA) oven which combines IR curing and conductive heating or in a Hybrid Variable Frequency Microwave (HVFM) oven associating microwave curing with conductive heating. During this thermal transfer, increase of thermal agitation is governed by the second law of thermodynamics: $\delta Q < T \cdot dS$. Entropy of the nanoparticulate system thus facilitates atomic displacements not only as a consequence to crystal defect recovery but also from crystalline rearrangement to a more stable orientation. Various types of sintering coexist according to the involved materials and relative composition at the sintering temperature: solid-state sintering, liquid phase sintering, transient liquid phase sintering and viscous flow sintering. In this study, only solid-state sintering will be involved since only one material will be considered.

i. Stages of sintering process

In literature, the coalescence of nanoparticles is usually described phenomenologically as divided into three main steps: initial, intermediate and final stages. Distinction between each stage is made from the geometric evolution of the nanoparticulate system (see Figure II-6-b), essentially in the neck area, so that the frontiers between each step are not so clearly defined. While coalescing, the contact area thus evolves from a point contact to a line contact which constitutes a grain boundary between the two nanoparticles. As will be seen afterwards, this grain boundary could thereafter migrate into a nanoparticle driven by energy minimization phenomena. In general, the advance of coalescence is monitored by considerations of the neck size to particle diameter ratio or to the shrinkage rate.

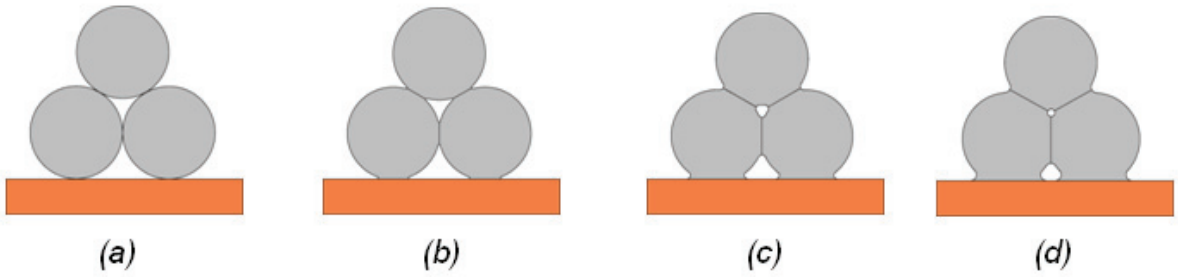

Figure II-6: The successive stages of sintering exhibiting the neck growth from the initial point contact (a). The neck is formed and grows during the initial stage (b) before being rounded during the intermediate stage (c) until reaching the final stage when pores.

Initial stage sintering is characterized by microstructures with high curvature gradients (see Figure II-6-b) that the system will tend to decrease in order to minimize the surface energy. This minimization induces a rapid neck growth between the nanoparticles maintained in point contact through low cohesive forces, *e.g.* van der Waals or capillary forces [83]. During this stage, as formulated in equation (II-3), the sintering stress associated withthe saddle surface between the nanoparticles is given by:

$$\sigma = \gamma_{sv} \cdot \left(\frac{4(G-x)}{x^2} - \frac{2}{x} \right) \qquad \text{(II-11)}$$

During this phase, nanoparticles can rearrange through rotation to minimize the grain boundary energy by accommodation of crystalline structures. This mechanism which operates at the very beginning of the sintering process is facilitated by the presence of the liquid phase. While not described in standard sintering theory, this geometrical rotation has been observed experimentally [20] and through molecular dynamics simulations [21, 22]. As demonstrated by Ding *et al.* [22], this rotation is more easily activated for small particle size and for low misalignment angles (smaller than 20°). If rotation conditions are fulfilled, the grain boundary between the two nanoparticles thus tends to vanish so that sintering process are significantly affected due to the missing prevalent diffusion channel.

Since only a minor level of densification is achieved during the initial stage, free space between nanoparticles – designated by the term 'pores' – forms interconnected channels along each grain edges. As the sintering proceeds, nanoparticle assembly acquires a more stable structure where the grains exhibit a truncated cubo-octahedral conformation, as previously depicted in Figure II-2, with tubular channels at their boundaries. During the intermediate stage, densification of the film induces the collapse of these channels which eventually isolates the pores (see Figure II-6). This stage is then specifically characterized by the reduction of pore curvature more than by the reduction of grain curvature. In this configuration, for two neighbor pores, the smaller one will tend to migrate into the bigger

one, and thus acts as a vacancy source. As a consequence, this leads to the coarsening of large pores and the annihilation of small ones.

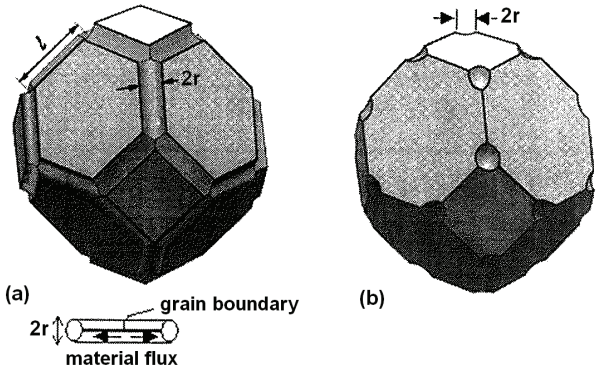

Figure II-7: Effect of grain boundary diffusion-controlled sintering as first presented by Coble [23]. During the intermediate stage, grain boundaries are modeled by tubular channels (a) that are progressively resorbed in the final stage (b). (Reproduced from [24])

During the intermediate and final stages, equilibrium of curvatures, whether for grains or pores, is defined by a geometrical parameter: the dihedral angle ϕ. This angle refers to the angle at the junction between the two particles. This angle is defined from the equilibrium of the solid and vapor interface at the junction, by:

$$\gamma_{gb} = 2\gamma_{sv} \cos\frac{\phi}{2} \qquad \text{(II-12)}$$

where γ_{gb} is the surface energy of the particle boundary (solid-solid interface) and γ_{sv} is the surface energy of the solid-vapor interface. The equilibrium condition is reached when this angle matches the angle formed by the neck diameter relative to the particle center (see Figure II-8). Further increase of the neck diameter is thus conditioned by an additional increase of the particle size according to the following relation:

$$\frac{X}{G} = \sin\frac{\phi}{2} \qquad \text{(II-13)}$$

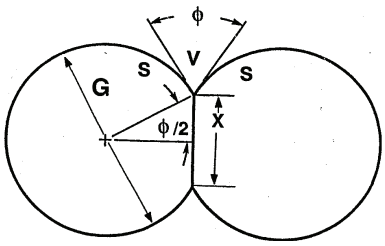

Figure II-8 : Equilibrium state between two nanoparticles to maintain the dihedral angle [6].

When pores are eventually isolated in the film, either at a triple junction, at particle boundaries or inside particles, the surface stress which drives the final stage of sintering derives from a contribution of pore resorption and particle final growth:

$$\sigma = \frac{2\gamma_{gb}}{G} + \frac{4\gamma_{sv}}{d_p} \qquad \text{(II-14)}$$

where d_p is the pore diameter. During the final stage, pores can present several geometries according to their position at equilibrium: spherical shape when they are trapped inside a grain, lenticular when they are pinned along a particle boundary (either on edges or on faces) or rounded tetrahedral at particle corners.

Decomposing the sintering process in three stages constitutes an artificial treatment that can only be used for phenomenological purposes to render microstructure evolution (see Table II-3). During these sintering stages, several mechanisms are operating concomitantly. In general, at least one of them dominates diffusion processes in a given temperature range. Impact of individual mass transport mechanisms on microstructure will be considered in the next paragraphs, essentially through the evolution of the neck diameter to particle diameter ratio or through the shrinkage rate whenever applicable.

Table II-3: Principal characteristics distinguishing sintering stages [25].

	Initial stage	**Intermediate stage**	**Final stage**
Neck diameter to grain size ratio	< 0.3	0.3 – 0.8	0.8 – 1
Relative density to bulk	< 70 %	70 – 92 %	92 – 100 %

Several atomic mass transport mechanisms are commonly accepted to explain the sintering process in the classic sintering theory: surface diffusion, lattice diffusion in the bulk and at grain boundaries, viscous flow, plastic flow and evaporation-condensation phenomena [26, 27]. Those sintering routes have been extensively described theoretically and experimentally by authors for micron-sized particles. But given the important proportion of surface atoms in nanoparticles, it has been reported that mainly surface diffusion and grain boundary diffusion were occurring during their coalescence [21]. Nonetheless, for the sake of completeness, each mechanism will be addressed in the following paragraphs. The mechanisms can be grouped into two families which compete for the definite amount of available thermal energy: densifying and non-densifying regimes. A densifying mode is characterized by centers of mass of particles that moves closer during the sintering process, so that both shrinkage and neck growth are taking place [28]. Conversely, a mechanism is qualified as a non-densifying regime when atoms are transported to the neck area without any shrinkage of the center-to-center distance, so that only neck growth is carried out.

Usually, non densifying mechanisms involve surface atoms while densifying mechanisms are related to core atoms. Final microstructure of the film is thus dictated by which one of these two families is predominant during the process.

ii. Non-densifying mass transport mechanisms

Non-densifying mechanisms are atomic transport processes that require the lowest activation energy. As presented before, these mechanisms preferentially involve surface effects as curvature-induced stress. Nonetheless, even though diffusional atomic motion is increasing the neck diameter, film density is not modified since distance between particles doesn't shrink. Indeed, pore size is not reduced because they only change in shape due to the movement of surface atoms. As demonstrated by some authors [21], since activation energies of these mechanisms are lower than densifying regimes, they usually dominate in the low temperature range. The most notable mechanisms contributing to the sintering process are, by order of prevalence, surface diffusion, evaporation-condensation in vapor phase and lattice diffusion from the surface (see Figure II-9).

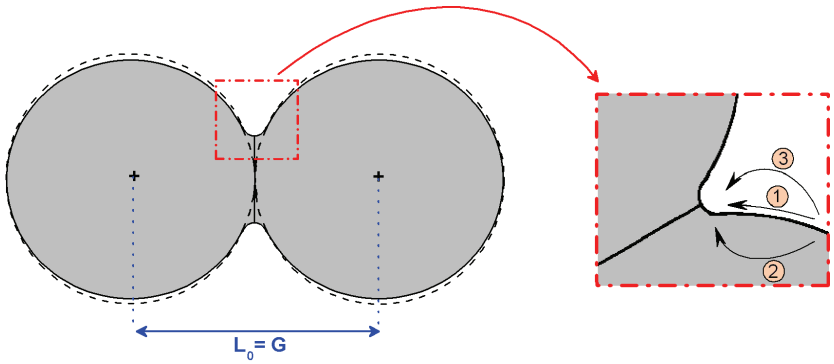

Figure II-9 : Main surface transport mechanisms: surface diffusion (1), lattice diffusion from surface (2), and evaporation-condensation (3).

Surface diffusion involves atoms moving from several sites of crystalline defects on the surface. Crystalline particles are commonly described using the Terrace Ledge Kink (TLK) model to render their spherical shape or curvature. Defects on this surface can be punctual, linear or planar. Amongst the most encountered surface defects, kinks and punctual defects such as atomic vacancies or adatoms are current on terraces of dense planes (see Figure II-10).

Surface diffusion is a thermally activated mechanism which prevails at low temperature for most metals. While relaxation time of crystalline recovery at ambient temperature is very long, increasing the temperature reduces it drastically. Thermal agitation indeed enhances the breaking of metallic bonds leaving atoms unbound. Such free atoms can subsequently

move randomly to an available site to form a new bond, usually driven by a minimization of the energy. In this process, steps are privileged host sites for such atoms which rearrange on the surface without any densification. As surface defects density drops off, atomic transport tends to lessen and vanish.

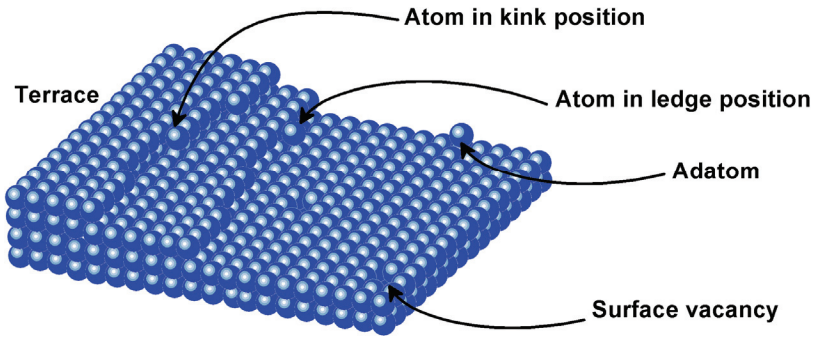

Figure II-10 : Main defects of a curved (100) surface for a FCC crystal.

Volume diffusion from the surface involves the movement of vacancies through the crystalline lattice before emerging at the neck surface. Material deposition in the neck area thus operates without densification. Considering the displacement of a vacancy as a quasi-particle is indeed easier than the complex movement of successive crystal planes in the opposite direction. Atomic diffusion is ruled by the Fick's first law which states that vacancy flow is proportional to its concentration gradient on a short range. Volume diffusion depends on three main parameters: temperature, chemical composition and curvature. In the nanosized range, this atomic mass transport is marginal in most sintering cycles. Indeed, only high temperatures and huge vacancy gradients will allow their mobility activation.

Evaporation-condensation occurs at the nanoparticle surface through atomic transport in vapor phase. Untied atoms condensate on a nearby surface on the same host sites as presented in Figure II-10. As reported previously, evaporation occurs preferentially on convex surfaces, while condensation occurs on concave surfaces where the vapor pressure is slightly lower than the equilibrium pressure. This mechanism is generally dominant for poorly stable materials, such as lead derivates. This rearrangement of surface atoms does not produce any densification of the film.

As a consequence of its low kinetics, this mass transport mechanism is often negligible in macroparticle sintering. However, since pressure is drastically increased at nanoparticle interfaces due to high curvatures, it could be assumed that the impact of such mechanisms can play a key role in nanopowders while no evidence of that has been found yet. Experiments from Readey *et al.* [29] showed that the vapor transport could be exacerbated by the presence of reactive species in the atmosphere such as hydrogen, oxygen, carbon monoxide or chlorine. The neck growth continues until reaching the equilibrium state defined by the dihedral angle (see Equation (II-13)).

iii. Densifying mass-transport mechanisms

As the term suggests, densifying mechanisms lead to film shrinkage during sintering. Contrary to the above-mentioned mechanisms, here the neck growth originates from the center of mass of the two particles moving closer. These mechanisms involve atomic transport through the crystal lattice and eventually using grain boundaries as channels towards the neck surface. The presence of such grain boundaries is thus a pre-requisite for them to occur, so that if nanoparticles perfectly realign themselves during the initial stage causing the grain boundary to disappear, these mechanisms will be hindered as previously mentioned. Given the required energy to diffuse through the crystal lattice, densifying regimes usually operate at higher temperatures. The most notable mechanisms contributing to the sintering process are, by order of prevalence, grain boundary diffusion, volume diffusion at grain boundaries and plastic flow (see Figure II-11).

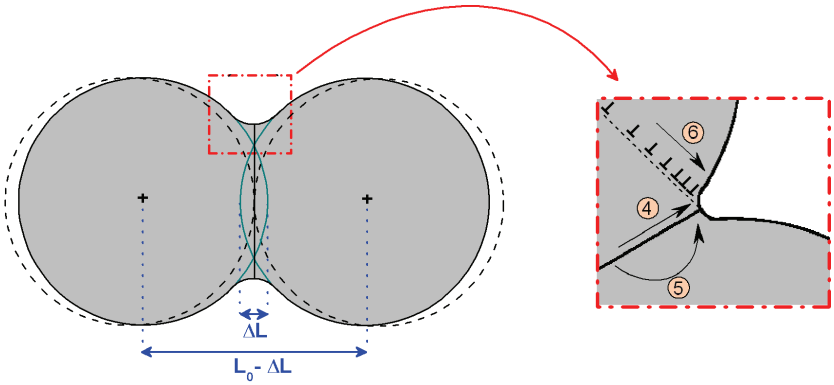

Figure II-11: Main volume transport mechanisms: grain boundary diffusion (4), volume diffusion at grain boundary (5) and plastic flow (6).

Diffusion at grain boundaries is a mechanism that highly contributes to densification of most crystalline materials during sintering. A grain boundary is formed at the interface between two nanoparticles due to a local disorientation of the crystal lattice (see Figure II-12). Due to this disorientation and to the terraces at the nanoparticle surfaces, the junction of both nanoparticles gives birth to diffusion channels along terrace edges. Atoms can easily diffuse along these channels with an energetic contribution halfway between that of surface diffusion and volume diffusion. The work of Coble enabled a theoretical description of coalescence driven by grain boundary diffusion [23].

Whether at nanoparticles junction, at interstices or even inside multicrystalline nanoparticles, grain boundaries operate as annihilation sites for vacancies. Atoms follow these diffusion channels which Coble's model assimilates to tubes at the nanoparticle interface (see Figure II-7). Such channels form a three-dimensional network in tetradecahedra at the center of which nanoparticles are localized.

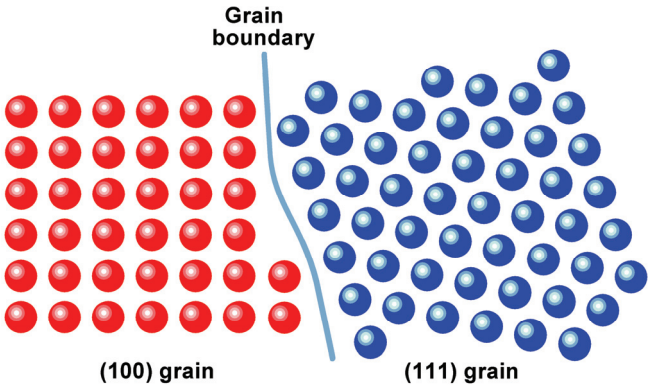

Figure II-12 : Disorientation of crystal lattice forming a grain boundary between a (100) and a (111) grains, in the case of coplanar lattices.

Volume diffusion can lead to a film densification when vacancies move from the neck surface to the grain boundary. This process induces a shrinkage because of atomic planes moving in the opposite direction with centers of mass moving closer. This diffusion path generally involves slips, twist or accommodation steps at the grain boundary.

The effect of viscous flow was first considered by Frenkel [28] and involves the displacement of vacancies under the action of a shearing stress. Even though this mechanism mainly concerns amorphous materials, Frenkel has shown that it could be applied to crystalline bodies such as metals in a lesser extent [28, 30]. Under the action of temperature and high pressure gradients, the crystal can behave as a Newtonian fluid, whose viscosity increases with temperature. Upon healing, atomic layers slip in an orderly fashion in specific directions until being stopped by the microstrain of the crystal lattice, *e.g.* due to dislocations.

Plastic flow is characterized by the mobility of dislocations under application of an additional stress. While its existence is controversial amongst authors, plastic flow is believed to affect compacted powders during the heating step. Indeed, compacted powders tend to present higher initial density of dislocations.

Originally developed by Herring [26], the formalism associated with the solid-state diffusion in the continuum model has been successively improved and adapted by significant contributions from Coble [23, 31] and other authors [32, 33]. Each of the previously described mechanisms is usually studied under the angle of neck size evolution with time. The ratio between the neck size x and the particle diameter G is given by:

$$\left(\frac{x}{G}\right)^n = \frac{H}{G^m}t \qquad \text{(II-15)}$$

Table II-4: Values for the parameters in Equation (II-15).

Mechanism	n	m	H
Non-densifying:			
Surface diffusion	7	4	$56\ \delta_s \cdot D_s \cdot \gamma_{sv} \cdot \Omega / kT$
Volume diffusion from surface	4	3	$20\ \delta_v \cdot D_v \cdot \gamma_{sv} \cdot \Omega / kT$
Evaporation-condensation	3	2	$3\ p \cdot \gamma_{sv} / kT$
Densifying:			
Volume diffusion from GB	5	3	$80\ D_v \cdot \gamma_{sv} \cdot \Omega / kT$
Grain boundary diffusion	6	4	$20\ \delta_{gb} \cdot D_{gb} \cdot \gamma_{sv} \cdot \Omega / kT$
Viscous flow	2	1	$3\ \gamma_{sv} / \eta$
Plastic flow	2	1	$9\pi\ \gamma_{sv} \cdot b \cdot D_v / kT$

where Ω is the atomic volume ($1.71 \cdot 10^{-29}$ m^3), γ_{sv} is the surface energy of silver (1.14 $J \cdot m^{-2}$), and D_i are the diffusion coefficient of the i mechanism. Diffusion coefficients are given by the general form: $D_i = D_o \cdot \exp(-Q_i/RT)$ where $\delta_s \cdot D_{os}$ is the pre-exponential factor of surface diffusion ($1.50 \cdot 10^{-6}$ $m^3 \cdot s^{-1}$), Q_s is the activation energy of surface diffusion (266 $kJ \cdot mol^{-1}$), D_{ov} is the pre-exponential factor of lattice diffusion ($4.40 \cdot 10^{-5}$ $m^2 \cdot s^{-1}$), Q_v is the activation energy of lattice diffusion (185 $kJ \cdot mol^{-1}$), $\delta_{gb} \cdot D_{ogb}$ is the pre-exponential factor of grain boundary diffusion ($6.94 \cdot 10^{-15}$ $m^3 \cdot s^{-1}$), Q_{gb} is the activation energy of grain boundary diffusion (89.8 $kJ \cdot mol^{-1}$) [27].

From the Table II-4, it can be noticed that each mechanism doesn't have the same impact on the microstructure, either from a neck growth point of view or from the densification process. The scaling laws developed by Herring in 1950 [26] thus allow the organization of several mechanisms according to their importance and extent during the sintering operation. This enabled in particular that the main contribution originates generally from surface diffusion and grain boundary diffusion mechanisms which is consistent with observations that will be developed afterwards.

From equations in Table II-4, diagrams can be constructed to represent the dominant mechanism which operates at a given temperature and a given ratio between the nanoparticle size and neck size. This formalism has been first developed by Ashby and extended by Swinkels [27]. Calculation based on the limit conditions of each domain for silver nanoparticles with a diameter of 25 nm – corresponding to the conductive ink used in JetPac – has been performed to determine the dominant mechanisms during the sintering step (see Figure II-13). The resulting diagram corroborates previous considerations that only grain boundary and surface diffusions are key in nanoparticle sintering.

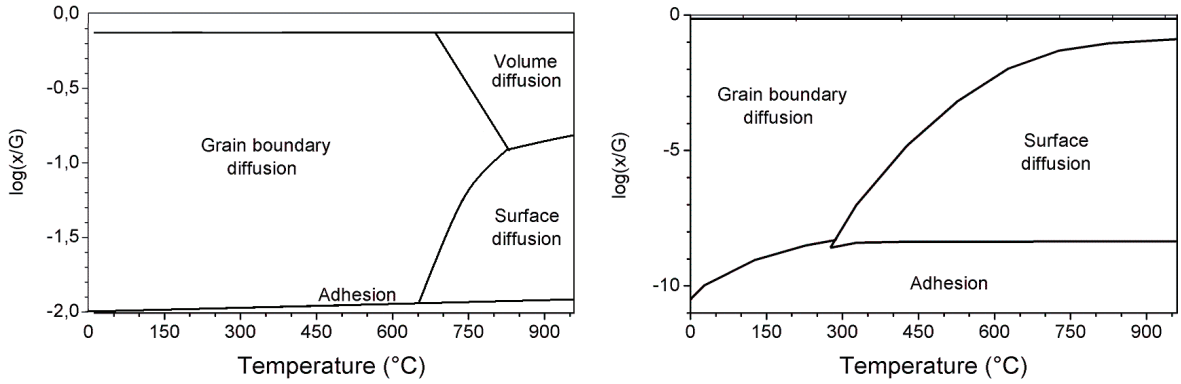

Figure II-13: Sintering diagrams of silver spheres with a diameter of 200 µm from Swinkels [27] (left) and simulated for our configuration of silver nanoparticles with a 25 nm diameter (right).

In particular, this diagram underlines that only grain boundary diffusion is operating during a sintering of nanoparticles below 300 °C. When plastic substrates are used, the curing temperature is well below this value, generally comprised between 90 °C and 150 °C. Furthermore, above 300 °C, both mechanisms are alternatively dominating the process, what could eventually contribute to diverse microstructural behaviors. Nonetheless, being based on phenomenological equations, this kind of diagram should be taken with caution and used for qualitative purpose only.

iv. Limitations to continuum sintering models

Most of the sintering models are based on particles considered as perfectly spherical and of the same size. These hypotheses have been obviously made to simplify calculations through the reduction of considered objects and through the simplification of limit conditions with a simpler geometry. In general, the condition on nanoparticle sphericity is verified in a first approximation. However, except when a bottom-up chemical synthesis is used, nanoparticles are rarely monodispersed in a solution and especially when a mechanical attrition process is applied (see Chapter I).

Another limitation to conventional theories is that each mechanism is considered independently. It is indeed commonly accepted that several mechanism are operating concurrently. They are characterized by specific activation energy and kinetics so that one mechanism usually predominate in a given temperature range. In this matter, numerical simulations offer interesting perspectives to render a closer evolution of the film microstructure. The main limitation of numerical simulations is the number of atoms that can be modeled and the consecutive computing time or ability. This makes simulations particularly valuable for nanoparticle sintering since the number of involved atoms is limited. Amongst the most developed numerical simulations techniques for nanoparticles, one could notably mention finite element analysis [34], variational technique [35] and

molecular dynamics [22, 36]. The later technique in particular is suitable for modeling nanoparticle sintering at the atomic scale (see Figure II-14).

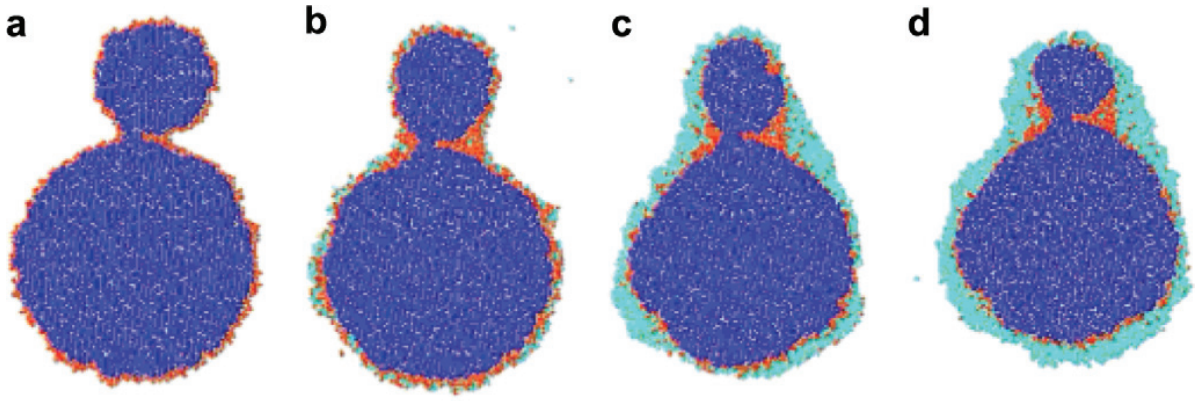

Figure II-14: Sintering of two unequal size nanoparticles as modeled by molecular dynamics simulations $T=0.63 \cdot T_m$ [22]. Atom history is depicted by a coloring scheme: bulk atoms in blue, surface atoms in red and vapor atoms in cyan.

It should be noted that a lot of work had to be performed in order to acquire a better understanding and knowledge of phenomena at stake during the sintering of nanoparticles. Indeed, not only the numerical simulations are complex but also the experimental validation by observations or measurement is hard to implement with adequate accuracy at the nanoscale.

C. Grain growth in thin films

Grain growth is a phenomenon inducing a grain coarsening that occurs only when recovery is complete. While originating from the same minimization of surface energy phenomenon, grain growth has to be clearly differentiated from sintering process. Since both of them occur concomitantly at high temperatures, it is therefore difficult to differentiate their respective impacts. The main difference lies in the underlying mechanism which involves the movement of grain boundaries in the case of grain growth but long range atomic diffusion in the case of sintering. The grain boundary is indeed moving by local adjustment of atomic position when atoms leave one grain lattice to attach to the lattice of the adjacent grain. Energetic stabilization is achieved by an increased lattice coherency through assimilation of smaller grains or grain with less stable crystalline orientation.

Grain growth studies usually describe the microstructural evolution of a thin film with two growth modes: normal and abnormal growths. In normal grain growth, the total free energy is reduced through a decrease of the grain boundary area per unit volume. In a single-phase film, grains are thus growing isotropically and uniformly in the film so that the grain

size distribution remains monomodal (see Figure II-15). As shown by the Laplace equation (see Equation (II-3)), the pressure exerted on the grain boundary is proportional to the reciprocal difference of the radii. As a consequence, the grain boundary area will tend to move into the smaller grain in order to reduce its curvature. Therefore, small grains dissolve into larger grains as described by the Lifshitz-Slyozov-Wagner (LSW) formalism of particle coarsening [37, 38] and popularized under the term of Ostwald ripening. The several LSW-derived models agree on the asymptotic behavior of the mean grain size evolution following a scaling law:

$$G = K(T) \cdot t^n \tag{II-16}$$

Due to surface grooving induced by the compliance with the dihedral angle condition, a stagnation of grain growth has been observed when the average grain size reaches two to three times the film thickness [39, 40]. Further increase of the grain growth then occurs by abnormal (or secondary) growth.

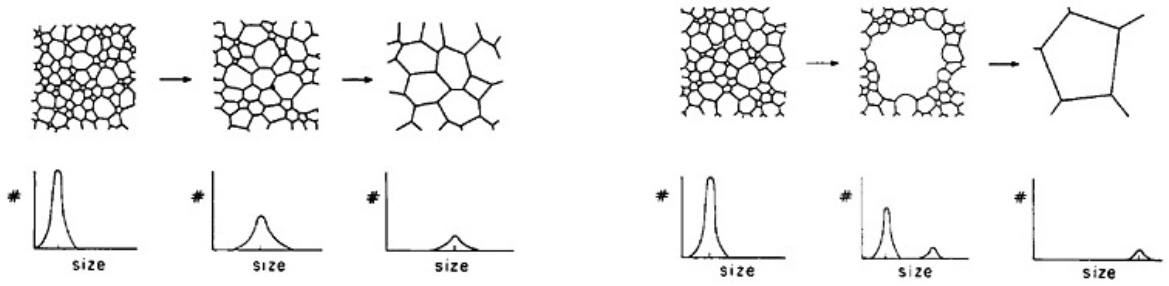

Figure II-15: Schematic of microstructure and grain size evolution during a normal grain growth (left) and abnormal grain growth (right).

During the abnormal grain growth, a few grains grow substantially in a matrix of fine grains. As a consequence, abnormal grain growth results in a bimodal grain size distribution. As demonstrated by Thompson's group which extensively studied their kinetics mechanisms, abnormal grain growth is more driven by the reduction of surface energy anisotropy than merely by the reduction of grain boundaries energies [41]. The driving force Γ for this phenomenon can be expressed by [42]:

$$\Gamma = \frac{2\Delta\gamma}{h \cdot \gamma_{gb}} \tag{II-17}$$

where γ_{gb} is the grain boundary energy, $\Delta\gamma$ is the surface energy difference between

abnormal and normal grains and h is the film thickness. The anisotropy of grain surface energy between grains thus induces a bimodal distribution of grain size. Amongst the sources of such anisotropy, the crystallographic orientation has to be mentioned. Indeed, as depicted in Table II-5 for the main crystalline directions, {111} surfaces will be more stable than {110} surfaces. Consequently, grains with low free-surface energies will tend to consume the stagnant normal grains.

Table II-5: Surface energies (in $J \cdot m^{-2}$) of some common FCC metals derived from the full charge density method [43].

Metal	(100)	(110)	(111)
Silver	1.200	1.238	1.172
Gold	1.627	1.700	1.283
Copper	2.166	2.237	1.952
Aluminum	1.347	1.271	1.199

Thermodynamically, the growth rate of grains with favored orientations will thus be higher than the normal growth rate. In particular, grains with (111) orientations are theoretically promoted. Nonetheless, as shown on silver by Greiser *et al.* [40], the emergence of preferentially-oriented abnormal grains is conditioned by the film thickness. Indeed, sub-micron thin films will tend to develop <111>-oriented grains whereas <100>-grains will grow when the film thickness is above 1 µm, and especially in the case of high yield stress. Other authors also reported that high energy brought to thin films either by ion bombardment or laser shots could lead to the promotion of <100>-grains at the expense of <111> grains [44]. As will be seen afterwards, {111} textures are linked to the minimization of surface and interface energies while {100} textures are related to the minimization of the elastic strain energy [45].

II. Microstructure evolution during sintering

A better understanding of the underlying mechanisms operating during the sintering of nanoparticles cannot be suitably achieved without a proper observation of its consequences on the microstructure evolution. Data on the grain shape and size are particularly crucial in this matter. Nonetheless, the geometric resolution and the high topography of inkjet-printed silver thin-films are particularly challenging to address with conventional tools (see Figure II-16). In the following section, a methodology and analysis tools will be developed in the purpose of microstructure analysis for developing a nanoparticle coalescence scenario.

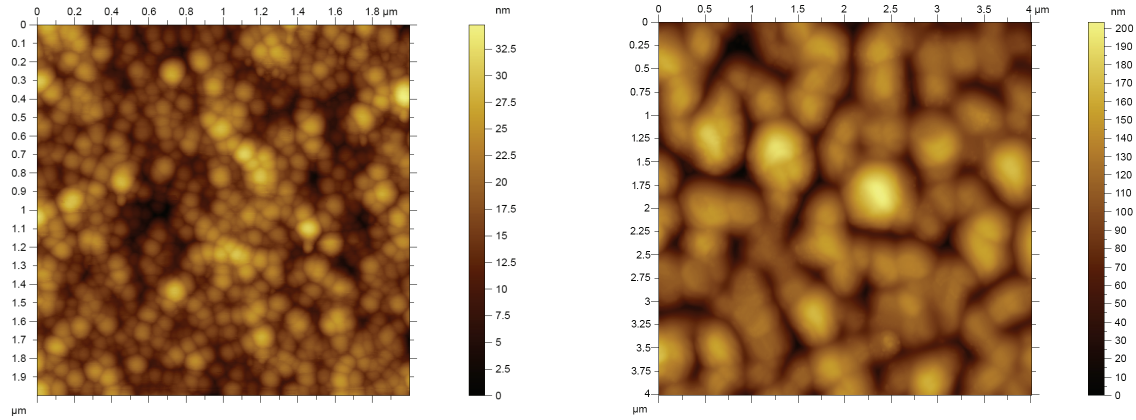

Figure II-16: Topography maps of nanoparticulate silver thin film surface exhibiting the microstructure evolution between a thermal curing at 150 °C (left) and 500 °C (right). Measured by AFM in AAC mode.

A. Morphological approach: contribution of scanning electron microscopy image analysis

Given the nanometric size of objects to be observed, Scanning Electron Microscopy (SEM) is particularly adapted for the observation of atomic diffusion impact on microstructure during the coalescence. The wavelength λ associated with the electron beam with an acceleration bias V_0 is much smaller than for photons in the visible spectra. The angular resolution of a SEM is then improved compared to optical microscopes. The wavelength is given by the de Broglie relation:

$$\lambda = \frac{h}{m\nu} = \frac{h}{\sqrt{2em_eV_0}} \sim 8\ pm \text{ at } 20\ kV \qquad \text{(II-18)}$$

Where h is Planck's constant, e is the elementary charge, m_e is the electron mass and ν is the electron's speed.

Scanning electron microscopes are usually equipped by electrostatic or electromagnetic lenses whose aberrations are limited to a few hundredths of a radian (~0.6°). The associated resolution from the interaction of an electron beam with matter is given by Abbe's formula [46]:

$$\delta = \frac{0{,}61\lambda}{n sin\alpha} \qquad \text{(II-19)}$$

where δ is the angular resolution of the equipment, n is the refractive index and α the semi-angle of illumination.

Whatever the type of detector used for the observation (SE2, BSE, etc…), images are in

grayscale. Each shade of gray is thus correlated to the intensity of signal received by the detector. Depending on the nature of the incident electrons on the detector – secondary electrons, Auger electrons, backscattered electrons, or X photons – the image contrast thus provides information on topography, on microstructure or on chemical nature. From a SEM image in topography (typically, an image reconstructed from the signal of secondary electrons), it is therefore possible to extract information about the average grain size of silver nanoparticles, and *a fortiori* about the average pore size. Indeed, in this case, the grain boundary which is located at a lower height appears with a lower intensity (*i.e.* in black).

Several approaches could be considered to determine the average grain (or pore) size from an electron microscopy images. The first one is to draw lines randomly on top of the image and to determine the average distance between each intersection with grain boundaries. Repetition of this procedure on several areas of the sample should lead to a sufficient amount of data from the statistical point of view to determine the average grain size with reasonable accuracy (*i.e.* so that the estimator bias is as small as possible, typically below 5 %). Figure II-17 explains the principle of this methodology for a SEM image.

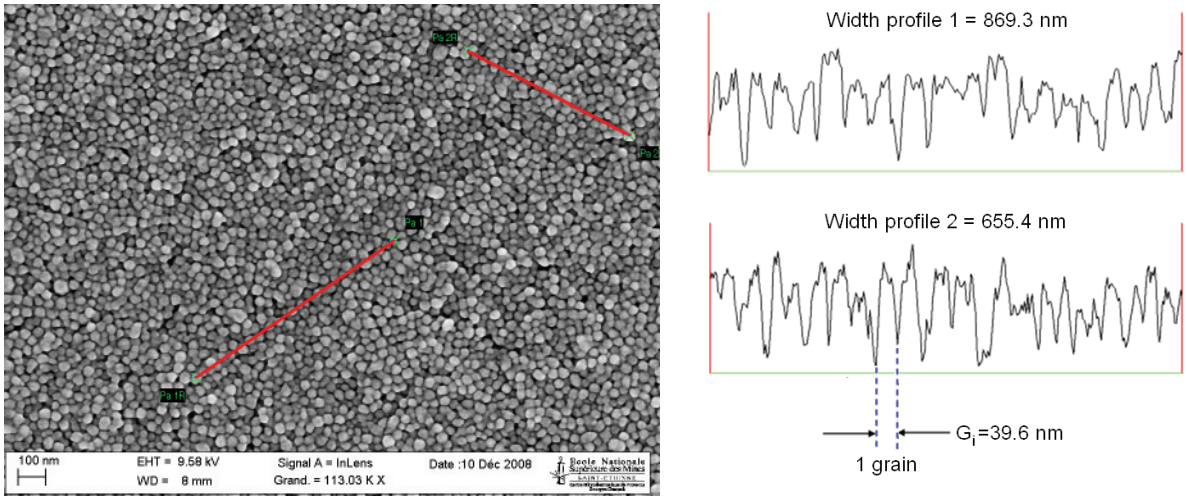

Figure II-17: Schematic of the grain size extraction principle from line intersection on a nanoparticulate surface. Nanoparticles are printed on silicon and dried at 90 °C for 5 min.

In order to establish how convergent the estimator is, the measure is reproduced several times on the same sample. Figure II-18 indicates that the grain size estimator, $\hat{G}_{1D}$, in the case of line intersection method, quickly converge to a target value of 26 nm. This value corresponds to the expected value of the grain size estimator, $E(G_{1D})$. Figure II-18 also reveals that the bias is below 5 % after only 74 iterations.

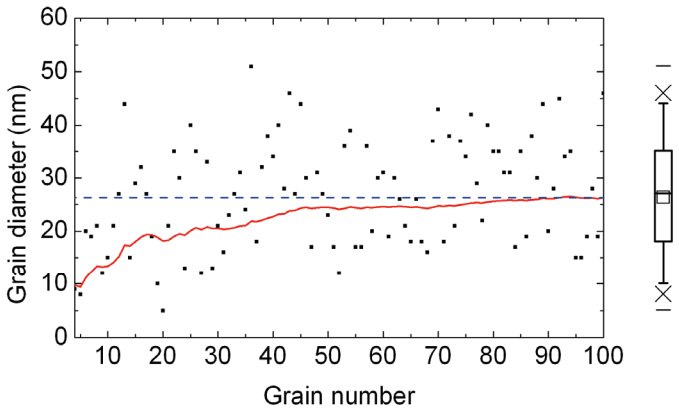

Figure II-18: Evolution of $\hat{G}_{1D}$ estimator (red curve) with respect to the realization number (black dots). The expected value of the estimator is represented with blue dashes. The box plot depicts the grain distribution from the first to third quartile, with standard deviation between the first and ninth decile.

This approach can be extended to two dimensions on the same SEM image. This can be achieved using an image treatment software that will allow discretization of grains using a threshold operation. This operation is decisive for a successful implementation of this method. Since all image data points are coded in grayscale, a numerical threshold value is attributed for the shade of grey corresponding to either a grain, a pore or a grain boundary. *In fine*, this will lead to a monochrome image with only black and white pixels.

The chosen value for thresholding is very sensible for topographic images since a same shade of gray can be related to either a grain surface or a grain boundary. This is especially confirmed when the sample surface is kept unprepared, *i.e.* neither mechanically nor chemically polished. Thus, the value should be finely adjusted to reflect reality and cannot be automated through a routine. Basic operations of image processing, such as opening, closure, erosion and dilatation, are then applied to each pixel of the image to achieve the best agreement with the grains (see Figure II-19). After a few back-and-forths between the resulting and the original images, the result should be appropriate. Basic operations include:

- Erosion: a pixel is converted to white if at least one pixel of the 3x3 neighborhood is white. The resulting image thus removes pixels from the edges of black objects.
- Dilatation: a pixel is converted to black if at least one pixel of the 3x3 neighborhood is black. The resulting image is thus obtained by adding pixels to the edges of black objects.
- Opening: performs an erosion operation, followed by a dilatation. Objects of the resulting image are smoothened and isolated pixels are removed.
- Closure: performs a dilatation operation, followed by an erosion. Objects of the resulting images are also smoothed and small holes are filled.

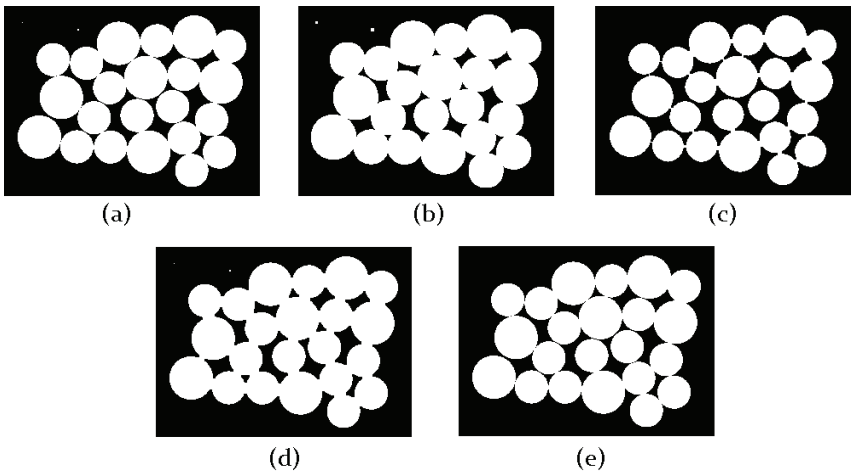

Figure II-19: Effect of fundamental morphologic operations on a reference image (a): erosion (b); dilatation (c), opening (d), closure (e).

In this study, the ImageJ software developed by the U. S. National Institutes of Health was used as the image processing program [47]. Applying the above-mentioned operations to the image presented in Figure II-17, ImageJ can automatically determine the average surface area of detected objects from which an Equivalent Circle Diameter (ECD) can be derived. This is an extrapolation of the diameter of a circle that would have the same area as the detected grain. This approximation is particularly relevant for green body particles (*i.e.* prior to any thermal curing) since they are spherical. But for sintered grains whose circularity (ratio between surface area and perimeter) can be very low, the equivalent circle diameter is an appropriate parameter to render the dimension of a grain. Automating the image treatment allows a greater statistical sampling of grain size thus leading to a better estimation of its expected value, *i.e.* with a smaller standard deviation. According Figure II-20, as for the linear intercept method, the expected value of 25 nm can be determined in only 100 iterations with an error below 1%.

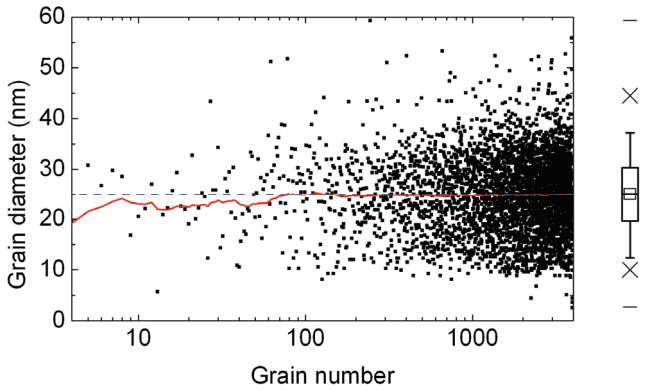

Figure II-20: Evolution of the estimator $\hat{G}_{2D}$ (red curve) according to the number of iterations (black boxes). The expected value $E(G_{2D})$ is shown with a blue dashed line. The box chart exhibits the data distribution of the lower and upper quartiles (25 and 75% of data points), with whiskers from the 1st to the 9th decile (resp. 10 and 90% of data points).

To check that the grain diameter extracted from SEM images is accurate, and thus validate the method, the nanoparticle-based conductive ink was processed at room temperature using granulometry equipment based on dynamic light scattering measurements (with a limit of resolution of 0.2 nm) [48]. The analysis exhibited two Gaussian distributions centered on 6.7 nm and 34 nm (see Figure II-21), which is consistent with the SEM image treatment.

Since the method is validated experimentally, it can be exploited to study the morphological evolution of the inkjet-printed silver film (see Figure II-22). Afterwards, the expected value of the ECD estimator determined from two-dimension surfaces, $E(G_{2D})$, will be considered as the mean grain size of the film, and thereafter simply designated as G. The mean pore size will be designated by the letter P.

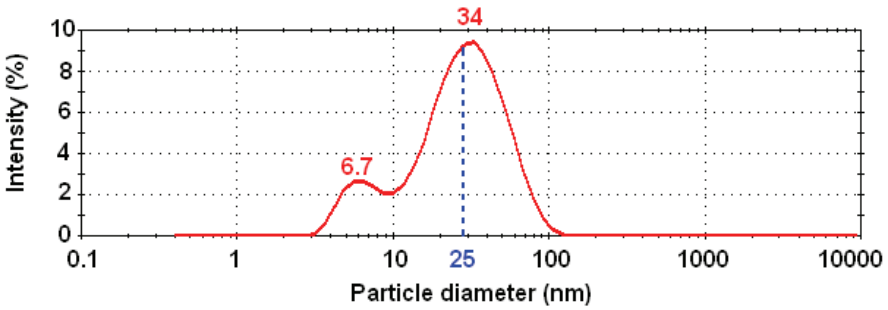

Figure II-21: Size distribution by intensity obtained from a granulometer (Zetasizer nano series) where the previously reported average grain diameter extracted from the SEM image is represented with a blue dashed line.

As seen in part I, silver nanoparticles undergo sintering during the thermal curing which leads to both grain growth and pore shrinkage. Both parameters can be monitored with image analysis according to the sintering conditions, such as temperature, time and thermal ramp.

Gaussian fits of grain size distribution extracted from SEM images indicates that the average grain size changes from 25.0 ± 0.2 nm after 5 min at 200 °C (which corresponds to the green body state), to 72.3 ± 3.4 nm after 120 min (see Figure II-23). Those results are consistent with observation since the grain size increases with the sintering time as expected. Image processing also indicates that, owing to the increase of contact surface between grains, pores are sliding alongside the grains and merging into bigger pores. With the same treatment, pore size is indeed increasing from 3.7 ± 0.1 nm to 7.6 ± 0.4 nm. The growth of pore size is thus correlated to a drop of the porosity density – defined as the ratio of apparent surface area of porosities to the total surface area of the SEM image – from 42.4 % to 20.9 %.

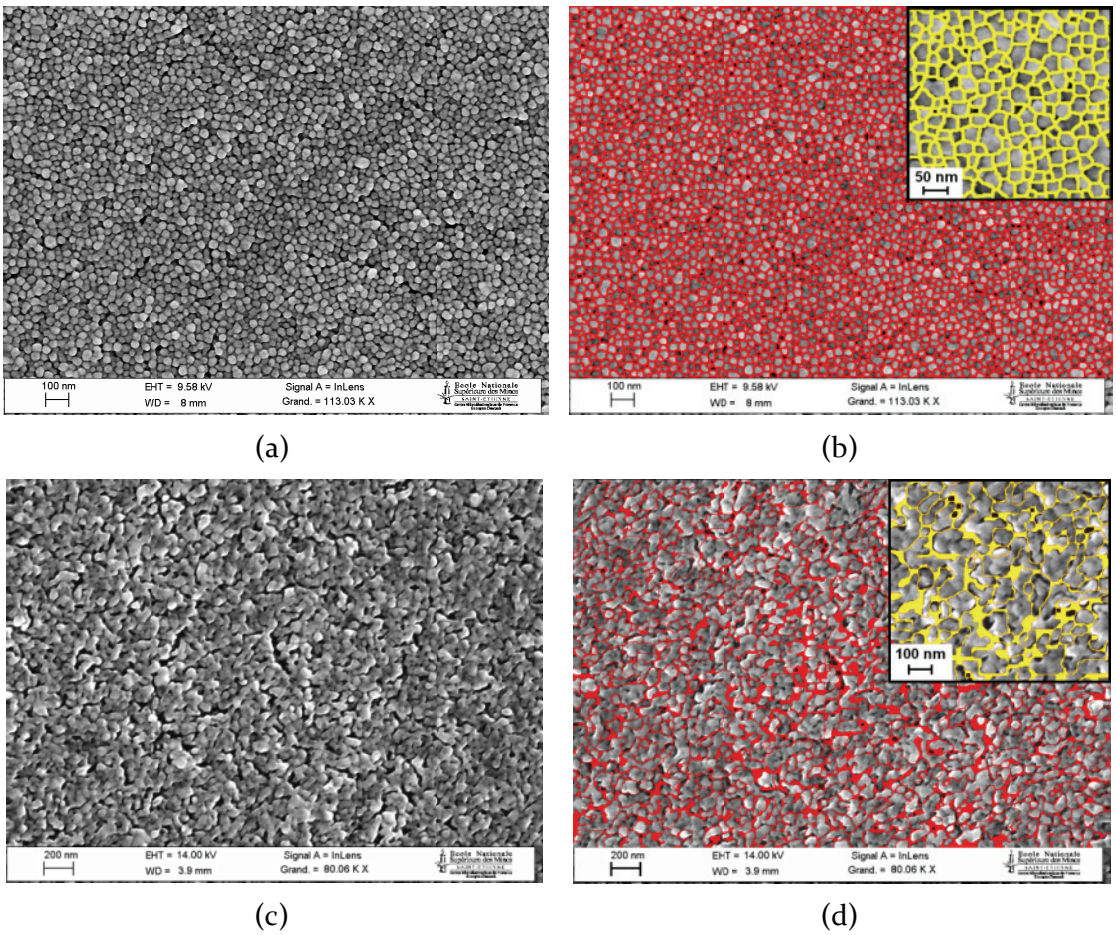

Figure II-22: Surface morphology evolution of silver nanoparticles on a silicon nitride substrate from SEM images for isothermal sintering at 200°C in an atmospheric oven after 5 min (a) and 120 min (c); and corresponding superimposition of grain boundary outlines resulting from the image analysis process (b and d).

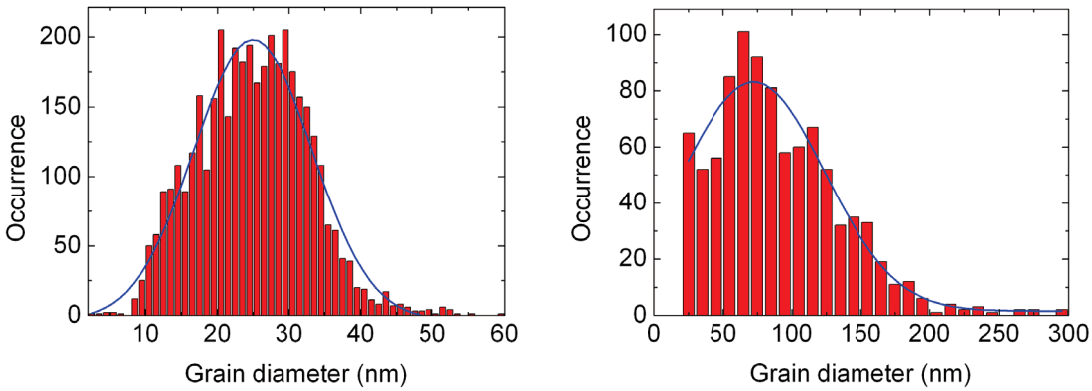

Figure II-23: Grain diameter distribution after image analysis process for an isothermal sintering at 200°C of 5 min (left) and 120 min (right).

As seen in part I, sintering can occur through densifying regimes. Those regimes are usually achieved at higher temperature (T/Tm > 0.5) since activation energy of volume diffusion mechanisms are more important. Thus, quickly reaching higher temperatures

allows focusing of the thermal budget on densifying regimes and limiting of energy-consuming surface diffusions. This can be performed using a Rapid Thermal Annealing oven (RTA) with thermal ramp up to 150 °C/s. In this study, we assessed the impact of the thermal ramp on microstructure of the printed silver films, with ramp ranging from 0.1 °C/s – corresponding to a common atmospheric oven ramp – to 150 °C/s, immediately followed by an isothermal plateau of 15 min.

Following the same procedure of image processing, grain size together with pore size can be determined (see Table II-6). As expected from micrographs in Figure II-24, the mean grain size has increased from 76.3 ± 6.9 nm at 0.1 °C/s to 91.5 ± 8.6 nm at 50 °C/s, showing an improved sintering process compared to the mean grain size obtained after 2 hours in an atmospheric oven. Meanwhile, the mean pore diameter has respectively increased from 32.0 ± 4.1 nm to 50.2 ± 8.2 nm. These results indicate that using a fast ramp activates other diffusion mechanisms than just surface diffusion. This is particularly valuable since no densification is achieved through surface diffusion. Limiting this mechanism is thus required to enhance the mechanical stiffness and the electrical resistivity.

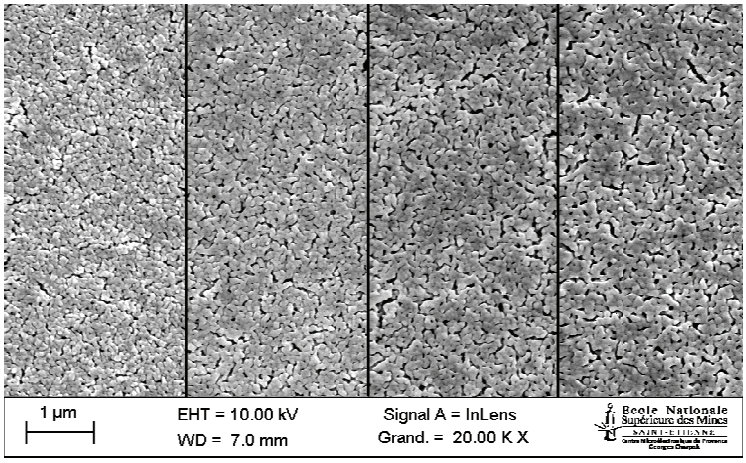

Figure II-24: SEM images of inkjet-printed silver film surface on silicon nitride substrates after a sintering step at 200 °C for 15min and with a ramp of 0.1 °C/s (left), 1 °C/s (middle left), 50 °C/s (middle right) and 150 °C/s (right) in a RTA oven under N2 atmosphere.

Table II-6: Morphological parameters extracted from image processing of SEM images for several thermal ramps.

Ramp	**0.1 °C/s**	**1 °C/s**	**10 °C/s**	**50 °C/s**	**150 °C/s**
Mean grain diameter (nm)	76.3	82.8	96.0	91.5	108.2
Mean pore diameter (nm)	32.0	41.9	45.0	50.2	59.8
Porosity fraction (%)	8.8	11.8	11.1	17.3	18.1

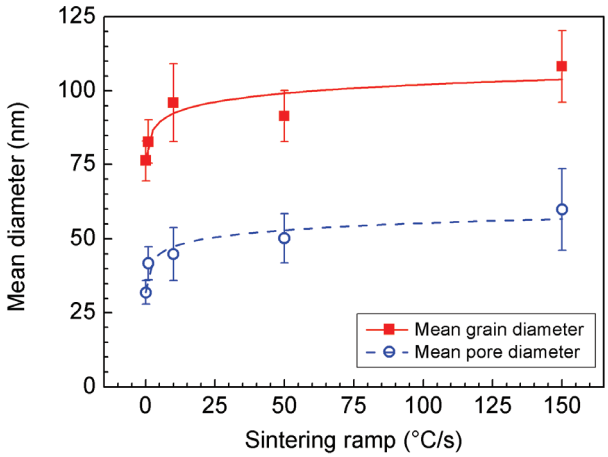

Figure II-25: Mean grain and pore diameters (resp. red box and blue circle) of inkjet-printed silver films on silicon nitride according the sintering ramp up to 200 °C in a RTA under N2 atmosphere.

Repartition of data points in Figure II-25 indicates that the mean grain diameter G (resp. pore, P) shows a tendency to follow a natural logarithmic law with the sintering ramp (see Equations (II-20) and (II-21) below). According to the importance of error bars, related to standard error of grain diameter measurements, several models could fit the data points. Nonetheless, in this study, the best fit model was chosen according to the method of least squares.

$$G = 24.97 + 66.23\left[1 - \exp\left(-14.9\frac{dT}{dt}\right)\right] \quad \text{(II-20)}$$

$$P = 3.74 + 42.09\left[1 - \exp\left(-11.12\frac{dT}{dt}\right)\right] \quad \text{(II-21)}$$

Mean grain diameter reaches quite quickly a steady state according to the sintering ramp value. Given that above a ramp of 50 °C/s, evaporation of solvents is nearly instantaneous at the experiment timescale, this result points out that at 200 °C one dominant sintering mechanism is operating which leads to grains diameter of about 110 nm. Consequently, as expected, using a fast sintering ramp indeed limits energy consumption in surface diffusion mechanisms which is activated at low temperatures. Since high sintering ramp greatly affects the conformality of printed features, a ramp of 10 °C/s will be used afterward for all experiments. According to Equation (II-20), the grain diameter would thus be affected by 12.7 % only, corresponding to a variation of about 10 nm.

Morphological approach enables fast assessment of grain diameter as a derivation from original nanoparticle size which is particularly well suited for determination of sintering

mechanisms and for laws of macroscopic behavior, as much for electrical as for mechanical behavior. Nonetheless, image analysis of SEM images is a tedious process which is prone to errors given the subjectivity of the threshold operation, and can only denote estimations of grain size evolution.

B. Crystallographic approach: contribution of EBSD and XRD

The crystalline nature of the considered nanoparticles requires specific tools to address issues at the nanoscale. Indeed, a polycrystal can contain several grains which can themselves be constituted by several subgrains, also known as crystallites. In this part, grain boundaries will particularly attract our attention as they separate materials in definite entities. Grain boundaries are interfaces between grains or crystallites which affect as much mechanical as electrical behavior. This will be addressed in the next chapter. Within a grain, several crystallites can coexist in the same matrix. According to their origin, they could be separated by twin boundaries or by large angle and low angle grain boundaries.

As a low stacking fault energy metal, silver tends to easily generate twins as a predominant deformation mechanism when subjected to a strain [49-51]. It is thus of particular interest to use an apparatus capable of discriminating this kind of crystallite inside a grain matrix. From now on, the term crystallite will thus designate a coherent volume which is comprised within a supercell that will be simply named as a grain, consistently with the previous paragraph. Generation and evolution of twin is represented in Figure II-27.

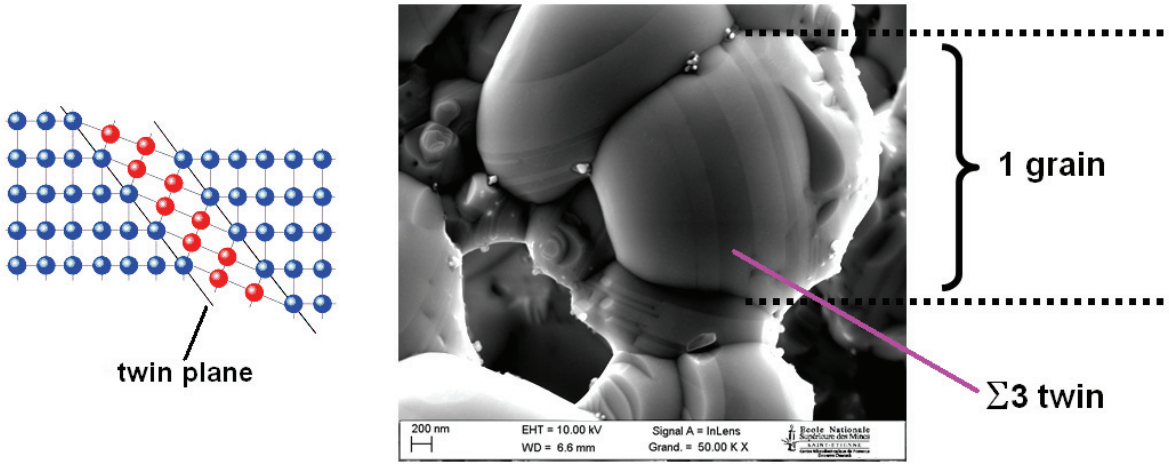

Figure II-26: SEM view of a Σ3 twin system formed by lattice slip and rotation.

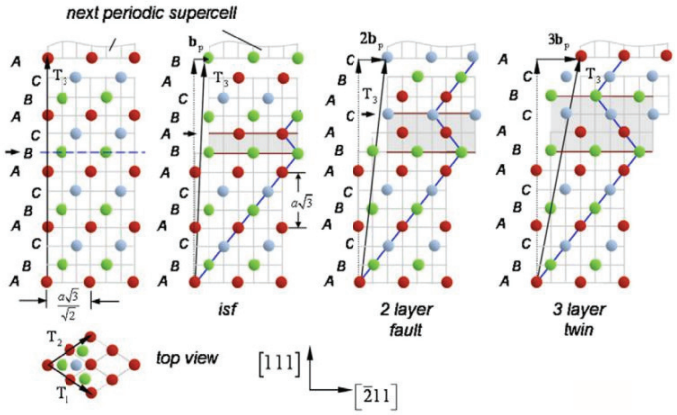

Figure II-27: Crystallographic schematic of twinning growth from a perfect FCC (left) to a twin with a two- or three-layer fault (right), including the intermediate state of an intrinsic stacking fault (isf, center left) [51].

i. Contribution of Electron Back-Scattered Diffraction

A more extensive analysis of a thin film structure can be achieved using Electron BackScattered Diffraction (EBSD) technique in a SEM. From this analysis, one can perform a crystallographic orientation estimation together with a grain size determination of each crystallite. EBSD technique is based on the diffraction pattern produced by backscattered electrons emitted from the surface of a 70°-tilted sample surface under an accelerated electron beam. Backscattered electrons will be diffracted by the silver crystal lattice and escape the sample, toward a phosphor screen, only if the Bragg condition is fulfilled (see Equation (II-22)). Intersection of the screen with the diffraction cones will then form Kikuchi bands corresponding to each of the lattice diffracting planes (see Figure II-28). Position and angles between each detected band of a pattern enables the computation of interplanar angles and, by comparison to international crystal databases, of crystal orientation.

$$n\lambda = 2d_{hkl}sin\theta \qquad \text{(II-22)}$$

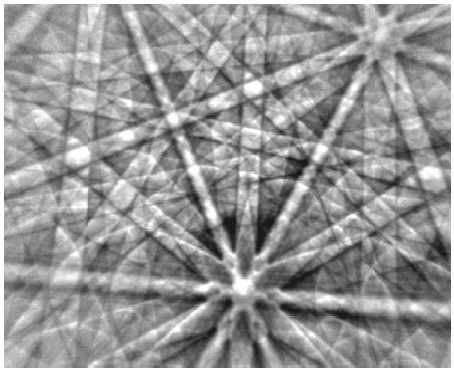

Figure II-28: Electron backscatterred pattern (left), also known as Kikuchi pattern, of a silver nanoparticle under 30 kV acceleration beam and its related bands indexation (right) related to a {111}-oriented voxel.

The electron backscattered pattern is related to the electron interaction volume underneath the incident electron beam. The penetration length can be determined by Monte-Carlo simulations. According to our simulation on Casino software [52], the interaction volume for electrons accelerated at 30 kV is restricted to 30-40 nm in depth (see Figure II-29), which is consistent with the Kanaya-Okayama formula (see Equation (II-23))[53].

$$\delta_{KO} = \frac{0.0276 \cdot A \cdot E_0^{5/3}}{\rho \cdot Z^{8/9}} \qquad \text{(II-23)}$$

where δ is the penetration depth, A the atomic weight (in $g.mol^{-1}$), E_o the incident beam energy (in kV), ρ the density (in $g.cm^{-3}$) and Z the atomic number.

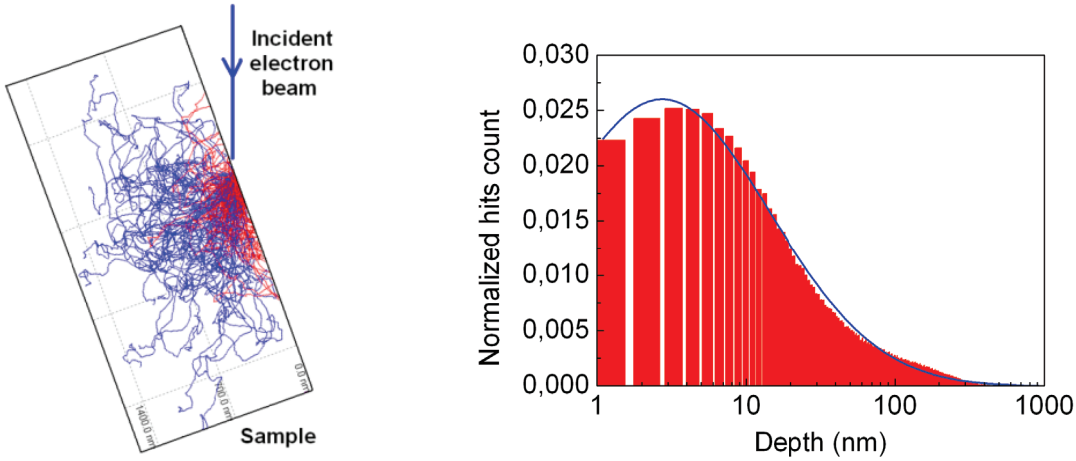

Figure II-29: Monte-Carlo simulation of 200 electrons trajectories in the silver layer under a 70°-tilt showing backscattered electrons emerging from the surface in red (left, square scale of 700 nm) and distribution of penetration depth for 5×10^5 electrons which follow a log-normal distribution with a mean value of 40.7 nm and a 6 nm-mode.

Scanning the sample surface thus enables acquisition of maps where each pixel is correlated to the crystallographic orientation of the interaction volume. In our case, EBSD analysis performed at 30 kV will thus be related to the crystalline orientation of 40 nm-thick voxels with a standard deviation of 6 nm. A color scale is adopted by convention to represent each crystalline orientation (see Figure II-30). In the following work, unless mentioned otherwise, ESBD maps will be acquired through HKL Channel 5 system under a 30 kV acceleration voltage with a step size of 50 nm. Acquisitions will be performed with a 4x4 binning setup on a 24 ms per frame basis. Indexation is performed on at least 5 band edges with Maximum Angle Deviation (MAD) of 2°.

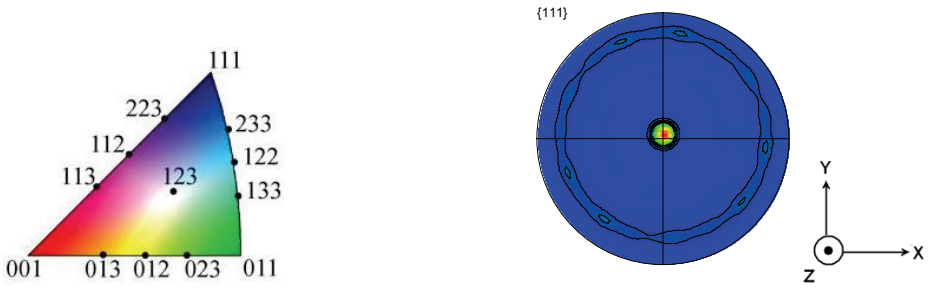

Figure II-30: Standard triangle for Inverse Pole Figure indicating the color scale for common crystallographic orientations in a FCC crystal (left) and Pole Figure of an evaporated silver thin film presenting a {111} preferential orientation along the normal of the film (right).

Isothermal sintering at several temperatures, ranging from 200 °C to 500 °C, is performed on inkjet-printed silver thin films on {100} oriented silicon during 15 min. Orientation mapping is consecutively carried out by EBSD to assess any preferential orientation which could rise from the film. Fiber crystallographic texture generation was indeed previously reported in sputtered and evaporated films either spontaneously, by bombardment, or by thermal treatment [44, 54-57]. Physical vapor deposited FCC thin films usually develop a {111} fiber texture during deposition due to surface/interface energy minimization. Indeed in FCC materials, surface free energy $\gamma_{(111)}$ is lower than $\gamma_{(200)}$ which in turn is lower than in any other direction [58, 59]. A subsequent treatment or self-annealing usually induces a <100>-direction enhancement due to strain energy minimization.

According to {111}-pole figures, EBSD data exhibits no preferential crystallographic orientation on the surface of nanoparticles-based films whatever the sintering temperature, up to 500 °C (see Figure II-31). Silver grains are thus growing without apparent order which does not comply with expected energy minimization processes observed with other deposition process in previous works. Indeed, conventional thin film deposition techniques such as sputtering, evaporation, and electroplating usually leads to the development of films with preferential {111} orientation as will be shown afterwards in Figure II-44.

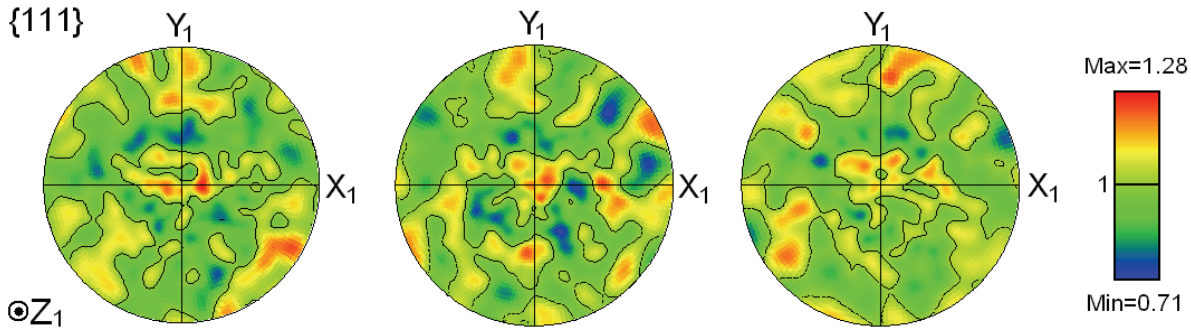

Figure II-31: {111} pole figures of inkjet-printed silver films on silicon after being sintered at 300 °C (left), 400°C (middle) or 500 °C (right) during 15 min in a RTA under N_2 atmosphere at 10 °C/s. Stereographic projection of the upper hemisphere is represented in equal area in the sample coordinate system. Contour lines are in multiples of the mean uniform pole density (MUD).

Contrary to common deposition techniques, inkjet printing technology thus appears as a means to fabricate non-textured patterned thin films. Since {111} and {100} are the more thermodynamically stable grain orientations for FCC crystals, as shown in part I-C, they should develop during the deposition and consecutive evolution during the curing with grain growth. Even though it could also be observed in micron-sized thick films, the absence of any preferential orientation could thus be a sign of limited grain growth in comparison to mere neck growth induced by sintering. In other words, the energy barrier over which grain growth is activated by surface or strain energy minimization has not been overcome yet by the supplied thermal budget. It could then be speculated that thermal budget is consumed preferentially by the sintering process.

Activation energy of the normal grain growth mechanism involved under isothermal sintering can be derived from an Arrhenius empirical equation [60, 61]:

$$G = K_0 \cdot t^n \cdot exp\left(\frac{-E_A}{RT}\right)^n \qquad \text{(II-24)}$$

where G is the diameter of the grain, K_o is a pre-exponential rate constant, t is the isothermal annealing time, n the grain growth exponent, E_A is the apparent activation energy for grain growth, R is the ideal gas constant (R=8.314472 J.mol^{-1}.K^{-1}) and T is the absolute temperature. Integration of this grain growth law over an interval $\Delta t = t - t_o$ between the initial green state and the current state after isothermal sintering, where n is assumed to be independent of temperature and equal to 2, leads to:

$$ln\left(\frac{G^2 - G_0^2}{t}\right) = lnK_0 - \frac{E_A}{RT} \qquad \text{(II-25)}$$

Grain size analysis performed on EBSD orientation maps (see Figure II-32) is used to trace the $ln[(G^2-G_o^2)/t]$ data points versus $1/T$ in Figure II-33. This Arrhenius plot with four data points thus yielded an activation energy of 4.657 ± 0.487 kJ.mol^{-1}. This apparent activation energy corresponds to our specific situation where the grain growth phenomenon is occurring simultaneously with the sintering process. The thermal energy provided during the curing is then allocated separately to sintering and grain growth. Being the vector of both coalescence and grain growth, atomic diffusion is at the very core of our study leading to the evolution of microstructure. As this diffusion process is affected by a complex set of parameters such as curing temperature, grain size, diffusion paths (see part I) and stresses, comparison with other authors should be taken with caution. Assumption of the n value as equal to 2 is also a possible source of error. This value indeed considers that the grain growth is mainly driven by grain boundary diffusion. Since several mechanisms are at stakes, as explained in section I, this assumption may not be as suitable as it should be.

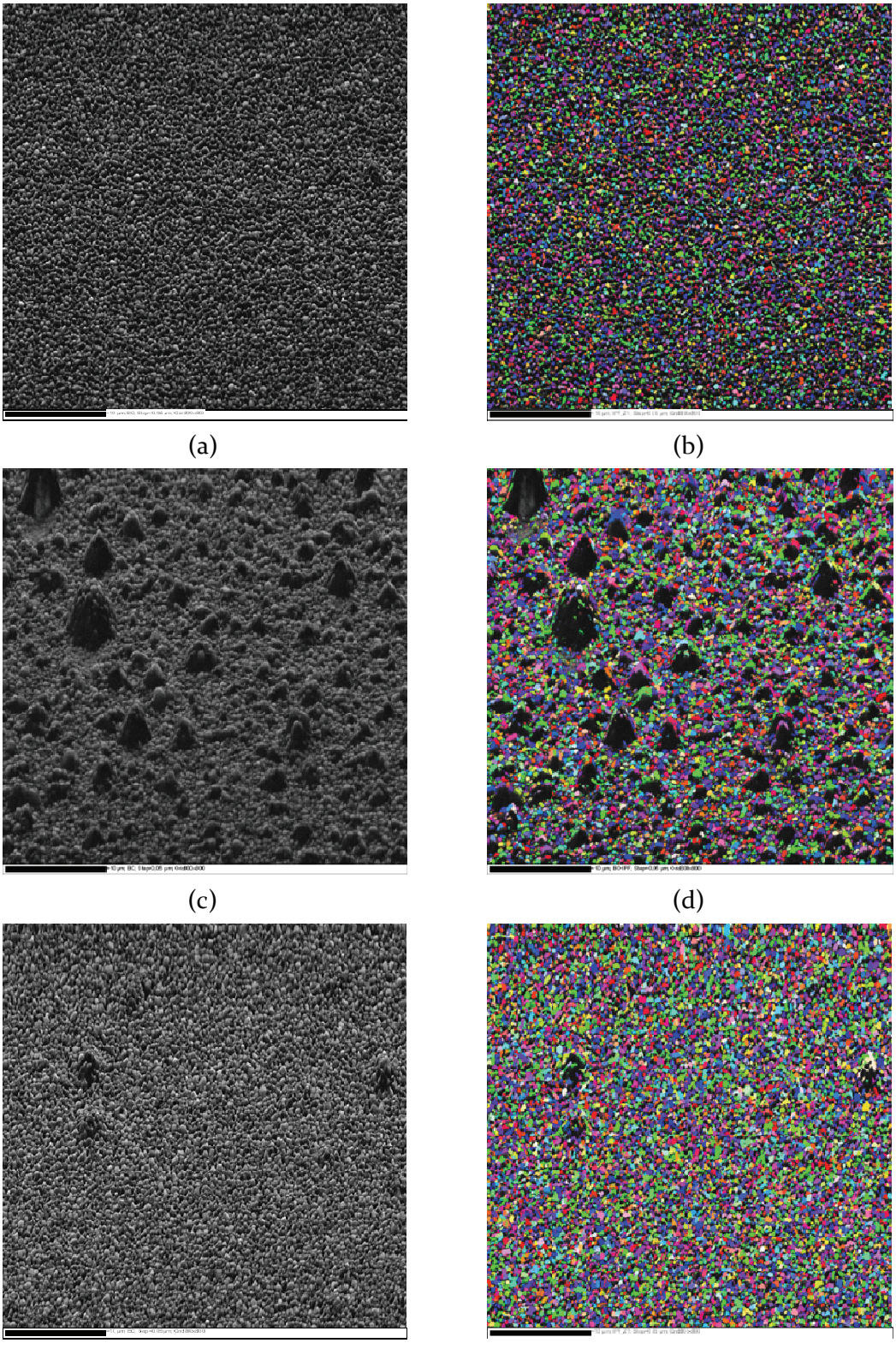

Figure II-32: Band contrast and orientation maps along the normal direction Z_1 using IPF coloring (acquired with a step size of 200 nm) for inkjet-printed silver films on silicon substrate sintered at 300°C (a-b), 400°C (c-d) and 500°C (e-f) during 15 min in a RTA under N_2 atmosphere. Scale bars on maps represent 10 µm.

Our activation energy is then far below the 53 kJ·mol^{-1} activation energy of normal grain growth found by Dannenberg *et al.* [62] for 40-50 nm sputter-deposited silver films. Since the grain size is similar in our study, this discrepancy is believed to originate both from the high stress present in such deposits induced by the deposition process and from the thickness of the film. Indeed, the film thickness is only double that of the initial mean grain size in Dannenberg's study, while more than six times in ours. Thompson indeed showed that a low thickness to grain size ratio would impede the abnormal grain growth [63] whose activation energy is much lower at 27 kJ·mol^{-1} [64]. The lower activation energy calculated in this work could also be credited to the higher defect densities in nanoparticles compared to sputtered thin films, for it is the driving force for sintering and grain growth.

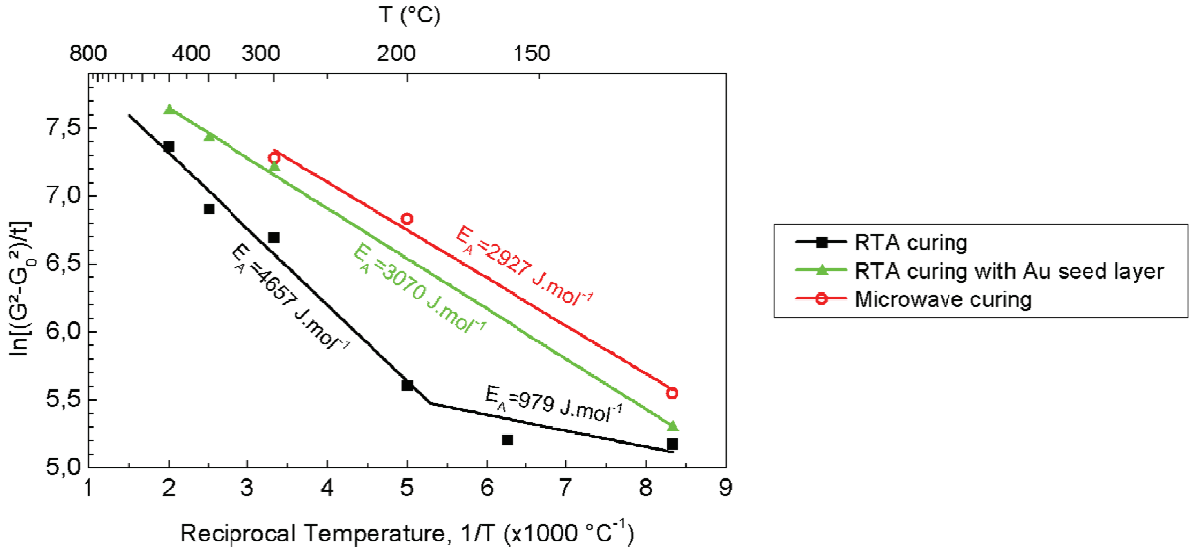

Figure II-33: Arrhenius plot of grain growth data of silver crystallites extracted from EBSD grain size analysis.

Since activation energy of our grain growth is significantly lower than that of grain boundary diffusion in silver, about 95 kJ·mol^{-1}, it is consistent with a surface diffusion process reported at 30 kJ·mol^{-1} [65]. The system considered in our study is nonetheless very complex. While a high stress is usually generated during thin film deposition and the consecutive thermal stabilization (in the range of 200 MPa for sputtered films), inkjet-printed thin films develop very low level of stress, as will be seen in the next chapter. The presence of high stress contributes positively to the grain growth by smoothing the progress of the sintering process. Even though our inkjet-printed deposits cannot benefit from this effect to enhance coalescence and grain growth, the microstrain at the crystal scale nonetheless influences the diffusion process. The very low activation energy can thus be related to the stored enthalpy resulting from the mechanical attrition during the nanoparticle fabrication (see Chapter 1). This available elastic energy could thus be used by the system during the grain growth and explain the reduced energetic barrier of activation.

ii. Contribution from X-ray Diffraction

The size of small crystallite can also be determined by another technique based on crystallographic structure: X-Ray Diffraction (XRD). This method is a non-destructive measurement which is based on the diffraction of X-rays by the different lattice plane families. Compared to EBSD, XRD provides more quantitative data for it involves much more grains than just those at surface-level. In addition, XRD is richer in terms of information since it gives also access to the quantitative crystallographic texture analysis, the size, the microstrain or the internal/residual stress as will be exposed in Chapter 3. In this part, the evolution of microstructure is considered via the analysis of X-ray peak broadening which is correlated to the size and the microstrain of crystallites or Coherent Diffraction Domains (CDD). The measured intensity is the convolution between the atomic arrangement and the function describing the shape of the crystal [66]. These measurements were performed in collaboration with the Claude Goux Laboratory (UMR CNRS 5146) on high-resolution X-ray diffractometer.

X-ray diffraction measurements were performed using a PANalytical MPD Pro diffractometer in high-resolution double-crystal mode. The incident beam of a sealed copper tube was monochromatized by a parabolic X-ray mirror coupled to a double-bounce channel-cut monochromator (Ge, 220) present for the Cu-$K\alpha_1$ radiation. The diffracted beam was measured with linear PIXcel detector. The particle size, the planar fault density and the microstrain were determined according to the Warren-Averbach analysis using the 111/222 and 200/400 reflection pairs.

Let us first recall some theoretical background about the implementation of XRD before considering the Warren-Averbach methodology used for the peak broadening analysis. As reminded in the previous paragraph, diffraction of waves – whether electron wave or X-ray waves – produces constructive interferences only when the Bragg's condition is fulfilled:

$$2d_{hkl}sin\theta = n\lambda \qquad \text{(II-26)}$$

where d_{hkl} is the distance between the lattice planes of the crystal, θ is the angle between the incident beam and the scattering planes, n is an integer (in our case n=1) and λ is the wavelength of the incident beam (see Figure II-34).

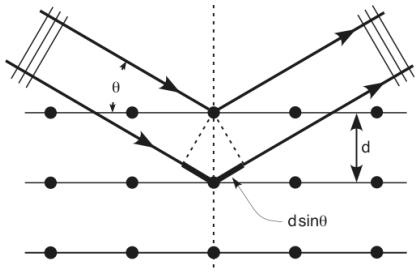

Figure II-34: Illustration of the Bragg condition of X-ray diffraction on crystalline planes.

The diffracted intensity is usually decomposed using an inverse Fourier transform to relate the Fourier coefficients to the mean crystallite size and to the lattice microstrain. According to the theory developed by Warren and Averbach, the real part of the Fourier coefficient A_L of diffraction line can be derived as:

$$ln(A_L) = ln\left(A_L^S\right) - 2\pi\langle\varepsilon_L^2\rangle L^2 g^2 \qquad \text{(II-27)}$$

where A_L^S is the size coefficient, $\langle\varepsilon_L^2\rangle$ is the mean quadratic microstrain with $\varepsilon_L=\Delta L/L$, L is the Fourier parameter (a length perpendicular to the reflecting atomic planes) and g is the diffraction vector.

Figure II-35 shows diffraction patterns measured on silver ink samples cured at 150°C, 300°C and 500°C. The Bragg peaks measured on the sample cured at the lowest temperature (150°C) are the broadest. Heat treatment at higher temperatures leads to a narrowing of the peaks, indicating a possible increase of the crystallite size and/or a decrease of the lattice microstrain. In addition to the peaks of the pure FCC structure, Figure II-35 shows the {400} reflection of the silicon substrate and a characteristic peak (at $2\theta \approx 36°$). The latter has been predicted theoretically by Warren [67] and it is known to be the consequence of planar faults (twins in the present case). The intensity of the "Warren peak" decreases with increasing curing temperature indicating the decrease of twin density.

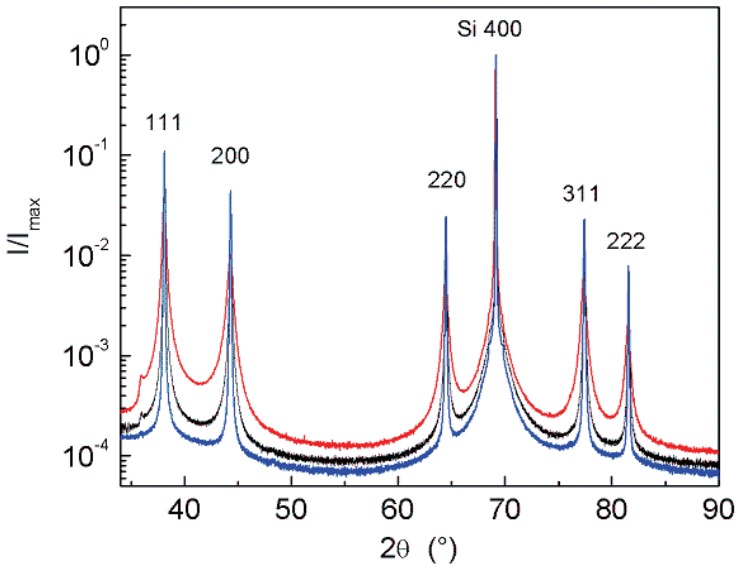

hkl	I/Io	2θ (°)
111	100	37.117
200	40	44.279
220	25	64.428
311	26	77.475
222	12	81.539
400	4	97.891
331	15	110.501
420	12	114.928
422	13	134.890

Figure II-35: High-resolution diffraction peaks observed on silver nanoparticle thin film after being cured at 150 °C, 300 °C or 500 °C. X-rays are produced with the Kα radiation of a copper filament (λ=1.54 Å) under 45 kV with 40 mA.

The Williamson-Hall plot [68] presented in Figure II-36 shows the behavior of the Full Width at Half Maximum (FWHM) of silver peaks as a function of the magnitude of the

scattering vector. The characteristic anisotropic broadening – larger widths of the {200}/{400} reflections compared to the {111}/{222} [69] – indicates again the presence of twins. This anisotropy persists after heat treatment at higher temperatures, in spite of the huge reduction in peak widths. The plot showing the FWHM in reciprocal space units indicates the presence of microstrain as the width of the upper harmonics (222/400) is larger than the width base reflection (111/200). Additionally, this microstrain is higher in the {200} crystallographic direction compared to {111}. Since planar faults do not produce micro-strain the origin of this should be sought in the specific shape of the nanocrystals and surface effects [70, 71].

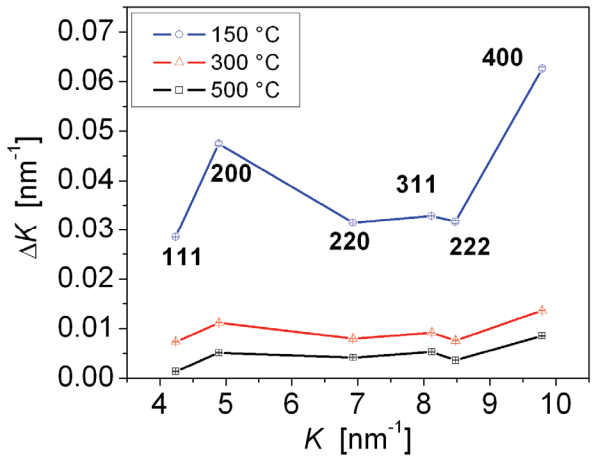

Figure II-36: Williamson-Hall plot exhibiting the FWHM as a function of the diffraction vector.

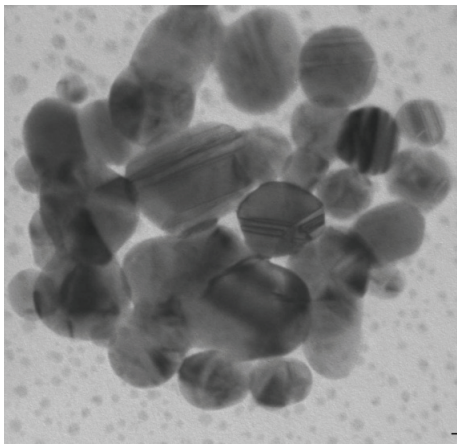

Figure II-37: TEM micrograph of silver nanoparticles in green state exhibiting significant twinning.

The high proportion of crystal twins in the nanoparticles (see Figure II-37) makes it difficult to differentiate the respective effects of size and microstrains. The average particle size, twin fault density and average microstrain were calculated according to the Warren-Averbach procedure [69, 72]. Before evaluations, the measured profiles were corrected for instrumental broadening according to the Stokes method [73]. The instrumental profiles

were measured on a standard Y_2O_3 powder and could be well approximated by a pseudo-Voigt peak shape. Figure II-38 shows the size Fourier coefficients A^S corresponding to the sample cured at 150°C as a function of the Fourier parameter *L*.

The effective particle size (column length) influenced by the presence of twins is obtained from the intercept of the initial slope with the horizontal axis and is equal to 11 nm and 14 nm in the {111} and {200} directions, respectively. These direction-dependent values were used in a second step for the determination of the twin fault density β, and the true particle size *D* according to Eq. (13.70) of [69]. The results for all the samples are presented in Table II-7.

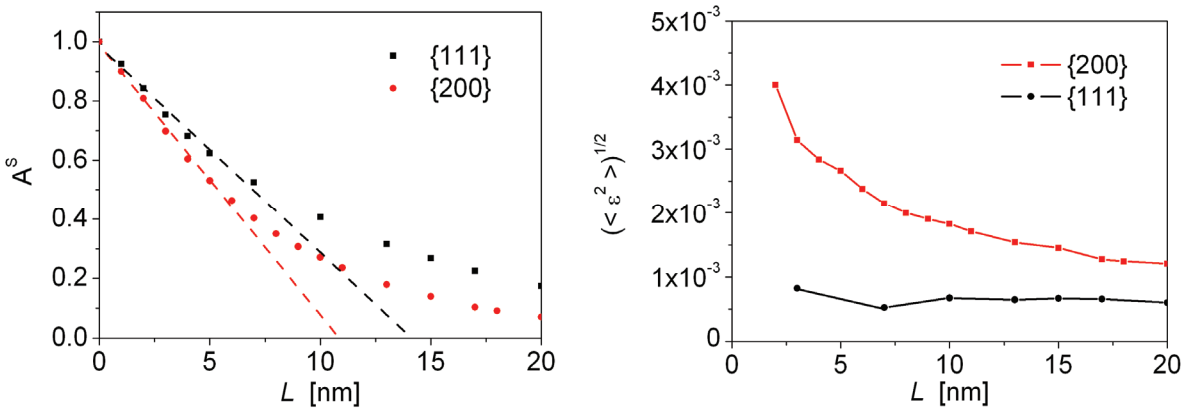

Figure II-38: Size Fourier coefficients of diffraction peaks and mean quadratic microstrain of silver thin film cured at 150 °C.

Table II-7: Average particles size *D*, twin density *β*, average microstrain (root mean square strain = $<\varepsilon^2>_{hkl}^{1/2}$) and their standard deviations as a function of curing temperature.

Curing temperature	***D* (nm)**	**β [%]**	$<\varepsilon^2>_{111}^{1/2}$	$<\varepsilon^2>_{100}^{1/2}$
20 °C	13 ± 1	1.8 ± 0.16	$30 \pm 2 \cdot 10^{-4}$	$40 \pm 11 \cdot 10^{-4}$
150 °C	18 ± 2	1.6 ± 0.10	$7 \pm 1 \cdot 10^{-4}$	$21 \pm 8 \cdot 10^{-4}$
300 °C	96 ± 10	0.8 ± 0.05	$4 \pm 4 \cdot 10^{-4}$	$9 \pm 4 \cdot 10^{-4}$
500 °C	160 ± 20	0.3 ± 0.02	$2 \pm 0.8 \cdot 10^{-4}$	$3 \pm 0.5 \cdot 10^{-4}$

From the Warren-Averbach treatment, the fundamental result is the non-destructive and direct characterization of the real mean size of crystallites *D*, in terms of domains of coherent diffraction. As expected from coalescence and grain growth, the average size increases with the curing temperature, confirming previous observations. While morphological approaches using SEM images or EBSD analysis only focus on the mean grain size on the film surface, XRD deals with the crystallites in the whole thickness of the film which is more representative of the crystallographic state. This exact representation of the sample microstructure will be the basis from which mechanical and electrical behavior will be derived in the next chapter, and especially taking into consideration the impact of crystal twins.

Derivation of the twin density β exhibits a significant proportion of twins in the thin film which is consistent with the TEM observations of nanoparticles in the initial state in Figure II-37. Indeed, during the fabrication process of our nanoparticles, mechanical attrition generates a high level of microstrain due to the successive impacts between the milling balls and nanoparticles. As mentioned in Chapter 1, a high density of crystalline defects is generated during this process, up to 10^{16} m^{-2}. Since the stacking fault energy of silver is very low (see Table II-8), the solicitation can easily be accommodated through the formation of crystal twins. Results reported in Table II-7 clearly show that the higher the sintering temperature is, the lower the twin density will be, indicating that twin density is resorbed by thermal curing. It should be noted that the opposite result is expected since twins usually appear in thin films due to internals stress generated because of CTE mismatch for instance. While this issue of internal stress will be addressed later in this manuscript (see Chapter 3), it is important to mention that inkjet-printed films develop very little stress during curing. As a consequence, the thermal energy given to the system is partly used to restore these twins.

Table II-8: Intrinsic stacking fault energy γ_{isf} for common FCC metals.

Metal	Silver	Gold	Copper	Aluminum	Platinum
γ_{isf} ($mJ \cdot m^{-2}$)	18	33	41	130	324

In addition, according to Figure II-38, the mean quadratic microstrain distribution can be attributed to a characteristic evolution of the microstrain field near triple junctions, and more generally at the vicinity of grain boundaries. The decrease of the projected average microstrain along both directions <111> and <200> was expected since the crystal defects disappear as recovery is occurring. As presented previously, one of the aspects of this minimization of surface energy is indeed the creation of grain boundaries between nanoparticles. A confirmation of this phenomenon is shown in the XRD measurements. This microstrain release originates from the recovery process during which crystalline defects inside the diffracting coherent domains are annihilated.

C. Crystalline texture transfer assisted by atomic interdiffusion

As mentioned in previous sections, in FCC metals, surface energy minimization tends to promote the growth of {111} grains while strain energy minimization is supporting {100} grain growth [74]. It is commonly accepted that surface energy minimization is dominant in polycrystalline thin films, leading to a preferential {111} orientation when these films are cured. Other mechanisms can also lead to the preferential growth of {100} grains. For silver nanoparticles, at the initial sintering stage, the surface energy minimization tends to

promote the neck growth before any thermal activation of Ostwald ripening phenomenon, leading to coarse grains. As observed in the previous paragraph, contrary to conventional thin film deposition, inkjet-printing technology enables the fabrication of patterned and non-textured thin films. While sintering tends to be impeded by coarse grain due to the annihilation of grain boundaries as diffusion channels (see Chapter 2 part I-B), grain growth is boosted by the high coherency of grains with similar crystalline orientation (see Chapter 2 part I-C). Crystallographic texture of polycrystalline films thus indirectly affects both electrical and mechanical properties of such films. These correlations will be addressed in the next sections. For some specific applications, it could be interesting to take advantage of the high elastic anisotropy of silver (anisotropy coefficient of 3) to control the stiffness of printed films and the electrical behavior. This can be performed by controlling the crystallographic texture of nanoparticulate films through process parameters.

Since silver nanoparticles are randomly disposed on the substrate during the printing step, nanoparticles do not exhibit any preferential orientation. In order to develop a specific crystallographic texture, the grain growth of this given orientation has to be amplified both kinetically and energetically. We suggest in this work to boost the growth of specific grains, for example {111} grains because of their higher energetic stability, by purposely inserting {111} nuclei in the printed layer. Preliminary experiments of this study concentrated on providing a high number of {111} grains to feed the transfer process.

As mentioned in the introduction to this section, PVD deposition is known for inducing preferential orientation of thin films [44, 45]. Introduction of {111} grains can thus be performed by depositing a thin layer by thermal evaporation prior to nanoparticle deposition. A 200 nm-thick gold layer was evaporated on a titanium-coated silicon wafer (see Figure II-39). The titanium layer, whose thickness is set at 50 nm, acts both as a diffusion barrier between gold and silicon and as an adhesion-promoter layer. Deposition of the bilayer was carried out at nominal room temperature leading to the development of a <111> fiber texture as expected from [75].

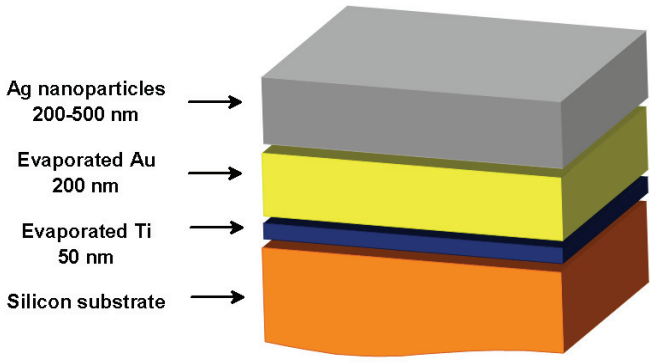

Figure II-39: Structure of stacked layers with the inkjet-printed silver layer on top of a {111}-textured gold thin film prepared by thermal evaporation.

The gold element was chosen for the seed layer because the high interdiffusion coefficient of gold with silver ($D = 4 \cdot 10^{-16}$ cm²·s⁻¹ at 300 °C) [76] guaranties a perfect compatibility for the texture transfer. This compatibility is strengthened by the total miscibility of both species, as shown by the binary diagram in Figure II-40, originating from the similar electronic and lattice structure. Indeed, silver and gold are transition metals from group 10 that both crystallize in a FCC unit cell with a lattice parameter of 4.86 Å and 5.06 Å respectively.

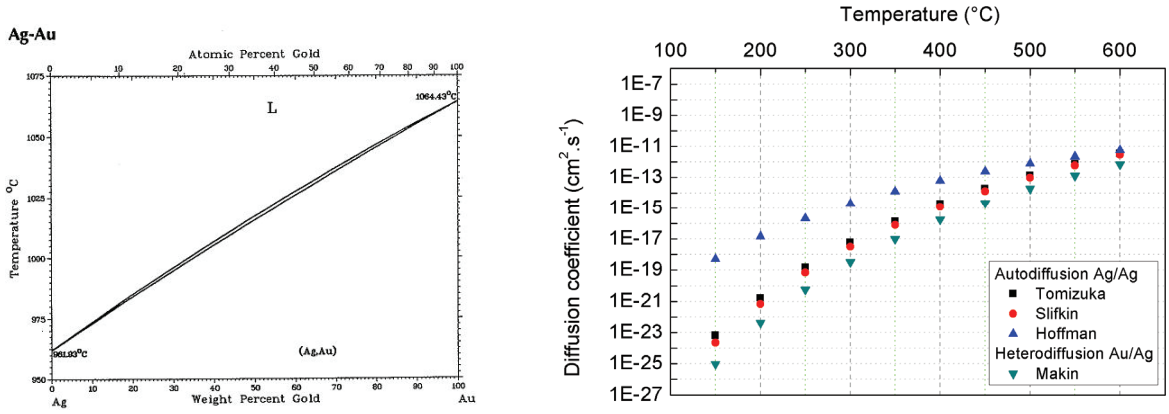

Figure II-40: Binary diagram of gold-silver system (left) [77] and their relative diffusion coefficients (right) [78-80].

The mixing of the silver/gold system was verified by Electron Dispersive X-ray (EDX) analysis performed on thin film cross sections after curing at 300 °C and 500 °C (see Figure II-42 and Figure II-43). The progression of gold in silver – particularly visible between these two conditions – is related to the speed of interdiffusion which varies exponentially with the temperature.

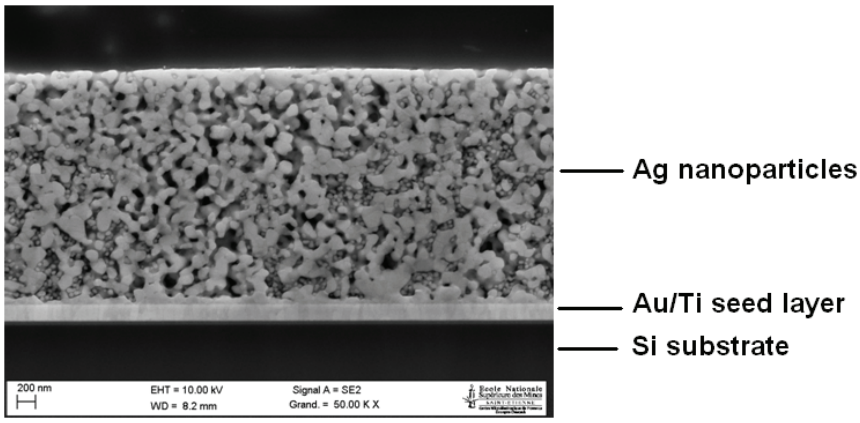

Figure II-41: SEM image of the Ag/Au/Ti/Si film cross section obtained by ion polishing after curing at 300 °C. The difference of microstructure between the silver nanoparticles layer (top) and the textured underlying gold layer (bottom) should be noted.

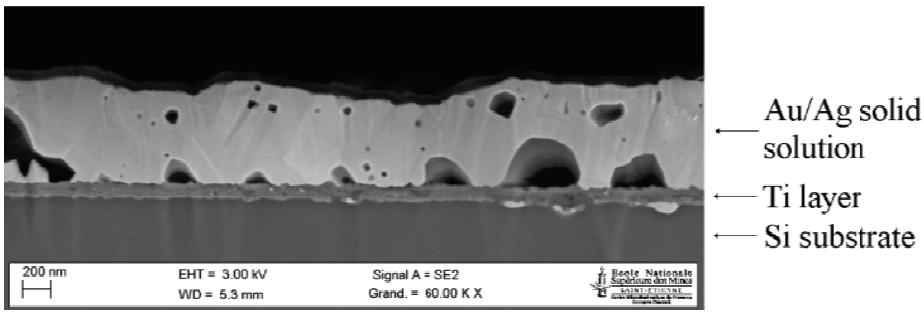

Figure II-42: SEM image of the Ag/Au/Ti/Si film cross section obtained by ion polishing after curing at 500 °C. The presence of traversing grains should be noted in comparison to the previous porous state.

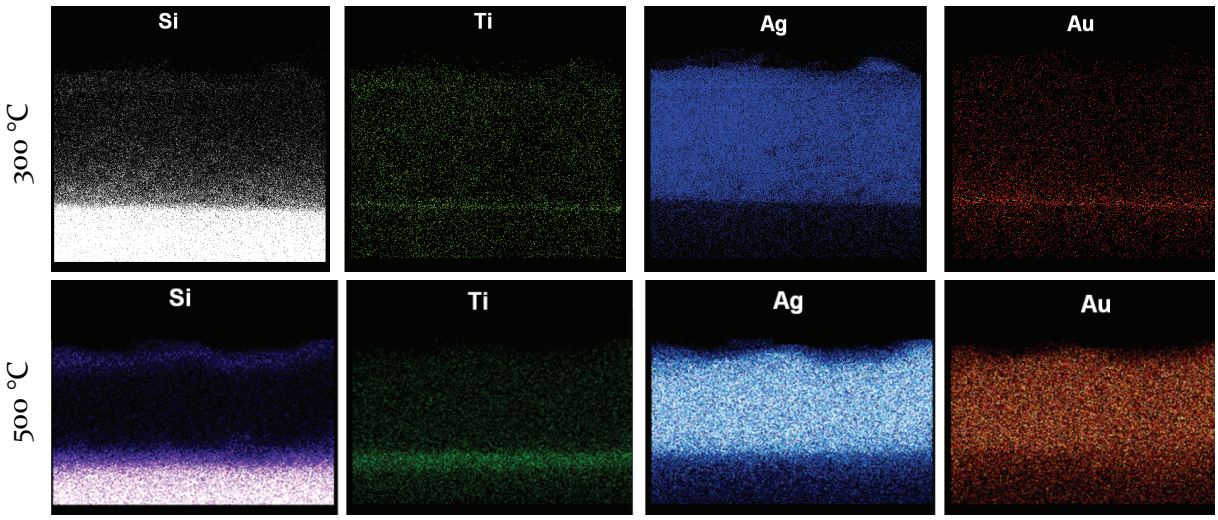

Figure II-43: EDX mapping of Kα1 of Si and Ti, Lα1 of Ag and Mα1 of Au after curing at 300 °C (top) and 500 °C (bottom).

Since normal and abnormal grain growths are thermally activated, impact of the sintering temperature has been analyzed through EBSD measurements. The additive effect of the textured underlying layer was considered through comparison between the stacked layers presented in Figure II-39 and silver nanoparticles printed on an amorphous substrate of silicon nitride. The crystallographic texture is monitored via the orientation maps of inkjet-printed silver thin films (see Figure II-44).

Figure II-45 displays the pole figures of sintered silver nanoparticles on amorphous silicon nitride and on gold. On silicon nitride substrate, the activation energy for {111} texturation is achieved at 500°C when one pole of the {111} grains is emerging (red spot at the pole figure center). However, for silver nanoparticles being sintered on textured gold substrate, this activation energy is reached as low as 300°C because of the driving energy supplied by out-of-plane interdiffusion of gold into silver. By further increasing the sintering temperature, the fiber texture is totally marked at 500 °C (see Figure II-45.h). Through the deposition of a textured layer before the inkjet printing step, a texture transfer has thus been carried out and the grain growth has been enhanced in a large extent as indicated by the presence of traversing grains in Figure II-42.

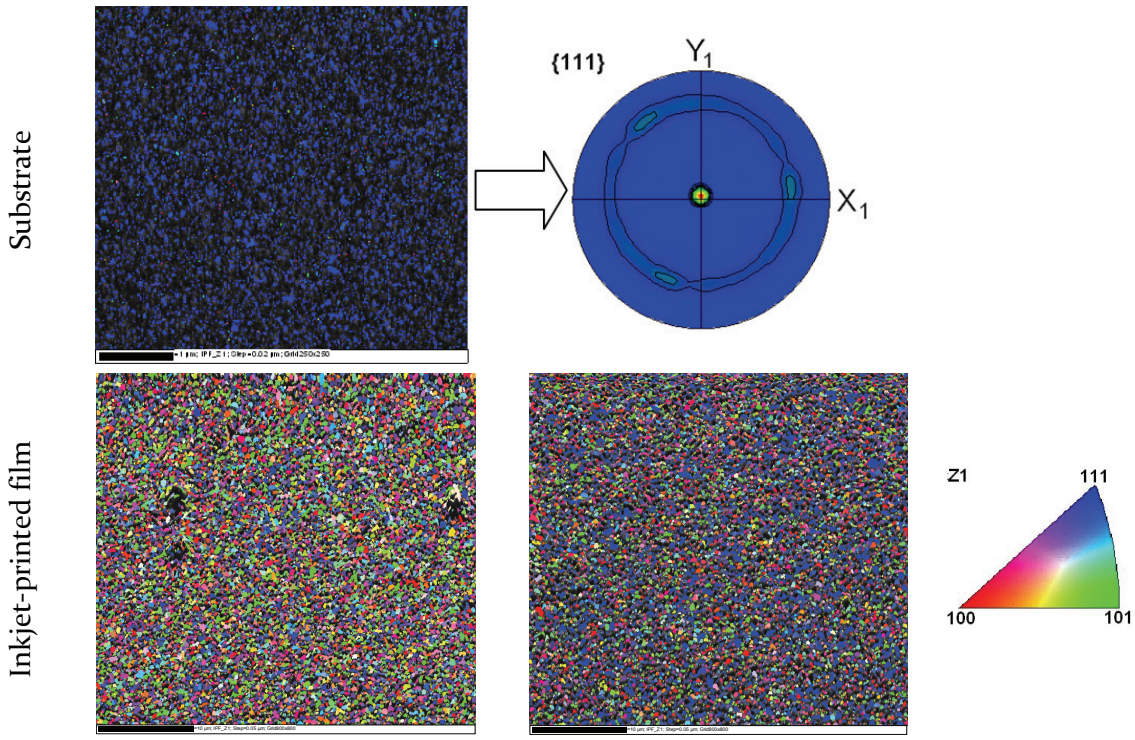

Figure II-44: Orientation maps performed on the initial gold substrate surface (top) and on silver nanoparticles films after curing at 500 °C on a silicon substrate (bottom left) and on a gold substrate (bottom right). Scale bar = 10 µm.

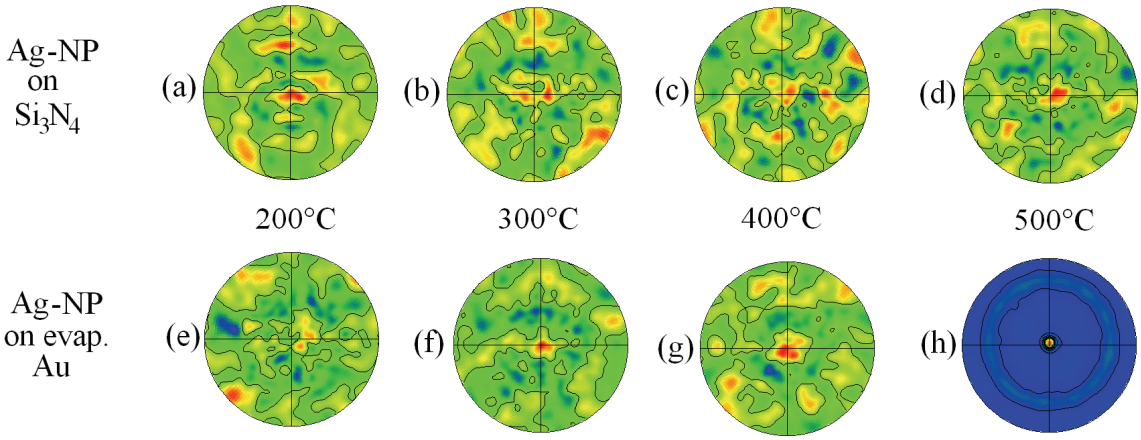

Figure II-45: {111}-pole figures of inkjet-printed silver nanoparticles film on a silicon nitride substrate (a-d) and on {111} evaporated gold substrate (e-h) sintered at 200°C (a, e), 300°C (b, f), 400°C (c, g) and 500°C (d, h) for 15 min with a ramp of 10°C/s under N_2 atmosphere.

A comparative texture analysis was performed by X-ray diffraction on silver thin films printed on silicon nitride and on gold substrates. The qualitative measurements with standard resolution were performed in situ during the heating step. Given that XRD penetrates throughout the thickness, the signal related to the gold substrate is over-dominant in diffractograms. Since the evaporated gold presents a huge {111}-fiber texture, the

{111} peak is very intense. Evolutions of the {111} and {200} peaks with temperature are reported for both cases in Figure II-46. Since {111} and {200} grains are more stable energetically, it is believed that any preferential orientation will be achieved according to one of these directions. The higher the sintering temperature is, the higher the peak intensity will be. This increase of peak intensities are linked with a peak sharpening indicating a convergence of grain orientation around the {111} and {200} orientations, thus confirming the results of EBSD analyses.

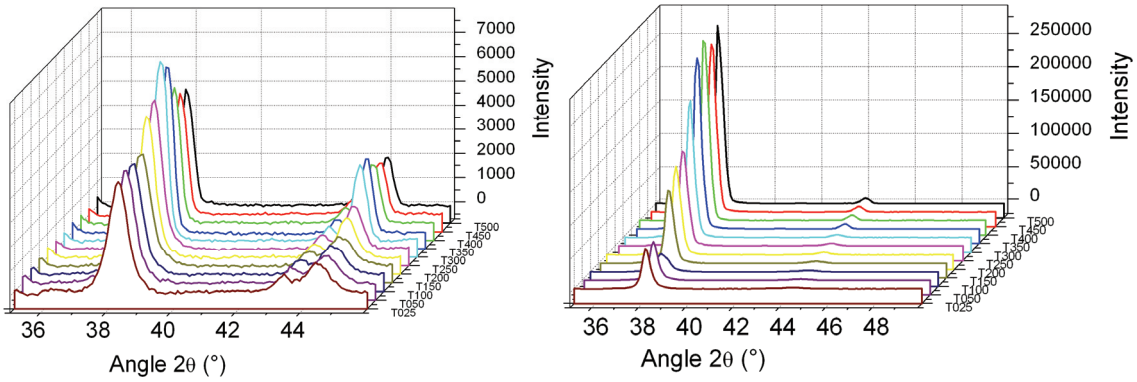

Figure II-46: Diffractograms of silver thin films centered on (111) and (200) peaks, respectively around 2θ=38 and 2θ=45°, on both silicon nitride (left) and gold substrates (right).

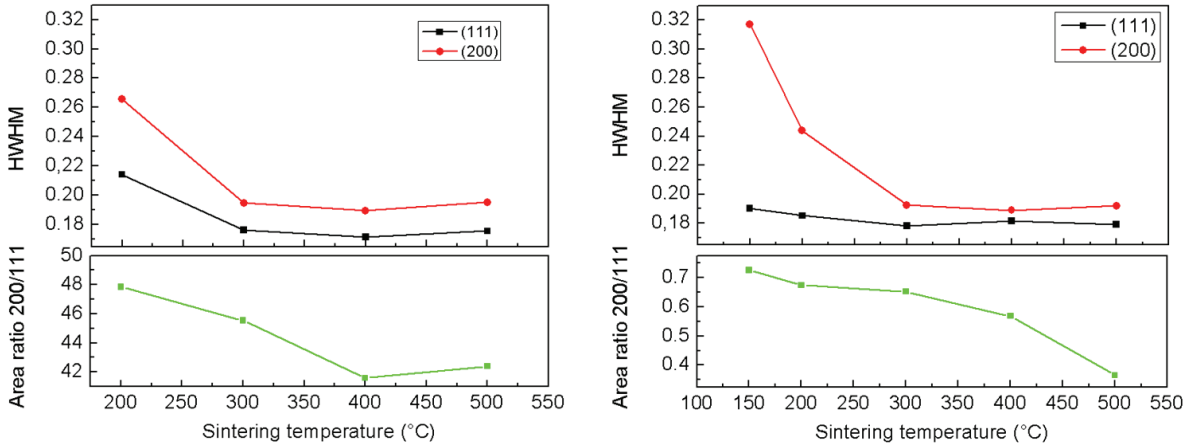

Figure II-47: Half-width at half-maximum values of (111) and (200) peaks with the ratio of their respective area for both silicon nitride (left) and gold substrates (right).

Further investigation has been performed to assess the peak broadening and the ratio of peak area. Peak broadening is mainly impacted by the local microstrain state and the average size of crystallites whose orientation is generally comprised within 10° around the crystallographic direction. As depicted in Figure II-47, on both substrates, a sharpening of {111} and {200} peaks is observed indicating a recovery/recrystallization phenomenon that stabilizes from 300 °C. This phenomenon tends to impact the {200} grains to a larger extent.

In addition, referring to the surface area ratio of the {200} to the {111} peak, results indicates a diminution of the {200}-grains population to the benefit of {111} grains. These observations argue in favor of a sintering driven by a minimization of surface/interface energy which is more favorable to {111} orientations.

It is believed that the observed texture transfer originates either from a preferential {111} grain growth of silver nanoparticles during sintering or a columnar growth from the PVD gold toward the silver surface. To elucidate the underlying mechanism of texture transfer, an additional characterization was performed on samples with various thicknesses. For each sample, an EBSD orientation map was performed on approximately 2900 to 3900 grains. Results indicate that for very thin films a strong {111} fiber texture is observable. This texture is progressively inhibited with increasing thicknesses (see Figure II-48). Consequently, thin films with a thickness above 1 µm don't exhibit any preferential orientation on the surface. Our result is consistent with the limit value of 1.5 µm specified by Greiser [40]. During the sintering process, {111} grain matrix tends to stagnate at the benefit of {100} grain growth related to an abnormal grain growth phenomenon.

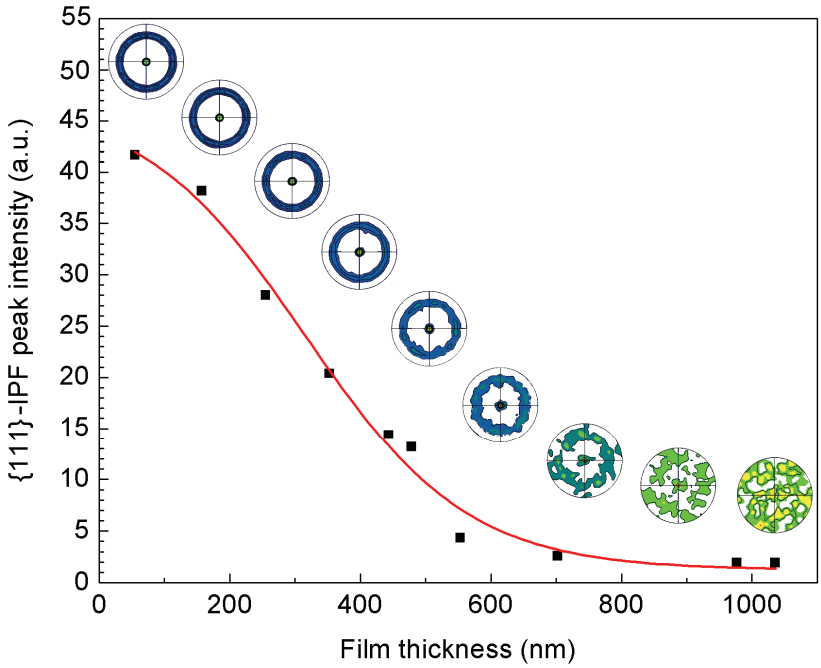

Figure II-48: Variation of the {111} pole intensity with the film thickness as observed from the {111} inverse pole figures where the fiber texture vanishes.

This texture transfer is obviously dependant on the temperature and the thickness of the film. The first and most obvious reason is linked to the sintering time during which the sample is thermally cured. Indeed, the thicker the silver layer, the higher the distance to cover for the diffusional atoms. Another contribution originates from the internal stress

which is even higher whenthe thickness is very low. As a consequence, decreasing the silver thickness will tend to improve the texture transfer by assisting the interdiffusion phenomenon.

To further decrease the interdiffusion initiation temperature between textured substrate and nanoparticles-based thin films, one approach would consist in reducing those nanoparticles size to few nanometers. Indeed, as previously explained, a nanoparticle diameter shrink entails a decrease of the sintering temperature because of their increased surface to volume ratio.

Chapter conclusions

In this chapter, microstructure evolution of inkjet-printed silver thin film during thermal curing has been addressed. The main diffusion mechanisms which sustain the coalescence and growth have been presented. While mainly focusing on micron-sized particles for industrial applications, the sintering community has become more and more interested in nano-sized particles which raise a new conundrum to researchers. The thermodynamic size effect of nanoparticles has been a source of many hypotheses and misunderstanding amongst non specialists, notably on the melting temperature of such objects.

If nanoparticle sintering is a brand new and emerging technique that is of particular interest for electronic applications, working at the atomic scale remains a very hard topic given all the interactions and quantum effects at stake. Given the complexity of the sintering phenomenon for nanoparticles, only the physical principles in the frame of the continuum model theory have been presented. Even though new models and simulation techniques are emerging and enlighten progressively the understanding of previous experimental results, still a lot of work has to be done. In this matter, atomic scale simulations through molecular dynamics give very promising results in predicting the microstructure evolution.

A particular interest has been the grain size assessment and crystallographic texture measurement. Electron back-scattered diffraction and X-ray diffraction were employed as complimentary characterizations tools for very fine grains. The analysis of process parameter impact on microstructure enabled the suggestion of an original approach to transfer a texture to nanoparticulate thin films. If this approach proved to be successful in the case of thermodynamically favored crystalline orientation, such as {111} grains, it appeared harder to transfer a {110} texture for instance.

In the next chapter, the influence of the average grain size will be put in perspective with mechanical and electrical behaviors of inkjet-printed silver lines. Transmission of radio-frequence signals will thus be addressed as correlation with the pore density. Efficient line reinforcement to increase the hardness of printed deposits will eventually be emphasized in order to fabricate electronic packages fully compatible with conventional interconnection technologies such as wire-bonding or the flip-chip process.

References

[1] W. P. Halperin, "Quantum size effects in metal particles," *Reviews of Modern Physics*, vol. 58, pp. 533–606, 1986.

[2] C. Dupas and P. Houdy, *Nanoscience: nanotechnologies and nanophysics*. Springer, 2007.

[3] M. F. Ashby, P. J. S. G. Ferreira, and D. L. Schodek, *Nanomaterials, nanotechnologies and design: an introduction for engineers and architects*. Butterworth-Heinemann, 2009.

[4] W. H. Qi, "Size effect on melting temperature of nanosolids," *Physica B*, vol. 368, pp. 46–50, 2005.

[5] K. K. Nanda, A. Maisels, F. E. Kruis, H. Fissan, and S. Stappert, "Higher surface energy of free nanoparticles," *Physical Review Letters*, vol. 91, pp. 106102–, 2003.

[6] R. M. German, *Sintering Theory and Practice*. Wiley-Interscience, 1996.

[7] Z. Fang, *Sintering of Advanced Materials*. Woodhead Publishing, 2010.

[8] P. Buffat and J.-P. Borel, "Size effect on the melting temperature of gold particles," *Physical Review B*, vol. 13, pp. 2287–2298, 1976.

[9] P. Pawlow, "The dependency of melting point on the surface energy of a solid body," *Zeitschrift für Physikalische Chemie*, vol. 65, p. 545, 1909.

[10] K. J. Hanszen, "Theoretische untersuchungen über den schmelzpunkt kleiner kügelchen," *Zeitschrift für Physik A Hadrons and Nuclei*, vol. 157, no. 5, pp. 523–553, 1960.

[11] C. R. M. Wronski, "The size dependence of the melting point of small particles of tin," 1967.

[12] J. R. Sambles, *A study of the evaporation of small particles in the electron microscope*. PhD thesis, University of London, 1970.

[13] P. R. Couchman and W. A. Jesser, "Thermodynamic theory of size dependence of melting temperature in metals," *Nature*, vol. 269, pp. 481–483, 1977.

[14] G. Guisbiers, O. Van Overschelde, and M. Wautelet, "Nanoparticulate origin of intrinsic residual stress in thin films," *Acta Materialia*, vol. 55, pp. 3541–3546, 2007.

[15] T. Castro, R. Reifenberger, E. Choi, and R. P. Andres, "Size-dependent melting temperature of individual nanometer-sized metallic clusters," *Physical Review B*, vol. 42, pp. 8548–8556, 1990.

[16] M. Wautelet, "Estimation of the variation of the melting temperature with the size of small particles, on the basis of a surface-phonon instability model," *Journal of Physics D: Applied Physics*, vol. 24, no. 3, p. 343, 1991.

[17] Q. Mei and K. Lu, "Melting and superheating of crystalline solids: From bulk to

nanocrystals," *Progress in Materials Science*, vol. 52, pp. 1175–1262, 2007.

[18] B. T. Anto, L.-Y. Wong, R.-Q. Png, S. Sivaramakrishnan, L.-L. Chua, and P. K. H. Ho, *Functional nanomaterials*, vol. 5 of *Handbook of nanophysics*, ch. Printable metal nanoparticle inks, pp. 2.1–2.24. CRC Press, 2011.

[19] M. Hosokawa, K. Nogi, M. Naito, and T. Yokoyama, *Nanoparticle technology handbook*. Elsevier, 2007.

[20] J. Rankin and B. W. Sheldon, "In situ TEM sintering of nano-sized ZrO_2 particles," *Materials Science and Engineering A*, vol. 204, pp. 48–53, 1995.

[21] P. Zeng, S. Zajac, P. C. Clapp, and J. A. Rifkin, "Nanoparticle sintering simulations," *Materials Science and Engineering A*, vol. 252, pp. 301–306, 1998.

[22] L. Ding, R. L. Davidchack, and J. Pan, "A molecular dynamics study of sintering between nanoparticles," *Computational Materials Science*, vol. 45, pp. 247–256, 2009.

[23] R. L. Coble, "Initial sintering of alumina and hematite," *Journal of the American Ceramic Society*, vol. 41, no. 2, pp. 55–62, 1958.

[24] S.-J. L. Kang, *Sintering: densification, grain growth, and microstructure*. Butterworth-Heinemann, 2005.

[25] M. Rahaman, *Ceramic processing and sintering*. M. Dekker, 2003.

[26] C. Herring, "Effect of change of scale on sintering phenomena," *Journal of Applied Physics*, vol. 21, no. 4, pp. 301–303, 1950.

[27] F. Swinkels and M. Ashby, "A second report on sintering diagrams," *Acta Metallurgica*, vol. 29, pp. 259–281, 1981.

[28] J. Frenkel, "Viscous flow of crystalline bodies under the action of surface tension," *Journal of Physics USSR*, vol. 9, no. 5, pp. 385–391, 1945.

[29] D. Readey, T. Quadir, and J. Lee, "Effects of vapor transport on microstructure development," in *Proceedings of the International Materials Symposium Ceramic microstructures '86* (A. Pask, J.A. ; Evans, ed.), vol. Role of interfaces, pp. 485–496, University of California, Berkeley, Plenum press, 1987.

[30] W. D. Kingery and M. Berg, "Study of the initial stages of sintering solids by viscous flow, evaporation-condensation, and self-diffusion," *Journal of Applied Physics*, vol. 26, p. 10, 1955.

[31] R. L. Coble, "Sintering crystalline solids. ii. experimental test of diffusion models in powder compacts," *Journal of Applied Physics*, vol. 32, no. 5, pp. 793–799, 1961.

[32] H. E. Exner, "Principles of single-phase sintering," *Reviews on Powder. Metallurgy and Physical Ceramics*, vol. 1, no. 1-4, pp. 7–251, 1979.

[33] W. S. Coblenz, J. M. Dynys, R. M. Cannon, and R. L. Coble, "Initial stage solid state sintering models. a critical analysis and assessment," in *Sintering Processes. Materials Science Research* (G. C. Kuczynski, ed.), vol. 13, pp. 141–157, Plenum press, 1980.

[34] A. C. F. Cocks, "Overview no. 117 the structure of constitutive laws for the sintering of fine grained materials," *Acta Metallurgica et Materialia*, vol. 42, pp. 2191–2210, 1994.

[35] A. C. Cocks, S. P. Gill, and J. Pan, "Modeling microstructure evolution in engineering materials," *Advances in Applied Mechanics*, vol. Volume 36, pp. 81–162, 1998.

[36] J. Pan, "Modelling sintering at different length scales," *International Materials Reviews*, vol. 48, no. 2, pp. 69–85, 2003.

[37] I. Lifshitz and V. Slyozov, "The kinetics of precipitation from supersaturated solid solutions," *Journal of Physics and Chemistry of Solids*, vol. 19, pp. 35–50, 1961.

[38] C. Wagner, "Theory of precipitate change by redissolution," *Zeitschrift für Elektrochemie*, vol. 65, pp. 581–591, 1961.

[39] J. E. Palmer, C. V. Thompson, and H. I. Smith, "Grain growth and grain size distributions in thin germanium films," *Journal of Applied Physics*, vol. 62, no. 6, p. 2492, 1987.

[40] J. Greiser, P. Müllner, and E. Arzt, "Abnormal growth of "giant" grains in silver thin films," *Acta Materialia*, vol. 49, pp. 1041–1050, 2001.

[41] C. Thompson, H. Frost, and F. Spaepen, "The relative rates of secondary and normal grain growth," *Acta Metallurgica*, vol. 35, pp. 887–890, 1987.

[42] H. Frost, C. Thompson, and D. Walton, "Simulation of thin film grain structures - ii. abnormal grain growth," *Acta Metallurgica et Materialia*, vol. 40, pp. 779–793, 1992.

[43] L. Vitos, A. Ruban, H. Skriver, and J. Kollar, "The surface energy of metals," *Surface Science*, vol. 411, pp. 186–202, 1998.

[44] M. Seita, C. M. Pecnik, S. Frank, and R. Spolenak, "Direct evidence for stress-induced texture evolution and grain growth of silver thin films upon thermal treatment and self-ion bombardment," *Acta Materialia*, vol. 58, pp. 6513–6525, 2010.

[45] C. V. Thompson and R. Carel, "Texture development in polycrystalline thin films," *Materials Science and Engineering B*, vol. 32, pp. 211–219, 1995.

[46] E. Abbe, "Beiträge zur theorie des mikroskops und der mikroskopischen wahrnehmung," *Archiv für Mikroskopische Anatomie*, vol. 9, no. 1, pp. 413–418–418, 1873.

[47] W. Rasband, "ImageJ," U. S. National Institutes of Health, 1997-2011.

[48] R. Pecora, "Dynamic light scattering measurement of nanometer particles in liquids," *Journal of Nanoparticle Research*, vol. 2, no. 2, pp. 123–131–131, 2000.

[49] H. Suzuki and C. Barrett, "Deformation twinning in silver-gold alloys," *Acta Metallurgica*, vol. 6, pp. 156–165, 1958.

[50] A. Art and A. Ponslet, "Macles de croissance dans les cristaux d'argent des couches minces," *Journal de Physique Supplément Physique Appliquée*, vol. 21, no. S7, pp. 134–136, 1960.

[51] S. Kibey, J. Liu, D. Johnson, and H. Sehitoglu, "Predicting twinning stress in fcc metals: Linking twin-energy pathways to twin nucleation," *Acta Materialia*, vol. 55, pp. 6843–

6851, 2007.

[52] D. Drouin, A. R. Couture, D. Joly, X. Tastet, V. Aimez, and R. Gauvin, "Casino v2.42 - a fast and easy-to-use modeling tool for scanning electron microscopy and microanalysis users," *Scanning*, vol. 29, no. 3, pp. 92–101, 2007.

[53] K. Kanaya and H. Kawakatsu, "Secondary electron emission due to primary and backscattered electrons," *Journal of Physics D: Applied Physics*, vol. 5, no. 9, pp. 1727–, 1972.

[54] D. B. Knorr and D. P. Tracy, "A review of microstructure in vapor deposited copper thin films," *Materials Chemistry and Physics*, vol. 41, no. 3, pp. 206–216, 1995.

[55] I. Petrov, P. B. Barna, L. Hultman, and J. E. Greene, "Microstructural evolution during film growth," *Journal of Vacuum Science & Technology A*, vol. 21, no. 5, pp. S117–S128, 2003.

[56] S.-J. Hwang, H. Park, J.-H. Lee, K. H. Oh, and Y.-C. Joo, "Evolutions of surface morphologies in sputtered and electroplated Cu films during thermal cycling," *Materials Science Forum*, vol. 408-412, pp. 1651–1666, 2002.

[57] H. Lee, S. S. Wong, and S. D. Lopatin, "Correlation of stress and texture evolution during self- and thermal annealing of electroplated cu films," *Journal of Applied Physics*, vol. 93, pp. 3796–3804, 2003.

[58] B. Sundquist, "A direct determination of the anisotropy of the surface free energy of solid gold, silver, copper, nickel, and alpha and gamma iron," *Acta Metallurgica*, vol. 12, pp. 67–86, 1964.

[59] W. Winterbottom and N. Gjostein, "Determination of the anisotropy of surface energy of metals–ii: Experimental [gamma]-plot of gold," *Acta Metallurgica*, vol. 14, no. 9, pp. 1041–1052, 1966.

[60] T. R. Malow and C. C. Koch, "Grain growth in nanocrystalline iron prepared by mechanical attrition," *Acta Materialia*, vol. 45, no. 5, pp. 2177–2186, 1997.

[61] F. Humphreys and M. Hatherly, *Recrystallization and Related Annealing Phenomena*. Pergamon, 2nd revised edition ed., 2004.

[62] R. Dannenberg, E. Stach, J. R. Groza, and B. J. Dresser, "TEM annealing study of normal grain growth in silver thin films," *Thin Solid Films*, vol. 379, pp. 133–138, 2000.

[63] C. V. Thompson, "Grain growth in thin films," *Annual Review of Materials Science*, vol. 20, pp. 245–268, 1990.

[64] R. Dannenberg, E. A. Stach, J. R. Groza, and B. J. Dresser, "In-situ TEM observations of abnormal grain growth, coarsening, and substrate de-wetting in nanocrystalline Ag thin films," *Thin Solid Films*, vol. 370, pp. 54–62, 2000.

[65] R. Hummel and H. Geier, "Activation energy for electrotransport in thin silver and gold films," *Thin Solid Films*, vol. 25, pp. 335–342, 1975.

[66] A. Guinier, *X-ray diffraction in crystals, imperfect crystals, and amorphous bodies*.

Dover, 1994.

[67] B. E. Warren, "X-ray diffraction in random layer lattices," *Physical Review*, vol. 59, no. 9, pp. 693–698, 1941.

[68] G. K. Williamson and W. H. Hall, "X-ray line broadening from filed aluminium and wolfram," *Acta Metallurgica*, vol. 1, no. 1, pp. 22–31, 1953.

[69] B. Warren, *X-ray diffraction*. Dover Publications, 1990.

[70] T. P. Martin, "Shells of atoms," *Physics Reports*, vol. 273, no. 4, pp. 199–241, 1996.

[71] A. S. Barnard, "A thermodynamic model for the shape and stability of twinned nanostructures," *Journal of Physical Chemistry B*, vol. 110, pp. 24498–24504, 2006.

[72] B. E. Warren and B. L. Averbach, "The effect of cold-work distortion on x-ray patterns," *Journal of Applied Physics*, vol. 21, no. 6, pp. 595–599, 1950.

[73] A. R. Stokes, "A numerical fourier-analysis method for the correction of widths and shapes of lines on x-ray powder photographs," *Proceedings of the Physical Society*, vol. 61, no. 4, pp. 382–, 1948.

[74] C. V. Thompson, "Secondary grain growth in thin films of semiconductors: Theoretical aspects," *Journal of Applied Physics*, vol. 58, no. 2, pp. 763–, 1985.

[75] Y. Zeng, Y. L. Zou, and T. L. Alford, "Texture in evaporated Ag thin films and its evolution during encapsulation process," *Thin Solid Films*, vol. 307, pp. 89–95, 1997.

[76] A. Bukaluk, "Analysis of diffusion mechanisms in thin polycrystalline Au-Ag films using auger electron spectroscopy," *Surface and Interface Analysis*, vol. 5, no. 1, pp. 20–27, 1983.

[77] H. Okamoto and T. B. Massalski, "The Ag-Au (silver-gold) system," *Journal of Phase Equilibria*, vol. 4, no. 1, pp. 30–38, 1983.

[78] L. Slifkin, D. Lazarus, and T. Tomizuka, "Self-diffusion in pure polycrystalline silver," *Journal of Applied Physics*, vol. 23, pp. 1032–1034, 1952.

[79] C. T. Tomizuka and E. Sonder, "Self-diffusion in silver," *Physical Review*, vol. 103, pp. 1182–1184, 1956.

[80] R. E. Hoffman and D. Turnbull, "Lattice and grain boundary self-diffusion in silver," *Journal of Applied Physics*, vol. 22, no. 5, pp. 634–639, 1951.

3

Fabrication of inkjet-printed interconnects for electronic packaging

Introduction

In the previous chapter, the microstructure dependency to sintering conditions was investigated. Evolution of grain size which characterizes the sintering process was notably determined from a morphological approach in a SEM Electron BackScattered Diffraction and from X-ray diffraction. It has thus been shown that conditions supporting grain growth such as interdiffusion-assisted sintering or fast sintering ramps led to denser films with lower proportion of porosity.

In this chapter, microstructural evolution will be correlated to macroscopic variable such as mechanical and electrical properties. As mentioned in the general introduction, since final applications include application for flash products, both direct current and radio-frequency behavior will be addressed.

I. Mechanical characterization of printed thin films

Mechanical characterization of thin films can be performed by a wide range of methods: 3- or 4-point flexural bending test, bulge testing, substrate curvature measurement, microsystem bending, nanoindentation, raman microspectroscopy or X-ray diffraction for example [1-4]. Our goal here is not to develop an extensive study of mechanical properties of nanoparticulate films using each and every existing method. Taking precaution is required when determining mechanical properties of a complex polycrystalline thin film with porosities. Therefore, the consolidation of extracted data by at least two methods is compelling. In this study, nanoindentation was chosen as a preferential approach to determine mechanical properties of printed silver films. This technique is relatively commonplace for thin film characterization [5-8]. Given that the indenter tip has a defined radius of curvature which can easily interact with pore observed previously, the bulge test technique was employed as an additional measurement. Residual and internal stress analysis will also be carried out with X-ray diffraction.

A. Determination of printed silver thin film Young's modulus

i. Contribution of nanoindentation

Great strides have been made in the last two decades of the twentieth century to adapt the traditional indentation techniques, such as Brinell or Vickers hardness tests, to thin films. This has been achieved by developing apparatus capable of applying small loads (in the range of several millinewtons) and continuously measuring the penetration depth of the tip into

the film whose typical experimental resolution has to be below the nanometer range (taking into account the noise effect). Since the indenter tip geometry is well known, the contact area can be determined at each position by the penetration depth and the known angle or radius of the indenter.

In this study, measurements were performed on a Nano Indenter XP™ apparatus from MTS Nano Innovation Center, with a Berkovich indenter tip (see Figure III-1). The radius of curvature of the diamond tip is in the order of 20 nm. The instrument was operated in the Continuous Stiffness Mode (CSM) and the indentations were made using a constant nominal strain rate ($\dot{P}/P$) of 0.05 s^{-1}.

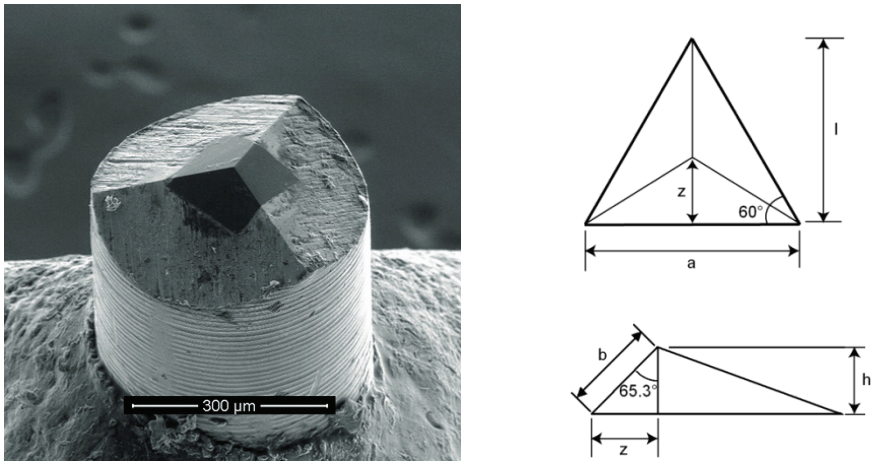

Figure III-1: SEM image (left, reproduced from University of Nebraska-Lincoln) and projected area of a Berkovich tip.

Experiments are performed according the Oliver-Pharr data analysis procedure [9] which consists in calculating the contact stiffness S from the slope of the initial portion of the elastic unloading curve. It is achieved by differentiating the load at the maximum depth of penetration during the unloading part of CSM oscillations (see Equation (III-1) and Figure III-2).

$$S = \left.\frac{dP}{dh}\right|_{h=h_{max}} = 2\beta\sqrt{\frac{A_c}{\pi}}E_r \qquad \text{(III-1)}$$

where β is a constant depending on the indenter geometry (β=1.034 for a Berkovich tip), E_r is the reduced elastic modulus (*i.e.* the measured modulus) and A_c is the projected contact area defined by [10]:

$$A_c = \sum_{n=0}^{8} C_n \left(h_c + \xi + h_p\right)^{1-n} \quad \text{(III-2)}$$

with

$$C_0 = 3\sqrt{3}\tan^2\theta \approx 24.494 \quad \text{(III-3)}$$

where h_c is the contact depth, $C_{1\text{-}8}$ are constants, ξ is the blunting distance, h_p is the pile-up height and θ is the half-angle of the Berkovich tip (θ=65.27°) [11].

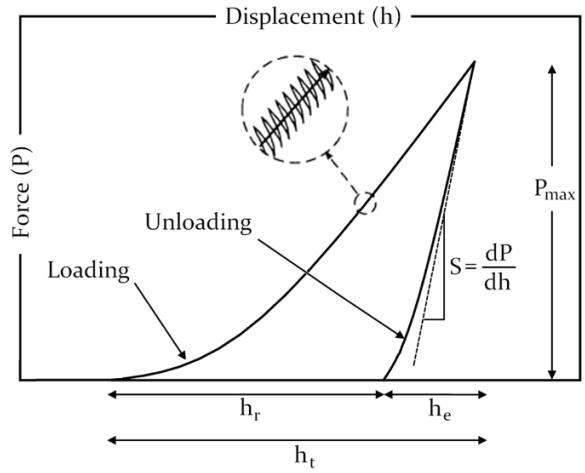

Figure III-2: Typical load-displacement curve for an elastic plastic solid.

Since indentation is a mechanical interaction between the sample surface and the tip edge, the reduced elastic modulus E_r can be expressed in terms of the elastic properties of the indenter (E_i, ν_i) and the indented material (E_{im}, ν_{im}) from the Hertz theory [12]:

$$\frac{1}{E_r} = \frac{1-\nu_i^2}{E_i} + \frac{1-\nu_{im}^2}{E_{im}} \quad \text{(III-4)}$$

Elastic constants for the diamond indenter we used are E_i = 1141 GPa and ν_i = 0.07 [62]. This standard method was initially developed for bulk materials and doesn't apply to film-on-substrate systems. To get free from the substrate influence on the measure, the common rule of thumb is to consider an indentation depth lower than 10 % of the film thickness [9]. This approach is difficult to apply when considering very thin films, *i.e.* for samples with a thickness below the micron. The discrepancy is far more obvious when the mismatch between both film and substrate is significant. Many authors have suggested their own interpretation and model for submicron films composition lying anywhere between soft-on-hard to hard-on-soft systems. Amongst the most commonly used, one can mention the models from Doerner and Nix [5], King modified [14, 15], Gao [16] and Bec [17].

Bec *et al.* [17] developed an approach for film/substrate systems based on a model with two springs in series. This model appeared to be the most appropriate to fit our data compared to the models of Doerner-Nix, King and Gao. The main benefit of their model is to not depend on an adjustable fitting parameter (see Equation (III-5)). This model is all the more efficient that the reduced modulus of the film is smaller than the substrate's one. The reduced elastic modulus of the system, E_r, is given as a function of the contact area A_c and of the respective reduced modulus of the silicon substrate E_s and silver thin film E_f according to:

$$\frac{1}{E_r} = \frac{1-\nu_i^2}{E_i} + \frac{2\sqrt{A_c}(1-\nu^2)}{\sqrt{\pi}+\frac{2t}{\sqrt{A_c}}}\left(\frac{t}{E_f A_c} + \frac{\sqrt{\pi}}{2E_s\sqrt{A_c}}\right) \qquad \text{(III-5)}$$

During our experiments, nanoindentation tests have been conducted on inkjet-printed silver nanoparticles deposited on a silicon substrate and sintered in a RTA oven at several temperatures comprised between 130 °C and 800 °C during 15 min. The typical thickness of those films was comprised between 800 and 1000 nm. Impact of the thermal ramp on load-displacement curves is shown in Figure III-3. Experiments are conducted through a batch of 64 nanoindentations separated by 50 µm on each sample. Tests exhibiting pop-in/pop-out events were dispelled from the batch since they are believed to originate from an indentation test localized in a valley or a larger porosity, and therefore giving false information on the film.

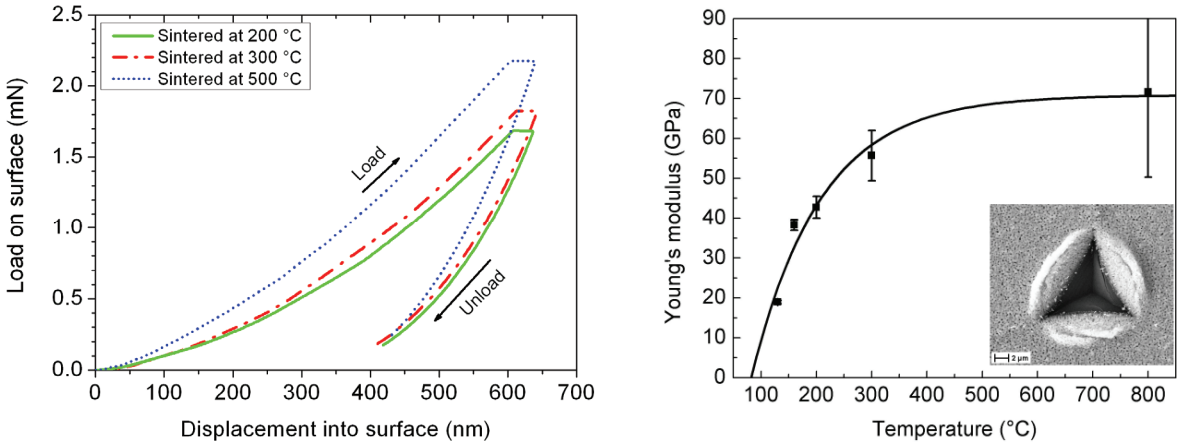

(a) (b)

Figure III-3: Load-displacement curves of printed silver nanoparticles on a silicon substrate (left) and the evolution of the extracted Young's modulus as a function of sintering temperature (right). An indent performed on inkjet-printed silver film sintered at 400 °C is depicted in inset view.

Nanonindentation measurements were performed on printed silver samples and the mechanical properties of the film at different sintering temperatures are plotted in Figure III-3-b. The Young's modulus is increasing with temperature until reaching an asymptotic value

around 72 ± 20 GPa (see Figure III-3-b). The dispersion of the nanoindentation curves significantly increases as the sintering temperature augments indicating that the thin film is not uniform as a consequence of the sintering and grain growth phenomena. Since porosities are more localized after a high temperature treatment, the dispersion of the nanoindentation measurement is quite large between dense and porous zones, especially at 800 °C (see Figure III-3-b). Conversely, when the sintering temperature is limited below 300 °C, the porosity fraction is more important but equally distributed on the surface so that each nanoindent is probing several grains and pores at each iteration. Porosity indeed affects the mechanical stiffness of the film by decreasing the value of the effective Young's modulus. While the bulk value of silver Young's modulus is referenced at 83 GPa, it is believed that the inkjet-printed film tend to reach a bulk state near the melting point at 800 °C. At such temperature, the porosity fraction is indeed very low (see previous chapter). Conversely, at low temperature, the Young's modulus is very low – around 19 ± 0.4 GPa at 130 °C – which is correlated to a higher proportion of porosity within the printed film. A simple law of mixture between silver and pores, whose stiffness is zero, would explain the decrease of the stiffness with a high porosity density.

The measurement of hardness on thin films is all the more complex that during the indentation of ductile metals as silver, the small volume under contact is deformed plastically. The deformation field is usually assumed to evolve radially in a hemispherical zone around the indenter tip. If this plastic zone is sufficiently increased through indentation until intersecting the substrate, the measure will be affected. This phenomenon is particularly observable in thin films and is termed as the Indentation Size Effect (ISE) [18]. The hardness measured during the nanoindentation test is then the sum of the film hardness contribution and the ISE originating from the substrate hardness and from the film surface roughness [19, 20]. Extraction of the measured hardness is thus a complex measurement which tends to overestimate the intrinsic hardness. A qualitative analysis can nonetheless be performed to assess its dependency to the sintering temperature.

The extracted value of hardness is increasing from 0.27 ± 0.03 GPa to 0.51 ± 0.4 GPa between 130 and 800 °C. Since Berkovich tip is very similar to a pyramidal tip, the true hardness measured by nanoindentation can be assimilated to a Vickers hardness and compared to previous works performed on nanocrystalline silver. Our results are lower than the previously reported hardness values of sputtered nanocrystalline silver at 1.5 GPa and 0.7 GPa for grain size of 100 nm and 400 nm, respectively [21], and 0.9 GPa for a spincoated nanoparticulate films with a grain size of 50 nm [63]. Moreover, Qin *et al.* [23] showed that the hardness of nanocrystalline silver could increase from 0.63 to 1.37 GPa when the sample density varies from 94 % to 99 %. Their results clearly indicate the dependency of the true hardness to the density and/or porosity as observed in our case. Similarly to the Young's moduli measured on our silver thin films, the hardness is very sensible to the porosity level underneath the indenter which evolves during the test as porosities are collapsing [24].

Measurement of intrinsic mechanical properties of such inhomogeneous films is thus a major issue since conventional models are not appropriate.

More generally, as demonstrated by Vlassak's group [24], the proportion of pores greatly affects mechanical properties of thin films. Even though elastic modulus, hardness and yield stress are impacted by porosity, the question regarding a hypothetical impact of porosity on the Poisson ratio is not relevant in our case. Mesarovic and Fleck have indeed shown that Poisson ratio has a minor effect on the nanoindentation results [25]. According to morphological data, our results point out that an increase of porosity fraction causes a decrease of the elastic modulus of printed films, which is consistent with results published by Fleck *et al*. deriving from a cavity expansion model [26].

Quantitative measurement of thin films porosity is very difficult since conventional methods usually involve the intrusion of fluids (gaseous or liquid) in the materials and requires a perfect knowledge of either the mass or the volume of the measured sample. An alternative method has to be used to determine the proportion of pores within the film, and thus assess the densification achieved during the curing step. Significant studies have been conducted on the effect of porosity – taken as inclusions embedded in a bulk matrix – on the mechanical properties [27, 28] but none of them consider interconnected porosity systems. A simplistic model was applied to estimate the order of magnitude of the relative density. According to the model of the cellular structure (see Figure III-4) treated by Gibson and Ashby with the assumption of an elastic deformation of the open cell porous solid [29], the Young's modulus of the nanoporous film is correlated to the bulk one through its porosity fraction [30]:

$$\frac{E_f}{E_0} = C_2\left(\frac{t}{L}\right)^4 = C_2\left(\frac{\rho_f}{\rho_0}\right)^2 = C_2(1-f)^2 \qquad \text{(III-6)}$$

where E_o and ρ_o are the Young's modulus and the density of the bulk material (E_o=83 GPa and ρ_o=1049 kg.m^{-3}), E_f and ρ_f are the Young's modulus and the density of the porous film, C2 is a geometric parameter which is equal to 1.06 for an open cell foam [29], L is the cell edge length and t is the cell wall thickness with $t \ll L$.

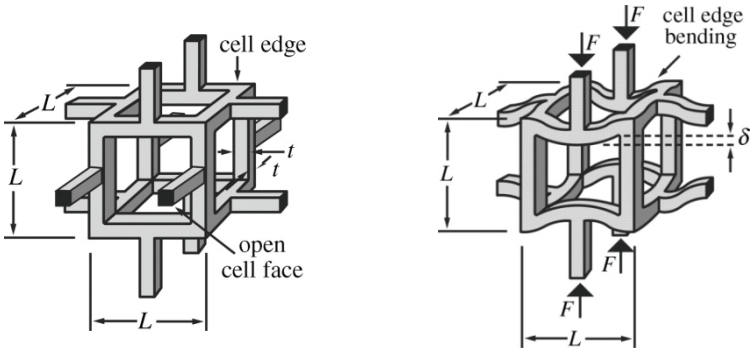

Figure III-4: Idealized cell in an open cell porous structure before and after a load application [29]

The Young's modulus of printed films on silicon determined by nanoindentation is injected in Equation (III-6). Knowing the bulk density, the approximated relative density (ratio between the film density and bulk density) is estimated between 45 and 90 % within the 130-800 °C range (see Figure III-5). The relative density is thus quickly reaching an asymptotic value which indicates that the densification dwindle above 300 °C. This result is thus with consistent with the microstructural evolution observed in Chapter 2. The stabilization of mechanical properties is occurring simultaneously with a stabilization of electrical properties as will be addressed in the next section.

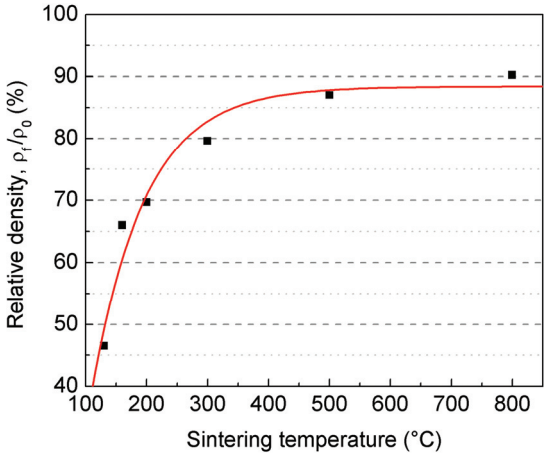

Figure III-5: Evolution of relative density with the curing temperature according to the Gibson-Ashby model. The curing was performed in RTA at 10 °C/s.

It is believed that while the porous structure model is an approximation of the film mechanical behavior, it can nonetheless be used as an estimator of the porosity fraction. Indeed, in both cases (nanoindentation and image analysis), the variation of the relative density is following the same trend. Doubts on the mechanical stiffness value is correlated with the lower confidence attributed to the Bec model for porous thin layers on soft substrates. As mentioned before, this model is indeed limited to the modeling of soft films on hard substrates. Moreover, this specific thin film has a submicron thickness and a pore size in the same order of magnitude than the indenter tip diameter. It is thus believed that during the nanoindentation test, the porous structure collapses and subsequently packs under the applied vertical load. This phenomenon could reasonably explain why the measured Young's modulus of porous layers, with relative density above 90 %, exhibits mechanical properties similar to the bulk one. Even though nanoindentation measurements seems to give accurate results for the Young's modulus and the film hardness when considering a soft-on-hard system with silicon substrate, some discrepancies have been observed when pore fraction is significant and when a flexible substrate, such as polyimide, is studied. To prove that our experimental measurements are consistent, another method which is not sensible to pore collapsing has been used to determine the Young's modulus.

ii. Contribution of bulge test

Another technique to characterize thin films is based on the behavior of a freestanding membrane under mechanical deformation: the bulge test, also known as the blister test (see Figure III-6). Firstly reported by Beams [31], the purpose of this method is to measure the deflection of a thin membrane under a differential pressure load (see Figure III-7). Indeed, the amplitude of the deflection is directly correlated to the Young's modulus E and the residual stress σ of the thin film. This technique is particularly interesting in the case of inkjet-printed film because it doesn't involve the collapsing of porosities during the bending, contrary to nanoindentation. The load-deflection characterization is indeed first performed on calibrated membranes before to be printed with the nanoparticles and consecutively cured. As a consequence of this differential measurement, the mechanical properties of the sole silver thin film can be extracted without undergoing a parasitic interaction between the indenter and nanoporosities. Measurements using the bulge techniques have been performed in collaboration with the LAAS-CNRS in Toulouse, France.

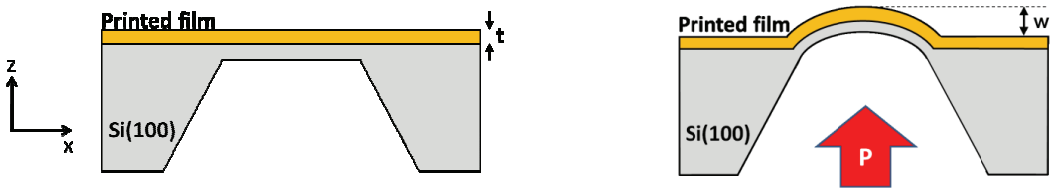

Figure III-6: Schematic principle of the bulge test before and after a differential pressure application.

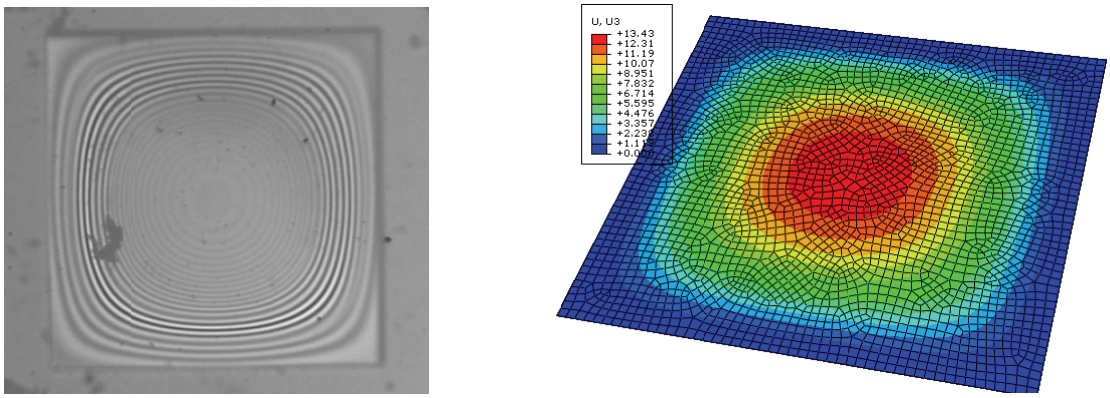

Figure III-7: The deflection observed on our inkjet-printed membrane with silver nanoparticulate film (left) and a finite element model of a square membrane deformation under a differential pressure [34].

The maximal deflection at the membrane center is commonly measured with light-interferometry. Timoshenko [32] developed an original approach in the fifties to correlate the membrane deflection under an applied pressure with mechanical properties of the membrane constitutive material. The developed approach has been further improved by

Vlassak and Nix [33]. The elastic load-deflection as well as the effect of the residual stress are both taken into account in this model where both square and rectangular membranes are considered.

The relation between the applied pressure P and the deflection w can be derived from the Hooke's law, equilibrium equations and using boundary conditions of perfectly clamped membrane. Minimizing the potential energy of the system leads to the following relation:

$$P = \left(C_1 \frac{t \cdot \sigma_0}{a^2} + + \frac{t^3 \cdot E}{12\alpha \cdot a^4 \cdot (1-\nu^2)} \right) w + C_2 \frac{t \cdot E}{a^4 \cdot (1-\nu^2)} w^3 \qquad \text{(III-7)}$$

where t is the thickness of the membrane, σ_0 is the initial residual stress, a is the half-length of the membrane, α, C_1 and C_2 are three constants related to the Poisson's ratio and membrane geometry (see Table III-1). Based on Timoshenko model, the α coefficient is taken as equal to 20.16×10^{-3} [32]. One could note that in the case of large strain ($t^2/w^2 \ll 1$), the second term of the equation associated with the free bending of the membrane is negligible. For our study, the derivation of Bonnotte will be considered for C1 and C2 [35].

Table III-1: Coefficients for a 2a side square membrane [36, 37].

C1	C2	Ref.
3.044	$\frac{\pi^6}{32(1+\nu)}\left[\frac{5}{64} + \frac{(5-3\nu)^2}{9\pi^2(\nu-9)-64(1+\nu)}\right]$	[38]
3.393	$(0.8 + 0.062\,\nu)^{-3}$	[33]
3.41	$1.981(1 - 0.295\,\nu)$	[39]
3.45	$1.994(1 - 0.271\,\nu)$	[40]
3.42	$1.91(1 - 0.207\,\nu)$	[35]

Given the important porosity in our printed layers, such a membrane could not withstand any differential pressure. Using a buffer substrate is thus mandatory to expect any deflection when applying the pressure load. Single crystal silicon membranes were fabricated from a SOI {100} wafer after several process steps of Low-Pressure Chemical Vapor Deposition (LPCVD) silicon nitride deposition, photolithography and Reactive-Ion Etching (RIE) steps. The structure of the tested membranes is presented in Figure III-8. Details of the process steps have been previously reported in literature [41, 42].

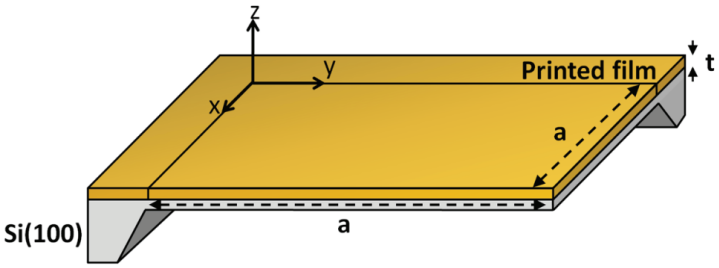

Figure III-8: Schematic structure of a freestanding membrane prepared from a SOI wafer. Only the quarter of the membrane is represented given the two perpendicular symmetry planes

A preliminary characterization of the bare silicon membrane is thus required as a calibration step. After that, silver thin film is printed above each of calibrated silicon membrane. Once sintered, the silver/silicon system membrane exhibits a greater stiffness than the silicon membrane denoted by the decrease of the maximal deflection for same applied pressures (see Figure III-9).

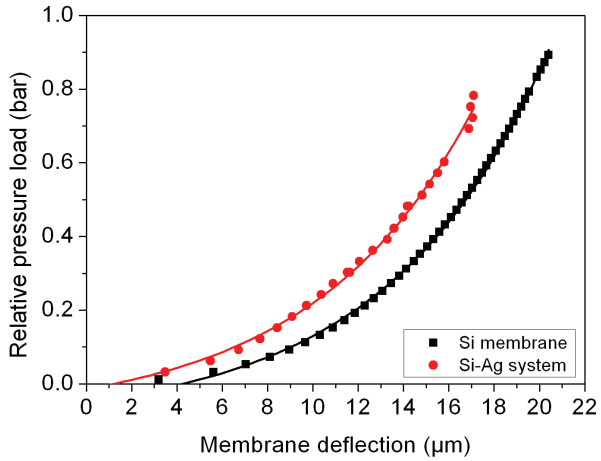

Figure III-9: Pressure-deflection curves of a silicon (black boxes) and silver/silicon system (red circles) membranes exhibiting a stiffness increase.

Considering Equation (III-7), the Young's modulus and the initial stress in the film can be calculated from the slope A and the intercept B to the origin of the coordinate system when considering the linear relation between P/w versus w^2. The values of Young's modulus and initial residual stress are thus defined as follow:

$$E = A\frac{a^4(1-\nu)}{C_2 t} \tag{III-8}$$

$$\sigma = \frac{a^2}{C_1 t}\left[B - \frac{t^3 E}{12\alpha a^4(1-\nu^2)}\right] \tag{III-9}$$

Bulge test characterization were performed on silver printed membranes sintered between 200 °C and 500 °C during 15 min, using a ramp of 10 °C/s. Results clearly points out that the Young's modulus is increasing with temperature until reaching a maximum value of 85 GPa at 500 °C (see Figure III-10). The error couldn't be determined given that only one measure was performed on each condition. A characterization of the reproducibility however agrees on a usual error of about 3 GPa. This is consistent with previous results of an improved coalescence state where porosities are merging and grains are growing toward a bulk structure.

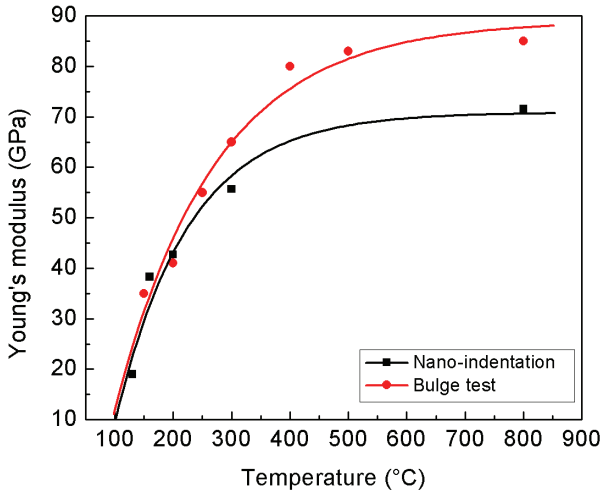

Figure III-10: Young's modulus of a film based on silver nanoparticles sintered in RTA with a ramp of 10 °C/s on a silicon membrane, determined by the bulge test technique (red dot) and nanoindentation (black box).

Comparison of Young's modulus of printed films and characterization both by nanoindentation and by the bulge test shows a good correlation especially at low temperature (see Figure III-10). The discrepancy of about 10 GPa could originate from diverse sensibility of the measurement system to the presence of porosities. Indeed, nanoindentation is sensible to the collapsing structure of nanoporous film than bulge test which tends to explain why nanoindentation underestimates the Young's modulus.

B. Internal stress in printed thin films

Induced residual stress fields rely on several factors amongst which the materials or films generation during a curing, thermo-mechanical properties, variation of microstructure, or geometry. Predicting and tailoring this heterogeneous stress distribution are particularly interesting in microelectronics given their specific impact in terms of charge carrier mobility or electromigration phenomenon, especially when heterogeneous multimaterials systems are considered. Given the increasing degree of miniaturization reached in current micro- and

nanotechnologies, it is of major importance to develop experimental techniques allowing multiscale stress analysis.

Several non-destructive methods to characterize the residual stress in thin films have been proposed, from common techniques such as curvature measurement [43] or X-ray diffraction (XRD) [44], or more experimental approaches such as photothermal inspection [45] or Raman scattering [46]. Each of them has assets and limitations according to the sample dimension or materials and to the geometric resolution. For microelectronics applications, a common treatment is to use the Stoney relation which links the flexural bending of thin films on circular wafers to their residual stress after being processed [43]:

$$\sigma_f = \frac{t_s^2}{6t_f}\left(\frac{1}{R} - \frac{1}{R_0}\right)\left(\frac{E_s}{1-\nu_s}\right) \qquad \text{(III-10)}$$

where t_s and t_f are the substrate and the film thickness respectively, R_o and R are the radii of curvature before and after the process respectively, E_s is the Young's modulus of the substrate and ν_s is the Poisson ratio of the substrate. This technique can be applied in the case of full wafer deposits such as spin coating deposition or PVD/CVD-derived techniques.

X-ray diffraction proved to be widely used for determination of residual stress in thin films coatings, due to its high rank precision when probing directly crystallographic structures. Extraction of residual stress is performed from the $\sin^2\psi$ [47, 48] law which relates the evolution of interplanar spacing to XRD peaks shifts and the underlying stress:

$$\varepsilon_{\phi\psi} = \frac{d - d_0}{d_0} = \frac{1}{2}S_2(hkl)\cdot\sigma_\phi\cdot sin^2\psi + S_1(hkl)\cdot[\sigma_{11} + \sigma_{22}] \qquad \text{(III-11)}$$

where S_1 and S_2 are the X-ray elasticity constants for the family of {hkl} lattice plane, ϕ is the rotation angle around the specimen surface normal and ψ is the inclination of the diffraction vector with respect to the specimen surface normal. This technique can nonetheless be limited in the case of very thin film because of the high penetration depth of θ-2θ XRD scans. Diffraction signal from the film can indeed be so weak that it can be hidden by the background signal and substrate diffraction. An optimization of the experimental setup has to be performed to ascertain the exact position of the peaks.

Since residual stress is highly correlated to process conditions, through the microstructure, several measurements were conducted in collaboration with the Claude Goux Laboratory of ENSM.SE in Saint-Etienne, France to assess the impact of process parameters, such as sintering temperature, time and ramp, and of Coefficient of Thermal Expansion (CTE) mismatch on residual stress. All else being equal, inkjet-printed thin films were cured in a RTA with varying thermal ramps – from 0.1 to 150 °C/s – and sintering times –

from 15 to 60 min. X-ray measurements were performed on {311} diffracting planes. Results show that the contributions from thermal ramp and sintering time to residual stress are almost negligible since the stress variation is comprised within a range of 10 MPa (see Table III-2). The very low stress observable in such printed structures after annealing has to be emphasized because of its great difference with the expected behavior of conventional thin films during thermal cycles. If attention is nevertheless put on these process parameters, one could assert that while the impact of sintering time was predictable since microstructure is already established after a 15 min-curing, the reason of the limited impact of thermal ramp is more unclear. Indeed, as seen previously, both grain and pore sizes are affected by thermal ramp but seem insufficient to affect the residual mechanical state.

Table III-2: Values of residual stress after a 300 °C sintering cycle showing the very low impact of both sintering ramp and sintering time.

Sintering ramp (°C/s)	**0.1**	**10**	**50**	**150**	10	10
Sintering time (min)	15	**15**	15	15	**45**	**60**
Residual stress (MPa)	22.5 ± 2.9	22.1 ± 0.6	31.9 ± 1.5	23.2 ± 2.1	21.3 ± 2.5	29.3 ± 1.1

In order to explain these very low residual stresses, implementation of in-situ measurements is particularly appropriate to monitor the internal stress evolution during the heating and cooling steps. Such measurement will thus enlighten underlying mechanisms of stress generation. Hodge *et al.* [49] have considered the evolution of internal stress with temperature for both sputtered and electroplated silver thin films on silicon substrate, with a thickness of 150 nm. As depicted in Figure III-11, residual stress of thermally processed films is higher than freshly deposited films in both cases.

While initial stress is tensile, an elastic deformation of the film (CTE) is occurring during the curing until reaching the elastic limit when irreversible deformation arises. As expected from Hall-Petch equation [50, 51], the yield stress is highly dependent from the microstructure and especially to the average grain size of the deposit. Since the average grain size is smaller in sputtered films than electroplated films, the elastic limit will occur at higher temperature for PVD thin films (100 °C vs. 200 °C according to Figure III-11). This phenomenon is all the more noticeable that electroplated films are highly reactive and subject to substantial grain growth during thermal curing. Above the yield stress, the stress induced by CTE mismatch is more or less accommodated by plastic deformation. As temperature increases, several mechanisms of stress relaxation are usually activated such as vacancy consumption, dislocation annihilation, recovery, recrystallization, grain boundary sliding or creep.

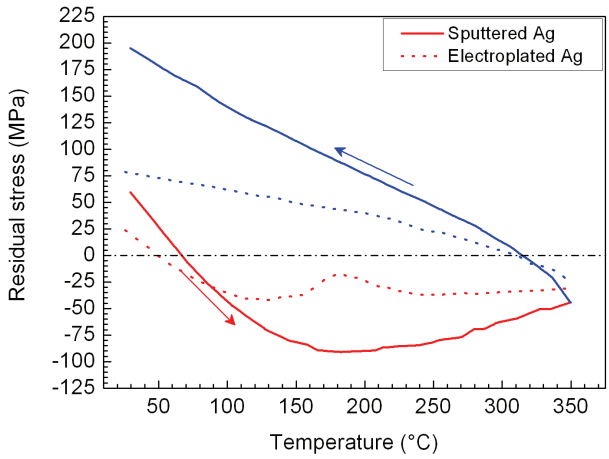

Figure III-11: In-situ measurement of residual stress in 200 nm-thick sputtered and electroplated silver thin films on silicon substrate using the Stoney method [49].

Internal stress determination of our inkjet-printed samples on silicon substrate was performed using in-situ X-ray diffraction. These XRD analyses have been performed in collaboration with the CEA LETI in Grenoble, France on printed silver squares of 1 cm² with an average thickness of 330 nm. The resultant evolution is presented in Figure III-12 for a thermal cycle up to 550 °C. Due to experimental limitations, a gentle drying at 60 °C has been applied to samples in order to remove a majority of the solvent phase and avoid ink flowing off from the substrate when placed vertically.

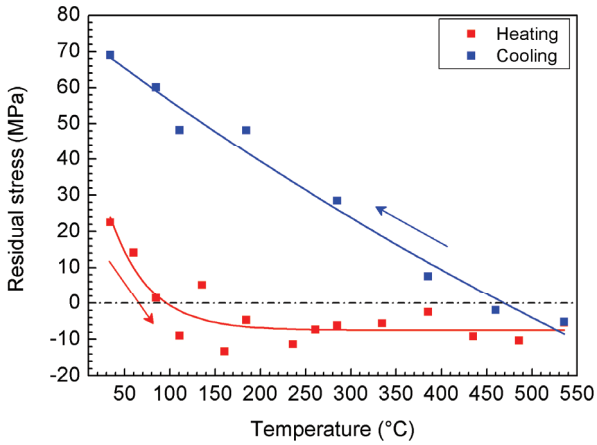

Figure III-12: In-situ XRD measurement of internal stress performed on our 330 nm-thick inkjet-printed thin film.

The first conclusion than can be emphasized is the very low residual stress level within the printed films which is in the same range than electroplated silver films. The residual stress of 70 MPa in our nanoparticulate film is indeed three times lower than within a 200 nm-thick polycrystalline silver film deposited by sputtering. The similitude with the

unstable and highly evolutive structure of electroplated silver films gives credit to our measurement. However, the low internal stress generated within the inkjet-printed silver thin film is quite unlike the one developed in electroplated films. Indeed, the 75 MPa observable after a curing at 350 °C would results in a stress of about 150 MPa which is twice as much as what is measured in printed films.

As shown in Figure III-12, initial stress within the inkjet-printed silver film is in tension. Indeed, as mentioned previously, the sample has been fairly dried before the experiment to materialize a viscous/solid film without initiating any sintering mechanism. As described by the consecutive studies of Hoffman and coworkers [52-54], when adjacent grains are close enough, grain boundaries are forming between impinging islands through the reduction of surface energy. Thus, the formation of a continuous film by gap closing, during the preliminary curing, generates a tensile stress with the help of the relative mismatch in thermal expansion between the film and the substrate.

During the heating step, residual solvents are progressively evaporating and adhesion between nanoparticles and the substrate is initiating. As a consequence, stress decreases until entering in compression at about 100 °C, just as sputtered or electroplated silver films [49]. But unlike PVD thin films, the initial slope of the stress cycle is totally unrelated to the thermoelastic phenomenon since the film is not yet fully formed and adherent to the substrate. The initial slope of the curve is indeed much lower that what it would be for a thermoelastic behavior, whose associated stress is given by:

$$\frac{d\sigma}{dT} = \left(\alpha_s - \alpha_f\right)\frac{E_f}{1-\nu_f} \qquad \text{(III-12)}$$

where α_s and α_f are respectively the coefficients of thermal expansion of the silicon substrate ($\alpha_s = 3{\cdot}10^{-6}$ K^{-1}) and the film ($\alpha_f = 19{\cdot}10^{-6}$ K^{-1}), and E/1-ν is the biaxial modulus. With the sole contribution of CTE mismatch between the substrate and the film, the stress of a fully dense silver film would be -115 MPa at 100 °C.

Above 100 °C, the nanoparticulate silver film can be considered as stress free. As seen previously, it is assumed that, between 100 °C and 550 °C, tensile stress induced by thermal expansion mismatch is mitigated not only by plastic deformation but also by atomic mass transport associated with sintering phenomenon. The presence of porosities plays also a key role in the accommodation of the stress by increasing the flexibility of the silver/substrate system. Recovery of the film moreover contributes to grain growth initiation by removal of dislocations that impinge grain boundaries movements. This counterweighing operation is easily comparable to electroplated films which are undergoing substantial microstructural evolution [49]. This result is in total adequacy with previous observations in Chapter II part II-B where a stabilization of the microstructure is observed from 300 °C (see Figure III-13).

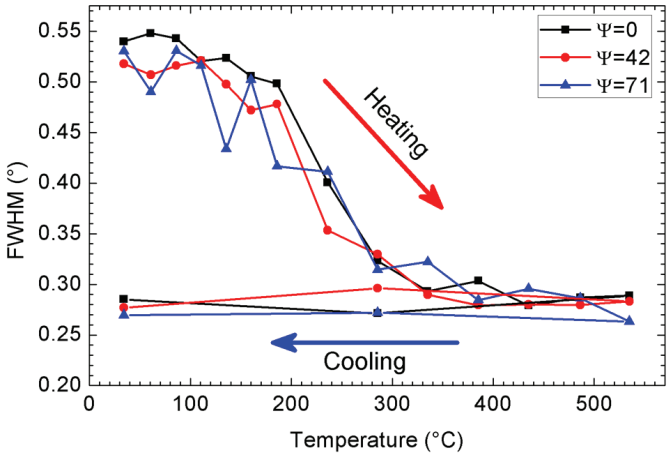

Figure III-13: In-situ measurement of the FWHM evolution of the (111) peak with respect to temperature at several ψ angles, showing a stabilization of the microstructure above 300°C and during cooling.

The final residual stress is mainly generated during the cooling. In our case, the microstructure is stabilized from 300 °C but the interface is not perfect (see Figure III-14) with size porosities up to 1 µm which are still present at the interface with the silicon substrate. As a consequence, the stresses generated at the interface due to thermal mismatch are quickly accommodated by the layer without transferring the solicitation. Furthermore, strain can also be locally accommodated due to the free surfaces related to porosities (see Figure III-4).

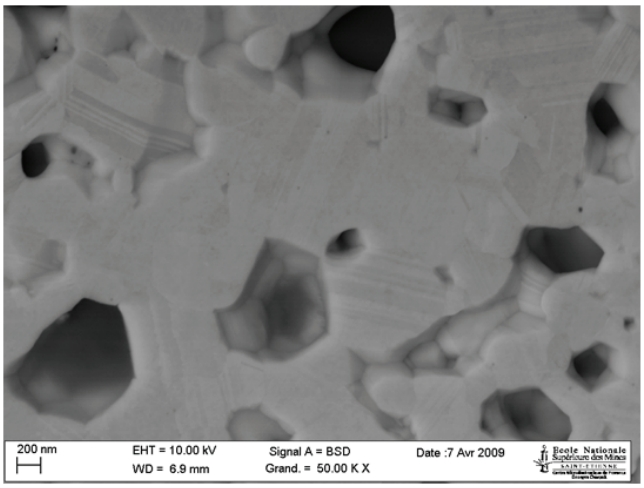

Figure III-14: SEM image of the printed silver film surface at the interface with a silicon substrate (after being peeled off). Porosities are clearly observable and grains have been hammered.

Bolstered by these in-situ measurements performed on a specific sintering condition at 550 °C, the behavior of the internal stress during the thermal cycle attests that the final temperature determines the resultant microstructure and associated residual stress. As a

consequence, the residual stress can be analyzed to conclude on the impact of thermal stress contribution which relates as much to the temperature range to the CTE mismatch. Regarding the impact of sintering temperature, as expected, the lower the sintering temperature is, the lower the residual stress will be (see Figure III-15). The temperature indeed tends to eliminate crystalline defects and especially decreases the density of dislocations where microstrain is usually stocked.

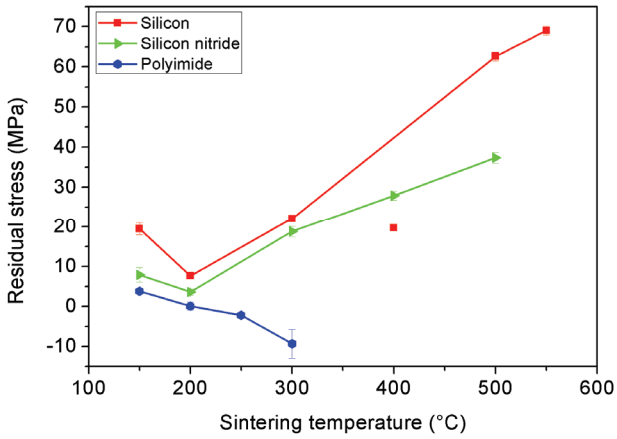

Figure III-15: Residual stress of printed thin films according to the sintering temperature on silicon (red box), silicon nitride (green triangle) and polyimide substrates (blue circle).

As demonstrated by Zoo *et al.* [55], thermal expansion phenomenon in thin films is highly dependent of the underlying substrate. Indeed, important CTE mismatch induces stress generation at the interface which constrains the film expansion or contraction. Impact of several substrates on the silver thin film residual stress was thus studied: silicon ($\alpha_{Si} = 3{\cdot}10^{-6}$ K^{-1}), silicon nitride ($\alpha_{SiNx} = 3.3{\cdot}10^{-6}$ K^{-1}) and polyimide ($\alpha_{PI} = 20{\cdot}10^{-6}$ K^{-1}). Silicon-based substrates exhibit lower CTE than silver ($\alpha_{Ag} = 19{\cdot}10^{-6}$ K^{-1}) which is in the same range than that of polyimide. Since printed structures are usually limited in dimension (from tens of micron to a centimeter), structures are quickly pinned at triple junction with the substrate when heated, as seen in Chapter 1. Edges pinning is then assumed to constrain the lateral expansion of thin films which can impact internal stress in the case of diverse CTE. The printed layer will thus compensate with anisotropic expansion in the normal direction. If stress is assumed to be negligible during the heating step so that the major contribution to the residual stress originate from the cooling step, silver thin films will develop tensile stress on silicon-based substrates and compressive stress on polymeric substrate. This point has been verified experimentally as shown in Figure III-15. It should be noted than due to the better adhesion of silver thin film to the rough polyimide and to similar CTE, inkjet-printed silver thin film can be considered as stress free when curing is limited below 300 °C which is a significant result for plastic electronics.

Inkjet-printed thin films are all the more interesting that this very low residual stress –

when compared to conventional PVD thin films – even after a thermal treatment at 500 °C, is achieved for 200 nm-thick layers only. As explained in section I-B, residual stress is highly dependent to film thickness. As a consequence, increasing the thickness of printed layers, *e.g.* with several overprints, should further decrease this residual stress. This asset is particularly valuable since the inkjet-printing step is supposed to occur at the very end of the Back-End-Of-Line (BEOL) process, *i.e.* the top level of 3D interconnects architectures. During the whole BEOL process, a great attention is put on stress control to avoid delamination between metallization layers [56] or compression in CMOS channels that impacts electron mobility [57]. Our experiments thus demonstrated that whatever the process conditions (temperature, thermal remap and dwell time), the residual stress of inkjet-printed thin films remains very low.

II. Electrical behavior of inkjet-printed lines

In microelectronics, fine conductive structures are employed to convey the signal across the device and toward the 'outside world'. With the reduction of features size in integrated circuits, the line dimensions are shrinking significantly. When the geometrical confinement is in the same order than the electron mean free path, Thomson has shown in 1901 that surface and grain boundary scattering were contributing to an increase of resistivity [58]. In this section, electrical properties of thin films will be investigated in direct and alternative currents and correlated to the previous microstructural results. Both silicon and polyimide substrate will be considered for their respective interest in flexible electronics or in coil-on-chip applications. In the following, except mentioned otherwise, curing treatments are performed in a RTA oven.

A. Electrical resistivity of thin metal films

Many scattering factors can affect electrical resistivity in thin films, from background scattering – originating from phonons and crystalline defects – to a distribution of planar potentials or from external surfaces. If the independence of each scattering source is assumed, application of the Matthiessen's rule asserts that each scattering phenomenon contributes additively to the thin film electrical resistivity, ρ_f, so that:

$$\rho_f = \rho_0 + \rho_{gb} + \rho_{ss} + \rho_{sr} \qquad \text{(III-13)}$$

where ρ_o is the bulk resistivity, ρ_{gb} is the grain boundary scattering contribution, ρ_{ss} is the

surface scattering contribution and ρ_{sr} is the surface roughness contribution.

Surface scattering has been initially described by Fuchs [59] and Sondheimer [60]. Based on Boltzmann equations, Fuchs developed his model of free electron transport assuming that electron scattering doesn't depend on the film thickness, that external interfaces are perfectly planar and parallel and that only isotropic scattering is occurring in the film so that it can be characterized by an effective electron mean free path. Fuchs and Sondheimer introduced a specularity parameter, p, to render the proportion of electrons which are elastically scattered at the surface. According to Fuchs-Sondheimer (FS) model, the electrical resistivity of thin films is thus given by:

$$\rho_f = \rho_0 \left[1 - \frac{3}{2\kappa}(1-p) \int_1^{\infty} \left(\frac{1}{t^3} - \frac{1}{t^5} \right) \frac{1 - e^{-kt}}{1 - p \cdot e^{-kt}} dt \right]^{-1} \qquad \text{(III-14)}$$

where κ is the ratio between h and λ_o ($\kappa = h/\lambda_o$), h is the film thickness, λ_o is the electron mean free path and p is the surface scattering factor. The value of p is comprised between 0 for totally diffusive scattering and 1 for specular reflexion of electrons at surfaces. As a consequence, in the limits of very thin ($\kappa \ll 1$) and very thick films ($\kappa \gg 1$), Equation (III-14) can be approximated by:

$$\rho_f = \rho_0 \left(\frac{4}{3\kappa \cdot ln(\kappa^{-1})} \cdot \frac{(1-p)}{(1+p)} \right) \qquad (\kappa \ll 1) \qquad \text{(III-15)}$$

$$\rho_f = \rho_0 \left(1 + \frac{3}{8\kappa}(1-p) \right) \qquad (\kappa \gg 1) \qquad \text{(III-16)}$$

Even though not formally considered in this work, the FS model has been extensively discussed to meet particular experimental deviations from initial hypotheses, such as the presence of two different surfaces with respective specularity parameters p and q [61, 62] or anistropic mean free paths [63] or the incident angle-dependency of specularity parameter [64].

An extension of the FS model has been derived by Ziman [65] and Soffer [66] to take the surface roughness into account in the surface specularity parameter. The Ziman-Soffer (ZS) model considers the plane wave nature of the electron cloud as developed by de Broglie [67]. In this model, the surface roughness will affect the specularity parameter if, and only if, the root mean square (RMS) surface roughness is larger than the de Broglie wavelength λ. Indeed, in this case, most of electrons are scattered with a random phase change (see Figure III-16).

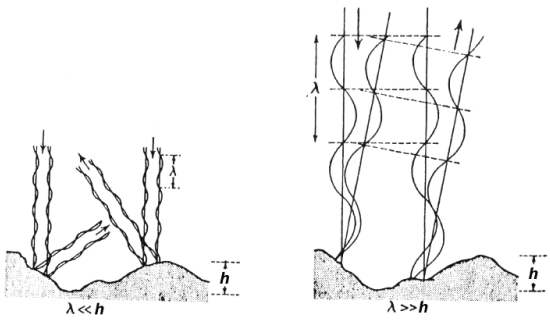

Figure III-16: Effect of electron wave scattering induced by the surface roughness according to the ratio between the electron mean free path and the RMS roughness [65].

In this model, the specularity parameter is defined by:

$$p_{ZS} = exp\left[-\left(\frac{4\pi R_q}{\lambda}\right)^2 cos^2\theta\right] \tag{III-17}$$

where R_q is the RMS surface roughness, λ is the de Broglie wavelength of silver ($\lambda \approx 6$ Å) and θ is the angle between the surface and the incident plane wave. Given that the RMS surface roughness is on the nanometer range, λ is negligible compared to R_q and consecutively the limit of this specularity parameter is zero. This states that the contribution of surface roughness to the thin film resistivity will thus be neglected thereafter.

The effect of electron scattering at grain boundaries is considered by the Mayadas-Shatzkes (MS) model [68]. In this model, grain and twin boundaries are assimilated to potential barriers for the travelling electrons whose probability to be reflected is assessed by the grain boundary reflection coefficient R (see Figure III-17). According to the Mayadas-Shatzkes model, the electrical resistivity of thin films is given by:

$$\rho_f = \rho_0 \cdot \left[1 - \frac{3}{2}\alpha + 3\alpha^2 - 3\alpha^3 ln\left(1 + \frac{1}{\alpha}\right)\right]^{-1} \tag{III-18}$$

with

$$\alpha = \frac{\lambda_0}{G}\frac{R}{1-R} \tag{III-19}$$

where λ_o is the electron mean free path, R is the grain boundary reflection coefficient and G is mean grain diameter. The value of R is ranging from 0 for totally transparent grain boundaries to 1 for a total reflection of electrons. In the later case, electrons are thus confined within individual grains. Additionally, in this model, the grain and twin boundaries contributions to the scattering are combined in the mesoscopic parameter *R*.

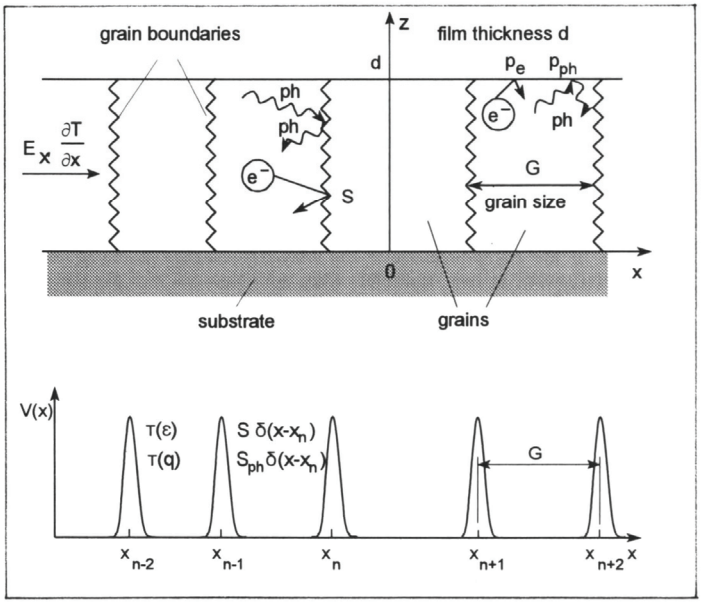

Figure III-17: Model of charge carrier in thin polycrystalline films

In the MS model, grain boundaries are assumed as perpendicular to the electric field generated by traveling electrons. Grain boundaries are localized at the position x_n, with a potential $V_x=S\cdot\delta(x-x_n)$ where S is the strength of the planar scatterer. Grain boundary positions are assumed to follow a Gaussian distribution with a mean distance between each position equivalent to the average grain diameter G (see Figure III-17).

Although Mayadas and Shatzkes initially derived their model for thick polycrystalline films where surface scattering can be neglected, they expanded the model to consider the presence of external surfaces in the case of thin films. Solving Boltzmann equations using Fuchs formalism resulted in a general equation for electrical resistivity in thin films:

$$\rho_f = \rho_0 \left[1 - \frac{3}{2}\alpha + 3\alpha^2 - 3\alpha^3 ln\left(1+\frac{1}{\alpha}\right) - \frac{6(1-p)}{\pi\kappa}\int_0^{\pi/2} d\phi \int_1^{\infty} \frac{cos^2\phi}{H^2}\left(\frac{1}{t^3}-\frac{1}{t^5}\right)\frac{1-e^{-\kappa tH}}{1-p\cdot e^{-\kappa tH}}d\theta \right]^{-1} \quad \text{(III-20)}$$

with

$$H = 1 + \frac{\alpha}{cos\phi\sqrt{1-\frac{1}{t^2}}} \quad \text{(III-21)}$$

In this new form, the electrical resistivity depends on both the grain boundary scattering and surface specularity. Nonetheless, since the integrand is related to the grain size via α and to the external surface via p, the Matthiessen's rule is not applicable anymore. Given that the

electron mean free path of silver (see Table III-3) is on the same order of magnitude than the film thickness and the average grain size determined in the previous chapter, the Equation (III-20) cannot be simplified easily.

Table III-3: Electrical properties of some usual metals in microelectronics at 300 K [69-71]

	Ag	Au	Cu	Al
Bulk resistivity (µOhm·cm)	1.617	2.255	1.712	2.709
Electron mean free path (nm)	52	42	39	15

Now that the theoretical models have been presented, the electrical characterization of the inkjet-printed silver deposits will be performed as a function of the sintering temperature and time.

B. DC analysis of inkjet-printed films

Electrical resistivity of inkjet-printed silver structures and films is measured at room temperature using four-point techniques. In these methods, two probes are used to set an electrical current while the other two probes are used to sense the voltage. This enables to neglect the contact resistance of sensing probes. The most general method has been developed by van der Pauw on films with random shapes [72]. This technique requires two set of measurements with a permutation in probes position (see Figure III-18-a). Each probe is placed at the edge of the sample with micro-positioners. In the case of a thin film with a thickness *t*, the electrical resistivity is given by:

$$\rho_f = \frac{\pi}{2ln2}\left(\frac{V_{CD}}{I_{AB}} + \frac{V_{DA}}{I_{BC}}\right) \cdot f\left(\frac{V_{CD}I_{BC}}{V_{DA}I_{AB}}\right) \cdot t \qquad \text{(III-22)}$$

where *f* is a correction factor related to the film shape, which equates to 1 for square films.

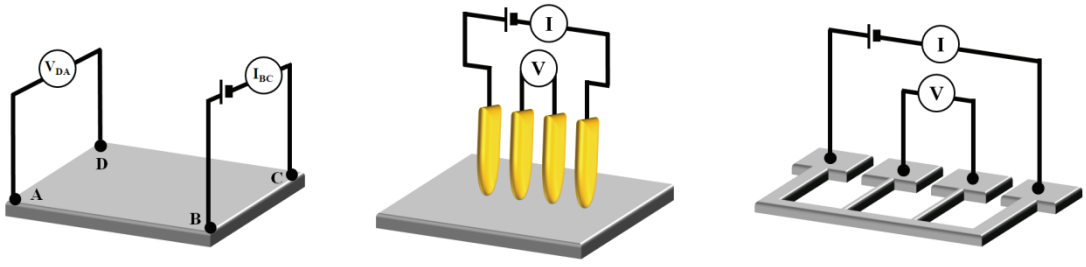

(a) (b) (c)

Figure III-18: Measurement principles of the van der Pauw (a), four-point probe (b) and Kelvin structure (c) methods.

Four-point probe measurement uses two outer probes to apply a controlled electrical current I and the inner probes are used to sense the electrical potential difference V. Since the distance between the tips (0,635 mm for a tip radius of 100 µm) is way larger than the film thickness, t, the electrical resistivity of the film is given by:

$$\rho_f = \frac{\pi}{ln2}\frac{V}{I}t \qquad \text{(III-23)}$$

The four-point probe method is particularly suitable for non-patterned and uniform films whose dimensions are large enough to avoid current overcrowding effects. This is a fast method which can suitably be used for electrical resistivity measurement from a material point of view.

A more specific structure was also employed to characterize microelectronics patterns: Kelvin structures. In this configuration, inkjet-printed stripes are confined in at least two dimensions, usually the thickness and width. The measurement principle is the same as in the previous technique at the exception that probes are micro-positioned and spacing between them is not necessarily equal. A symmetric setup is however required. The corresponding electrical resistivity is then given by:

$$\rho_f = \frac{w}{l}\frac{V}{I}t \qquad \text{(III-24)}$$

where w is the stripe width and l is the distance between the voltage contacts.

As previously mentioned, the electrical resistivity of printed silver films is highly dependent to the thermal process, and thus to the microstructure. According to the Mayadas-Shatzkes model, it is expected that silver films with large grains and few materials defects will exhibit lower electrical resistivity. Indeed, in this case, electrons will have to travel through less potential barriers and thus undergo less scattering. Results of electrical measurements with respect to sintering temperature and time are reported in Figure III-19.

Electrical resistivity is decreasing exponentially with temperature and time towards the asymptotic value of the bulk resistivity ρ_o. It is nonetheless observed that for a curing at 150 °C, the asymptotic value is not ρ_o because sintering mechanisms are first activated through surface diffusion paths which are limited by the residual PVP coating polymer. While being conductive because of contact between nanoparticles being initiated during the contact step, further decrease of the electrical resistivity is hindered by the lack of thermal energy. The asymptotic value is assumed to depend on the curing temperature and the initial nanoparticle size as it conditions the temperature of sintering initiation.

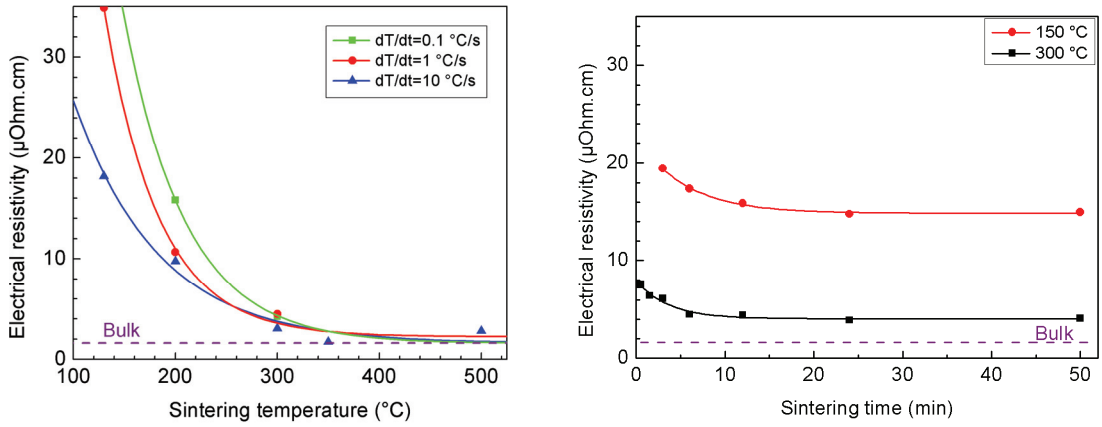

Figure III-19: Evolution of electrical resistivity with respect to the sintering temperature for a curing time of 10 min in RTA (left) and time for temperatures of 150 °C and 300°C(right).

Impact of external surfaces was minimized by printing silver layers with thickness above 500 nm so that the contribution of surface specularity to electron scattering is negligible. Only the model of Mayadas and Shatzkes will then be considered. To determine the reflection coefficient of silver grain boundaries, experimental data was confronted to the Mayadas-Shatzkes model (see Figure III-20). The reflection coefficient at grain boundaries are thus computed independently on the basis of the measured electrical resistivity and extracted grain size from the previous chapter.

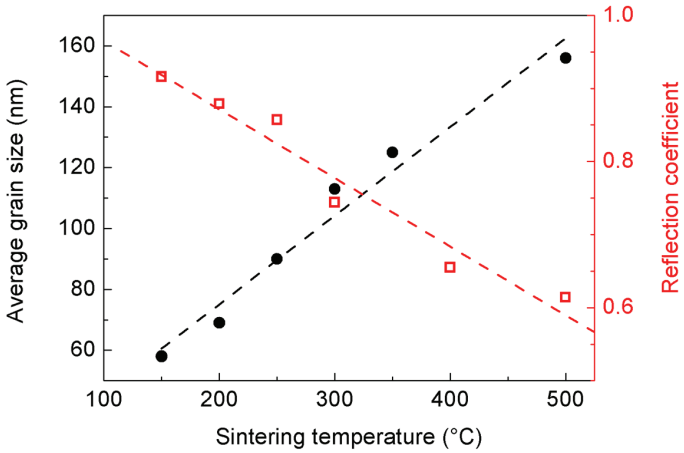

Figure III-20: Experimental grain size and reflection coefficient at grain boundaries for our inkjet-printed silver film according to the Mayadas-Shatzkes model, as a function of temperature. Curing is performed in RTA.

The result shows that there is no constant value of R – that would be material-dependent – which fit the data points as expected from the model. Instead, experimental data seems to show that R varies with the sintering temperature and is comprised roughly between 0.9 and 0.6 in the range of 150 °C to 500 °C. This indicates that the grain boundary reflection coefficient depends on the microstructure which is related to the thermal

treatment. This is consistent with previous observation from Marom *et al.* [73]. The variation of scattering during the curing step is therefore a good assessment to monitor the improved quality of the grain boundary in term of contact surface and the grain growth which limits the number of potential barriers to overcome. Figure III-21 depicts a linear evolution of the *R* coefficient which is estimated at 0.6 at 500 °C indicating that a major proportion of electrons are scattered at grain boundaries. Electron scattering could thus contribute to the development of an electrical potential difference between grains.

A further decrease of this reflection coefficient, which is an indicator of the grain boundary quality, could only be reached by increasing the lattice coherency between grains/twins. As seen in Chapter 2, these both conditions could be achieved using a textured seed layer such as {111} gold on titanium. Figure III-21 is showing the impact of such layer on electrical resistivity and on reflection coefficient. A significant decrease of electron scattering is observed with only 30 % of electrons being scattered corresponding to half as much scattering than silver nanoparticles directly on a silicon substrate. This result is consistent with previous observations from Zhang *et al.* [71] on thin films with {111} preferential orientation and columnar grains which give credit to the method. The highest value computed for silver nanoparticles at 0.6 for a sintering temperature of 500 °C is then indicating a lower quality of grain boundaries. Therefore, this high scattering effect in printed films without seed layer is also impacted by the high porosity fraction.

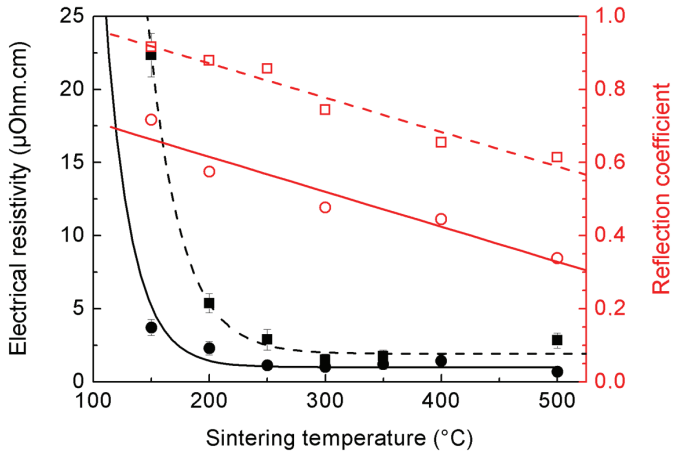

Figure III-21: Evolution of grain boundary reflection coefficient (red line) according to the Mayadas-Shatzkes model derived from the measured electrical resistivity (black line). Boxes and circles represent the data points of silver nanoparticles cured in RTA respectively on silicon and textured evaporated gold substrates.

This method was subsequently used on an alternative sintering process such as Hybrid Variable Frequency Microwave (HVFM). In the previous chapter, a significant impact on grain growth has been reported. Impact of process parameters has been considered with respect to RTA curing (see Figure III-22). A huge shrink in electrical resistivity is particularly

observable for samples prepared in RTA, while those prepared in HVFM quickly exhibit resistivities below 8 μΩ·cm. In both cases, the highest the thermal ramp is, the lower the electrical resistivity will be. Nonetheless, since all curves are converging, the asymptotic value seems relatively independent from the ramp and more related to the sintering temperature. Regarding the reflection coefficient at grain boundaries, it is observed that the values are very similar in both cases in spite of improved electrical resistivity. The electrical resistivity shrinkage at high temperature for HVFM and RTA is thus mainly originating from the contribution of the grain size rather than from the lower reflection coefficient. These results thus accredit the fact HVFM doesn't improve the quality of grain boundary and that only interdiffusion-assisted sintering can lead to much lower reflection with R=0.3 at 500 °C.

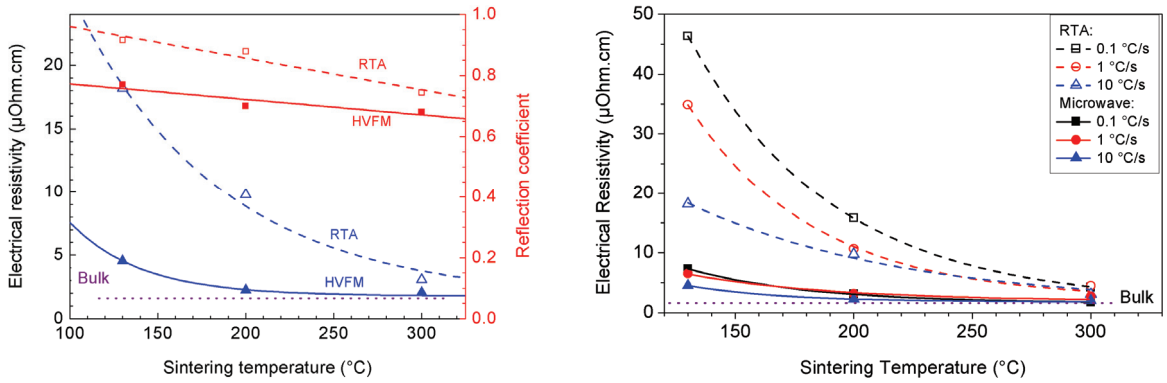

Figure III-22: On the right, comparative evolution of reflection coefficient for HVFM and RTA with a ramp of 10 °C/s. On the left, evolution of electrical resistivity after a 15 min-curing in HVFM oven (plain lines) or in RTA (dashed lines).

According to the thermal ramp, electrical resistivity achieved at 300 °C by RTA is 4 to 5 times the bulk resistivity which is consistent with literature. This result is clearly due to a partial sintering of the film which presents a high number of porosities. In the case of HVFM sintering, was it not the presence of residual porosities, the density reached at 300 °C seems indeed close to a fully dense polycrystalline silver film from SEM observations of the surface. This increased density is probably due to the volumetric curing performed through microwave excitations. This deposit exhibits a very low resistivity at 2.1 μΩ·cm which deviates from the bulk value because of electrons scattering at grain boundary.

C. Electrical behavior modeling of nanoporous lines

Whereas conductors exhibit a specific resistance R_{DC} to the flow of electrons in direct current measurements, when submitted to an alternating current, frequency dependent capacitance C and inductance L could impact the propagation of the electrical signal. As

explained by Johnson and Graham [74], low frequency currents usually flow through the least resistive paths, and high frequency currents tend to follow the least inductive paths.

As a consequence of frequency increase, the electrical current will concentrate at the conductor surface within a limited depth, known as the skin depth δ. According to the classical skin effect theory derived by Wheeler [75], the skin depth is given by:

$$\delta = (\pi \cdot f \cdot \mu \cdot \sigma)^{-1/2} \qquad \text{(III-25)}$$

where f is the frequency, $\mu = \mu_r \cdot \mu_o$ is the material permeability (with μ_r considered as 1 for the non-magnetic silver and $\mu_o = 4\pi \cdot 10^{-7}$ H·m^{-1}) and $\sigma = 1/\rho$ is the material conductivity ($\sigma_{Ag\ bulk} = 6.2 \cdot 10^7$ S·m^{-1}). As reported in previous part, the electrical resistivity of silver films sintered in RTA (15 min, 200 °C, 10 °C/s) is at about 10 µOhm·cm and the corresponding electrical conductivity is then $1 \cdot 10^7$ S·m^{-1}. In Table III-4, analytical values of corresponding skin depth in printed silver films are given.

The skin effect results in the confinement of the current-voltage at the boundary of conductors. The surface resistance of a conductor becomes a frequency dependant and it is linked to the skin depth by:

$$R_S = (\delta \cdot \sigma)^{-1/2} \qquad \text{(III-26)}$$

As reported earlier, the electrical resistivity of sintered silver films varies with the microstructure through the thermal process. This indicates that the skin depth and the surface resistance will vary within the microstructure as a consequence of the resistivity evolution. One could expect that the skin depth tends to decrease when the curing temperature-ramp increases. In Table III-4, an example of the analytical values of corresponding skin depth in printed silver films sintered in RTA (10 °C/s) at 200°C and 500 °C are given.

Table III-4: Some value of the skin depth as a function of frequency for silver thin films sintered at a temperature of 200 °C and 500 °C. The conductivity is taken as 10^7 S·m^{-1} and $3 \cdot 10^7$ S·m^{-1}, respectively.

Frequency	**50 MHz**	**100 MHz**	**500 MHz**	**10 GHz**	**20 GHz**
Skin depth at 200 °C (µm)	22,5	23.9	11.0	1,7	0.5
Skin depth at 500 °C (µm)	12.3	17.7	9.5	1,5	0,4

Thus, specific electromagnetic considerations have to be considered when operating at high frequencies. So, an electrical circuit can be modeled as four-terminal network, or quadripole (see Figure III-23). Instead of using conventional current and voltage formalism, a standard approach consists in considering signals as incident and reflected waves at the ports of the Device-Under-Test (DUT). At port k, the incident wave is represented by a_k and the reflected wave by b_k (see Figure III-23).

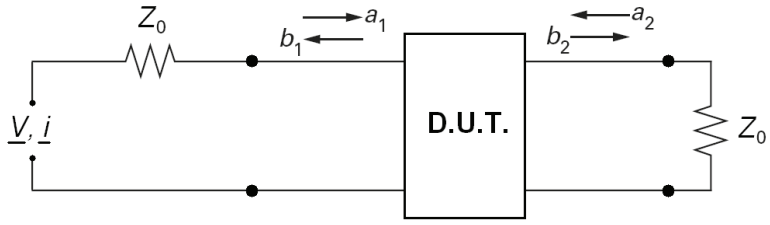

Figure III-23: Electrical circuit of the DUT characterization in a quadripole configuration for the determination of scattering parameters.

Incident and reflected power waves are related to a scattering matrix defined by S-parameters:

$$\begin{pmatrix} b_1 \\ b_2 \end{pmatrix} = \begin{pmatrix} S_{11} & S_{12} \\ S_{21} & S_{22} \end{pmatrix} \begin{pmatrix} a_1 \\ a_2 \end{pmatrix} \qquad \text{(III-27)}$$

where S_{ii} is the reflection parameter at port i and S_{ij} (i≠j) is the transmission parameter from the port i to the port j. Those parameters will characterize the ability of a conductor to transport an electrical signal with corresponding power level and quality factor.

i. Design of a coplanar waveguide

When the length of a conductor is greater than the wavelength of the signal, the electrical potential can no more be considered as evenly distributed across the conductor and it must then be treated as a transmission line. Reflection at lines extremities and the resultant phase delay indeed generates interferences which modify the local voltage-current waves. In this matter, a factor of 10 between the line length and the wavelength is usually considered as a common rule of thumb to apply the transmission line theory.

CoPlanar Waveguide (CPW) structures are commonly used to characterize the Radio-Frequency (RF) behavior of transmission lines. Those lines are usually used for integration of passive and active devices on silicon substrate in a single-sided configuration. Here, a central conductor is surrounded by two ground strips in order to reduce the coupling effects (see Figure III-24).

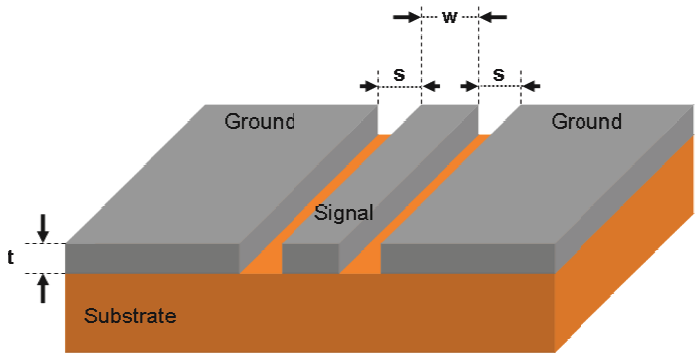

Figure III-24: Geometry of the coplanar waveguide with finite ground width configuration used in this study.

The characteristic impedance of CPW is strictly dependent on the structure geometry and on the constitutive materials properties. For a coplanar waveguide with finite ground width, the characteristic impedance can be analytically estimated by [76]:

$$Z_0 = \frac{30\pi}{\sqrt{\varepsilon_{eff}}}\left[\frac{K(k_1')}{K(k_1)} + \frac{t}{b-a}\right]^{-1} \quad \text{(III-28)}$$

with

$$\varepsilon_{eff} = 1 + \frac{\varepsilon_r - 1}{2} \cdot \frac{K(k_2')}{K(k_2)} \cdot \left[\frac{K(k_1')}{K(k_1)} + \frac{t}{b-a}\right]^{-1} \quad \text{(III-29)}$$

$$k_1 = \frac{c}{b}\sqrt{\frac{b^2 - a^2}{c^2 - a^2}} \quad \text{(III-30)}$$

$$k_2 = \frac{sinh\left(\frac{\pi c}{4h}\right)}{sinh\left(\frac{\pi b}{4h}\right)}\sqrt{\frac{sinh^2\left(\frac{\pi b}{4h}\right) - sinh^2\left(\frac{\pi a}{4h}\right)}{sinh^2\left(\frac{\pi c}{4h}\right) - sinh^2\left(\frac{\pi a}{4h}\right)}} \quad \text{(III-31)}$$

and, for n=1, 2

$$k_n' = \sqrt{1 - k_n^2} \quad \text{(III-32)}$$

where $K(k_i)$ is the complete elliptic integral of the first kind for k_i, ε_{eff} is the effective dielectric constant and ε_r is the relative dielectric constant of the substrate. Computation of complete elliptic integrals was performed using Scilab software.

To maximize the power transfer of the signal across the transmission lines, the characteristic impedance of CPW has to match the system impedance in which it is inserted. Unmatched impedances will lead to increase signal losses. Conventionally, RF systems are matched with a 50 Ω characteristic impedance.

For the design of inkjet-printed CPW, a strict consideration has to be given to the spatial resolution that is achievable in inkjet before printing. This resolution is substrate-dependant since the spreading of ink varies with the surface energy of each of those substrates (see Chapter I), except if a special surface treatment is used before printing in order to match the surface energies. For example, the finest resolutions achievable on polyimide and silicon nitride substrates are 50 µm and 80 µm, respectively.

Given that the electrical characterization of CPW requires specific probes in a ground-signal-ground configuration (G-S-G) for both measurement ports, an additional specification is put on the pitch between the central signal and lateral grounds. Indeed, only discrete values of (G-S-G) pitch between 75 µm and 2500 µm are commercially available. Thus, an adequate CPW geometry is determined numerically using a dichotomous approach using Equation (III-28).

In the next step, 50 Ω CPW were designed both on polyimide and on high resistivity (100) silicon wafer (4 kOhm·cm) covered with a bilayer dielectric material. This bilayer is formed using 0.8 µm thick thermal and silicon oxide followed by 0.6 µm thick LPCVD silicon nitride. Once realized, a special attention has to be given to the printing quality. The conformality of lines has to be perfect and the distance between the central conductor and grounds should be respected. This verification is mandatory since any instability in the printing process could result in deviating droplet jet and thus imperfection in line geometry (see Figure I-30).

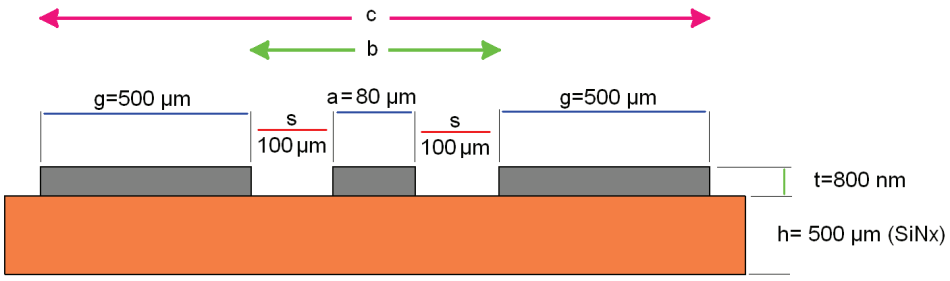

Figure III-25: Dimensions of inkjet-printed CPW studied in this thesis.

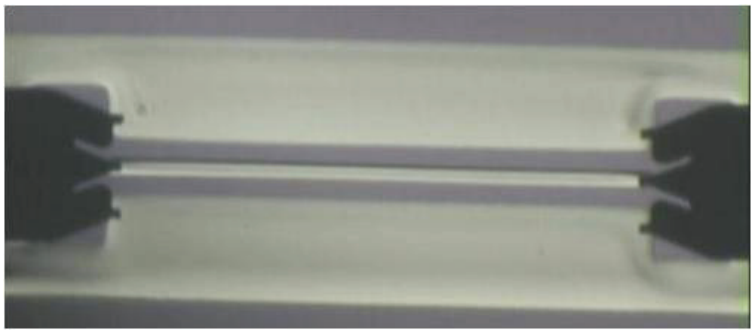

Figure III-26: Micrograph of inkjet-printed CPW with a length line of 4.5 mm after being cured at 200 °C on silicon nitride substrate (optical microscope).

ii. Frequency behavior of inkjet-printed coplanar waveguide

Frequency characterization of inkjet-printed coplanar waveguides was conducted in collaboration with the LAAS-CNRS in Toulouse, France. Inkjet-printed CPW were characterized over a frequency band comprised between 40 MHz and 20 GHz using a Vector Network Analyzer (VNA). S parameters of printed lines were extracted using G-S-G configuration with a probe pitch of 125 µm (ACP40 from Cascade Microtech), and a Short-Open-Line-Through (SOLT) calibration procedure has been performed. This step allows the elimination of parasitic electrical response coming from probes, cables, etc., and thus the electrical reference plane is measured from the line entrance.

From the complex S-parameters, the real and imaginary parts can be used to calculate the transfer power gain in insertion or reflection and the phase of the signal. Given that the passive transmission line is linear and reciprocal, the $S_{11}=S_{22}$ and $S_{12}=S_{21}$ conditions are verified by our printed structures. The reflection loss, or the input return loss, determined by the gain of S_{11} (see Equation (III-33)) is an indicator of the impedance matching between the quadripole and the system. The matching is then perfect if the gain is equal to infinity (*i.e.* when $S_{11}=0$). This gain has to be maximized in absolute value for a better transmission. On the other hand, the insertion loss is the logarithmic magnitude of S_{12}. It represents the loss between the entrance and the exit of the line originating from the intrinsic loss in the DUT or in the substrate. This gain has thus to be minimized in absolute value.

$$G_{ij} = 20\log\left|S_{ij}\right| \qquad \text{(III-33)}$$

When considering various lengths of transmission lines fabricated on HR silicon wafer and sintered at 500 °C, the insertion loss is increasing simultaneously (see Figure III-27). This is consistent with increasing resistive loss within the conductor. Moreover, the plot of the insertion loss per unit length shows superposition of curves. This is an indication that the printed silver film presents homogeneous microstructure (see Figure III-27).

The attenuation of the signal per unit length is oscillating between 2.5 dB/mm and 2.7 dB/mm at 10 GHz, and between 3dB/mm and 3.1 dB/mm at 20 GHz. In addition, when considering the variation of phase, a phase shift is observed at different frequencies according to the length indicating that when associating two inkjet-printed lines of dissimilar length in parallel, two signals can be superimposed without interfering.

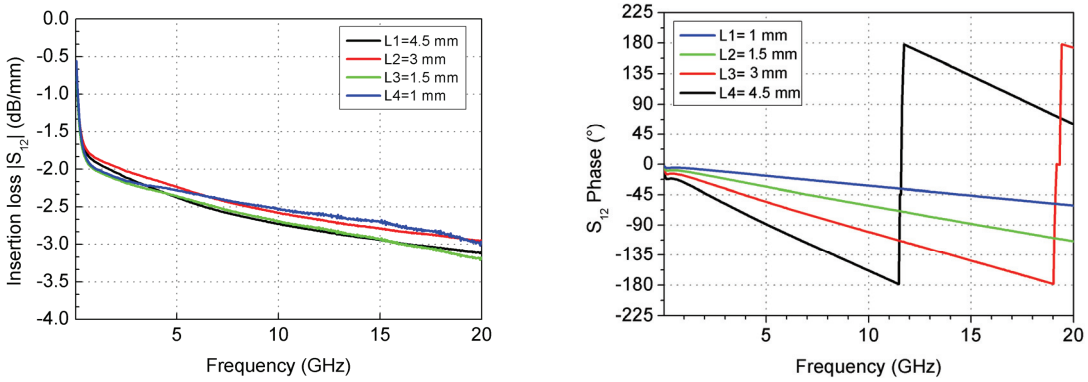

Figure III-27: Insertion loss (left) and phase (right) of CPW sintered at 500 °C with various length lines on a high resistivity silicon substrate covered with nitride.

To reduce the scattering at grain boundaries and further decrease the surface resistance, the impact of the sintering temperature is examined for printed CPW on HR silicon wafer. As shown in Figure III-27, a little effect is observed when temperature increases from 200°C to 500°C which corresponds to a decrease of the insertion loss from 2,6 dB/mm to 2,2 dB/mm (at 10 GHz). The conductivity of printed silver films at 500°C is about 3 µOhm·cm compared to its value at 200°C at 10 µOhm·cm. The little decrease of the insertion loss even when CPW were cured at higher temperature shows the major influence of the surface resistance and the skin depth on the total signal loss. As reported, the insertion loss in this case can be diminished by increasing the thickness of the deposit with an appropriate electrical conductivity.

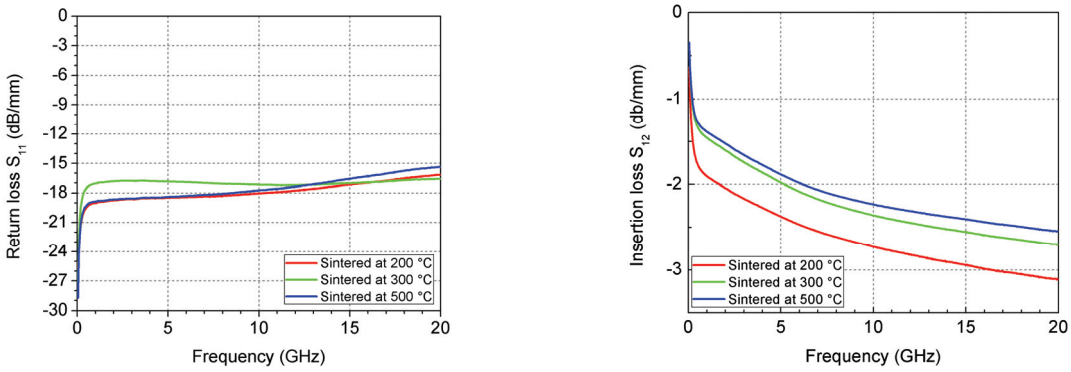

Figure III-28: Return and insertion losses per unit length of inkjet-printed CPW as a function of sintering temperature on a silicon nitride substrate (thermal ramp of 10 °C/s in RTA).

For the same sintering conditions, insertion and return losses of CPW printed on both polyimide and high resistive silicon substrate were compared and plotted in Figure III-29. It shows that CPW made on silicon exhibits insertion loss that are ten time higher than that on polyimide. This notable difference can only be explained by the dielectric loss involved

within the substrate, even though precaution has been put using a high resistive silicon substrate to eliminate the coupling effect within the substrate. In the meantime, the insertion loss on polyimide is in an acceptable range. Pynttari *et al.* [77] reported a similar value for CPW made in the same fashion as it is presented here, and on polyimide substrate. Moreover, they have shown that this insertion loss could be further decreased for example by a factor 5 (at 10 GHz) when a combination of deposited thickness, printing resolution, ink and curing profile is fulfilled.

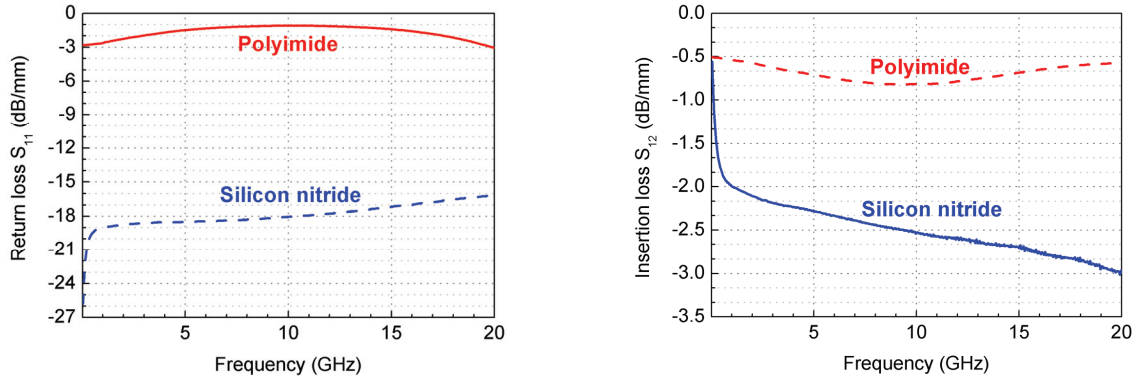

Figure III-29: Return and insertion losses per unit length of inkjet-printed CPW according to the substrate: silicon nitride (blue) or polyimide (red) and a sintering temperature of 200 °C (RTA, 10 °C/s).

Further investigation and optimization should be conducted focusing on the technological aspects, such as the substrate, the film thickness, other inks with smaller nanoparticles or different process conditions. Tailoring of these parameters would lead to improved performances.

iii. Extraction of lumped elements

CPW are usually modeled using (R, L, C) lumped element model [78]. In this model, the resistance and the inductance of the conductors are varying with the frequency, and the associated capacitor is due to the lateral coupling of the electromagnetic field between the central and grounds conductors. The lumped element model can thus be used as an interesting approach to extract the associated (R, L, C) discrete elements within the inkjet-printed structures. One can seek to follow the variation of lumped elements within the used process steps to fabricate the CPW.

This commonly used lumped model has been adopted and simulated for our printed CPW structures. The results show that a zero solution is obtained when the classic model is used. For that, we proposed a new and simple lumped elements model for printed CPW.

This proposed model takes into account the presence of pores within conductors and

considers that the electrical conduction is supposed to happen at only at grain boundaries. It is therefore assumed that the skin depth will be adopted also at the grain level. Both studied models are presented in Figure III-30.

Figure III-30: Equivalent circuit as commonly proposed for transmission lines (left) and our model (right).

Both models were computed and fitted using Mathcad software. For simplicity reason, the fits were processed on the complex conductance G and susceptance B according to Equations (III-34) and (III-35). They are respectively the real and imaginary parts of the complex admittance in Siemens, *i.e.* the reciprocal impedance. The equivalent admittance in the transmission line (TL) and our grain boundary (GB) model are given by:

$$Y_{TL} = \frac{R_G + jC\omega}{jRL\omega}\left(\frac{1}{R} + jC\omega + R_G + \frac{1}{jL\omega}\right)^{-1} \tag{III-34}$$

$$Y_{GB} = \frac{1}{R_{NP}}\left(\frac{1}{jL_{GB}\omega} + jC_{GB}\omega + \frac{1}{R_{GB}}\right)\left[\frac{1}{R_{NP}} + \frac{1}{jL_{GB}\omega} + jC_{GB}\omega + \frac{1}{R_{GB}}\right]^{-1} \tag{III-35}$$

It should be noted that the coupling capacitance in the GB model is negligible in our case and has not been considered in the following treatment.

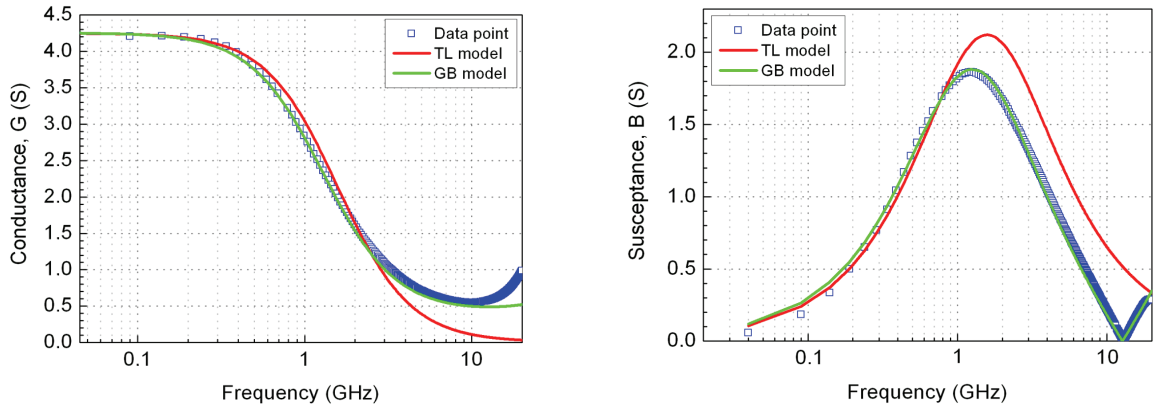

Figure III-31: Fit of experimental data with the TL and GB models on an inkjet-printed CPW sintered at 200 °C for a conductor length of 4.5 mm.

Experimental data of CPW are computed for each sintering conditions and fitting parameters are reported in Table III-5. The resistive contribution of the model R_{SK} is frequency independent till 1 GHz, and then it starts to increase gradually till a stabilization phase. Following the proposed model, the increase of the total resistance is supposed to be due to the current crowding around the grains because of the skin effect. The increase of sintering temperature tends to increase the grain size as explained earlier. It is supposed that, as current is flowing at grains periphery due to a localized skin effect, one would expect that the surface resistance associated with grain growth will tend to increase when the sintering temperature rise up, and this is confirmed in Table III-5.

In parallel, a resonance behavior occurs at a frequency of 1.3 GHz. This electrical resonance is a contribution of internal inductance and capacitor. It is suspected here that the associated capacitor can be attributed to the presence of pores within the conductors. It should be noted that Shao et al. measured a capacitance of 1.18 pF/cm on inkjet-prrinted CPWs on quartz glass substrate [79]. We see that this capacitor is decreasing with the annealing temperature, and this can be explained by the fact that pores tends to merge and disappear because of materials densification when the temperature increases.

Finally, the internal inductance can be attributed to the presence of an important intra-pore electrical coupling, whose value is supposed to be higher than the inductance associated with the grain itself. The value of this inductance is increasing when temperature rise up. This is logic because when pores tend to merge into one pore, this distance between pores will shrunk and the inductance will be logically enhanced.

Table III-5: Lumped elements extracted from our grain boundary model

Sintering temperature	**R_{NP} (mΩ)**	**R_{SK} (Ω)**	**C_P (pF)**	**L_{SK} (pH)**
200 °C	240	1.7	6	24
300 °C	90	2	5	29.5
500 °C	100	2	5.5	29.5

This model gives a good illustration of the evolution of resistive, capacitive and inductive properties of inkjet-printed transmission line. Several hypotheses were however done to derive this model. Electromagnetic numerical simulations will thus have to be performed in order to verify the validity of these hypotheses on nanoporous transmission line. It remains nonetheless interesting to correlate this model to the microstructural evolution during the curing.

III. Fabrication of redistribution lines compatible with conventional electrical interconnections

The implementation of printed structures for electronics packaging technology is addressed. One of the key steps to fabricate functional devices is to perform successful wire-bonding operation between the device and interconnection pads. This step usually requires a thick and dense pad metallization in order to absorb the mechanical deformation resulting from the wire loading. The direct bondability of gold wire on printed silver pads will be discussed in this part by connecting the lead-frame to the IC chip. The wire bondability of porous silver thin films is a challenging operation with the development of issues related to the nature of these inkjet-printed nanoporous silver thin films. It has indeed been observed that direct bonding presented some issues during the realization.

Our approach consists in performing successful wire bonding of gold wire on printed silver films. Then, the bonding quality and strength is characterized. In order to characterize electrical and mechanical behaviors of inkjet-printed structures, a test pattern has been designed to implement several test structures (see Figure III-32). From left to right, the structures include a test of inkjet capability through the assessment of nozzle deviation with printed dots, a test to characterize the contact resistance of wire bonds on printed structures (Kelvin structures), a basic redistribution pattern to test the functionality of implemented integrated circuit chips, a structure to characterize the loss of resistance with the conductor length and a plain square for adhesion measurements. It should be noted that all structures of the pattern are connected in order to simplify the electroless process that will be presented afterwards.

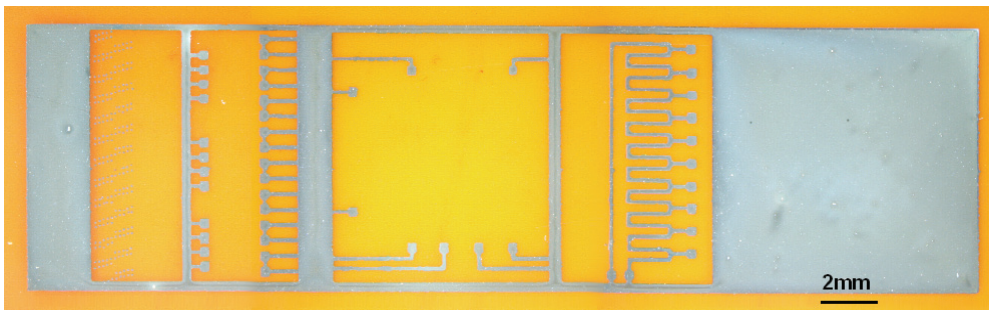

Figure III-32: Inkjet-printed test structures on Kapton substrate.

A. Wire bonding performed on thin films with a preferential orientation

Wire-bonding is a key process which is commonly used in microelectronics to perform electrical interconnections between the integrated circuit chips and the substrates. In the most conventional process, a molten free air ball is formed at the end of the gold wire which

is passing through a ceramic capillary. The free air ball is then compressed against the bond pad combining ultrasonic vibration, moderate heating and a mechanical force. This thermosonic ball bonding process is depicted in Figure III-33. A loop is consecutively performed by raising the capillary and moving to another location. The final bond, called a wedge bond, is obtained by vertical compression and shear motion of the wire under the capillary. Due to the capillary geometry, the wedge bond presents a characteristic tail bond in the contact area.

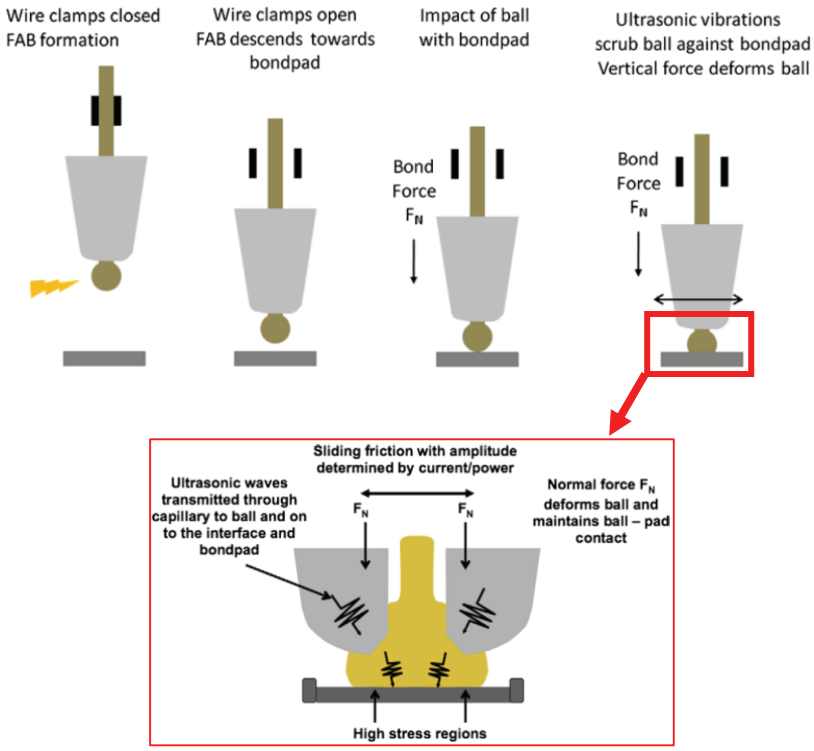

Figure III-33: Schematic of the ball formation and compression on a bond pad or a substrate during the thermosonic ball bonding process. Reproduced from [80].

When performed on sintered silver nanoparticle thin films, the ball bonding process failed whatever the curing conditions for sintering temperatures ranging from 200 °C to 500°C. A Design Of Experiments (DOE) was conducted on the bonding process parameters to find a combination which would be successful. Several parameters were studied such as the bonding force, the bonding time, the ultrasonic power, and the temperature. No combination was found to be successful on nanoparticulate films. Three modes of failure were observed during the tests: ball or metallization lift off and cratering (see Figure III-34). From the SEM pictures, the role of adhesion between the printed silver film and the substrate seems to play a key role in the process since the silver metallization tends to be lifted off. The addition of a seed layer as previously studied in Chapter 2 would thus be able to make a more cohesive interface between the ball and the thin film.

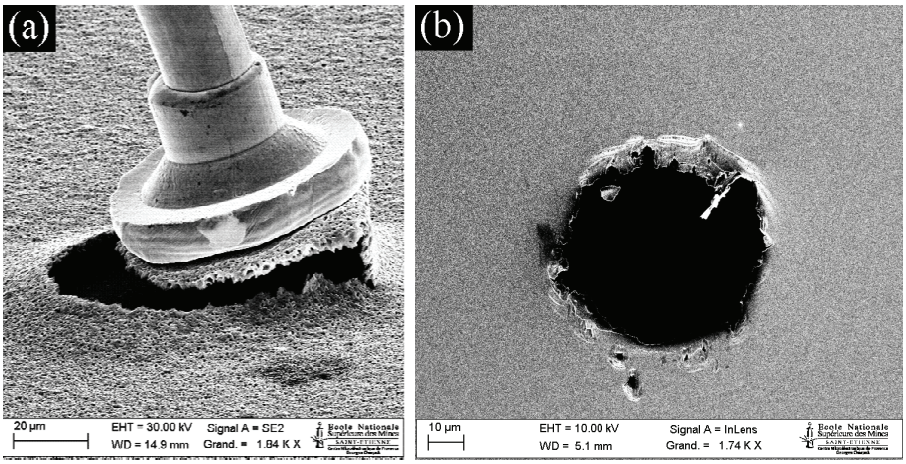

Figure III-34: Two failure modes observed during the ball-bonding process on nanoparticulate silver thin film with a standard 25 µm gold wire: metallization lift-off (a) and cratering (b).

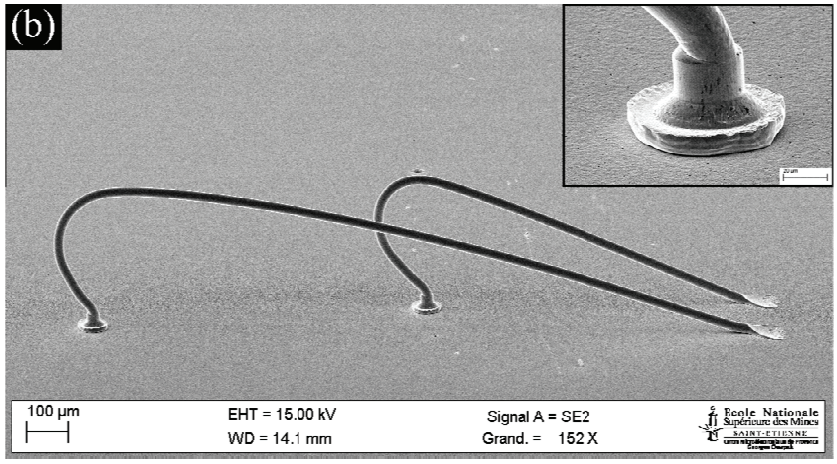

Figure III-35: Successful ball bonding loop performed on silver nanoparticles deposited on evaporated gold on silicon nitride and sintered at 200 °C. Close view of the ball is depicted in the inset.

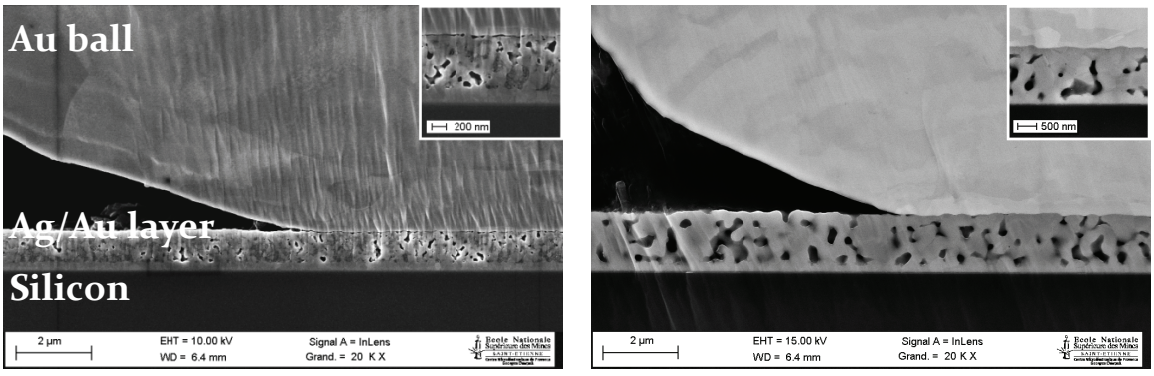

Figure III-36: InLens SEM images of the gold ball/silver nanoparticulate film interface for a sintering temperature of 200 °C (left) and 500 °C (right) at 10 °C/s. A zoom at the interface zone is presented in insets.

In the case of a textured substrate (PVD gold) with diffusion-assisted sintering, the mechanical properties are sufficiently improved to perform a successful gold wire bonding in every film with a sintering temperature above 200 °C. The {111}-texturation of silver pads observed previously above 200°C thus tends to increase both interfacial adhesion and hardness (see Figure III-35). It appeared that conventional bonding parameters were sufficient to implement the thermosonic process. Bonding parameters with a gold wire diameter of 25 µm were an impact force of 400 mN, a bonding force of 350 mN, a bonding time of 7 ms and an ultrasonic power of 26 %. Cross sections of balls on silver nanoparticles sintered at 200 °C and 500 °C are shown in Figure III-36.

Once the wire bonding has been successfully performed, its quality can be assessed following two testing methods: the ball-shear test and wire-pull test (see Figure III-37). While the former characterizes the ball bond strength, the later characterize the mechanical stiffness of the wire loops. Each experimental condition was tested on at least ten ball bonds. A ball-shear test was performed on gold wires bonded to silver nanoparticle thin film and compared to the process directly on the evaporated gold layer (*i.e.* without nanoparticulate silver film). For a test speed of 250 µm·s^{-1}, the load applied to rupture the ball/film interface was 33.9 ± 3.5 g (*i.e.* 332 mN) on silver nanoparticles while being of 47.0 ± 1.9 g (*i.e.* 461 mN) on evaporated gold. These values are comparable to the ones achieved by Krzanowski *et al.* [81] with shear values comprised between 20 g and 37 g for gold ball bonding on aluminum thin films.

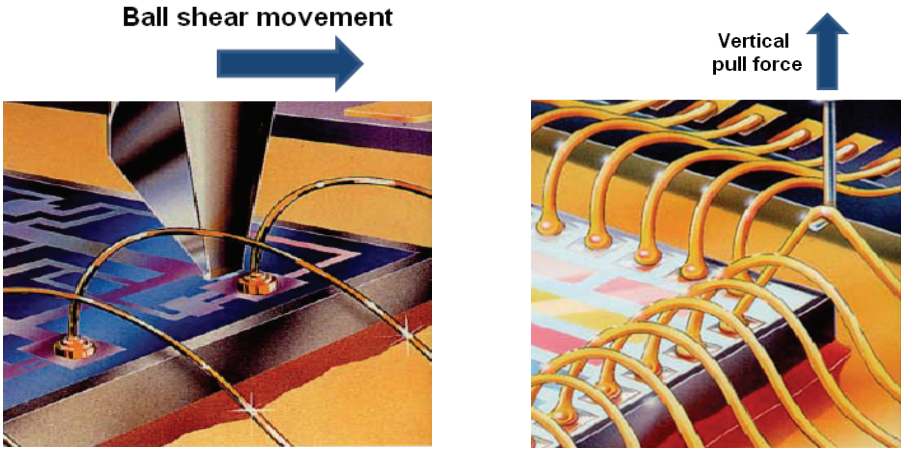

Figure III-37: Principles of the ball-shear test (left) and wire-pull test (right). Reproduced from DAGE.

Regarding the wire pull test, the wire bond strength is evaluated by positioning a hook underneath the wire and applying an upward force on the wire loop until the bond breaks. This is the most accepted method to test the quality of a wire bonding process in order to fabricate reliable devices. Test procedure and acceptance/rejection criteria are specified in the military standard MIL STD 883. The test was executed on wire bonds which sustained a

load up to 3 g before breaking. The main failure mode (80 %) during the wire pull test was concentrated in neck breaks, which is the area located just above the ball. These results show a very good performance of the bondability of gold wires with silver nanoparticles on textured films given the close values. It has to be mentioned that these values comply with MIL STD 883.

Enhancement of the wire-bonding process step with the gold seed layer is attributed to several factors. The major contribution is believed to derive from the improved interface quality with the substrate. It has indeed been suggested in Chapter 2 that the texture transfer was occurring from the seed/printed film interface towards the silver thin film surface. Consequently, the adhesion matching between the evaporate nickel/gold seed layer and the silicon substrate is extended to the whole silver film through the atomic interdiffusion. The interfaces between the gold ball, the nanoporous silver layer and substrate are depicted in Figure III-36. While the adhesion between the ball and the printed film seems weaker at 200 °C, it can be observed a perfect matching at 500 °C. Additionally, after being cured at 500 °C, the porosities tend to be confined within the film thickness while being clogged at interfaces. This texture transfer has indeed been shown to lower the number of porosities which should increase the contact surfaces between the ball and the film.

Moreover, the texturation of the printed silver film is correlated to an increased stiffness of the film which is believed to enhance the gold wire bondability. Indeed, the <111> direction corresponds to close packed planes in FCC materials with higher Young's modulus: $E_{<111>} > E_{<110>} > E_{<100>}$. With a same mechanical load applied, the deformation of the film will thus be lower. Yet, the residual porosities allow enough mechanical accommodation through deformation during the impact of the ball bonding. Using a {111} fiber-textured thin film underneath an inkjet-printed film thus allows a sufficient film rigidification with an accommodation layer as required by wire bonding process.

This approach thus enables to perform wire bonding interconnection on inkjet-printed films through the reinforcement achieved by the interdiffusion-assisted sintering developed in the previous chapter. While this technique has shown very interesting results with high strength of the ball bond on textured films, the main drawback of this technique is the requirement of a seed layer and its consecutive curing to transfer the texture. Indeed, in an industrial context, integration of a PVD step in the process flow before an inkjet-printed step seems inappropriate to our knowledge since it requires high vacuum pressure to be applied and introduce production delay. Another route could be suggested to achieve the same goal such as using a selective electroless growth.

B. Reinforcement of printed deposits through electroless growth

The robustness of the printed layer can be achieved using a very common operation: the electroless nickel immersion gold (ENIG) plating process. This is an autocatalytic technique which enables a selective deposition of nickel on existing metallic structures. This selectivity is particularly valuable in the case of printed structures on flexible substrate since the conductive line thickening is achieved without damaging the substrate or passivated parts of the device. This process has been implemented on inkjet-printed patterns to increase the thickness of film above 1.5 µm in order to guaranty the success of subsequent wire bonding operation. It should be noted that this step is carried out without any seed layer to solicit the contribution from the thickness increase and the improved mechanical stiffness of nickel.

i. Growth and properties of electroless nickel layer

This key issue of rigidification has been addressed using selective electroless nickel plating in order to reinforce the pads for the gold wire bonding step and to increase the thickness in the case of flip chip interconnection. This process has been widely adopted in microelectronics industry for the past few years as a consequence of lead-free solders specifications and for under-pads damage protection. Electroless nickel is an auto-catalytic process that is deposited from a hypophosphated nickel bath. The reaction equation is given by [82]:

$$Ni^{2+} + 2\,H_2PO_2^- + 2\,H_2O \Leftrightarrow Ni + 2\,H_2PO_3^- + H_2 + 2H^+ \qquad \text{(II-36)}$$

For electroless nickel plating on porous printed silver pads, an acid nickel bath with a pH of 5 was used at 90°C. The pH was increased compared to conventional recipe because acidic plating bath tends to chemically etch the silver pads. Reinforcement of inkjet-printed lines through electroless nickel plating was implemented on both silicon nitride and polyimide substrates. However, since the difference between the redox potential of silver nanoparticles and nickel bath is not sufficient to be autocatalytic, an activation is often required. This operation is usually performed using palladium catalyst which is expensive and is operated in a very acidic solution [83]. To avoid the degradation of the printed pattern, the activation was instead performed by a simple tweezer contact. It appeared that the process succeeded only when performed on polyimide (see Figure III-38) which is consistent with results obtained by Joo in 2009 [84]. He indeed calculated that the interfacial energy between silver and polyimide was 13 $J{\cdot}m^{-2}$ while being 3.1 $J{\cdot}m^{-2}$ between silver and silicon nitride substrate. It is then believed that the adhesion of silver thin film on its substrate plays a key role in this matter.

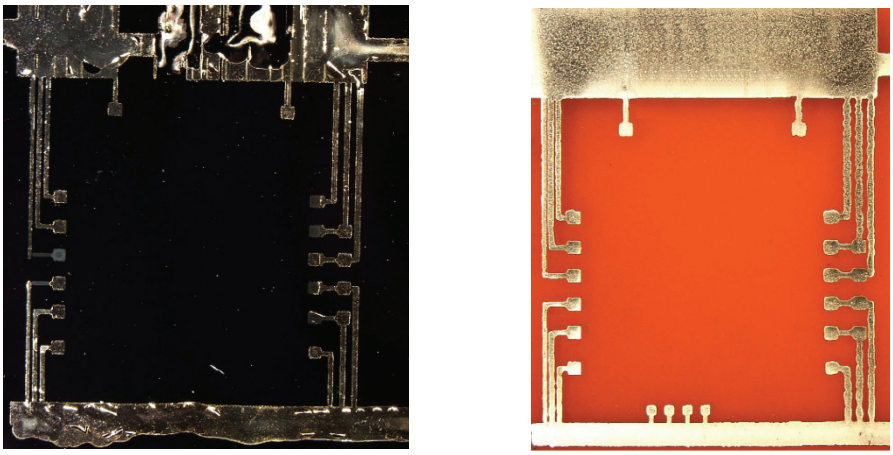

Figure III-38: Test pattern printed on silicon nitride (left) and polyimide (right) after the electroless nickel plating operation.

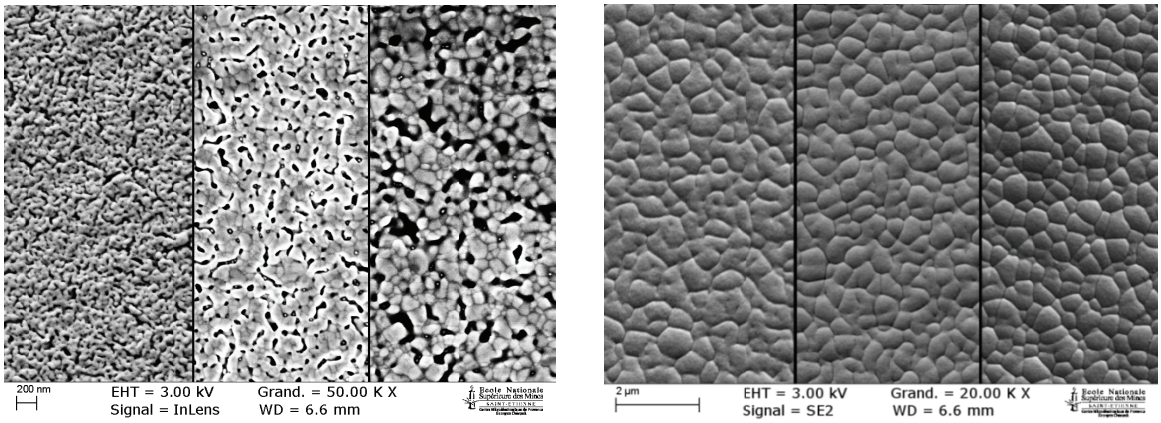

Figure III-39: Surface microstructures before (left) and after (right) the electroless nickel plating step, showing characteristic nickel nodules, on silver sintered at 0.1, 10 and 50°C/s (resp. from left to right) via SEM observations.

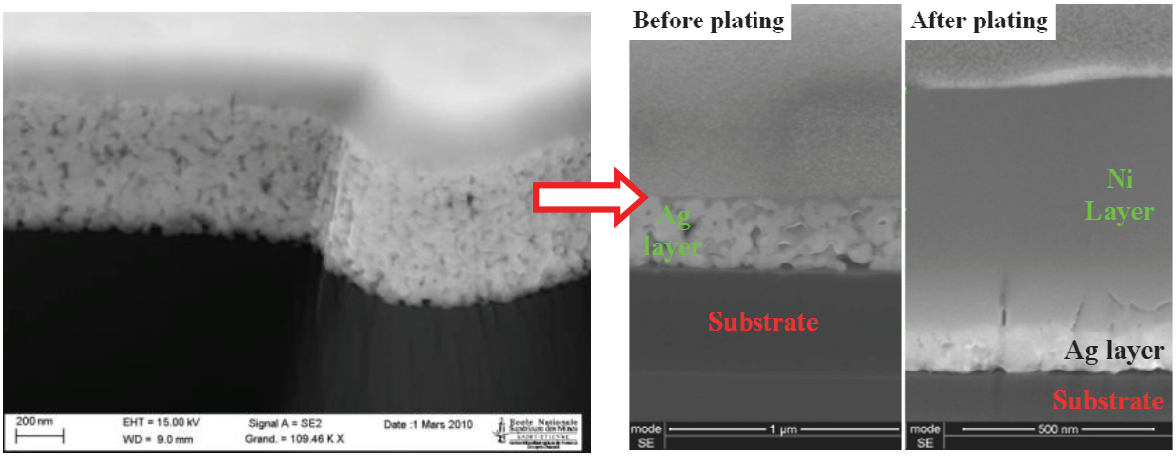

Figure III-40: SEM view of tilted cross-section of the pad before and after nickel plating process (RTA, 200 °C, 10 °C/s)

The growth of electroless nickel has been performed during 5 min in order to achieve a 1.7 µm-thick nickel layer. This thickness is sufficient to improve the wear mechanical resistance and the film hardness and tends to clog the film surface porosities. As can be seen from the Figure III-39 and Figure III-40, the film surface is completely covered with characteristic nickel nodules without apparent porosity. A cross-section of the silver thin film before and after electroless process indicates that the nickel growth is generated from the surface and not within the pores (see Figure III-40). As a consequence, porosities tend to be confined within the printed silver layer core.

Adhesion of the silver/nickel system was characterized using a pull-off procedure on an Instron 5900. Pull-off test consists in sticking pre-treated 6061-T6 aluminium alloy studs on both side of the film/substrate system [85] using an adhesive glue from Heraldite. The microporous surface of the studs enables mechanical interlocking of the adhesive after crosslinking. Both studs are then separated applying a normal load until break is observed. The more cohesive the interface will be, the higher the load will have to be to separate the film from the substrate. Results of pull tests are reported in Table III-6. After the test, image analysis is performed to assess the proportion of the film surface area remaining on the substrate (see Figure III-41). Experiments were conducted on silver films with and without electroless nickel plating to illustrate the influence of the process on the adhesion quality (see Table III-6).

Table III-6: Pull-off results performed on inkjet-printed silver film and electroless nickel plated films. The silver thin film is cured at 200 °C.

Thermal ramp (°C/s)	**0.1**	**10**	**50**
Printed silver on polyimide	15.3 MPa	11.2 MPa	9.0 MPa
Plated silver (Ni/Ag) on polyimide	4.0 MPa	8.9 MPa	1.4 MPa

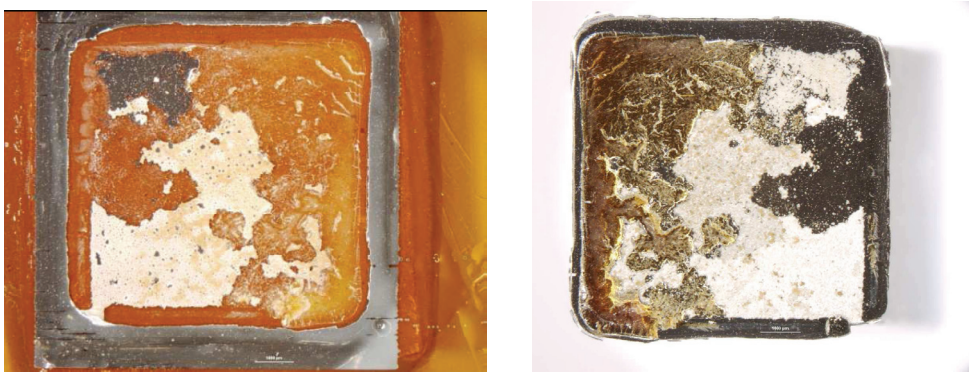

Figure III-41: Micrographs showing cohesive ruptures at the polyimide interface (left) and the corresponding dolly surface (right). Some parts of silver films remains on the substrate after the rupture.

Experimental results indicate a marked degradation of adhesion properties of the film to the substrate after the plating step. When the test is carried out on silver thin film, the silver/polyimide interface is peeling off with traction loads ranging from 9 to 15 MPa (see Figure III-41). Conversely, after an electroless growth, SEM observations of the rupture interface however showed that the most fragile interface wasn't between silver and polyimide substrate as expected, but between the silver film and electroplated nickel layer instead. It is believed that the acidic solutions used during electroless nickel plating are the cause of this degradation since cyanide ions in solution corrode silver atoms and thus weaken physicochemical bonds between film and substrate. The adhesion properties are thus of utmost importance but the volumetric mechanical properties should also be taken into account when considering the bonding strength.

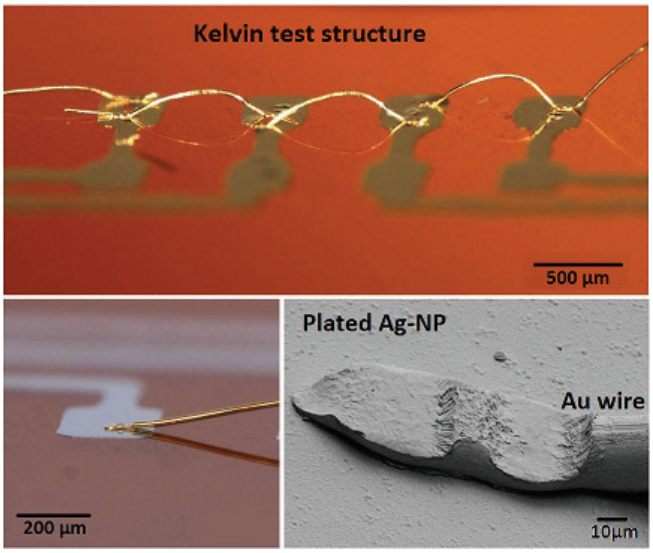

Figure III-42: Gold wire-bonds on silver printed structures plated with electroless nickel process on a polyimide substrate. The silver layer was preliminary cured at 200 °C (RTA, 10°C/s).

ii. Wire bonding and integrated circuit connections

In all cases, nickel electroless plating performed on silver thin film enabled wedge-bonding of 25 µm diameter gold wire with a bonding force comprised between 18 and 20 g (see Figure III-42). The success of the ball bonding operation is believed to originate from several factors amongst which the increased thickness and the accommodation seem to play the most prominent roles. As shown by Krzanowski *et al.* [81], aluminum thin films with thickness of 0.5 µm exhibited low strength or poor bondability. A thickness of 1 µm is often required to guaranty the ball bonding process. In addition, metallization presenting high hardness level and low roughness also tend to degrade the bondability. It is also believed that

the silver porous structure underneath the nickel plating tends to partly absorb the bonding impact by elastic/plastic deformation which tends to increase the success of the operation.

Since the feasibility is demonstrated, the process has to be validated by proving its capability in microelectronics systems. A lead-frame has thus been purposely designed and inkjet-printed on a polyimide substrate to host an IC chip in order to test performance of package from adhesion of plated interconnects to wire-bonds robustness, including contact resistance measurements between plated pads and gold wire. The testing package is shown in Figure III-43.

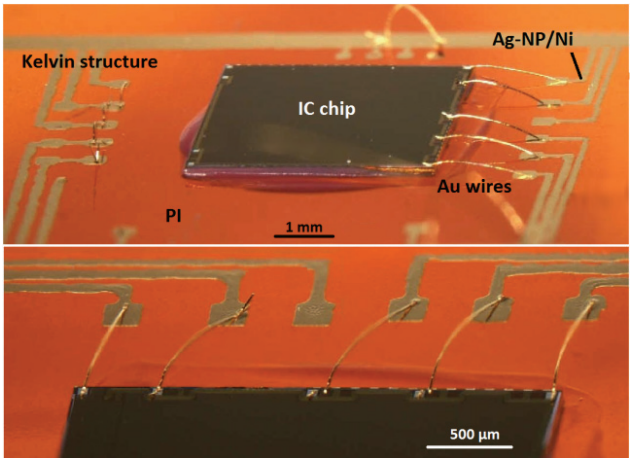

Figure III-43: Dummy flexible package with wire-bonds from an IC chip to plated lead frame (front right and bottom) and between plated pads (front left).

Robustness of wire bonds was evaluated performing wire-pull tests along the vertical axis. Due to the central position of the hook on the loop, this test sollicitates the wedge bonds both in normal and shear load. During the tests, 90 % of the failure modes involved neck break of the wedge bond located at the die side. The maximum pull load remains constant at 3.6 g whatever the previous thermal treatment. This shows the good surface finishing of the electroless nickel plating on silver which enables repeatability of the bonding process in an industrial environment without changing bonding parameters.

The good adhesion of gold wires to reinforced pads ensures sufficient electrical conduction for signal transmission while the device is under operation. Nonetheless, the interface between gold and nickel presents a given contact resistance that has to be measured to prove applicability of the whole process. A chain of wire bonds has been processed on Kelvin type structures printed and consequently plated with Ni/Au (see Figure III-44). Four point probing was used to eliminate the contact resistance of the probe tip during measurements. While current is injected and collected at both ends of the chain, each connection is probed in order to be averaged. Contact resistance measurements show no tendency with variations comprised between 10 mOhm and 45 mOhm.

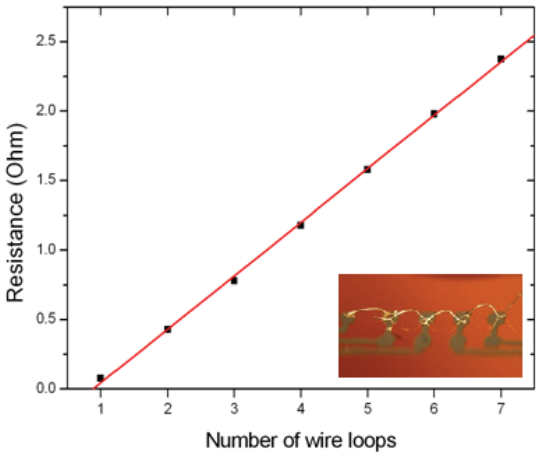

Figure III-44: Characterization of the contact resistance between gold wire and electroplated nickel on silver nanoparticulate film exhibiting a contact resistance of 40 mΩ.

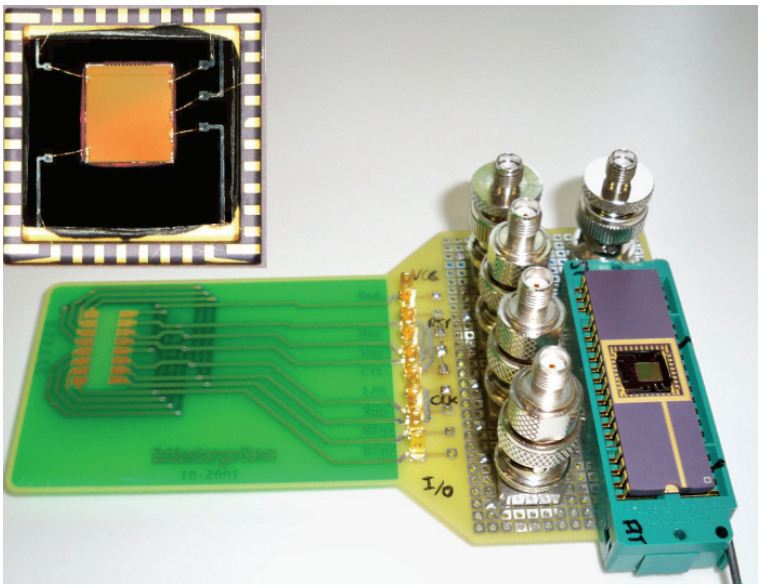

Figure III-45: Apparatus used for functionality tests where the chip-on-flex has been reported in a ceramic package (inset view) to be plugged-in an ISO test board.

The final validation came from the functionality test of the assembly where the IC-chip interconnected to the printed lead-frame using the above-mentioned technology has been reported in a ceramic package (see Figure III-45). The reporting step has been performed to be compatible with conventional electrical testing for microelectronic devices. Smartcard ISO pads on a PCB permitted Answer to Request query of the device, a test which happened to be conclusive with full functionality. This final test validated the pertinence of using inkjet printing jointly with electroless plating finishing for packaging applications.

Chapter conclusions

In this chapter, mechanical properties of inkjet-printed silver films have been investigated by mean of two characterization methods which are nanoindentation and bulge test. Naonindentation results have shown that the Young's modulus of nanoporous silver was progressively increasing with respect to the curing temperature. A value of 70 GPa was achieved after performing a 800 °C sintering. The high dependency of the Young's modulus to the porosity fraction was exploited by applying a simple model which gives qualitative evolution of the relative density. This cellular model indicated that a densification of 90 % is reached for high temperature treatment when the microstructural state is close to the bulk. It should be noted that the relative density of the film is stabilizing from 300 °C. These results have been corroborated by additional measurement performed by the bulge test technique through the deflection of silver membranes.

The residual and internal stresses in silver nanoparticulate film have also been considered as a key aspect for the subsequent process steps such as reinforcement or wire bondability. The characterization was performed using high resolution XRD or in-situ XRD. Contrary to conventional metal thin films deposited in vacuum process, inkjet-printed films exhibit very low residual stress. For a curing operated at 500 °C, the residual stress is thus limited to only 70 MPa. It is believed that this very low value derives from the presence of pores in the film which facilitate the stress relaxation. The microstructure has been observed to stabilize from 300 °C which is consistent with mechanical properties previously mentioned.

The electrical behavior of thin films was analyzed in direct current and in a radio-frequency band. Interestingly, the very same threshold value of 300 °C from which the electrical resistivity is reaching an asymptotic value has been observed. This stabilization has been directly correlated to the grain growth. A significant contribution to the electrical resistivity comes from the electron scattering at grain boundaries. It has been shown that, even though reflection coefficient at grain boundaries was reduced from 0.6 down to 0.3 using interdiffusion-assisted sintering (see Chapter 2), the densification achieved during HVFM sintering didn't had a major impact on this scattering. In addition, the radiofrequency characterization performed on coplanar waveguides gave promising results for smartcard applications where gigahertz frequencies can easily be reached. In addition, an electrical model is proposed in order to extract the lumped elements in the nanoporous silver films.

Eventually, two technological solutions were suggested in order to be compatible with a wire-bonding step for the implementation of inkjet printing technology within electronic packages. While interdiffusion-assisted sintering enables an improved densification and adhesion to the substrate through a seed layer with a preferential crystallographic orientation, a maskless electroless nickel growth increased pads thickness. The gold wire bonding performed on these systems gave good results that were implemented in a smartcard demonstrator.

References

[1] D. Hardwick, "The mechanical properties of thin films: A review," *Thin Solid Films*, vol. 154, pp. 109–124, 1987.

[2] W. Nix, "Mechanical properties of thin films," *Metallurgical and Materials Transactions A*, vol. 20, no. 11, pp. 2217–2245–2245, 1989.

[3] A. Griffin Jr., F. Brotzen, and C. Dunn, "Mechanical testing of thin metallic films," *Thin Solid Films*, vol. 220, pp. 265–270, 1992.

[4] O. Kraft and C. A. Volkert, "Mechanical testing of thin films and small structures," *Advanced Engineering Materials*, vol. 3, no. 3, pp. 99–110, 2001.

[5] M. Doerner and W. Nix, "A method for interpreting the data from depth-sensing indentation instruments," *Journal of Materials Research*, vol. 1, pp. 601–609, 1986.

[6] G. M. Pharr and W. C. Oliver, "Measurement of thin film mechanical properties using nanoindentation," *MRS Bulletin*, vol. 17, no. 7, pp. 28–33, 1992.

[7] A. J. Whitehead and T. F. Page, "Nanoindentation studies of thin film coated systems," *Thin Solid Films*, vol. 220, pp. 277–283, 1992.

[8] X. Chen and J. J. Vlassak, "Numerical study on the measurement of thin film mechanical properties by means of nanoindentation," *Journal of Materials Research*, vol. 16, no. 10, pp. 2974–2982, 2001.

[9] W. C. Oliver and G. M. Pharr, "An improved technique for determining hardness and elastic modulus using load and displacement sensing indentation experiments," *Journal of Materials Research*, vol. 7, no. 6, pp. 1564–1583, 1992.

[10] Y. Cao, S. Allameh, D. Nankivil, S. Sathiaraj, T. Otiti, and W. Soboyejo, "Nanoindentation measurements of the mechanical properties of polycrystalline Au and Ag thin films on silicon substrates: Effects of grain size and film thickness," *Materials Science and Engineering: A*, vol. 427, pp. 232–240, 2006.

[11] A. Fischer-Cripps, *Nanoindentation*. Springer, 2004.

[12] K. Johnson, *Contact mechanics*. Cambridge University Press, 1987.

[13] M. Levy, H. E. Bass, R. R. Stern, and V. Keppens, *Handbook of Elastic Properties of Solids, Liquids, and Gases: Elastic properties of solids: theory, elements and compounds, novel materials, technological materials, alloys, and building materials*. Academic Press, 2001.

[14] R. Saha and W. D. Nix, "Effects of the substrate on the determination of thin film mechanical properties by nanoindentation," *Acta Materialia*, vol. 50, pp. 23–38, 2002.

[15] R. King, "Elastic analysis of some punch problems for a layered medium," *International Journal of Solids and Structures*, vol. 23, no. 12, pp. 1657–1664, 1987.

[16] H. Gao, C. H. Chiu, and J. Lee, "Elastic contact versus indentation modeling of

multi-layered material," *International Journal of Solids and Structures*, vol. 29, pp. 2471–2492, 1992.

[17] S. Bec, A. Tonck, J. M. Georges, E. Georges, and J. L. Loubet, "Improvements in the indentation method with a surface force apparatus," *Philosophical Magazine A*, vol. 74, no. 5, pp. 1061–1072, 1996.

[18] G. M. Pharr, E. G. Herbert, and Y. Gao, "The indentation size effect: a critical examination of experimental observations and mechanistic interpretations," *Annual Review of Materials Research*, vol. 40, pp. 271–92, 2010.

[19] P. J. Burnett and T. F. Page, "Surface softening in silicon by ion implantation," *Journal of Materials Science*, vol. 19, pp. 845–860, 1984.

[20] S. J. Bull, "On the origins and mechanisms of the indentation size effect," *Zeitschrift für Metallkunde*, vol. 94, no. 7, pp. 787–792, 2003.

[21] A. Panin, A. Shugurov, and K. Oskomov, "Mechanical properties of thin ag films on a silicon substrate studied using the nanoindentation technique," *Physics of the Solid State*, vol. 47, pp. 2055–2059, 2005.

[22] J. R. Greer and R. A. Street, "Thermal cure effects on electrical performance of nanoparticle silver inks," *Acta Materialia*, vol. 55, pp. 6345–6349, 2007.

[23] X. Qin, X. Wu, and L. Zhang, "The microhardness of nanocrystalline silver," *Nanostructured Materials*, vol. 5, pp. 101–110, 1995.

[24] X. Chen, Y. Xiang, and J. J. Vlassak, "Novel technique for measuring the mechanical properties of porous materials by nanoindentation," *Journal of Material Research*, vol. 21, no. 3, pp. 715–724, 2006.

[25] S. D. Mesarovic and N. A. Fleck, "Spherical indentation of elastic-plastic solids," *Proceedings of the Royal Society of London. Series A: Mathematical, Physical and Engineering Sciences*, vol. 455, pp. 2707–2728, 1999.

[26] N. Fleck, H. Otoyo, and A. Needleman, "Indentation of porous solids," *International Journal of Solids and Structures*, vol. 29, no. 13, pp. 1613–1636, 1992.

[27] J. D. Eshelby, "The determination of the elastic field outside an ellipsoidal inclusion, and related problems," *Proceedings of the Royal Society London*, vol. 241, p. 376, 1957.

[28] L.-P. Chao and J. H. Huang, "Prediction of elastic moduli of porous materials with equivalent inclusion method," *Journal of Reinforced Plastics and Composites*, vol. 18, pp. 592–605, 1999.

[29] L. J. Gibson and M. F. Ashby, *Cellular solids: structure and properties*. Cambridge solid state science series, 1999.

[30] A. J. Birnbaum, K. J. Wahl, R. C. Y. Auyeung, and A. Piqué, "Nanoporosity-induced effects on ag-based metallic nano-inks for non-lithographic fabrication," *Journal of*

Micromechanics and Microengineering, vol. 20, no. 7, p. 077002, 2010.

[31] J. W. Beams, "Mechanical properties of thin films of gold and silver," in *International conference on structure and properties of thin films* (C. A. Neugbauer, ed.), (New-York), pp. 183–192, Wiley and Sons, 1959.

[32] S. Timoshenko and S. Woinowsky-Krieger, *Theory of plates and shells*. McGraw-Hill, 1959.

[33] J. Vlassak and W. Nix, "A new bulge test technique for the determination of young's modulus and poisson's ratio of thin films," *Journal of Materials Research*, vol. 7, pp. 3242–3249, 1992.

[34] H. Youssef, A. Ferrand, P. Pons, and R. Plana, "A new iterative algorithm for the solution for the load deflection square membranes," in *International Conference on Thermal, Mechanical and Multi-Physics Simulation and Experiments in Micro-electronics and Microsystems (EUROSIME)*, 2010.

[35] E. Bonnotte, P. Delobelle, L. Bornier, B. Trolard, and G. Tribillon, "Two interferometric methods for the mechanical characterization of thin films by bulging tests. application to single crystal of silicon," *Journal of Materials Research*, vol. 12, pp. 2234–2248, 1997.

[36] P. Martins, C. Malhaire, S. Brida, and D. Barbier, "On the determination of poisson's ratio of stressed monolayer and bilayer submicron thick films," in *DTIP of MEMS and MOEMS*, EDA Publishing, 2008.

[37] H. Youssef, A. Ferrand, P.Pons, and R.Plana, "Iterative algorithm with finite element method for bulge test characterization," in *20th MicroMechanics Europe workshop (MME),* 2009.

[38] O. Tabata, K. Kawahata, S. Sugiyama, and I. Igarashi, "Mechanical property measurements of thin films using load-deflection of composite rectangular membranes," *Sensors and Actuators*, vol. 20, pp. 135–141, 1989.

[39] J. Pan, P. Lin, F. Maseeh, and S. Senturia, "Verification of fem analysis of load-deflection methods for measuring mechanical properties of thin films," in *IEEE Solid-State Sensor and Actuator Workshop*, 4th Technical Digest, pp. 70–73, 1990.

[40] D. Maier-Schneider, J. Maibach, and E. Obermeier, "A new analytical solution for the load-deflection of square membranes," *Journal of Microelectromechanical Systems*, vol. 4, no. 4, pp. 238–241, 1995.

[41] H. Youssef, A. Ferrand, P. Calmon, P. Pons, and R. Plana, "Methods to improve reliability of bulge test technique to extract mechanical properties of thin films," *Microelectronics Reliability*, vol. 50, pp. 1888–1893, 2010.

[42] Y. Xiang, X. Chen, and J. Vlassak, "Plane-strain bulge test for thin films," *Journal of Materials Research*, vol. 20, no. 9, pp. 2360–2370, 2005.

[43] G. G. Stoney, "The tension of metallic films deposited by electrolysis," *Proceedings of the Royal Society of London. Series A, Containing Papers of a Mathematical and Physical Character*, vol. 82, no. 553, pp. 172–175, 1909.

[44] M. Gelfi, E. Bontempi, R. Roberti, L. Armelao, and L. Depero, "Residual stress analysis of thin films and coatings through XRD² experiments," *Thin Solid Films*, vol. 450, pp. 143–147, 2004.

[45] G. Goch, B. Schmitz, B. Karpuschewski, J. Geerkens, M. Reigl, P. Sprongl, and R. Ritter, "Review of non-destructive measuring methods for the assessment of surface integrity: a survey of new measuring methods for coatings, layered structures and processed surfaces," *Precision Engineering*, vol. 23, pp. 9–33, 1999.

[46] T. Wermelinger, S. A. Scott, M. G. Lagally, C. Hinderling, and R. Spoleank, "High lateral resolution analysis of stresses in silver thin films by means of raman microscopy," *AIP Conference Proceedings*, vol. 1267, pp. 776–777, 2010.

[47] E. Macherauch and P. Müller, "Effect of residual stresses on hydrogen permeation in iron," *Zeitschrift für angewandte Physik*, vol. 13, pp. 305–312, 1961.

[48] H. Dolle, "The infuence of multiaxial stress states, stress gradients and elastic anisotropy on the evaluation of residual stresses by x-rays," *Journal of applied crystallography*, vol. 12, pp. 489–501, 1979.

[49] T. C. Hodge, S. A. Bidstrup-Allen, and P. A. Kohl, "Stresses in thin film metallization," *IEEE transactions on Components, Packaging, and Manufacturing Technology—part A*, vol. 20, no. 2, pp. 241–250, 1997.

[50] E. O. Hall, "The deformation and ageing of mild steel: Iii discussion of results," *Proceedings of the Physical Society. Section B*, vol. 64, no. 9, pp. 747–, 1951.

[51] N. J. Petch *Journal of Iron Steel Institute*, vol. 174, pp. 25–, 1953.

[52] R. W. Hoffman, *Physics of thin films: advances in research and development*, vol. 3, ch. The mechanical properties of thin condensed films, pp. 211–. Academic Press, 1966.

[53] F. Doljack and R. Hoffman, "The origins of stress in thin nickel films," *Thin Solid Films*, vol. 12, pp. 71–74, 1972.

[54] R. W. Hoffman, "Stresses in thin films: The relevance of grain boundaries and impurities," *Thin Solid Films*, vol. 34, pp. 185–190, 1976.

[55] Y. Zoo, D. Adams, J. Mayer, and T. Alford, "Investigation of coefficient of thermal expansion of silver thin film on different substrates using x-ray diffraction," *Thin Solid Films*, vol. 513, pp. 170–174, 2006.

[56] S. M. Hu, "Stress-related problems in silicon technology," *Journal of Applied Physics*, vol. 70, no. 6, pp. R53–R80, 1991.

[57] S. L. Toh, K. P. Loh, C. B. Boothroyd, K. Li, C. H. Ang, E. Er, and L. Chan, "Reduction of local mechanical stress in a transistor using Si_3N_4 / SiO_xN_y contact ESL,"

Electrochemical and Solid-State Letters, vol. 8, no. 2, pp. G38–G40, 2005.

[58] J. J. Thomson, "On the theory of electrical conduction through thin metallic films," *Proceedings of the Cambridge Philosophical Society*, vol. 11, pp. 120–123, 1901.

[59] K. Fuchs, "The conductivity of thin metallic films according to the electron theory of metals," *Mathematical Proceedings of the Cambridge Philosophical Society*, vol. 34, no. 1, pp. 100–108, 1938.

[60] E. Sondheimer, "The mean free path of electrons in metals," *Advances in Physics*, vol. 1, pp. 1–42, 1952.

[61] H. J. Juretschke, "Electrical conductivity of thin metallic films with unlike surfaces," *Journal of Applied Physics*, vol. 37, pp. 435–435, 1966.

[62] M. S. P. Lucas, "Electrical conductivity of thin metallic films with unlike surfaces," *Journal of Applied Physics*, vol. 36, pp. 1632–1635, 1965.

[63] K. Saeger and R. Lück, "Evidence of anisotropic mean free path as furnished by galvanomagnetic measurements," *Zeitschrift für Physik B Condensed Matter*, vol. 9, pp. 91–97, 1969.

[64] H. Müser, "The physical nature of a metal surface in conduction theory," *Philosophical Magazine Series 7*, vol. 45, pp. 1237–1246, 1954.

[65] J. Ziman, *Electrons and phonons: the theory of transport phenomena in solids*. Clarendon Press, 1960.

[66] S. B. Soffer, "Statistical model for the size effect in electrical conduction," *J. Appl. Phys.*, vol. 38, pp. 1710–1715, 1967.

[67] L. de Broglie, *Recherches sur la théorie des quanta (Researches on the quantum theory)*. PhD thesis, Paris, 1924.

[68] A. F. Mayadas and M. Shatzkes, "Electrical-resistivity model for polycrystalline films: the case of arbitrary reflection at external surfaces," *Physical Review B*, vol. 1, pp. 1382–, 1970.

[69] F. W. Reynolds and G. R. Stilwell, "Mean free paths of electrons in evaporated metal films," *Physical Review*, vol. 88, pp. 418–419, 1952.

[70] D. Lide, *CRC handbook of chemistry and physics*. CRC Press, 81st ed., 2000.

[71] H. Zhang and C. A. Mirkin, "DPN-generated nanostructures made of gold, silver, and palladium," *Chemistry of Materials*, vol. 16, pp. 1480–1484, 2004.

[72] L. V. der Pauw, "A method of measuring specific resistivity and hall effect of discs of arbitrary shape," *Philips Research Reports*, vol. 13, no. 1, pp. 1–9, 1958.

[73] H. Marom, M. Ritterband, and M. Eizenberg, "The contribution of grain boundary scattering versus surface scattering to the resistivity of thin polycrystalline films," *Thin Solid Films*, vol. 510, pp. 62–67, 2006.

[74] H. Johnson and M. Graham, *High-speed digital design: a handbook of black magic*.

Prentice Hall, 1993.

[75] H. Wheeler, "Formulas for the skin effect," *Proceedings of the IRE. DOI - 10.1109/JRPROC.1942.232015*, vol. 30, no. 9, pp. 412–424, 1942.

[76] B. Wadell, *Transmission line design handbook*. Artech House, 1991.

[77] V. J. Pynttäri, R. M. Mäkinen, V. K. Palukuru, K. Östman, H. P. Sillanpää, T. Kanerva, T. Lepistö, J. Hagberg, and H. Jantunen, "Application of wide-band material characterization methods to printable electronics," *IEEE Transactions on Electronics Packaging Manufacturing*, vol. 33, no. 3, pp. 221–227, 2010.

[78] I. Chang and B. Lee, "Design of defected ground structures for harmonic control of active microstrip antenna," in *IEEE Antennas and Propagation Society International Symposium. DOI - 10.1109/APS.2002.1016779*, vol. 2, pp. 852–855 vol.2, 2002.

[79] B. Shao, R. Weerasekera, L.-R. Zheng, R. Liu, W. Zapka, and P. Lindberg, "High frequency characterization of inkjet printed coplanar waveguides," in *IEEE Workshop on Signal Propagation on Interconnects*, 2008.

[80] C. D. Breach and F. W. Wulff, "A brief review of selected aspects of the materials science of ball bonding," *Microelectronics Reliability*, vol. 50, no. 1, pp. 1–20, 2010.

[81] J. Krzanowski, E. Razon, and A. Hmiel, "The effect of thin film structure and properties on gold ball bonding," *Journal of Electronic Materials*, vol. 27, pp. 1211–1215, 1998.

[82] M. Charbonnier, M. Romand, and Y. Goepfert, "Ni direct electroless metallization of polymers by a new palladium-free process," *Surface and Coatings Technology*, vol. 200, pp. 5028–5036, 2006.

[83] T. C. Wang, B. Chen, M. F. Rubner, and R. E. Cohen, "Selective electroless nickel plating on polyelectrolyte multilayer platforms," *Langmuir*, vol. 17, pp. 6610–6615, 2001.

[84] S. C. Joo, *Adhesion mechanisms of nano-particle silver to electronics packaging materials*. PhD thesis, Georgia Institute of Technology, 2009.

[85] M. P. Turunen, P. Marjamäki, M. Paajanen, J. Lahtinen, and J. K. Kivilahti, "Pull-off test in the assessment of adhesion at printed wiring board metallisation/epoxy interface," *Microelectronics Reliability*, vol. 44, pp. 993–1007, 2004.

General conclusions and outlooks

Several direct-writing techniques were considered in Chapter 1 in the perspective of fabricating redistribution lines with high geometrical resolution. State-of-the-art approaches have been presented that were compatible with required line-width resolution. However, the throughput and fidelity of these technologies were determining when Gemalto and ENSM.SE have chosen to develop a drop-on-demand inkjet-printing system. Several conductive inks were examined with various size distributions and solvent vehicle composition. Driven by cost reduction considerations, conductive inks based on silver nanoparticles with an average diameter of 26 nm was chosen and the deposition process has subsequently been optimized. In the optimal conditions, lines with a width of 90 µm on polyimide and 130 µm on silicon nitride have been achieved using two pixels-width lines in order to guaranty the conformality of lines.

Regarding some perspectives, the prospective advantage of smaller nanoparticle size distribution should be considered. This size reduction would amplify the atomic diffusion processes and lower the sintering initiation temperature. This could eventually open new perspectives on low-Tg substrates such as PVC, PET or ABS (Figure 1). A reduction of line width can obviously be a source of improvement using specific printheads that deliver 1 to 5 pL droplets. However, issues concerning the formulation of the inks and especially regarding the evaporation of solvent will undoubtedly emerge and cause nozzle clogging. A more challenging outlook would be the formulation of composite or multiphysical inks (*e.g.* bi-metallic inks, ferromagnetic inks or Ag/Si composites). The curing step can then be used to produce alloys or specific behaviors, such as magnetic or mechanical properties.

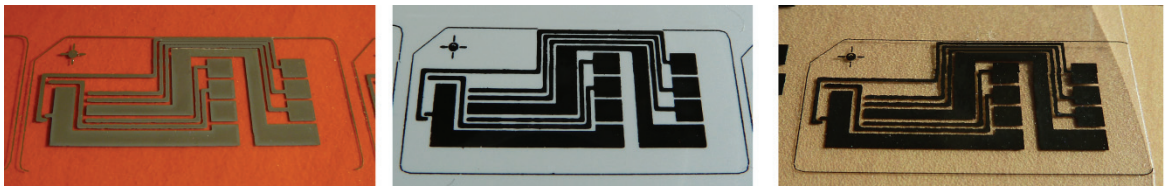

Figure 1: SIM card modules printed on Kapton, PVC and ABS (from left to right). Samples were cured at 110 °C during 2 h.

While conventional sintering treatments in printed electronics usually involve atmospheric oven, effects of sintering performed in rapid thermal annealing oven and hybrid variable frequency microwave oven are studied her. A special attention was put on a local characterization of crystalline state by electron backscattered diffraction in a SEM. This electronic diffraction technique was challenged at its lower detection threshold in order to finely probe the crystallographic orientation of grains in the nanoscale range. In particular, it has been shown in Chapter 2 that the sintering step of silver nanoparticles was interestingly not developing any preferential crystalline orientation. The sintering phenomenon was characterized by a grain growth activation energy with a value of 4.7 $kJ{\cdot}mol^{-1}$ which is lower

than other reports on evaporated polycrystalline thin films and could contribute to more accurate sintering modeling. High-resolution XRD measurements also indicated that the significant crystallite growth was associated to a decrease of the twin density from 1.6 % to 0.3 % between 150 °C and 500 °C. If a slight preferential orientation of grain were observed after being cured at 500 °C during 15 min on silicon, the phenomenon was all the more noteworthy when a seed layer was deposited with a preferential orientation. An approach taking advantage of diffusion-assisted sintering was thus suggested to transfer a crystallographic texture to the nanoparticulate film to increase mechanical properties of the deposit in the direction of subsequent solicitations, *e.g.* during a wire-bonding process.

Further development can be done on the sintering techniques, notably using emergent techniques such as the photonic curing which apply for interactions of radiations with matter. Optical absorption of nanoparticles is indeed a function of the wavelength. Applying an intense flash of light can indeed initiate coalescence phenomena, even in materials which easily oxidize, such as copper [1, 2]. A spontaneous reduction of copper oxides has indeed been reported recently [3]. Regarding microwave curing, very promising results have been achieved and reported [4], but further development and characterization have to be performed to mature the technique. Crystalline engineering can also be considered given the increased diffusivity of nanoparticles. Using atomic tracers as gold in silver can thus be suggested to acquire a better understanding of diffusion routes during sintering operation.

Electrical and mechanical properties of inkjet-printed thin films after the sintering step have been characterized in the Chapter 3. The Young's modulus evolution according to the sintering temperature was determined using both nanoindentation and bulge test techniques with a good agreement. A model based on the cellular structure of porous layers was exploited to assess the densification achieved during the curing treatment. A relative density of 90 % has thus been achieved after a sintering step of 800 °C during 15 min. The high density induced by the thermal treatment has been demonstrated to be correlated to localized microstrain. Printed films exhibited very low residual stress of 70 MPa. This result is all the more interesting that residual stress in microelectronic metallization is detrimental to reliability or bonding process. Nanoporous films are very complex structures with interconnected porosities which could interfere with probing during mechanical tests.

A threshold temperature at 300 °C has been brought to light during electrical measurement since the electrical resistivity is also equilibrating above 300 °C with a value of 3.4 µOhm·cm after 15 min. If electrical properties are very good on both polyimide and silicon, wire bonding performed on silver nanoparticulate film exhibited adhesion issues of the film to the substrate. Two approaches were suggested to enable the wire bondability on porous systems using either a seed layer or electroless nickel growth. The bond quality and strength were evaluated using wire pull test and ball shear test. Measured values of the load

at break were comparable to polycrystalline gold thin film with a resistance of 34 g in shear stress and 3 g in normal traction. The improved systems involving either a substrate with a {111} preferential orientation or an electroless nickel growth thus exhibits sufficient electrical and mechanical properties to successfully perform wire bonding operation. A demonstrator implementing an integrated circuit on a flexible polyimide substrate has been performed and shown the proficiency of inkjet printing technology for multimaterial microelectronics devices.

Several other elements can represent the technological heart of the future integration of inkjet-printing technology to production process flow. An extension towards flip chip process can therefore be considered given the porosity fraction which can accommodate easily the deformation consecutive to the insertion of studs or microinserts. We could also use inkjet to print on steps, for example across an integrated circuit edges. Other applications encompass filling large through silicon vias (TSV) or performing connection between chips and antennas. Comparatives approaches exploiting the inkjet-printing technology on flexible substrates are reported in Figure 2.

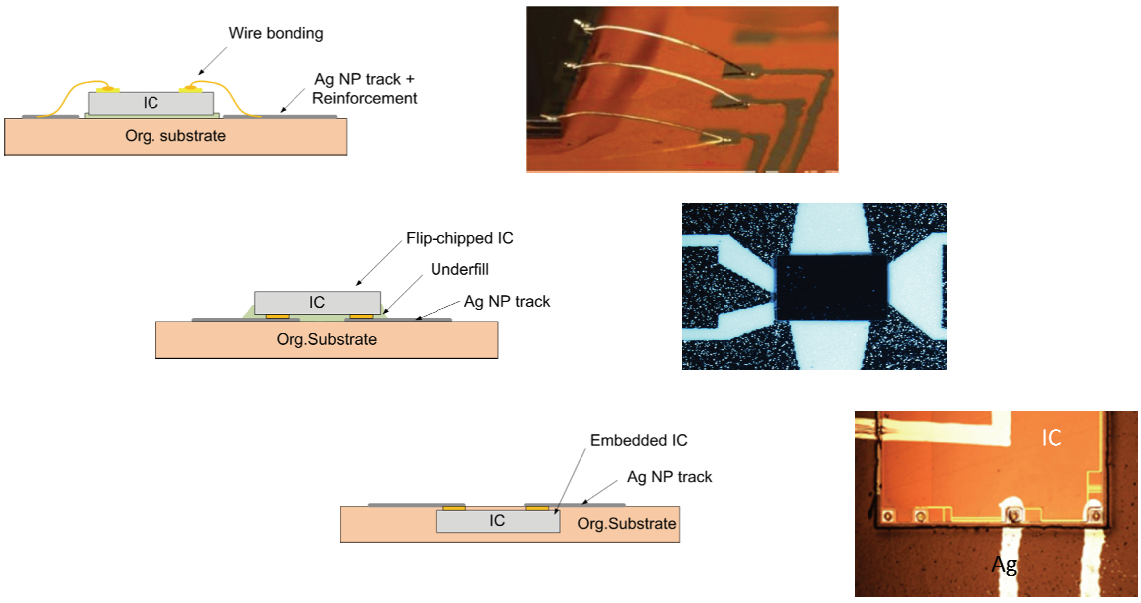

Figure 2 : Comparative approaches implementing the inkjet-printing technology with a decreasing degree of hybridization with conventional process, and a decreasing overall thickness.

To conclude, this work was the first PhD thesis funded by Gemalto on inkjet-printing technology. The very promising results presented in this work have conducted Gemalto to pursue this collaboration with the Ecole Nationale Supérieure des Mines de Saint-Etienne through another PhD thesis funding. This work has thus been the opportunity to find new outlooks as much from an industrial point of view for Gemalto than for academic perspectives for ENSM.SE.

References

[1] H.-S. Kim, S. Dhage, D.-E. Shim, and H. Hahn, "Intense pulsed light sintering of copper nanoink for printed electronics," *Applied Physics A: Materials Science & Processing*, vol. 97, pp. 791–798, 2009.

[2] N. Marjanovic, J. Hammerschmidt, J. Perelaer, S. Farnsworth, I. Rawson, M. Kus, E. Yenel, S. Tilki, U. S. Schubertc, and R. R. Baumann, "Inkjet printing and low temperature sintering of cuo and cds as functional electronic layers and schottky diodes," *Journal of Materials Chemistry*, vol. 21, pp. 13634–13639, 2011.

[3] K. A. Schroder, I. M. Rawson, D. S. Pope, and S. Farnsworth, "Photonic curing explanation and application to printing copper traces on low temperature substrates," in *44th International Symposium on Microelectronics IMAPS*, 2011.

[4] R. Cauchois, M. Saadaoui, A. Yakoub, K. Inal, B. Dubois-Bonvalot, and J.-C. Fidalgo, "Optimal sintering technologies applied to inkjet-printed silver nanoparticles for microelectronics applications," in *International Conference on Sintering*, 2011.

List of publications

Journal with peer review:

- Cauchois, R.; Saadaoui, M.; Yakoub, A.; Inal, K.; Dubois-Bonvalot, B. & Fidalgo, J.-C., "Impact of variable frequency microwave and rapid thermal sintering on microstructure of inkjet-printed silver nanoparticles", *Journal of Materials Science* (in Press), **2011** – doi: 10.1007/s10853-012-6366-6
- Cauchois, R.; Gergaud, P.; Borbély, A.; Saadaoui, M. & Inal, K., "In-situ stress measurements in nanoporous silver thin films", *Applied Physics Letters* (submitted)
- Cauchois, R.; Saadaoui, M. & Inal, K., "Dépôt par jet d'encre de nanoparticules métalliques et recuit sélectif associé : application à la réalisation de pistes métalliques pour la microélectronique", *Techniques de l'Ingénieur* (submitted)

Conferences with proceedings:

- Cauchois, R.; Saadaoui, M.; Legeleux, J.; Malia, T.; Dubois-Bonvalot, B.; Inal, K. & Fidalgo, J.-C., "Wire-bonding on inkjet-printed silver pads reinforced by electroless plating for chip on flexible board packages", *Electronic System-Integration Technology Conference (ESTC),* **2010** – doi: 10.1109/ESTC.2010.5642997

- Cauchois, R.; Saadaoui, M.; Inal, K.; Dubois-Bonvalot, B. & Fidalgo, J.-C. "Tailoring the crystallographic texture and electrical properties of inkjet-printed interconnects for use in microelectronics", *Materials Research Society Spring Meeting,* **2011** – doi: 10.1557/opl.2011.1264
- Yakoub, A.; Saadaoui, M. ; Cauchois, R. ; Li, J.-M. and Benaben, P., "An Improved In-Line Inkjet Printing Process for 3D Multilayer Passive Devices", *Materials Research Society Fall Meeting* (in Press), **2011**

Conferences without proceedings :

- Cauchois, R.; Saadaoui, M.; Inal, K.; Dubois-Bonvalot, B. & Fidalgo, J.-C. "Thermal optimization of silver nanoparticles sintering for low resistive printed applications", *MicroMechanics Europe Workshop,* **2009**
- Cauchois, R.; Saadaoui, M.; Inal, K.; Dubois-Bonvalot, B. & Fidalgo, J.-C. "Direct-writing of conductive patterns based on printed and sintered silver nanoparticles", *Arcsis Micropackaging Days,* **2009**
- Cauchois, R.; Saadaoui, M.; Inal, K.; Dubois-Bonvalot, B. & Fidalgo, J.-C. "Printed Ag nanoparticles on evaporated Au system: impact of microstructure on mechanical and electrical properties", *European Materials Research Society Spring Meeting,* **2011**
- Cauchois, R.; Saadaoui, M.; Yakoub, A.; Inal, K.; Dubois-Bonvalot, B. & Fidalgo, J.-C., "Optimal sintering technologies applied to inkjet-printed silver nanoparticles for microelectronics applications", *International Conference on Sintering,* **2011**
- Cauchois, R.; Sao-Joao, S. ; Borbély, A. ; Saadaoui, M.; Inal, K.; "XRD and TEM investigation of annealed silver nanoparticle thin films", *Conférence Rayons X et Matière* , **2011**
- Cauchois, R.; Saadaoui, M.; Legeleux, J.; Malia, T.; Dubois-Bonvalot, B.; Inal, K. & Fidalgo, J.-C., "Chip integration using inkjet-printed silver conductive tracks reinforced by electroless plating for flexible board packages", *IMAPS Micro/Nano-electronics Packaging and Assembly Design and Manufacturing Forum (MiNaPAD),* **2012**
- Cauchois, R.; Żymełka, D.; Inal, K. & Saadaoui, "Selective sintering of inkjet-printed silver inks using variable frequency microwave", *Global Congress on Microwave Energy Applications (GCMEA),* **2012**

Patent:

- Cauchois R. & Dubois-Bonvalot, B., "Procédé pour réaliser des lignes d'interconnexion ou de redirection d'au moins un composant à circuit intégré", European Patent # 10306192.5. Filled on **29/10/2010**

Microstructuration des dépôts imprimés par jet de matière : de la coalescence des nanoparticules d'argent vers la réalisation d'interconnexions de composants électroniques

Résumé

Introduction

La réalisation d'interconnexions est une étape fondamentale lors de la fabrication de micro-assemblages qui permet aux différents composants de communiquer entre eux via un signal électrique. Considéré comme le chef de file mondial de la sécurité numérique [1, 2], le groupe Gemalto cherche à rester à la pointe de l'innovation en termes de procédés et d'applications. En cela, le développement de l'électronique imprimée est perçu comme une nouvelle opportunité pour la fabrication d'objets fins et flexibles à bas coûts.

A l'heure actuelle, le procédé de photolithographie est couramment employé dans l'industrie microélectronique pour la réalisation de micro-assemblages. Ce procédé soustractif se déroule en 6 étapes principales : dépôt d'une couche mince métallique, dépôt et polymérisation d'une résine photosensible, insolation UV de la résine à travers un masque préalablement aligné, développement et suppression de la résine insolée, gravure de la couche métallique exposé et retrait de la résine résiduelle. L'impression par jet de matière, quant à elle, introduit un avantage technologique significatif en réduisant le nombre d'étapes de procédé d'un facteur 3 par rapport à la photolithographie (voir Figure 1). Le procédé se décompose en 2 étapes principales que sont le dépôt direct d'une encre à base de nanoparticules d'argent et son recuit pour permettre l'évaporation des solvants et la constitution d'un film conducteur continu. Le recuit peut être opéré dans une étuve traditionnelle ou par un recuit sélectif, que ce soit par laser, micro-onde ou effet Joule [7-9].

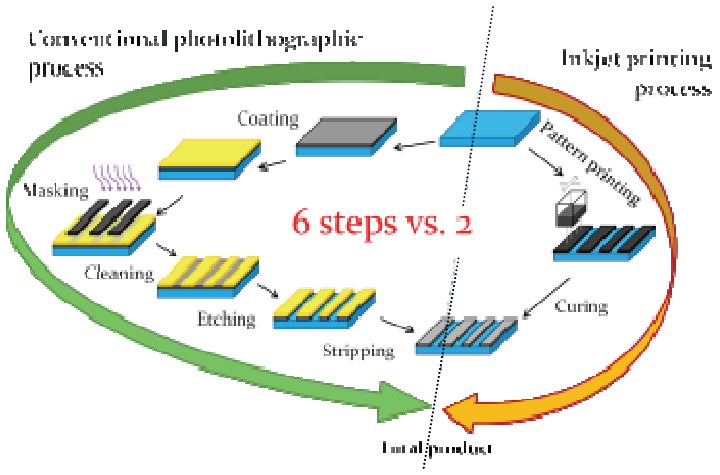

Figure 1 : Approches comparatives entre le procédé conventionnel de photolithographie et le jet de matière.

La possibilité de fabriquer des structures conductrices sans étape supplémentaire de procédé permet d'accroître le rendement de manière significative. Cette approche additive permet de gagner à la fois du temps et de l'argent en limitant les pertes de matière lors de la réalisation d'interconnections 2D et de composants électroniques passifs. D'autres applications de niches ont également été identifiées et des démonstrateurs fonctionnels ont

été présentés par le passé. Parmi les applications les plus notables de cette technologie, on peut citer les interconnections dans les microcircuits, les électrodes pour les antennes et le photovoltaïque, les couches actives de transistors organiques, les diodes électroluminescentes, les batteries et les cellules photovoltaïques.

D'un point de vue académique, la réalisation de telles structures soulèvent plusieurs problématiques qui sont adressées successivement dans le résumé de ces travaux. Dans une première partie, l'optimisation du procédé d'impression par jet de matière sera considérée en fonction de la rhéologie de l'encre utilisée et des interactions fluide/substrat, pour la réalisation d'interconnexions électriques. Une étude de l'évolution microstructurale sera ensuite présentée dans une deuxième partie pour permettre une meilleure compréhension de la relation entre le procédé d'impression et la microstructure fine du dépôt. Enfin, dans une troisième partie, cette évolution sera corrélée aux propriétés d'usage de ces motifs, à savoir la résistivité électrique et la rigidité mécanique. Ces deux propriétés conditionnent, en effet, la bonne tenue des étapes ultérieures de micro-assemblage qui seront implémentées pour la fabrication de démonstrateurs fonctionnels.

I. Implémentation du jet de matière pour les interconnections en microélectronique

Au cours des deux dernières décennies, l'utilisation des technologies d'écriture directe est apparue comme un changement du paradigme basé sur l'approche lithographique traditionnelle. Parmi les différentes techniques d'écriture directe, l'impression par jet de matière est celle qui a connu le développement le plus important, notamment en lien avec l'essor de la microinformatique et des imprimantes bureautiques. L'utilisation de cette technique a été rendue possible par le développement récent d'encres fonctionnelles, notamment à base de nanoparticules d'argent.

A. Technologie jet de matière pour l'écriture directe

L'impression par jet de matière est basée sur la formation de gouttelettes au niveau de l'orifice d'éjection sous l'action de la tension de surface, également connue sous le nom d'instabilité de Rayleigh-Tomotika [28, 29]. L'éjection de ces gouttelettes peut être réalisée de manière continue ou intermittente. Cette dernière méthode est l'approche privilégiée dans le domaine de l'électronique imprimée et est désignée sous le terme d'approche en « goutte à la demande ». Les gouttes sont en effet générées et éjectées de manière contrôlée sur le substrat en utilisant soit des têtes d'impression thermiques, soit des têtes d'impression piézoélectriques (voir Figure 2Figure I-5).

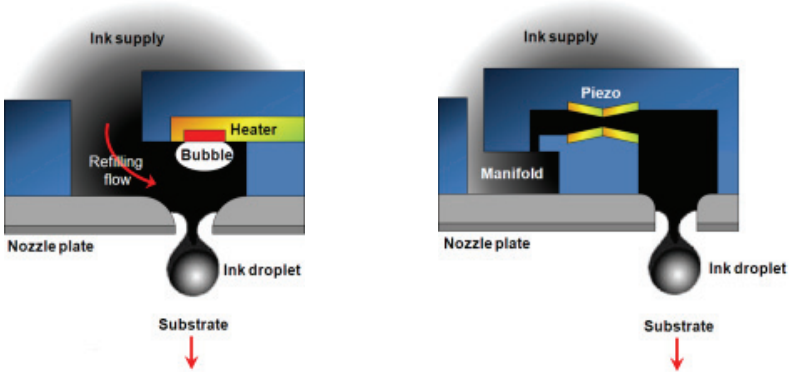

(a) (b)

Figure 2: Schémas de fonctionnement de têtes d'impressions en goutte à la demande : systèmes d'impression thermique (a) et piézoélectrique (b).

Dans le cadre de ces travaux de thèse, les impressions ont été réalisées à l'aide d'un prototype pré-industriel installé dans une salle blanche, environnement qui permet de contrôler la concentration de particules dans l'air. Cet équipement d'impression, appelé JetPac, a été développé sur la plateforme technologique de l'école en collaboration avec plusieurs industriels, dans le but de développer un procédé stable qui intègre différents modules dans une approche de procédé en ligne. Le substrat est placé sur un convoyeur qui se déplace entre chaque module suivant la procédure appliquée. Les différents modules intégrés dans JetPac incluent des équipements de pré-traitement de surface (torche plasma atmosphérique), d'impression (encre conductrice ou encre isolante UV) et de post-traitement (lampe UV et cavité micro-onde) qui sont représentés sur la Figure 3 et Figure 4.

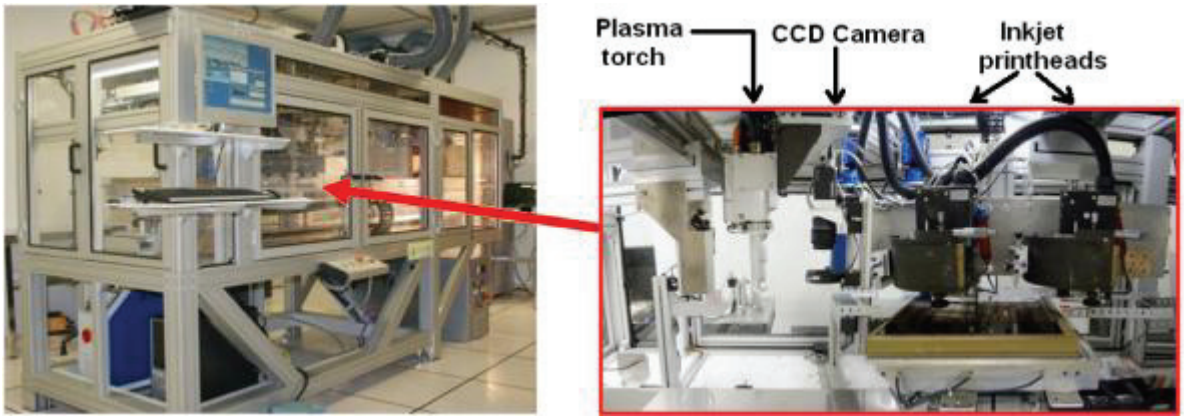

Figure 3: Vue du prototype JetPac dans une salle blanche de classe 1000 (gauche) avec les différents modules internes (droite).

Figure 4: View of the post-treatment equipments integrated in JetPac: UV lamp and microwave cavity in a HVFM configuration.

Le prototype JetPac met en œuvre des têtes d'impression piézoélectriques où les gouttelettes d'encre sont générées en accroissant la pression à l'intérieur des canaux d'alimentation des buses d'éjection grâce à un cristal piézoélectrique. L'activation de ces cristaux est réalisée grâce à une impulsion électrique bipolaire (voir Figure 5). La déformation mécanique du cristal permet de générer une onde acoustique dans le canal pour éjecter une goutte d'encre de la buse.

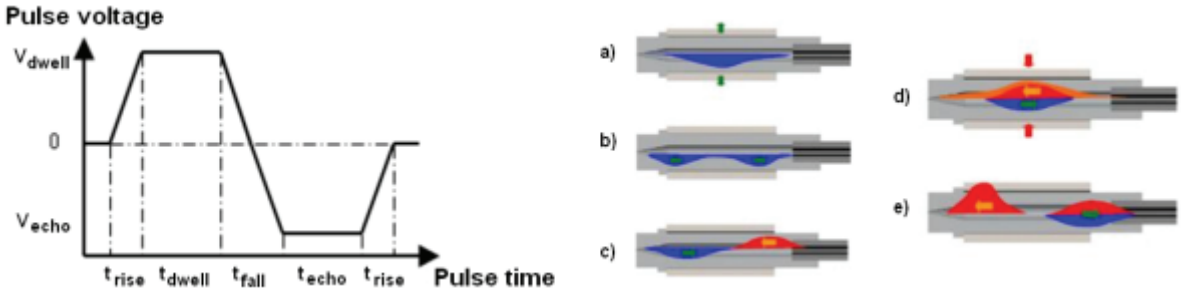

Figure 5: Schéma d'une impulsion bipolaire typique envoyée à un actionneur piézoélectrique (gauche) et son impact sur les interactions entre les ondes acoustiques générées (droite) [98].

En théorie, la résolution de la tête devrait être identique à celle obtenue lors de l'impression, mais en raison des interactions entre le fluide et le substrat, la goutte va avoir tendance à s'étaler au delà de cette résolution théorique. Un recouvrement partiel de ces gouttes va alors permettre de réaliser des lignes continues et rectilignes. Ce recouvrement dépend du volume des gouttes éjectées et des interactions entre le fluide et le substrat. A titre d'exemple, une goutte d'encre déposée sur polyimide aura en moyenne un diamètre de 50 µm alors que la résolution théorique définie par la tête d'impression est de 41 µm.

Plusieurs phénomènes peuvent toutefois conduire à des défauts du motif imprimé en raison, soit à un manque d'adéquation entre l'énergie de surface du substrat et la tension superficielle de l'encre, soit aux interactions opérant au niveau de la tête d'impression. Dans

ce dernier cas, les phénomènes les plus critiques sont notamment le bouchage total ou partiel des buses d'éjection dû à une évaporation trop importante des solvants de l'encre et à une coagulation partielle de l'encre, ainsi que la formation erratique de gouttelettes satellites. Ces deux phénomènes peuvent conduire à la formation de courts-circuits entre deux pistes contiguës ou d'un non respect des dimensions du motif notamment en termes de largeur de lignes (voir Figure 6Figure I-30).

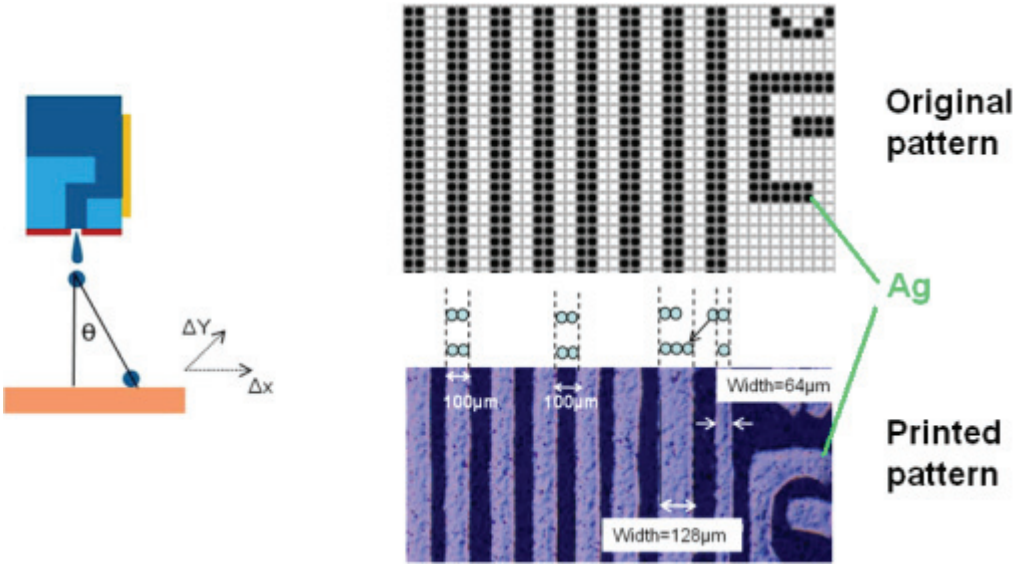

Figure 6 : Image d'un motif conducteur imprimé avec JetPac sur un substrat polyimide mettant en évidence deux lignes dont la largeur correspond à un ou deux pixels de large, alors que la largeur théorique correspond à deux pixels. Sur l'image, l'argent apparaît en bleu clair alors que le substrat apparaît en bleu foncé.

L'impression par jet de matière constitue un système complexe qui est le lieu de nombreuses interactions entre le système d'impression (diamètre de buse, tension d'éjection, mise sous pression, …), le substrat (énergie de surface, rugosité, température, …) et l'encre (viscosité, tension superficielle, taille de nanoparticules, …). Les différents paramètres sont en grande partie interdépendants et un compromis entre la résolution d'impression, la reproductibilité et l'adhésion doit être trouvé. L'analyse de la taille, du positionnement et de la déformation des gouttes déposées par JetPac dans des conditions standards permet ainsi de mettre en évidence une erreur quadratique moyenne en positionnement de 10 µm et une distribution bimodale de taille de goutte centrée autour de 90 et 104 µm. L'optimisation réalisée des paramètres d'impression permet donc de se conformer aux spécifications de résolution définies par Gemalto.

B. Préparation d'encres à base de nanoparticules métalliques

Le développement de l'électronique imprimée basée sur l'utilisation de technologies matures d'éjection a été rendu possible, ces dernières années, par le développement d'encres fonctionnalisées. Parmi les encres les plus courantes, les encres à base de nanoparticules métalliques, et notamment d'argent, ont connu le développement le plus important. L'utilisation de nanoparticules se justifie à la fois par les petites dimensions des buses d'éjection et par l'exploitation de l'effet thermodynamique de la taille de particule. En effet, plus le diamètre des particules est petit, plus la température apparente de fusion va diminuer, facilitant ainsi la coalescence. Cet effet est d'autant plus significatif quand la taille des nanoparticules est inférieure à 10 nm.

Pour réaliser l'impression, ces nanoparticules d'argent sont mises en solution dans un mélange de solvants. Ce mélange permet à la fois d'éviter la sédimentation des nanoparticules en exploitant le phénomène de répulsion stérique avec le polymère d'enrobage, ainsi que de garantir une viscosité suffisamment faible pour être processable dans les têtes d'impression. L'adjonction d'agents mouillants supplémentaires permet alors d'agir sur la tension superficielle de l'encre qui agira directement sur la résolution des lignes imprimées (voir Figure 7). Un substrat hydrophile sera alors capable de créer des liaisons hydrogène avec des solvants polaires, tels que les alcools présents dans notre encre.

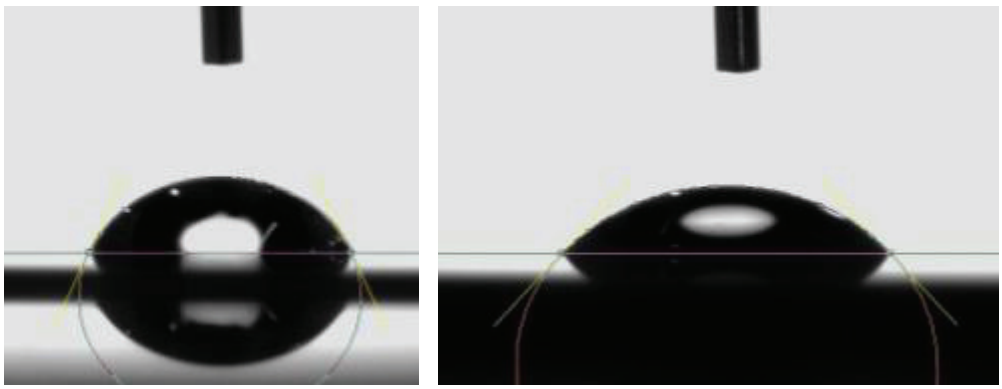

Figure 7 : Profil d'une goutte d'eau déposée sur un substrat de silicium (gauche) et de nitrure de silicium (droite), montrant une variation de l'angle de contact de 68° à 51°, respectivement.

Dans le cadre de l'électronique imprimée, les solvants présents dans l'encre doivent donc être évaporé afin d'établir le contact physique entre les nanoparticules et d'obtenir ainsi des lignes conductrices. L'encre argent utilisée dans le cadre de ces travaux est approvisionnée auprès de Sun Chemical, sous la référence Sun Tronic U5603. Les nanoparticules présentent une taille moyenne de 25-30 nm et sont mise en suspension dans un mélange d'éthanol (25 à 40 %, $T_{évap}$=79 °C), d'éthylène glycol (25 à 40 %, $T_{évap}$=197 °C) et de glycérol (10 à 25 %, $T_{évap}$=290 °C).

C. Traitement des dépôts métalliques

Lors de l'évaporation des solvants, la ligne imprimée peut perdre jusqu'à 70% de son volume et subit un léger retrait par rapport à la résolution précédemment observée (voir Figure 8). Ce retrait est directement corrélé à l'adhésion apparente de l'encre sur le substrat, i.e. à l'énergie de surface et à la rugosité du substrat notamment.

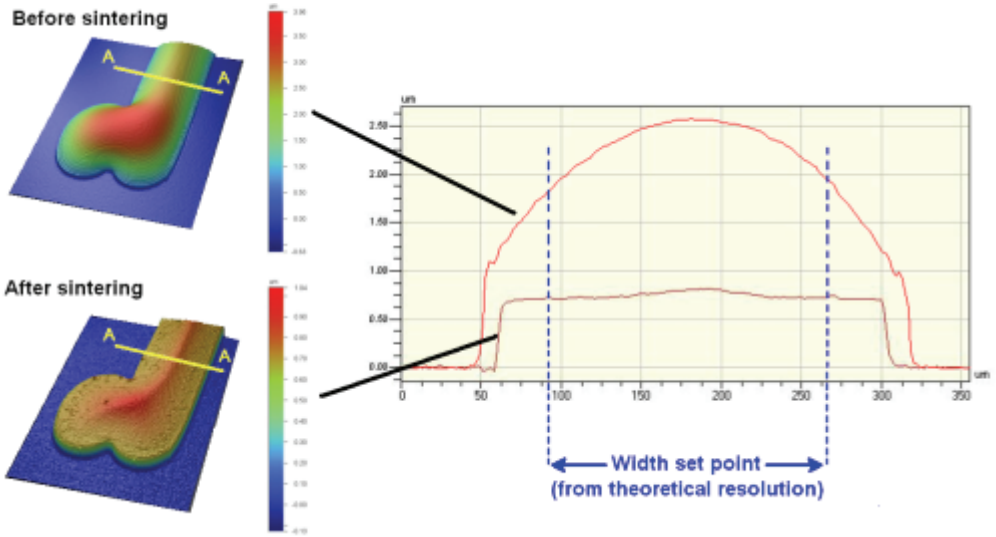

Figure 8 : Profil d'une ligne d'argent imprimé sur un substrat de nitrure de silicium avant et après un recuit de 15 min à 250 °C.

La surface de contact entre le substrat et l'encre, ainsi que la conductivité thermique influence la capacité d'évaporation des solvants. En effet, une analyse calorimétrique réalisée dans des conditions standards dans des creusets en aluminium montre un comportement radicalement différent des gouttes imprimées sur des substrats de silicium (Si) ou de nitrure de silicium (SiN_x). Si les températures d'évaporation des solvants dans un creuset en aluminium correspondent aux valeurs tabulées, les gouttes imprimées sur Si et SiN_x présentent des températures d'évaporation très nettement inférieures (voir Figure 9). Ainsi, un traitement thermique limité à 150 °C ne permettra d'évaporer que l'éthanol dans le cas d'un dépôt à la seringue sur aluminium, alors que tous les solvants présents seront évaporés dans le cas de gouttelettes imprimées par jet de matière.

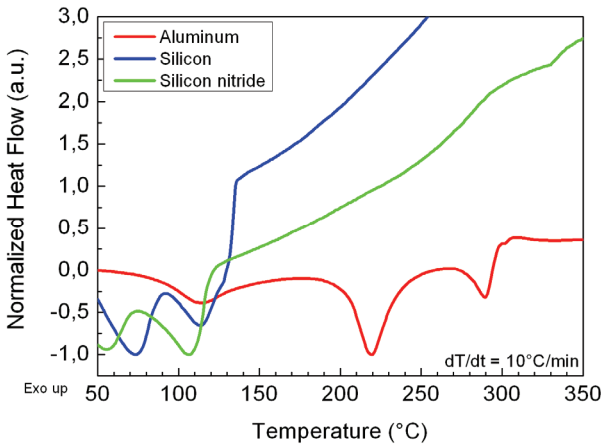

Figure 9 : Thermogramme de DSC de l'encre argent déposée à la seringue dans un creuset d'aluminium ou par jet de matière sur un substrat de silicium ou de nitrure de silicium. Les signaux sont normalisés sur l'intensité du pic de l'éthylène glycol.

Cette évaporation des solvants à basse température permet ainsi l'activation de la conductivité électrique très rapidement, dès 120 °C. Au plus la température de traitement sera importante, au plus la résistivité électrique sera faible et approchera la valeur de l'argent massif (1.61 µOhm.cm) (voir Figure 10). Par ailleurs, l'obtention de faibles résistivités électriques sera d'autant plus rapide que la température de chauffage sera élevée car celle-ci permettra l'activation de davantage de mécanismes de diffusion (voir section suivante).

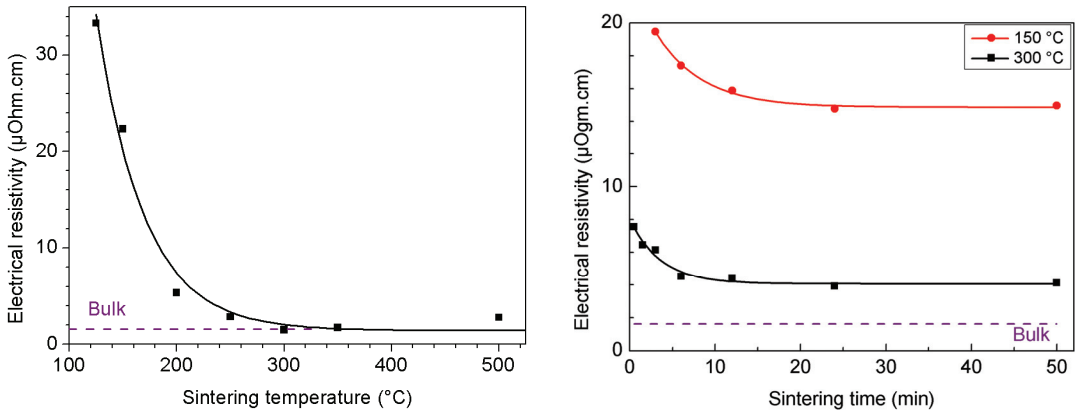

Figure 10 : Évolution de la résistivité électrique des films d'argent imprimés sur un substrat silicium en fonction de la température de recuit (pendant 15 min) et du temps de recuit (rampe de chauffage de 10 °C/s).

Pour des substrats plastiques, l'obtention de lignes faiblement résistives sera difficilement réalisable avec des procédés classiques. Pour le développement de l'électronique imprimée sur substrat flexible, il est donc nécessaire de trouver un procédé de recuit compatible avec une transition vitreuse à faible température. Pour cela, plusieurs approches sont possibles : soit réduire la taille des nanoparticules pour exploiter l'effet thermodynamique,

particulièrement prépondérant lorsque le diamètre est inférieur à 10 nm, soit utiliser une méthode de recuit sélectif compatible avec les nanoparticules métalliques. Un recuit sélectif permettra alors d'augmenter localement la température à l'intérieur de la couche imprimée sans provoquer d'échauffement du substrat. Parmi les différents recuits utilisés dans la littérature, les recuits micro-onde, photonique, laser, électrique ou chimique sont particulièrement étudiés. Dans ces travaux, un recuit infrarouge mettant en œuvre des rampes de températures élevées et un recuit micro-onde sont utilisés afin de réduire la résistivité des lignes. En agissant sur les paramètres du procédé de recuit (température, temps, rampe, puissance notamment), une variation de la microstructure sera observée (voir Figure 11 et Figure 12) en lien avec une évolution de la rigidité mécanique et de la résistivité électrique.

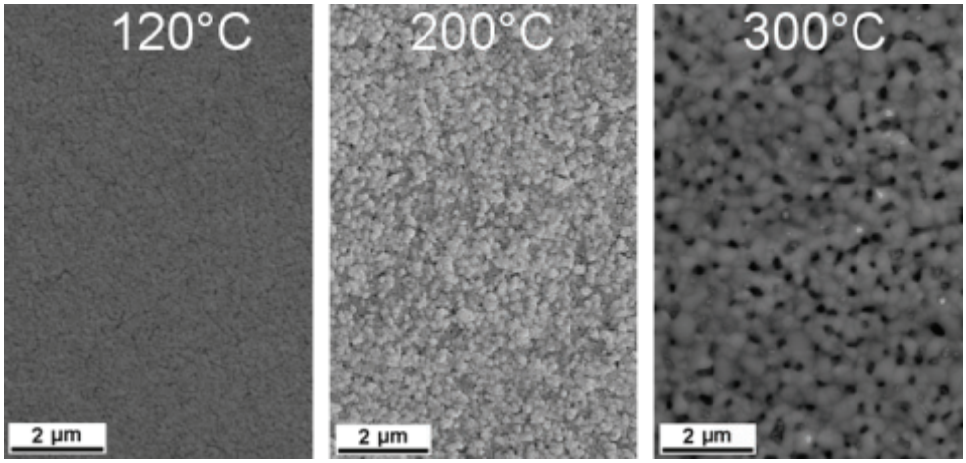

Figure 11 : Evolution de la microstructure à la surface de films minces d'argent après recuit au RTA pendant 15 min avec une rampe de chauffage de 10 °C/s.

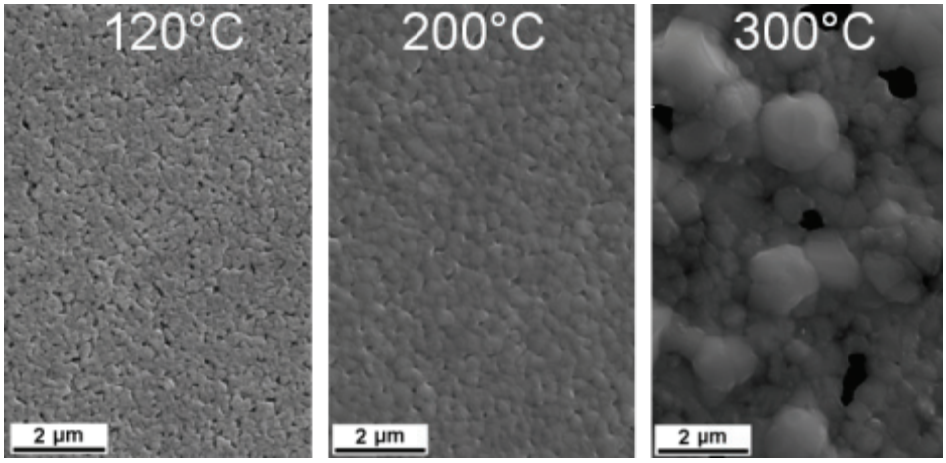

Figure 12 : Evolution de la microstructure à la surface de films minces d'argent après recuit micro-onde à fréquence variable pendant 15 min avec une rampe de chauffage de 10 °C/s.

II. Microstructure des films minces déposés par jet de matière

L'évolution de la microstructure en fonction des paramètres de recuit et du type de rayonnement utilisé joue un rôle primordial dans l'optimisation des propriétés d'usage du film imprimé, à savoir la rigidité mécanique et la résistivité électrique. Pour y parvenir, une meilleure compréhension des mécanismes en jeu et analyse fine de la microstructure est nécessaire.

A. Évolution microstructurale pendant la coalescence

Au cours du recuit, les différents mécanismes de diffusion de matière conduisent à une évolution de la microstructure du film déposé. En effet, lors d'une étape de chauffage, les nanoparticules métalliques du dépôt subissent deux phénomènes concomitants que sont la coalescence et la croissance de grain. Dans les deux cas, ces phénomènes mettent en jeu des diffusions atomiques induites par une minimisation de l'énergie de surface. Une variation de la microstructure peut être observée à travers l'évolution de la taille de grain ou de la taille de pore via l'analyse d'images obtenues dans un MEB. Il faut alors détourer les grains soit en appliquant une méthode de seuillage numérique (voir Figure 13) quand le contraste est suffisant entre le grain et le joint de grain, soit manuellement dans un logiciel de traitement d'images.

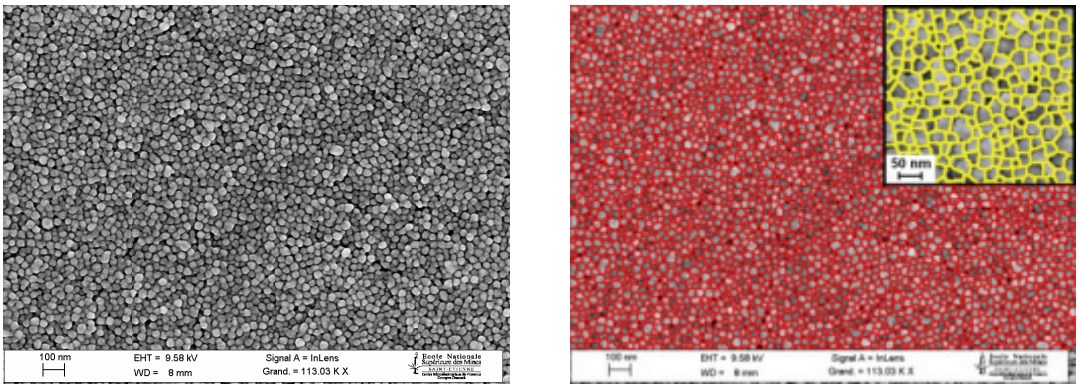

Figure 13 : Image MEB de la surface d'un film de nanoparticules d'argent après séchage de l'encre par en étuve à 200 °C pendant 5 min (gauche) avec le contour des grains obtenu après une opération de seuillage (droite).

Toutefois, lors des observations au microscope électronique en haute résolution, à l'échelle locale, des sous-structures ont été mises en évidence à l'intérieur des nanoparticules : sous-grain ou macle. En effet, lorsque le métal présente une énergie de faute d'empilement faible, comme c'est le cas de l'argent (γ_{isf} = 18 mJ·m^{-2}), il a tendance à former facilement des macles lorsqu'il est soumis à une sollicitation thermomécanique (voir Figure 14). Ces macles constituent des cristallites dont la structure cristalline est identique à celle de

la phase mère. La macle a donc une structure CFC mais présente une désorientation angulaire qui dépend du nombre d'atomes en cohérence entre les phases mère et fille.

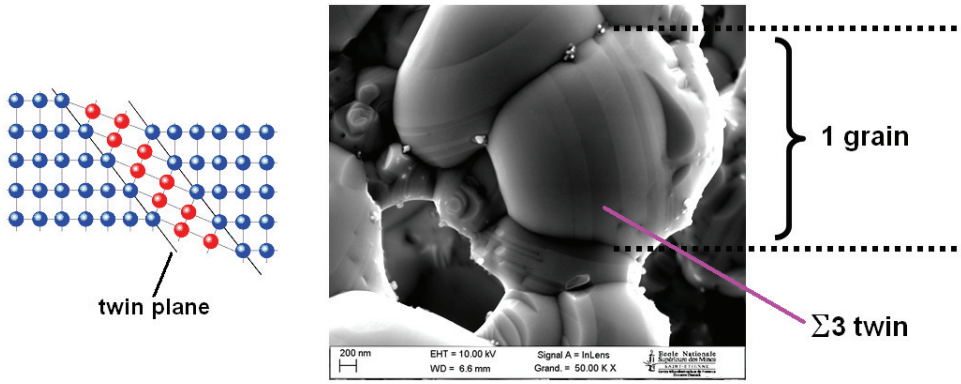

Figure 14 : Image MEB d'un système de macles Σ3 découlant d'une rotation-glissement à l'intérieur d'un grain d'argent obtenu après le chauffage de nanoparticules à 500 °C.

La taille de ces macles peut être déterminée en utilisant la technique de diffraction des électrons rétrodiffusés (*EBSD*, pour Electron BackScattered Diffraction) à l'intérieur d'un MEB. En déplaçant le faisceau électronique avec un pas fixe, cette technique permet de caractériser l'orientation cristallographique de chaque point via l'analyse du cliché de diffraction correspondant. La cartographie obtenue après avoir balayé la surface du film permet alors de déterminer l'orientation cristalline et la taille moyenne de chaque cristallite. En traçant l'évolution de cette taille moyenne de cristallites en fonction de l'inverse de la température, une énergie d'activation E_A peut être calculée en supposant qu'elle suit une loi d'Arrhenius d'ordre 2, telle que :

$$ln\left(\frac{G^2 - G_0^2}{t}\right) = lnK_0 - \frac{E_A}{RT} \qquad (1)$$

où G est le diamètre moyen du grain, K_0 est une constante pré-exponentielle, t est le temps de recuit isotherme, R est la constante des gaz parfait (R=8,314472 $J{\cdot}mol^{-1}{\cdot}K^{-1}$) et T est la température absolue. Comme reporté sur la Figure 15, une énergie d'activation de 4,7 ± 0,5 $kJ{\cdot}mol^{-1}$ est calculée. Cette énergie d'activation apparente correspond à notre situation spécifique où le phénomène de croissance de grain se déroule simultanément au processus de coalescence. Ainsi, l'énergie thermique fournie au système durant le recuit est répartie entre les deux phénomènes. Étant à l'origine de la coalescence et de la croissance de grain, la diffusion atomique est au cœur de notre étude sur l'évolution de la microstructure.

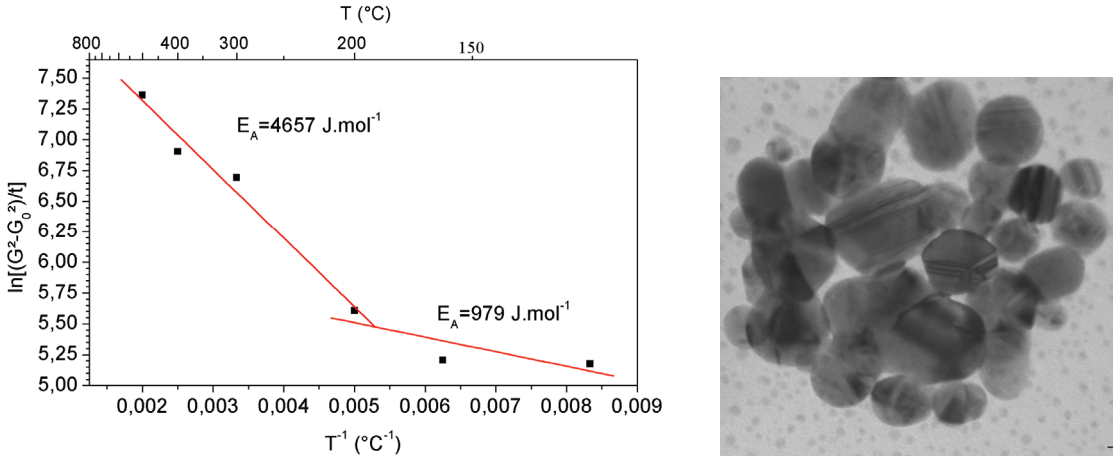

Figure 15: Graphique d'Arrhenius de la croissance des cristallites d'argent déterminée à partir des analyses par EBSD (gauche). Image en microscopie électronique en transmission des nanoparticules d'argent (droite).

L'énergie d'activation apparente est très inférieure aux 53 kJ.mol^{-1} nécessaires pour l'activation de la croissance normale de grains dans les travaux de Dannenberg *et al.* [62] pour des films d'argent déposés par pulvérisation cathodique. Cette différence par rapport à nos résultats peut provenir du faible niveau de contraintes présentes dans le film (voir partie suivante) malgré une épaisseur de films 6 fois inférieure à la configuration de Dannenberg. Thompson a en effet démontré qu'un faible rapport épaisseur de film/taille de grain limitait le développement de la croissance anormale de grain [63] dont l'énergie d'activation est beaucoup plus faible (27 kJ.mol^{-1}, [64]). Par ailleurs, une contribution à cette faible valeur peut aussi être attribuée à la grande densité de défauts dans les nanoparticules comparativement aux films évaporés. En ce sens, les microdéformations du réseau cristallin contribuent positivement à l'activation des mécanismes de diffusion conduisant aux phénomènes de coalescence/croissance.

La Diffraction par Rayons-X (DRX) peut également être employée comme technique non-destructive d'analyse. L'évolution de la microstructure peut être traitée par le biais de l'analyse de l'élargissement des pics qui est corrélée à la taille et aux microdéformations des cristallites. En ce sens, la DRX fournit d'avantage d'informations que l'EBSD car elle donne accès à une analyse quantitative de la texture cristallographique, de la taille moyenne de cristallites, des microdéformations, des contraintes internes. L'intensité des pics, quant à elle, est la convolution entre l'arrangement atomique et la fonction décrivant la forme du cristal [66]. La taille moyenne de cristallite, la densité de défauts planaires et la microdéformation moyenne sont déterminées selon la méthode de Warren-Averbach en utilisant les paires de réflexion 111/222 et 200/400 [69, 72]. Une correction préalable des erreurs instrumentales est réalisée suivant la méthode de Stokes [73].

Comme attendu avec les phénomènes de coalescence et de croissance de grain, la taille moyenne des cristallites augmente avec la température de recuit (voir Table 1), confirmant

ainsi les premières observations réalisées en microscopie électronique. Contrairement à l'EBSD qui renseigne uniquement sur les grains présents à la surface de l'échantillon considéré, la DRX permet d'avoir une approche plus représentative de l'état cristallographique du film car le faisceau incident sonde l'ensemble des cristallites dans l'épaisseur de la couche.

Table 1 : Taille moyenne des cristallites D, densité de macles β, microdéformation moyenne (déformation moyenne quadratique = $\langle\varepsilon^2\rangle_{hkl}^{1/2}$) en fonction de la température de recuit.

Température de recuit	D (nm)	β [%]	$\langle\varepsilon^2\rangle_{111}^{1/2}$	$\langle\varepsilon^2\rangle_{100}^{1/2}$
150 °C	18 ± 2	1.6 ± 0.10	$7 \pm 1 \cdot 10^{-4}$	$21 \pm 8 \cdot 10^{-4}$
300 °C	96 ± 10	0.8 ± 0.05	$4 \pm 4 \cdot 10^{-4}$	$9 \pm 4 \cdot 10^{-4}$
500 °C	160 ± 20	0.3 ± 0.02	$2 \pm 0.8 \cdot 10^{-4}$	$3 \pm 0.5 \cdot 10^{-4}$

L'évolution de la densité de macles β montre une proportion significative de macles dans le film comme observé précédemment (voir Figure 14 et Figure 15). La fabrication des nanoparticules par Cabot et le traitement ultérieur réalisé par Sun Chemical est probablement à l'origine de la présence initiale de ces macles due à l'accommodation aux sollicitations mécanique et thermique. Ainsi, lors du recuit, un phénomène de relaxation se produit, conduisant à une diminution de la densité des macles.

En ce qui concerne la moyenne quadratique des microdéformations, la distribution peut être attribuée à une évolution caractéristique du champ de déformation à proximité des joints triples, et plus généralement à proximité des joints de grains. Les projections de la déformation moyenne suivant les directions <111> et <200> ont tendance à décroître avec l'augmentation de la température de recuit, conformément aux prévisions. En effet, plus la température de recuit est importante, plus le phénomène de restauration sera important. La relaxation de ces microdéformations est ainsi la conséquence du phénomène de restauration au cours duquel les défauts cristallins à l'intérieur des cristallites sont annihilés.

B. Transfert de texture cristallographique assisté par diffusion atomique

Dans les métaux à structure CFC, la minimisation de l'énergie de surface a tendance à favoriser la croissance des grains {111} alors que la minimisation de l'énergie de déformation élastique favorisera davantage la croissance des grains {100} au détriment des autres orientations cristallographiques [74]. En règle générale, les méthodes conventionnelles de dépôt de couches minces CFC conduisent à des films qui ont une orientation cristallographique préférentielle {111} [44, 45]. Dans le cas du dépôt par jet de matière, les nanoparticules d'argent sont déposées aléatoirement sur la surface lors de l'impression. En

conséquence, le film de nanoparticules ne présente pas d'orientation cristallographique préférentielle.

Pour développer une texture cristallographique spécifique, il est nécessaire de favoriser la croissance des grains qui présentent cette orientation. Dans cette étude, il est proposé de favoriser la croissance des grains {111} en insérant des germes {111} dans la couche imprimée. Dans un premier temps, un grand nombre de grains {111} est utilisée comme source de matière pour le processus de transfert. Ceci peut être réalisé en déposant une couche mince orientée {111} par évaporation thermique avant l'étape d'impression de nanoparticules. Une phase d'accroche de titane de 50 nm est déposée à température ambiante sur silicium avant de procéder au dépôt de 200 nm d'or présentant une texture de fibre {111}, comme présenté dans [75]. En effet, du fait que l'or forme facilement une solution solide avec l'argent et que son coefficient d'hétérodiffusion dans l'argent est relativement élevé ($D = 4 \cdot 10^{-16}$ $cm^2 \cdot s^{-1}$ à 300 °C) [76], le transfert de texture est favorisé.

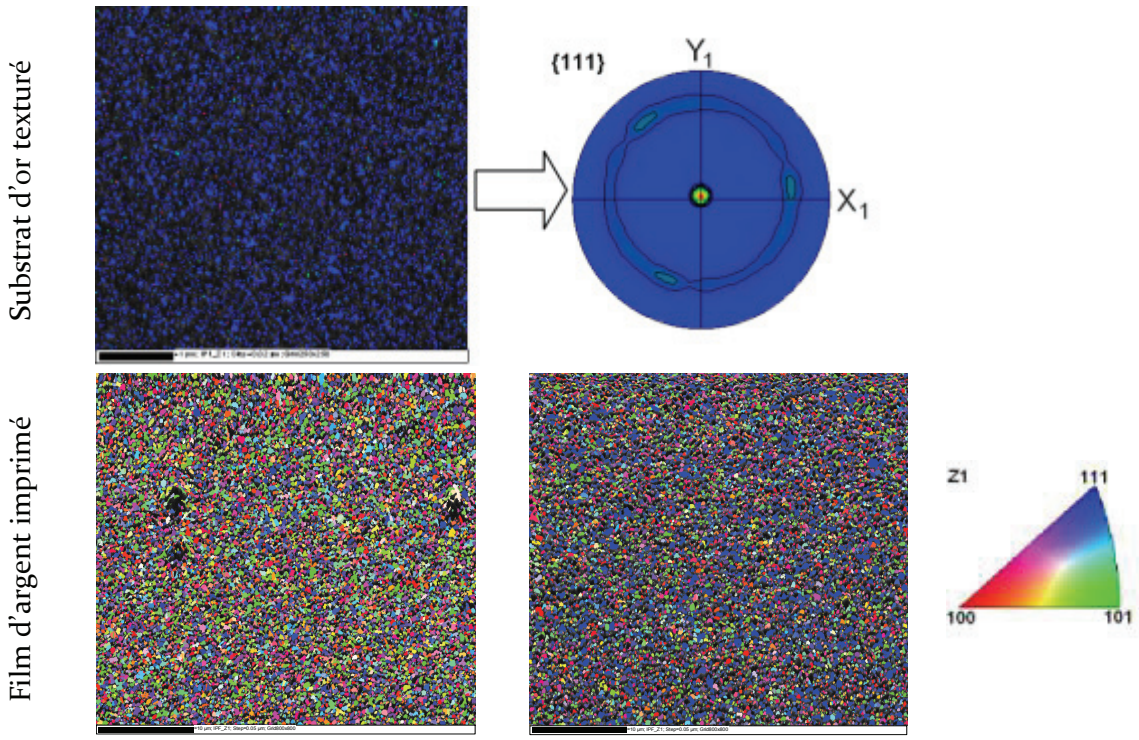

Figure 16: Cartographies d'orientations suivant la normale au plan du film (en couleurs d'IPF) réalisées à la surface du substrat d'or (haut gauche) avec la figure de pôle correspondante (haut droite) ; et à la surface d'un film d'argent après recuit à 500 °C sur un substrat de silicium (bas gauche) ou d'or (bas droite). Échelle = 10 µm.

Une analyse de la texture cristallographique des films minces d'argent imprimé est réalisée à partir des cartographies d'orientations obtenues par EBSD. Il apparaît que l'énergie d'activation pour une texturation {111} est obtenue pour une température de 500 °C. Dans le cas où les nanoparticules d'argent sont déposées sur un substrat texturé d'or, cette énergie

d'activation est atteinte à partir de 300 °C grâce à l'énergie fournie par l'interdiffusion verticale de l'or dans l'argent, et réciproquement. En augmentant davantage la température de recuit, une texture de fibre cristallographique {111} marquée est obtenue à 500 °C (voir Figure 16). Le dépôt d'une sous-couche texturée permet donc à la fois de transférer une texture mais aussi de favoriser la croissance de grain, comme observé avec la présence de grains traversant sur la Figure 17.

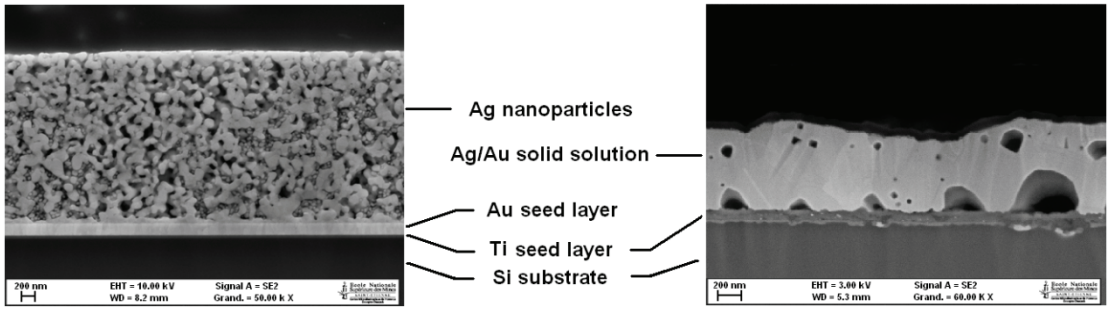

Figure 17 : Image MEB de la section d'un film Ag/Au/Ti/Si film obtenu par polissage ionique après un recuit à 300 °C (gauche) et après 500 °C (droite). La microstructure poreuse de la couche d'argent (gauche) doit être comparée à celle plus dense de la phase d'accroche, que l'on retrouve dans la solution solide Ag/Au (droite).

Une analyse de la couche mince d'argent par DRX a, par ailleurs, permis de mettre en évidence un affinement et une augmentation de l'intensité des pics correspondant à une convergence des orientations cristallographique des grains autour de {111} et {200}, confirmant ainsi les résultats obtenus par EBSD. L'affinement des pics {111} et {200} indique que le phénomène de guérison/recristallisation se stabilise à partir de 300 °C. Le rapport de l'aire sous le pic {200} et de celle du pic {111} indique, par ailleurs, une diminution de la population de grains {200} en faveur des grains {111}. Ces observations semblent plaider en faveur d'une coalescence motivée par la minimisation de l'énergie de surface/interface qui favorise la croissance des grains {111}.

Deux hypothèses peuvent expliquer ces observations : soit une croissance préférentielle des grains {111} dans l'ensemble du dépôt de manière homogène, soit une croissance colonnaire à partir de la couche d'or réalisée par évaporation. Des mesures exécutées par EBSD en fonction de l'épaisseur du film, sur environ 2900-3900 grains, montrent qu'après un recuit à 500 °C pendant 15 min une texture de fibre {111} est observable seulement sur les films dont l'épaisseur est inférieure à 1 µm. Cette valeur est cohérente avec la valeur critique de 1.5 µm trouvée par Greiser [40].

Ce résultat prouve donc la possibilité d'orienter cristallographiquement une couche mince imprimée de nanoparticules d'argent, tout en réduisant la porosité apparente (voir Figure 17). Ceci permet d'envisager un renforcement mécanique de la couche, notamment pour les étapes de connections filaire ou d'insertion flip chip. En outre, un contrôle des paramètres du procédé permet des réaliser des systèmes bi-couche avec une couche inférieure renforcée,

orientée préférentiellement {111}, qui garantira une meilleure adhésion avec le substrat, et une couche supérieure poreuse et ductile qui permettra dans une certaine mesure d'accommoder la déformation lors de l'étape de connexion comme on le verra dans la partie suivante.

III. Fabrication d'interconnections imprimées pour les assemblages microélectroniques

Après avoir considéré la dépendance de la microstructure avec les conditions de recuit, dans cette partie sera traitée l'influence de cette microstructure sur les propriétés d'usage des films imprimés par jet de matière.

A. Caractérisation mécanique des films minces imprimés

Les propriétés mécaniques des films minces polycristallins peuvent être caractérisées par plusieurs méthodes. En particulier, dans cette partie, les techniques de mesure du module d'Young par le test de gonflement de membrane et par nanoindentation sont appliquées aux films nanoporeux dont l'épaisseur est comprise entre 800 et 1000 nm.

Pour des températures de recuit comprises entre 130 °C et 800 °C, et un temps de recuit de 15 min, le module d'Young augmente de manière significative (voir Figure 18). Les mesures exécutées par gonflement et par nanoindentation donnent des résultats similaires pour des températures inférieures à 300 °C. Au-delà, les mesures ne concordent pas. Dans le cas de la nanoindentation, une valeur asymptotique est atteinte à 72 ± 20 GPa, alors que dans le cas des mesures par gonflement, cette valeur est portée à 90 ± 3 GPa. Ces valeurs sont à comparer à la valeur de l'argent massif, à savoir 83 GPa. Les mesures réalisées pour des recuits à haute température présentent une dispersion beaucoup plus importante que ceux à basse température. Pour un recuit à 130 °C, la valeur du module d'Young extraite par nanoindentation est ainsi de 19 ± 0.4 GPa. Cette dispersion provient de l'importante hétérogénéité de microstructure du film lorsque le recuit est réalisé à haute température. En effet, le phénomène de minimisation de l'énergie de surface a tendance à la fois à faire croître les grains et à favoriser le regroupement des porosités.

Il est à noter que les mesures de nanoindentation conduisent à des valeurs de module d'Young plus faible que celles fournies par la méthode de gonflement. En effet, la pression exercée par la pointe du nanoindenteur engendrerait l'effondrement de la structure poreuse, affectant ainsi la mesure.

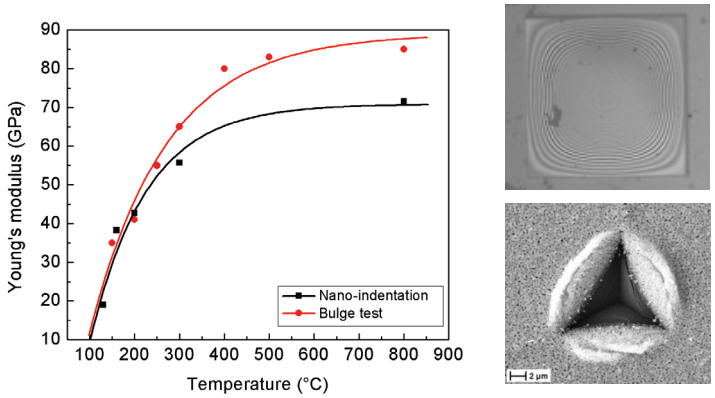

Figure 18: Évolution du module d'Young du film à base de nanoparticules d'argent recuit au RTA avec une rampe de 10 °C/s sur un substrat silicium par la technique du gonflement de membrane (rouge) et la nanoindentation (noir). Déflection observée par interférométrie (haut à droite) et indent sur un film recuit à 400 °C.

Lors de la constitution du film conducteur lors du recuit, un champ de contraintes internes peut être généré en lien avec les propriétés thermomécaniques des matériaux, ainsi que les variations de microstructures ou de géométrie. Le contrôle de ces contraintes internes est particulièrement recommandé lorsque des systèmes multi-matériaux hétérogènes sont considérés. La détermination des contraintes internes dans le film d'argent imprimé a été réalisée avec un montage in-situ qui permet de faire des mesures de diffraction au cours du cycle thermique (voir Figure 19, à gauche). L'expérience a montré que la génération de contraintes dans le film imprimé était vraiment très limitée et se produisait principalement au cours du refroidissement. En effet, alors que pendant le chauffage, les contraintes sont quasiment nulles, la contrainte résiduelle après refroidissement s'élève à 70 MPa, ce qui est environ trois fois inférieur aux contraintes observées dans les films d'épaisseur similaire déposés par pulvérisation cathodique [49].

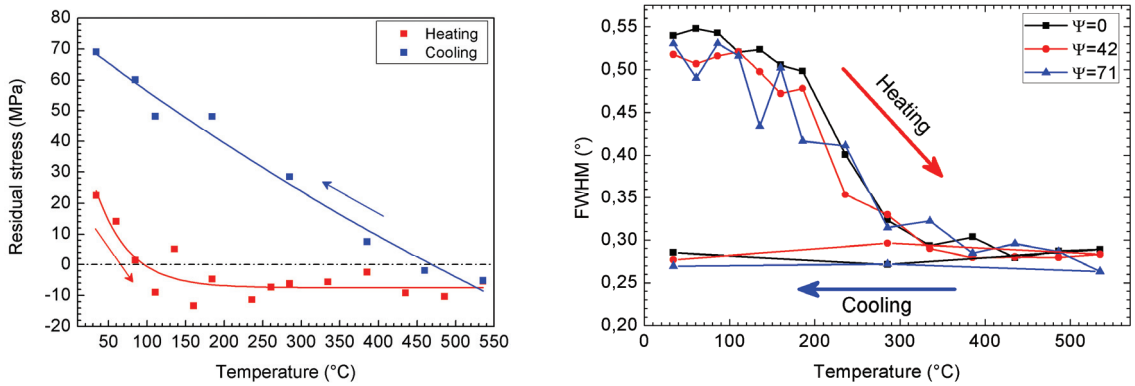

Figure 19 : Détermination par DRX in-situ des contraintes internes en fonction de la température réalisée sur un film de 330 nm d'épaisseur (gauche) et évolution correspondante de la largeur à mi-hauteur du pic de diffraction {111} réalisée à plusieurs valeurs d'angle de mesure ψ montrant une stabilisation de la microstructure à partir de 300 °C.

Il est à noter que lors de l'étape de chauffage, l'évaporation des solvants et l'adhésion entre les nanoparticules et le substrat s'initient. En raison de la différence de coefficient d'expansion thermique, les contraintes décroissent jusqu'à entrer en compression à partir de 100 °C, à l'instar des films déposés par évaporation ou pulvérisation [49]. Au-delà de cette température, le film peut être considéré comme totalement relaxé. La contrainte résiduelle en traction à la fin du cycle thermique est principalement générée lors du refroidissement (voir Figure 19). Dans notre cas, la microstructure se stabilise à partir de 300 °C mais l'interface avec le substrat n'est pas parfaite avec des porosités de l'ordre du micron. En conséquence, les contraintes en traction présentent à l'interface à cause de la différence de coefficients d'expansion thermique entre l'argent et le substrat sont accommodées sans transfert de charge.

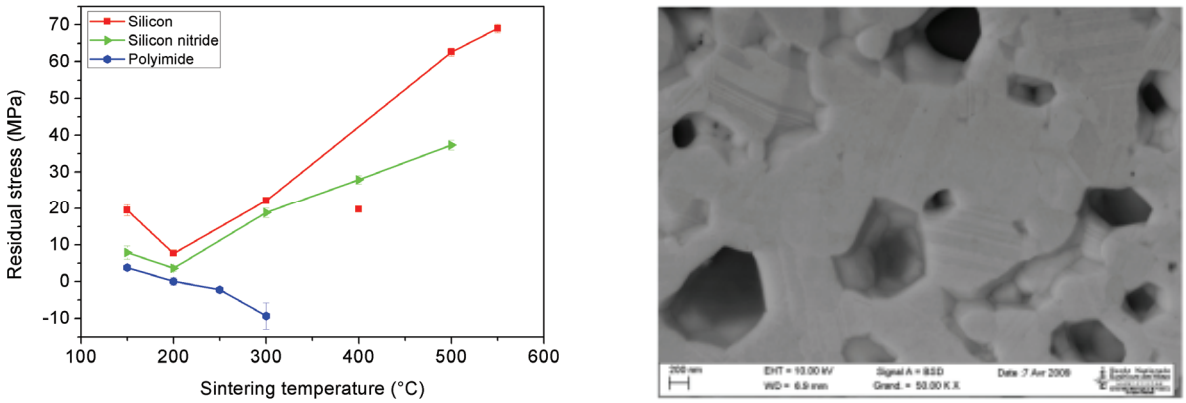

Figure 20 : Contraintes résiduelle en fonction de la température de recuit pour différent substrats (gauche) et image MEB de la surface d'un film d'argent imprimé et recuit, au niveau de l'interface avec le substrat de silicium (droite). Les porosités ainsi que le matage des grains sont clairement observables.

Une détermination des contraintes résiduelles, autrement dit après refroidissement, des films d'argent imprimés sur différents substrats indique que plus la température de recuit est faible, plus les contraintes résiduelles le seront également (voir Figure 20, à gauche). Lors du refroidissement, la différence de CET entre l'argent ($\alpha_{Ag} = 19 \cdot 10^{-6}$ K^{-1}) et le substrat sur lequel il est déposé (silicium $\alpha_{Si} = 3 \cdot 10^{-6}$ K^{-1}, nitrure de silicium $\alpha_{SiNx} = 3.3 \cdot 10^{-6}$ K^{-1} ou polyimide $\alpha_{PI} = 20 \cdot 10^{-6}$ K^{-1}) génère des contraintes qui sont partiellement accommodées par la présence des surfaces libres des porosités (voir Figure 20, à droite). La faible valeur de contraintes résiduelles générée dans les films minces imprimées est d'autant plus intéressante qu'elles ont tendance à diminuer quand l'épaisseur du film est augmentée ce qui ouvre la voie à des films complètement relaxés pour les architectures d'interconnexion 3D notamment.

B. Comportement électrique de lignes imprimées

Pour la réalisation d'interconnexions électroniques, il est particulièrement important que les pistes conductrices réalisées présentent une très faible résistivité à la fois pour éviter les pertes de signal notamment pour les applications préférentielles et les échauffements par effet Joule. Le problème est particulièrement significatif quand le confinement géométrique est du même ordre de grandeur que le libre parcours moyen des électrons (λ_0[Ag] = 52 nm).

i. Comportement en courant continu

Au cours du recuit, parallèlement à la modification de microstructure induite par la diffusion atomique, une importante diminution de la résistivité électrique s'opère. Ainsi, la résistivité est d'autant plus faible que la température ou le temps de recuit est important (voir Figure 21). Elle décroît, en effet, exponentiellement jusqu'à atteindre la valeur de l'argent massif, à savoir 1,617 µOhm·cm. Une variation de la rampe de chauffage ne semble toutefois impacter qu'à faible température (T < 300 °C). Ceci est directement corrélé à la variation de microstructure déjà observée précédemment.

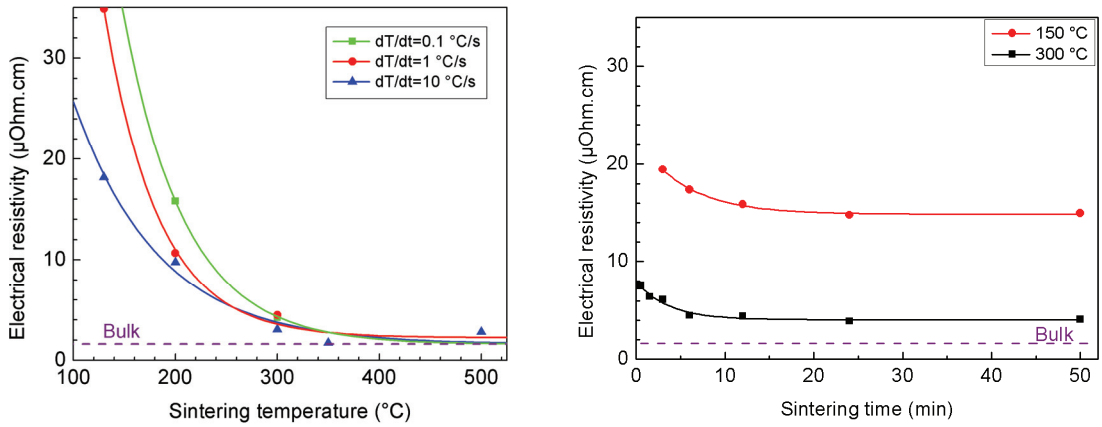

Figure 21 : Évolution de la résistivité électrique en fonction de la température, pour un temps de recuit fixé à 10 min (gauche), et en fonction du temps pour un recuit à 150 °C et 300 °C (droite).

La première condition pour permettre la conduction électrique étant que les nanoparticules métalliques entrent en contact, il faut pour cela évacuer les solvants et le polymère d'enrobage. Un recuit à faible température ne permet pas d'éliminer l'ensemble de ces composés et réduit donc les possibilités de diffusion atomique en surface. Un temps plus important de recuit ne permettra donc pas de réduire davantage la résistivité par manque d'énergie thermique pour activer des mécanismes de croissance de grain. En effet, la taille des grains du film impacte directement ses propriétés électriques car les joints de grains constituent des sources de diffusion pour les électrons. Ceux-ci agissent ainsi comme des

barrières de potentiel pour le passage des électrons. Les électrons sont donc d'autant plus ralentis qu'il y a de nombreux joints de grain.

Mayadas et Shatzkes ont formulés en 1970 l'impact de la taille moyenne des grains d'un film polycristallin sur sa résistivité électrique [68]. Pour cela, les joints de grains sont assimilés à des barrières de potentiel pour le transport des électrons dont la probabilité d'être réfléchi est donné par le coefficient de réflexion aux joints de grain, *R*. D'après le modèle de Mayadas et Shatzkes, la résistivité électrique d'un film polycristallin est donné par :

$$\rho_f = \rho_0 \cdot \left[1 - \frac{3}{2}\alpha + 3\alpha^2 - 3\alpha^3 ln\left(1 + \frac{1}{\alpha}\right)\right]^{-1} \quad (2)$$

avec

$$\alpha = \frac{\lambda_0}{G}\frac{R}{1-R} \quad (3)$$

où λ_o est le libre parcours moyen d'un électron, R est le coefficient de réflexion aux joints de grain, et G est le diamètre moyen des grains. La valeur de *R* peut ainsi varier entre 0 pour un joint de grain totalement transparent et 1 pour une réflexion totale. Dans ce dernier cas, les électrons sont alors confinés dans chaque grain.

Après détermination de G par EBSD, les mesures de résistivité électrique montrent que la valeur du coefficient de réflexion aux joints de grains évolue en fonction des conditions de recuit appliquées à la couche mince, comme observé précédemment par Marom *et al.* [73]. Ainsi, dans la plage de températures comprise entre 150 °C et 500 °C, le coefficient décroît de 0,9 à 0,6 (voir Figure 22). Cette diminution indique une amélioration de la qualité du joint de grains provenant d'une plus grande cohérence cristalline entre les grains et les macles.

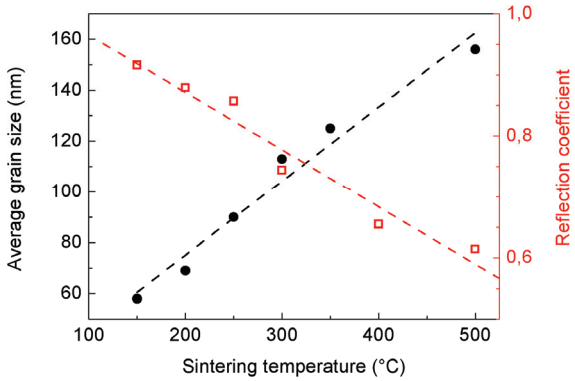

Figure 22 : Évolution de la taille de grain et du coefficient de réflexion aux joints de grain en fonction de la température de recuit (RTA), déterminé à partir du Modèle de Mayadas-Shatzkes.

Cette plus grande cohérence peut être obtenue par un recuit densifiant ou par un recuit assisté par diffusion (voir Partie II). La Figure 23 montre l'impact d'une sous-couche d'or

texturé sur la résistivité électrique et le coefficient de réflexion de la couche d'argent imprimée. Dans cette configuration, seulement 30 % des électrons diffusent à l'interface entre les grains pour un recuit à 500 °C, alors que la proportion s'élève à 60 % dans le cas où un substrat de silicium est utilisé (voir Figure 23). Cette valeur est cohérente avec les expériences réalisées en 2004 par Zhang *et al.* [71] sur des films minces présentant une orientation cristallographique préférentielle {111}. Cette méthode de transfert de texture permet donc d'améliorer la cohérence des joints de grain par rapport aux films déposés directement sur silicium (sans couche d'or donc).

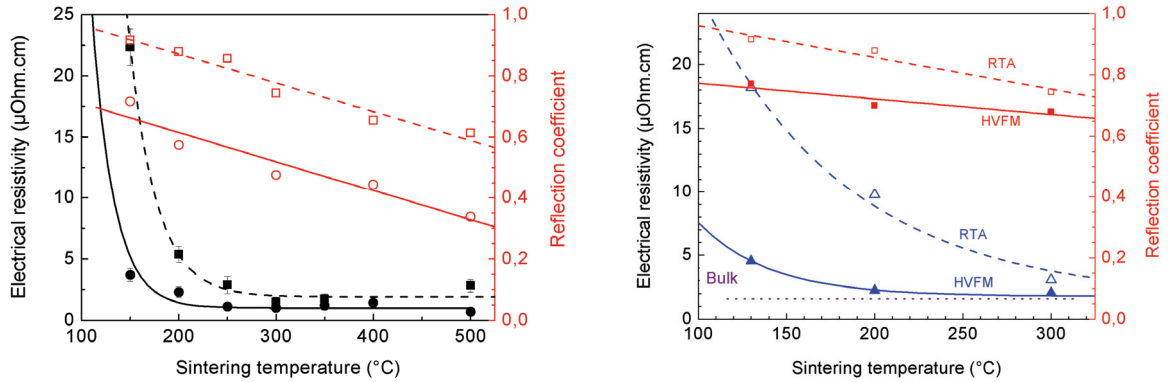

Figure 23 : Évolution de la résistivité électrique (noir) et du coefficient de réflexion aux joints de grain (rouge) pour un recuit au RTA avec ou sans sous-couche d'or (gauche) ou au micro-onde HVFM (droite). La rampe de chauffage est fixée à 10 °C/s et le temps de recuit à 15 min.

Cette méthode a aussi été utilisée sur les films d'argent imprimés et recuit par micro-ondes. Lors de ce type de recuit, une croissance importante des grains a été constatée en lien avec une importante diminution de la résistivité électrique, inférieure à 8 µΩ·cm (voir Figure 23). A l'instar du recuit rapide au RTA, la résistivité converge ainsi vers la résistivité de l'argent massif lorsque la température de recuit augmente. Dans les deux cas, les valeurs du coefficient de réflexion sont relativement proches en dépit d'une résistivité plus faible pour les recuits par micro-ondes. La décroissance de la résistivité observée est donc principalement liée à l'augmentation de la taille de grain, plutôt qu'à l'amélioration de la cohérence entre les grains. Le recuit par micro-ondes semble n'avoir qu'un effet limité sur la qualité des joints de grain, contrairement à la coalescence assistée par interdiffusion qui conduit à un coefficient de réflexion de 0,3 à 500 °C.

ii. Comportement radio-fréquentiel de lignes coplanaires

La présence de porosités dans les films d'argent après recuit peut conduire à l'apparition d'effets inductif ou capacitif lorsqu'un courant alternatif y circule. Ces effets, qui varient avec la fréquence, influent sur la propagation du signal et un phénomène de filtrage peut ainsi

apparaître. Sous l'effet de la fréquence, le transport des électrons a tendance à être confiné à la surface des conducteurs, dans une région appelée épaisseur de peau. Johnson et Graham ont ainsi montré en 1993 que les courants de faible fréquence avaient tendance à rechercher des chemins de conduction les moins résistifs alors que les courants à haute fréquence tendait à emprunter les chemins les moins inductifs [74].

Lorsque la longueur du conducteur est plus grande que la longueur d'onde du signal transporté, le potentiel électrique ne peut plus être considéré comme uniforme en tout point du conducteur. Le conducteur doit alors être considéré comme une ligne de transmission au sein duquel des interférences sont générées par le retard de phase entre les ondes incidentes et réfléchies aux extrémités. Des lignes coplanaires sont communément utilisées pour caractériser le comportement radiofréquence de ces lignes de transmission (voir Figure 24). Afin de minimiser les pertes de puissance du signal transmis, l'impédance caractéristique des lignes coplanaires doit être adaptée à l'impédance du système, conventionnellement fixée à 50 Ω. Cette impédance caractéristique de lignes coplanaires dépend à la fois de la géométrie des lignes conductrices et des capacités d'absorption du substrat (pertes diélectriques).

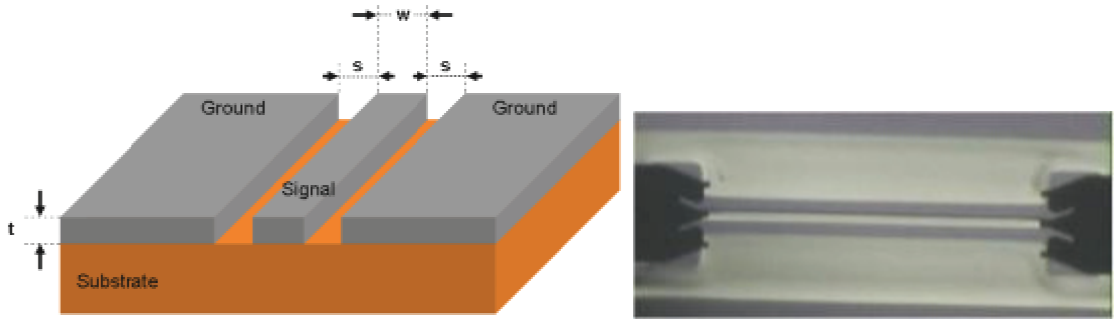

Figure 24 : Description d'un système de lignes coplanaires et photographie des pointes masse-signal-masse posées sur des lignes imprimées par jet de matière.

Les coefficients de diffraction donnés par les paramètres S reliant les ondes incidentes et réfléchies du quadripôle considéré sont extraits à l'aide d'un analyseur de réseau vectoriel et de pointes masse-signal-masse (voir Figure 24). Une mesure des pertes en insertion et en retour pour différentes longueurs de lignes mettent en évidence l'homogénéité de microstructure des lignes imprimées. L'atténuation du signal par unité de longueur varie ainsi de 2,6 dB/mm à 10 GHz, à 3 dB/mm à 20 GHz. La température de recuit des lignes imprimées ne semble que peu influer également sur les pertes (voir Figure 25). Ainsi, entre 200 °C et 500 °C, les pertes en insertion varient de 2,6 dB/mm à 2,2 dB/mm à 10 GHz. Cette faible diminution des pertes en insertion, alors que dans le même temps, la résistivité électrique décroît, montre l'influence majeure de la résistance de surface et de l'effet de peau sur les pertes totales. Les pertes en insertion ne peuvent alors être réduites qu'en augmentant l'épaisseur du dépôt.

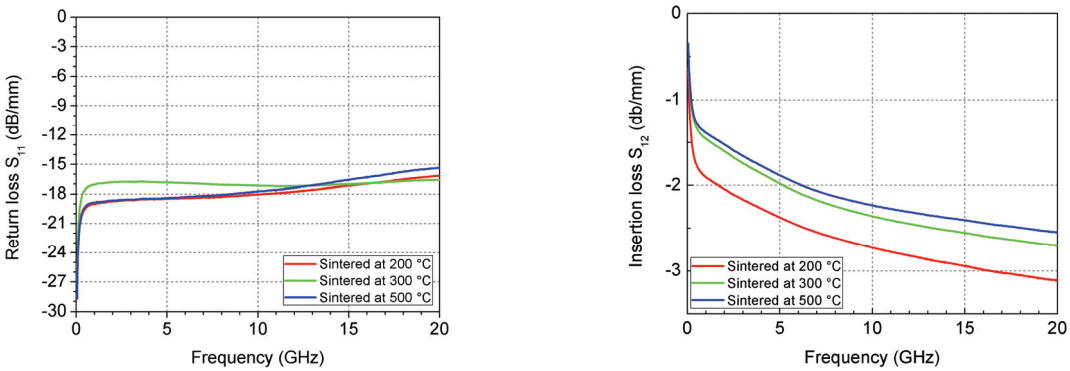

Figure 25 : Pertes en retour (gauche) et en insertion (droite) par unité de longueur en fonction de la température de recuit sur un substrat de nitrure de silicium (rampe de 10 °C/s au RTA).

Les lignes coplanaires sont généralement modélisées en utilisant un modèle à éléments distribués de type résistances, capacitances et inductances. Dans ce modèle, la résistance et l'inductance du conducteur varient en fréquence alors que le couplage avec les lignes de masses est pris en compte par une capacité de couplage latéral (voir Figure 26). Dans cette étude, un nouveau modèle est proposé pour prendre en compte la présence de pores à l'intérieur du conducteur métallique. Les deux modèles ont été confrontés aux données expérimentales en utilisant le logiciel Mathcad (voir Figure 27).

Figure 26 : Circuits équivalents d'une ligne de transmission (gauche) et d'une ligne nanoporeuse (droite).

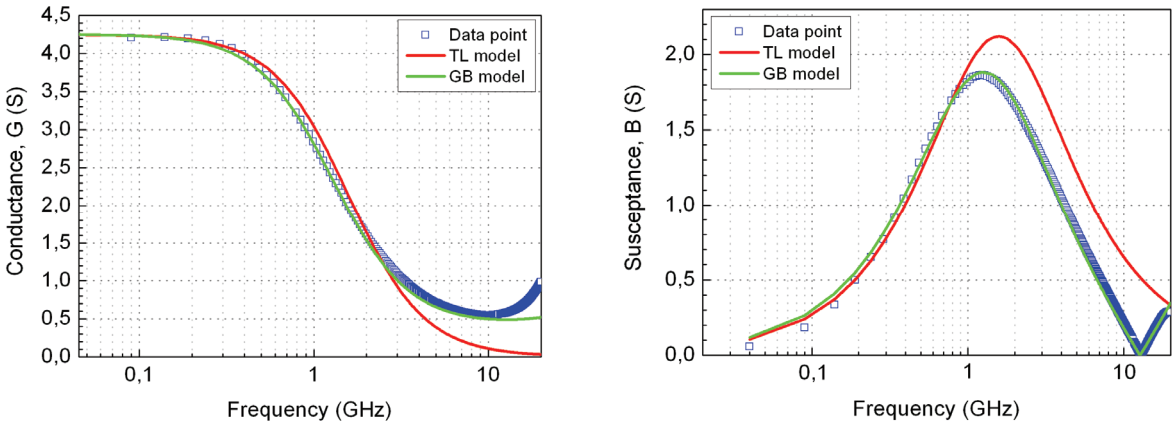

Figure 27 : Ajustement des deux modèles par rapport aux données expérimentales dans le cas de lignes de 4,5 mm recuites 200 °C.

La contribution résistive de l'impédance équivalente, notée RSK, est indépendante de la fréquence jusqu'à 1 GHz, fréquence à partir de laquelle elle augmente avant de se stabiliser. D'après le modèle proposé, l'augmentation de la résistance totale provient de l'augmentation de la densité de courant en périphérie de grain à cause de l'effet de peau. Étant donné que la taille des grains augmente avec la température de coalescence, la résistance de surface augmente de manière similaire (voir Table 2).

Table 2 : Extraction des éléments distribués à partir du modèle proposé

Température de recuit	R_{NP} (mΩ)	R_{SK} (Ω)	C_P (pF)	L_{SK} (pH)
200 °C	240	1.7	6	24
300 °C	90	2	5	29.5
500 °C	100	2	5.5	29.5

En parallèle, une résonance se produit à 1,3 GHz en raison d'un filtrage de type LC. L'effet capacitif est attribué à la présence des pores dans le conducteur qui décroît pour des températures de recuit plus élevées. En effet, lors du recuit, les pores fusionnent avant de s'annihiler sous l'effet de la densification de la couche. En ce qui concerne l'effet inductif, il est attribué à un couplage entre les porosités de la couche. Cette valeur est en effet considérée comme plus importante que l'inductance associée au grain en tant que tel. La valeur de cette inductance augmente avec la température de recuit ce qui est cohérent avec une fusion des pores pour minimiser l'énergie des surfaces libres, qui, en se rapprochant augmentent l'inductance associée.

C. Fabrication de lignes de redistribution compatibles avec les technologies conventionnelles d'interconnexion électrique

L'implémentation de structures imprimées pour les micro-assemblages électroniques est conditionnée à leur compatibilité avec les procédés ultérieurs de connexion filaire entre les pistes conductrices et les plots de connexion du circuit intégré. Cette étape requière généralement la présence d'une métallisation épaisse et rigide pour absorber la déformation mécanique lors de l'étape de câblage. L'impossibilité de procéder à un câblage direct des couches d'argent imprimées par jet de matière oblige à trouver des approches alternatives.

L'approche la plus couramment employée est le recours à une croissance electroless de nickel sur les couches métalliques suivi d'une étape d'immersion dans un bain d'or. Le procédé ENIG, pour *Electroless Nickel Imersion Gold*, se base sur une réaction autocatalytique qui permet un dépôt sélectif d'une couche rigide de nickel uniquement sur les structures métalliques. Ce procédé est donc particulièrement adapté pour la réalisation de

composant sur des substrats polymère souple car il laisse intact le substrat. Il permet de réaliser des couches dont l'épaisseur peut aisément atteindre le micron.

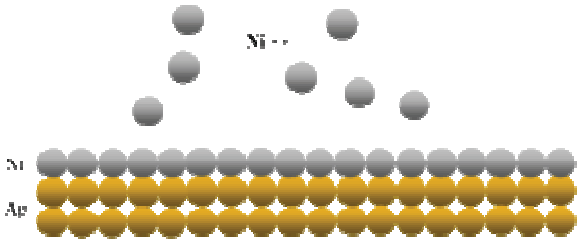

$$Ni^{2+} + H_2PO_2^- + H_2O \Leftrightarrow Ni + H_2PO_3^- + 2H^+$$

Figure 28 : Réaction en jeu dans le bain electroless lors du dépôt de la couche de nickel sur l'argent.

Le procédé ENIG peut être opéré avec succès sur des couches imprimées sur polyimide. Ces structures renforcées sont alors parfaitement compatibles avec la réalisation de câblage filaire en or dans des conditions de procédé standards (voir Figure 29).

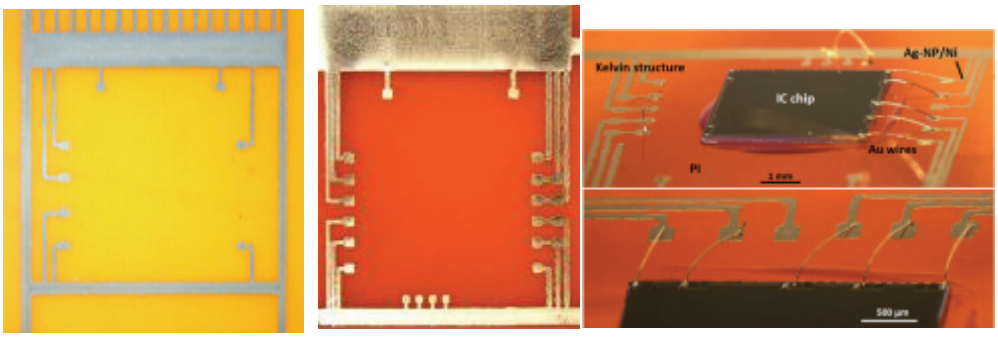

Figure 29 : Structure de test imprimée sur polyimide.

Une caractérisation de la tenue des fils par une méthode standardisée d'arrachement de fil rend compte de la compatibilité de ce procédé avec les standards de la microélectronique MIL STD 883. Les fils d'or sur pistes renforcées présentent ainsi une résistance à la traction normale de 3 g. Cette amélioration de la soudabilité peut s'expliquer à la fois par une augmentation de l'épaisseur, par une augmentation de la rigidité et une amélioration de l'adhésion. Une résistance à la traction de cette couche imprimée de 9 MPa a ainsi été mesurée avec une rupture de l'interface entre le nickel et l'argent.

Des résultats probants ont été également été mis en œuvre sur le système bi-couche obtenue par texturation partielle {111}. Dans cette configuration, les connexions filaires résistent en effet à une traction normale allant jusqu'à 10 g, et à une force de cisaillement allant jusqu'à 34 g. Ces performances accrues ouvrent ainsi de nouvelles voies pour la réalisation d'interconnexions sur des motifs imprimés par jet de matière.

Conclusion

L'objet de ces travaux était de configurer un prototype d'impression par jet de matière afin d'obtenir des structures conductrices permettant l'interconnexion de composants microélectroniques. Pour parvenir à cela, les différentes interactions en jeu lors du procédé d'impression ont été considérées. L'optimisation des différents paramètres de l'équipement a ainsi permis de réaliser avec une bonne reproductibilité des lignes conductrices présentant des largeurs de 90 µm sur polyimide et 130 µm sur nitrure de silicium, pour une épaisseur de 500 nm. Ces dimensions caractéristiques sont compatibles avec les spécifications définies par Gemalto.

Afin de garantir des propriétés optimales de ces lignes, tant sur le plan électrique que mécanique, une étude de l'évolution microstructurale des dépôts en fonction de la méthode de recuit et des paramètres employés a été conduite. Cette étude a permis de mettre en évidence une croissance particulièrement importante des grains au cours du recuit, pouvant aller jusqu'au micron. Le suivi de la microstructure, par EBSD et DRX, montre clairement une corrélation entre une faible énergie d'activation de la croissance de grain (< 5 $kJ.mol^{-1}$) et une importante densité de macles (1.6 %) à l'état initial. Cette diffusion améliorée dans les nanoparticules a ainsi pu être exploitée pour permettre des transférer une texture cristallographique depuis une phase d'accroche, présentant une orientation préférentielle, à la couche imprimée de nanoparticules. Un contrôle de l'extension du front de croissance permet alors réaliser un système bi-couche avec une répartition spécifique. Les propriétés mécaniques du système permettent alors d'envisager des étapes de connexions filaires.

Les films composés uniquement de nanoparticules coalescées d'argent présentent ainsi une forte densité de porosité qui rend la couche plus malléable que l'argent massif. La présence de porosités permet néanmoins à ces couches de limiter le développement de contraintes résiduelles (< 70 MPa), contrairement aux films minces déposés par méthode conventionnelle. D'un point de vue électrique, l'optimisation des paramètres de recuit permet d'atteindre de faibles valeurs de résistivité (3.4 µOhm·cm après 15 min), soit deux fois la valeur de l'argent massif. L'impact de la cohérence entre les réseaux cristallins des nanoparticules au niveau des joints de grains a été souligné via l'introduction d'un paramètre rendant compte d'un phénomène de réflexion aux interfaces. Ainsi, si l'utilisation d'un recuit par micro-ondes permet de réduire la température d'activation de la coalescence par rapport à un recuit par RTA, seule une méthode de recuit assisté par interdiffusion permet d'augmenter cette cohérence cristalline et de diminuer davantage la résistivité.

Un renforcement mécanique des lignes imprimées, soit via la mise en œuvre d'un système bi-couche par interdiffusion, soir par une méthode de croissance sélective par electroless, permet de réaliser les étapes de micro-assemblage filaires. Dans les deux cas, la qualité des soudures via leur résistance à une traction normale et en cisaillement qui sont compatibles avec les normes en vigueur dans l'industrie microélectronique. La réalisation de

démonstrateurs fonctionnels a ainsi permis de valider la capacité de la technologie d'impression pour la fabrication d'assemblages hétérogènes de composants électroniques.

Ces travaux de thèse ouvrent de nombreuses perspectives pour la réalisation de composants microélectroniques que ce soit au niveau du système d'impression ou de la réalisation d'encres composites. En particulier, les développements les plus avancés concernent l'impression d'encres fortement chargée en nanoparticules dont le diamètre est inférieur à 10 nm, couplé à un recuit sélectif de type thermo-photonique. Cette combinaison permettrait d'augmenter la capacité de production d'objets sécurisés couplant les technologies silicium et l'électronique imprimée.

Bibliographie

[1] D. Pellecuer, "Les tops et les flops depuis le début de la crise," url : http://archives.investir.fr/2008/jdf/20080930ARTJDF00116-les-tops-et-les-flops-depuis-le-debut-de-la-crise.php, 2008. Retrieved on 29/05/2012.

[2] N. Seth, "Gemalto - global leader in digital security," url: http://www.frost.com/prod/servlet/market-insight-top.pag?docid=76001395, 2006. Retrieved on 29/05/2012.

[3] S. H. Ko, H. Pan, C. P. Grigoropoulos, C. K. Luscombe, J. M. J. Fréchet, and D. Poulikakos, "All-inkjet-printed flexible electronics fabrication on a polymer substrate by low-temperature high-resolution selective laser sintering of metal nanoparticles," *Nanotechnology*, vol. 18, no. 34, p. 345202, 2007.

[4] J. Perelaer, B.-J. de Gans, and U. S. Schubert, "Ink-jet printing and microwave sintering of conductive silver tracks," *Advanced Materials*, vol. 18, no. 16, pp. 2101–2104, 2006.

[5] M. L. Allen, M. Aronniemi, T. Mattila, A. Alastalo, K. Ojanperä, M. Suhonen, and H. Seppä, "Electrical sintering of nanoparticle structures," *Nanotechnology*, vol. 19, no. 17, pp. 175201–, 2008.

[6] L. Rayleigh, "On the capillary phenomena of jets," *Proceedings of the Royal Society of London*, vol. 29, pp. 71–97, 1879.

[7] S. Tomotika, "On the instability of a cylindrical thread of a viscous liquid surrounded by another viscous fluid," *Proceedings of the Royal Society of London. Series A, Mathematical and Physical Sciences*, vol. 150, no. 870, pp. 322–337, 1935.

[8] J. Perelaer, *Microstructures prepared via inkjet printing and embossing techniques*. PhD thesis, Technische Universiteit Eindhoven, 2009.

[9] R. Dannenberg, E. Stach, J. R. Groza, and B. J. Dresser, "Tem annealing study of normal grain growth in silver thin films," *Thin Solid Films*, vol. 379, pp. 133–138, Dec. 2000.

[10] C. V. Thompson, "Grain growth in thin films," *Annual Review of Materials Science*, vol. 20, pp. 245–268, 1990.

[11] R. Dannenberg, E. A. Stach, J. R. Groza, and B. J. Dresser, "In-situ tem observations of abnormal grain growth, coarsening, and substrate de-wetting in nanocrystalline Ag thin films," *Thin Solid Films*, vol. 370, pp. 54–62, 2000.

[12] A. Guinier, *X-ray diffraction in crystals, imperfect crystals, and amorphous bodies*. Dover, 1994.

[13] B. Warren, *X-ray diffraction*. Dover Publications, 1990.

[14] B. E. Warren and B. L. Averbach, “The effect of cold-work distortion on x-ray patterns,” *Journal of Applied Physics*, vol. 21, no. 6, pp. 595–599, 1950.

[15] A. R. Stokes, “A numerical fourier-analysis method for the correction of widths and shapes of lines on x-ray powder photographs,” *Proceedings of the Physical Society*, vol. 61, no. 4, pp. 382–, 1948.

[16] C. V. Thompson, “Secondary grain growth in thin films of semiconductors: Theoretical aspects,” *Journal of Applied Physics*, vol. 58, no. 2, pp. 763–, 1985.

[17] M. Seita, C. M. Pecnik, S. Frank, and R. Spolenak, “Direct evidence for stress-induced texture evolution and grain growth of silver thin films upon thermal treatment and self-ion bombardment,” *Acta Materialia*, vol. 58, pp. 6513–6525, 2010.

[18] C. V. Thompson and R. Carel, “Texture development in polycrystalline thin films,” *Materials Science and Engineering B*, vol. 32, pp. 211–219, 1995.

[19] Y. Zeng, Y. L. Zou, and T. L. Alford, “Texture in evaporated Ag thin films and its evolution during encapsulation process,” *Thin Solid Films*, vol. 307, pp. 89–95, 1997.

[20] A. Bukaluk, “Analysis of diffusion mechanisms in thin polycrystalline Au-Ag films using auger electron spectroscopy,” *Surface and Interface Analysis*, vol. 5, no. 1, pp. 20–27, 1983.

[21] J. Greiser, P. Müllner, and E. Arzt, “Abnormal growth of "giant" grains in silver thin films,” *Acta Materialia*, vol. 49, pp. 1041–1050, 2001.

[22] T. C. Hodge, S. A. Bidstrup-Allen, and P. A. Kohl, “Stresses in thin film metallization,” *IEEE transactions on Components, Packaging, and Manufacturing Technology—part A*, vol. 20, no. 2, pp. 241–250, 1997.

[23] A. F. Mayadas and M. Shatzkes, “Electrical-resistivity model for polycrystalline films: the case of arbitrary reflection at external surfaces,” *Physical Review B*, vol. 1, pp. 1382–, 1970.

[24] H. Marom, M. Ritterband, and M. Eizenberg, “The contribution of grain boundary scattering versus surface scattering to the resistivity of thin polycrystalline films,” *Thin Solid Films*, vol. 510, pp. 62–67, 2006.

[25] H. Zhang and C. A. Mirkin, “Dpn-generated nanostructures made of gold, silver, and palladium,” *Chemistry of Materials*, vol. 16, pp. 1480–1484, 2004.

[26] H. Johnson and M. Graham, *High-speed digital design: a handbook of black magic*. Prentice Hall, 1993.

École Nationale Supérieure des Mines
de Saint-Étienne

NNT : *2012 EMSE 0643*

Romain CAUCHOIS

MICROSTRUCTURING INKJET-PRINTED DEPOSITS: FROM SILVER NANOPARTICLES COALESCENCE TO THE FABRICATION OF INTERCONNECTIONS FOR ELECTRONIC DEVICES

Speciality: Microelectronics

Keywords: Printed electronics, Inkjet-printing, Selective sintering, Coalescence, Nanoparticle, Resistivity, Interconnect

Abstract:

Several challenges are still holding back the technological transfer of printed electronics to industry in spite of recent progresses. In this thesis work, the printing method of inks based on silver nanoparticles (<Ø>=25 nm) was optimized according to its rheology and to the fluid/substrate interactions for the fabrication of electrical interconnections with a thickness of 500 nm. These lines were printed on silicon or flexible substrates and annealed either by conventional (oven or infrared) or selective methods (microwave) at temperatures comprised between 100 and 300 °C.

A better understanding of the relationship between process and microstructure of these printed thin films, based on several crystallographic equipments (XRD, EBSD and EDX), led to the optimization of nanocrystallites growth with an activation energy of about 3 to 5 $kJ \cdot mol^{-1}$. In addition to the low residual stress (70 MPa), this optimization is used to achieve low electrical resistivity (3.4 µOhm·cm) associated with a greater coherence of the crystal lattices at grain boundaries. The probability of electron scattering at such interfaces can be further reduced using an innovative approach of oriented crystallite growth by atomic interdiffusion from the substrate.

The low mechanical stiffness (E<50 GPa) of these porous lines requires a reinforcement step either by crystalline texturation or by electroless growth to withstand the assembly and wire-bonding steps. The fabrication of a functional demonstrator thus validated the printing technology for the manufacture of electronic components.

École Nationale Supérieure des Mines
de Saint-Étienne

NNT : *2012 EMSE 0643*

Romain CAUCHOIS

MICROSTRUCTURATION DES DEPOTS IMPRIMES PAR JET D'ENCRE : DE LA COALESCENCE DES NANOPARTICULES D'ARGENT VERS LA REALISATION D'INTERCONNEXIONS DE COMPOSANTS ELECTRONIQUES

Spécialité: Microélectronique

Mots clefs : Électronique imprimée, Jet d'encre, Recuit sélectif, Coalescence, Nanoparticule, Microstructure, Résistivité, Interconnexion

Résumé :

Plusieurs défis subsistent pour la migration de l'électronique imprimée vers l'industrie, malgré des avancées récentes. Dans ces travaux de thèse, l'optimisation du procédé d'impression d'encres à base de nanoparticules d'argent (<Ø>=25 nm) en fonction de sa rhéologie et des interactions fluide/substrat a permis de réaliser des interconnexions électriques d'une épaisseur de 500 nm. Ces lignes imprimées sur des substrats silicium ou flexibles sont ensuite recuites par des méthodes conventionnelles (étuve ou infrarouge) ou sélectives (micro-onde) à des températures comprises entre 100 et 300°C.

Une meilleure compréhension de la relation procédé/microstructure des couches minces imprimées, via plusieurs caractérisations cristallographiques (DRX, EBSD et EDX), a permis d'optimiser la croissance des domaines nanocristallins, activée pour des énergies de l'ordre de 3 à 5 $kJ \cdot mol^{-1}$. Outre les faibles contraintes résiduelles (70 MPa), cette optimisation permet d'atteindre de faibles résistivités électriques (3.4 µOhm·cm) associées à un accroissement de la cohérence des réseaux cristallins aux joints de grains. La probabilité de réflexion des électrons à ces interfaces peut être davantage réduite, grâce à une approche innovante de croissance orientée des cristallites par interdiffusion atomique à partir du substrat.

La faible rigidité mécanique (E<50 GPa) de ces lignes initialement poreuses nécessite une étape de renforcement par texturation ou par croissance electroless pour résister aux étapes de micro-assemblage et de soudure filaire. La réalisation d'un démonstrateur fonctionnel a ainsi permis de valider la technologie d'impression pour la fabrication de composants électroniques.